



PACIFIC EARTHQUAKE ENGINEERING RESEARCH CENTER

Seismic Evaluation of Reinforced Concrete Buildings Including Effects of Masonry Infill Walls

Alidad Hashemi

and

Khalid M. Mosalam

University of California, Berkeley

Seismic Evaluation of Reinforced Concrete Buildings Including Effects of Masonry Infill Walls

Alidad Hashemi

Department of Civil and Environmental Engineering
University of California, Berkeley

Khalid M. Mosalam

Department of Civil and Environmental Engineering
University of California, Berkeley

PEER Report 2007/100
Pacific Earthquake Engineering Research Center
College of Engineering
University of California, Berkeley

July 2007

ABSTRACT

A comprehensive study to evaluate the seismic performance of reinforced concrete (RC) buildings including unreinforced masonry (URM) infill walls is performed in three sequential parts: (1) shake-table experiments, (2) computational modeling, and (3) reliability-based performance evaluation. A hypothetical prototype building with RC frames, RC floor slabs, and URM infill walls is considered. A reduced-scale test structure was constructed to represent a substructure of the prototype building and subjected to a sequence of ground motions. The shake-table experiments and the global and local response of the test structure are discussed in detail. Several post-test computational modeling approaches and a detailed finite element (FE) model representing the URM infill walls are evaluated. The validated FE model is used to understand the in-plane and out-of-plane responses for RC frames with URM infill walls subjected to bidirectional seismic loading. A three-dimensional strut and tie (SAT) model is formulated for practical representation of the combined in-plane and out-of-plane failure surface in conventional computational platforms. Finally, the prototype building is considered to demonstrate a framework for practical reliability analysis of RC buildings containing URM infill walls, and fragility functions are determined for the prototype building subjected to near-fault ground motions.

ACKNOWLEDGMENTS

This work made use of the Earthquake Engineering Research Centers Shared Facilities supported by the National Science Foundation under award number EEC-9701568 through the Pacific Earthquake Engineering Research Center (PEER).

Any opinions, findings, and conclusions or recommendations expressed in this material are those of the author(s) and do not necessarily reflect those of the National Science Foundation.

The financial support for this project provided by the National Science Foundation under NSF contract no. CMS0116005 is gratefully acknowledged. The reinforcing bars for this project were generously donated by Mr. Tom Tietz, Western Regional Manager of the Concrete Reinforcing Steel Institute (CRSI).

Special thanks are due to Dr. Tarek Elkhoraibi and to EERC laboratory personnel at the Richmond Field Station, especially Dr. Shakhzod Takhirov, Mr. Don Clyde, and Mr. Wesley Neighbour for their assistance during the shake-table experiments.

CONTENTS

ABSTRACT	iii
ACKNOWLEDGMENTS	iv
TABLE OF CONTENTS	v
LIST OF FIGURES	ix
LIST OF TABLES	xvii
1 INTRODUCTION	1
1.1 General.....	1
1.2 Background and Objectives	3
1.3 Outline of Report	5
1.4 Report Contributions.....	7
2 PROTOTYPE STRUCTURE	9
2.1 Introduction.....	9
2.2 Test Structure	12
2.3 Computational Modeling	13
2.4 Effect of Column Axial Load	15
2.5 Effect of Lateral Loading.....	16
2.6 Modal Analysis of Prototype Building	21
2.7 Summary	23
3 DEVELOPMENT OF TEST STRUCTURE	25
3.1 Design Aspects.....	25
3.2 Construction Process.....	29
3.3 Shake-Table Facility and Fidelity Tests	32
3.4 Additional Mass Arrangement.....	34
3.5 Instrumentation	37
3.6 Summary.....	39
4 PRELIMINARY SYSTEM IDENTIFICATION	41
4.1 Component Tests	41
4.1.1 Concrete Cylinder Compression Tests.....	41
4.1.2 Concrete Cylinder Split Tension Tests	43

4.1.3	Masonry Compression Tests	43
4.1.4	Masonry Diagonal Tension (Shear) Tests.....	45
4.1.5	Masonry Bending Test.....	47
4.2	Snap-Back Tests.....	48
4.3	Summary.....	51
5	GROUND MOTIONS AND EXPERIMENTAL STAGES	53
5.1	Ground Motion Selection.....	53
5.2	Shake-Table Output Motions.....	57
5.3	Design Spectra and Intensity Levels.....	59
5.4	Stages of Experiments and Sequence of Loading.....	61
5.5	Summary.....	62
6	EXPERIMENTAL RESULTS AND DISCUSSIONS	63
6.1	Shake-Table Experimental Data	63
6.2	System Identification	64
6.3	Discussion of Stage One Results	68
6.3.1	Force-Deformation Behavior	68
6.3.2	Changes in Natural Period	72
6.3.3	Changes in Damping Ratio	75
6.3.4	Variation of Structural Properties within Each Test Run.....	79
6.3.5	URM Infill Wall.....	81
6.3.6	RC Slab	90
6.3.7	RC Frames.....	94
6.3.7.1	Description of Damage	94
6.3.7.2	Section Response.....	96
6.4	Discussion of Stage Two Results.....	100
6.4.1	Damage in Test Structure.....	100
6.4.2	Effective Slab Width.....	101
6.4.3	Effects of Post-Tensioning in Columns	105
6.4.3.1	Measurements in Post-Tensioning Rods	105
6.4.3.2	Variation of Axial Force in Post-Tensioning Rods	107
6.4.3.3	Self-Centering Force.....	109
6.5	Discussion of Stage Three Results.....	111

6.6	Comparing Results of All Three Stages of Experiments	113
6.6.1	Force-Deformation	113
6.6.2	Natural Period	115
6.6.3	Damping Ratio	116
6.6.4	Residual Displacements	117
6.6.5	Change of Demand Forces in RC Frame Joints	119
6.7	Summary	121
7	COMPUTATIONAL MODELING OF URM INFILLED FRAMES	123
7.1	In-Plane Failure Modes of URM Infill Walls	124
7.2	Strut Models	128
7.2.1	Background	128
7.2.2	Computational Modeling of Test Structure	130
7.2.3	Single-Strut FEMA Model	132
7.2.4	Calibrated Single-Strut Model	136
7.2.5	Comparison between FEMA and Calibrated Strut Models for URM Infill Wall	138
7.3	Finite Element Models	140
7.3.1	FE Model of Bare RC Frame	141
7.3.2	FE Model of Infilled RC Frame	147
7.3.3	Static and Modal FE Modeling of Shake-Table Test Structure	155
7.3.4	Dynamic FE Modeling of Shake-Table Test Structure	158
7.4	Out-of-Plane Modeling of URM Infill Walls	163
7.4.1	Background	163
7.4.2	FE Model	164
7.5	Combined In-Plane and Out-of-Plane Modeling of URM Infill Walls	166
7.5.1	Background	167
7.5.2	FE Model	168
7.6	Three-Dimensional SAT Model for URM Infill Walls	170
7.7	Summary	174
8	GENERALIZED FRAGILITY FUNCTIONS FOR URM INFILL WALLS	177
8.1	Introduction	177
8.2	Case Study Building	179

8.3	Ground Motions	179
8.4	Demand Analysis	182
8.5	Capacity Estimation	189
8.6	Limit-State Functions.....	190
8.7	Reliability Analysis and Discussion	191
8.8	Limitations and Future Extension	198
8.9	Summary	199
9	SUMMARY, CONCLUSIONS, AND FUTURE EXTENSIONS.....	201
9.1	Summary	201
9.2	Conclusions.....	203
9.3	Future Extensions.....	205
	REFERENCES.....	207
	APPENDIX A: INSTRUMENTATION DETAILS.....	215
	APPENDIX B: SNAP-BACK TEST RESULTS.....	221
	APPENDIX C: SAMPLES OF RAW EXPERIMENTAL DATA	229
	APPENDIX D: OUT-OF-PLANE CAPACITY OF URM INFILL WALLS.....	247
	APPENDIX E: FORMULATION OF 3D SAT MODEL FOR URM INFILL WALLS	251

LIST OF FIGURES

Figure 1.1	Development of shake-table test structure	2
Figure 1.2	Relationship between shake-table and pseudo-dynamic experiments.....	3
Figure 1.3	Overall study program on RC building systems with URM infill walls	6
Figure 2.1	Prototype structure ($\frac{3}{4}$ -scaled) (1" = 25.4 mm).....	10
Figure 2.2	Test structure	12
Figure 2.3	Axial load change of middle columns (B1 and B2) in prototype substructure and test structure during design-level ground motion.....	16
Figure 2.4	Comparison between responses of prototype substructure and test structure	17
Figure 2.5	Comparison between peak responses of prototype substructure and test structure	19
Figure 2.6	Comparison between cumulative hysteretic energy plots for prototype substructure and test structure	20
Figure 2.7	Effect of overturning moments on column axial loads of prototype structure.....	21
Figure 2.8	First five mode shapes of prototype structure	22
Figure 3.1	Construction drawings and details of test structure.....	26
Figure 3.2	Construction of test structure	31
Figure 3.3	Fidelity test for empty shake-table before experiments	34
Figure 3.4	Additional mass arrangement and details.....	36
Figure 3.5	Samples of different instrumentation used on test structure	37
Figure 4.1	Concrete compressive strength test	42
Figure 4.2	Concrete split tension test setup	43
Figure 4.3	Masonry prism tests.....	44
Figure 4.4	28-day compression stress-strain curves for masonry prisms	44
Figure 4.5	Diagonal force-deformation plots for masonry shear tests.....	46
Figure 4.6	Masonry diagonal tension (shear) test.....	47
Figure 4.7	Masonry bending test	48
Figure 4.8	Snap-back test configuration and sample results after building URM infill wall	49
Figure 5.1	Time-domain comparisons for original and filtered shake-table input signals	55
Figure 5.2	Frequency-domain comparisons for original and filtered shake-table input signals	56

Figure 5.3	Time-domain shake-table input and output comparisons for design level of Northridge earthquake	58
Figure 5.4	Frequency-domain shake-table input and output comparison for design level of Northridge earthquake	58
Figure 5.5	Five percent damping response spectra for selected ground motions	60
Figure 5.6	Complete testing sequence of shake-table experiments	62
Figure 6.1	System identification and column shear force calculation in test structure	65
Figure 6.2	Comparison between partial time-history of relative floor displacement obtained from wire potentiometers and accelerometers by double integration during level DUZ 8.....	66
Figure 6.3	Effect of contact between URM infill wall and columns in determining column shear force	67
Figure 6.4	Total base shear versus relative lateral displacement of RC slab for different test levels of stage one (1 kip/in. = 0.175 kN/mm).....	69
Figure 6.5	Variation of effective stiffness during stage one of shake-table experiments.....	72
Figure 6.6	Response of test structure to white-noise signal before level DUZ 7	73
Figure 6.7	Examples of transfer functions obtained for test structure.....	74
Figure 6.8	Variation of natural period of test structure during stage one of experiments	75
Figure 6.9	Variation of damping coefficient estimate \hat{c} of test structure during stage one of experiments.....	76
Figure 6.10	Total dissipated energy and sum of maximum strain energy during stage one of experiments.....	77
Figure 6.11	Variation of mean damping ratio of test structure during stage one of experiments.....	78
Figure 6.12	Variation of structural properties of test structure.....	80
Figure 6.13	Observed damage of URM infill wall	82
Figure 6.14	Effect of progression of damage on force distribution in test structure during stage one of experiments	83
Figure 6.15	Time histories of shear forces and displacements for level DUZ 7	84
Figure 6.16	Shear deformation of URM infill wall	85
Figure 6.17	Shear force versus shear deformation of URM infill wall	85
Figure 6.18	Displacement transducers (DT) along URM infill wall / RC frame interface	86

Figure 6.19	Relative displacement between URM infill wall and bounding RC frame for level TAR 6 (1 in. = 25.4 mm)	88
Figure 6.20	Relative displacement between URM infill wall and bounding RC frame for level DUZ 7 (1 in. = 25.4 mm)	89
Figure 6.21	Variation of shear demand in RC slab due to damage in URM infill wall	91
Figure 6.22	Shear deformation of RC slab	93
Figure 6.23	Damage in RC frames after level DUZ 7	95
Figure 6.24	Status in RC frames at end of stage one of experiments	96
Figure 6.25	Section analysis procedure in RC columns	98
Figure 6.26	Section rotation determination procedure in RC columns	99
Figure 6.27	Section response time histories at base of column B1, level DUZ 7	100
Figure 6.28	Damage in RC frame joints during and after stage two of experiments	101
Figure 6.29	Partial time history of strain gage number 222 during level TAR 4	102
Figure 6.30	Strain distribution in RC slab perpendicular to RC frames	104
Figure 6.31	Partial time-history of strain variation for column C1 post-tensioning rod during level LomaPr 9 compared with theoretical strains per Eqs. 6.11–6.12	106
Figure 6.32	Partial axial force variation time histories of columns C1 and C2 during level LomaPr 9	107
Figure 6.33	Axial force variation time histories for post-tensioning rods during level LomaPr 9	108
Figure 6.34	Range of variation of column post-tensioning forces during different levels of shaking	109
Figure 6.35	Total self-centering force versus lateral displacement plot during level LomaPr 9	110
Figure 6.36	Range of variation of total self-centering force during different levels of shaking	111
Figure 6.37	Damage in RC frame joints after stage three of experiments	112
Figure 6.38	State of test structure at end of stage three of experiments	112
Figure 6.39	Peak total base shear versus drift plots for different stages of shake-table experiments	114
Figure 6.40	Effective stiffness variation in test structure during stages two and three	115
Figure 6.41	Variation of natural period of test structure during shake-table experiments	116

Figure 6.42	Variation of mean damping ratio of test structure during shake-table experiments.....	117
Figure 6.43	Absolute value of residual displacement at RC floor slab during shake-table experiments.....	118
Figure 6.44	Total cumulative residual displacement at RC floor slab of test structure.....	119
Figure 6.45	Maximum moment versus maximum rotation at top and bottom of selected columns.....	121
Figure 7.1	SAT models for different in-plane failure modes of URM infilled RC frames	129
Figure 7.2	OpenSees model with single strut for URM infill wall.....	131
Figure 7.3	Concatenated input ground (shake-table) motion for simulations	131
Figure 7.4	Time histories of shake-table experimental results	132
Figure 7.5	OpenSees simulation results using FEMA strut model.....	135
Figure 7.6	Comparison between plots for base shear versus displacement of RC floor slab from experiments and simulations using FEMA strut model.....	135
Figure 7.7	OpenSees simulation results using calibrated strut model	137
Figure 7.8	Comparison of plots for base shear versus displacement of RC floor slab from experiments and simulations using calibrated strut model.....	138
Figure 7.9	Comparison of results of single-strut models and shake-table experiments	139
Figure 7.10	Shake-table and pseudo-dynamic test structures used for verifying FE models	141
Figure 7.11	FE model of bare RC frame.....	142
Figure 7.12	Concrete material model for FE analysis	143
Figure 7.13	Comparison of results of FE model and pseudo-dynamic experiments for bare RC frame.....	146
Figure 7.14	Comparison of peak results of FE model and pseudo-dynamic experimental results for bare RC frame	147
Figure 7.15	Deformed shape of bare RC frame at maximum deformation during level DUZ 7.....	147
Figure 7.16	FE models of URM infilled RC frame	148
Figure 7.17	Masonry material model for FE analysis.....	149
Figure 7.18	Pushover curves for FE models of URM infilled RC frame	150
Figure 7.19	Comparison of results of FE model and pseudo-dynamic experiments for URM infilled RC frame.....	151

Figure 7.20	Comparison of peak results of FE model and pseudo-dynamic experimental results for URM infilled RC frame.....	152
Figure 7.21	Pushover analysis for FE model of RC frame with URM infill wall.....	153
Figure 7.22	Final crack pattern observed during pseudo-dynamic experiments.....	154
Figure 7.23	Three-dimensional FE model of shake-table test structure.....	155
Figure 7.24	Monotonic pushover curve for 3D FE model of test structure.....	158
Figure 7.25	Comparisons of 3D FE analysis and shake-table results.....	160
Figure 7.26	Comparison of distribution of forces in 3D FE model and test structure.....	161
Figure 7.27	Comparison of cyclic transient and pushover analyses obtained from 3D FE model of shake-table test structure.....	162
Figure 7.28	Exaggerated deformed shapes of FE models subject to uniform out-of-plane pressure (1 psi = 6.895 kPa).....	165
Figure 7.29	Out-of-plane FE pushover analysis results compared with empirical approaches.....	166
Figure 7.30	Experimental results reported by Flanagan and Bennett (1999a) on bidirectional testing of clay tile infilled RC frames.....	168
Figure 7.31	In-plane pushover curves with varying out-of-plane force P_N	169
Figure 7.32	FE model of infilled RC frame subject to bidirectional loading.....	169
Figure 7.33	Interaction diagram for URM infill wall.....	170
Figure 7.34	Three-dimensional SAT model of URM infill wall.....	171
Figure 7.35	Failure surfaces for 3D SAT models.....	173
Figure 7.36	Failure surface for calibrated 3D SAT model compared to best-fit FE analysis results.....	174
Figure 8.1	Scaled earthquake spectra for level $SA = 1.61$ g (10/50).....	181
Figure 8.2	Scale factors for selected ground motions (earthquake designations are specified in Table 8.1).....	182
Figure 8.3	Sample results of nonlinear time-history analysis for CL-clyd ground motion at level $SA = 2.75$ g (2/50).....	183
Figure 8.4	Out-of-plane force calculation for URM infill wall located below i th floor.....	184
Figure 8.5	Time-histories of URM infill wall forces below third floor of case study building during CL-clyd ground motion at level $SA = 2.75$ g (2/50).....	185

Figure 8.6	Dispersion of URM infill wall bidirectional forces compared with capacity interaction curves.....	186
Figure 8.7	Distributions of demand forces	187
Figure 8.8	Demand distributions along building height	188
Figure 8.9	Schematic demand and capacity distributions.....	192
Figure 8.10	Fragility curves for in-plane (g_1), out-of-plane (g_2), and combined in-plane and out-of-plane (g_3) limit-state functions with actual in-plane capacity.....	194
Figure 8.11	Variation of failure probability with respect to correlation coefficient between in-plane and out-of-plane capacities of URM infill wall for intensity level $SA = 1.61g$ (10/50)	195
Figure 8.12	Fragility curves for in-plane (g_1), out-of-plane (g_2), and combined in-plane and out-of-plane (g_3) limit-state functions with increased in-plane capacity	197
Figure 8.13	Five-story RC building with URM infill walls damaged during magnitude 6.19 Nicaragua earthquake, 12/23/1972. Courtesy of Godden Collection, EERC, University of California, Berkeley	198
Figure A.1	Displacement transducers and accelerometers in horizontal planes.....	217
Figure A.2	Displacement transducers in vertical planes.....	218
Figure A.3	Strain gages for steel reinforcing bars of RC frames	219
Figure A.4	Strain gages for steel reinforcing bars of RC slab.....	220
Figure B.1	Snap-back tests before building URM infill wall and before post-tensioning columns (no additional mass).....	224
Figure B.2	Snap-back tests after building URM infill wall and after post-tensioning columns (no additional mass).....	226
Figure B.3	Snap-back tests after building URM infill wall, post-tensioning columns, and adding mass	228
Figure C.1	Selected raw data recorded during level TAR 4.....	231
Figure C.2	Selected raw data recorded during level TAR 6.....	233
Figure C.3	Selected raw data recorded during level DUZ 7	235
Figure C.4	Selected raw data recorded during level DUZ 8	237
Figure C.5	Selected raw data recorded during level AWR-TAR 6	239
Figure C.6	Selected raw data recorded during level AWR-DUZ 7.....	241

Figure C.7 Selected raw data recorded during level LomaPr 9.....	243
Figure C.8 Selected raw data recorded during level LomaPr 9-2-1	245

LIST OF TABLES

Table 2.1	Member sizes and reinforcement details of prototype substructure	11
Table 2.2	Concrete model properties	13
Table 2.3	Steel model properties	14
Table 2.4	Column-footing joint model parameters.....	14
Table 2.5	Masonry strut parameters	14
Table 2.6	Response spectrum analysis for prototype structure subjected to NEHRP design spectrum.....	23
Table 4.1	Mean uniaxial concrete compression test results.....	42
Table 4.2	COV of uniaxial concrete compression test results	42
Table 4.3	Concrete split tension tests	43
Table 4.4	28-day uniaxial compression test results for masonry prisms	45
Table 4.5	Masonry shear test results.....	46
Table 4.6	Mean of snap-back test results (see Fig. 1.1(c) for orientation of north (N) direction).....	50
Table 4.7	COV of snap-back test results (refer to Fig. 1.1(c) for orientation of north (N) direction)	51
Table 5.1	Ground motion specifications.....	54
Table 5.2	Scale factors for different levels of input ground motions	60
Table 7.1	In-plane modes of failure and their corresponding estimated capacities H_u and joint shear demands V_j of infilled systems.....	125
Table 7.2	Estimated lateral capacity of infilled RC frame of test structure based on plastic analysis	127
Table 7.3	Parameters for concrete compression material model.....	143
Table 7.4	Parameters for concrete tension material model.....	143
Table 7.5	Parameters for reinforcing steel material model.....	143
Table 7.6	Parameters for URM material model.....	149
Table 7.7	Progression of damage in URM infilled RC frame during pushover analysis using FE model (1 ksi = 6.895 MPa).....	154
Table 7.8	Mode shapes and natural frequencies and periods of 3D FE model of test structure	157

Table 7.9	Parameter sets used for 3D SAT model to generate different failure surfaces.....	173
Table 7.10	Parameter set used for 3D SAT model to generate FE failure surface.....	174
Table 8.1	Ground motion characteristics for testbed study (Lee and Mosalam 2006).....	181
Table 8.2	Demand statistics for URM infill walls in case study structure	189
Table 8.3	Correlation coefficient between in-plane and out-of-plane demands.....	189
Table 8.4	Capacity statistics for URM infill wall per FEMA 356 provisions.....	190
Table 8.5	Failure probability (%) of URM infill walls in case study structure for in-plane (IP), out-of-plane (OP), and combined limit-state functions.....	193
Table 8.6	Reliability indices (β) for URM infill walls in case study structure for in-plane (IP), out-of-plane (OP), and combined limit-state functions.....	193
Table B.1	Snap-back tests before building URM infill wall and before post-tensioning columns (no additional mass).....	223
Table B.2	Snap-back tests after building URM infill wall and after post-tensioning columns (no additional mass).....	225
Table B.3	Snap-back tests after building URM infill wall, post-tensioning columns, and adding mass	227

1 Introduction

1.1 GENERAL

Unreinforced masonry (URM) is widely used throughout the world, including seismically active regions, particularly as infill walls affecting both the structural and nonstructural performance of buildings. As non-structural elements, URM infill walls generally serve as important interior and exterior walls in buildings. The loss of these walls has serious implications not only for life safety but also the functionality of the building. Life safety can be compromised by the disintegration of URM infill walls in a brittle manner. Additionally, the loss of URM infill walls, which typically serve as partitions to define usable spaces and functionality, can negatively affect the building usage. As structural elements, URM infill walls change the dynamic behavior of the building in terms of stiffness (an increase in stiffness is often associated with an increase of forces on the building when subjected to earthquake loading), natural frequency, damping, and overall structural behavior. Typically, URM infill walls are made of brittle materials that lose capacity in a rapid manner. The combined effect of brittleness and high stiffness has a negative implication on the seismic performance of the bounding frames. In order to study the behavior of buildings with URM infill walls and to develop new experimental and analytical modeling techniques for such a complex structural system with multiple dissimilar components (hybrid systems), a three-phase experimental, analytical, and probabilistic study is conducted. The experimental investigation consists of shake-table and pseudo-dynamic (online hybrid simulations) experiments. The shake-table experiment (Fig. 1.1) serves as a benchmark test for (1) development of a unified online experimental technique combined with simulations utilizing the pseudo-dynamic concepts (Mosalam et al. 1998) with substructuring (Demitzakis et al. 1985) and (2) development and validation of computational models to represent the URM infill walls and their interaction with the surrounding frames of building systems.

The experimental study was carried out on a one-story reinforced concrete (RC) moment-resisting frame structure with URM infill wall on the shake-table test facility of the University of California, Berkeley, in January 2005. The $\frac{3}{4}$ -scale test structure represents the first-story middle frames of a hypothetical five-story three-bay by two-bay RC prototype building with URM infill walls inside only the interior (B-axis) frames as shown in Figure 1.1.

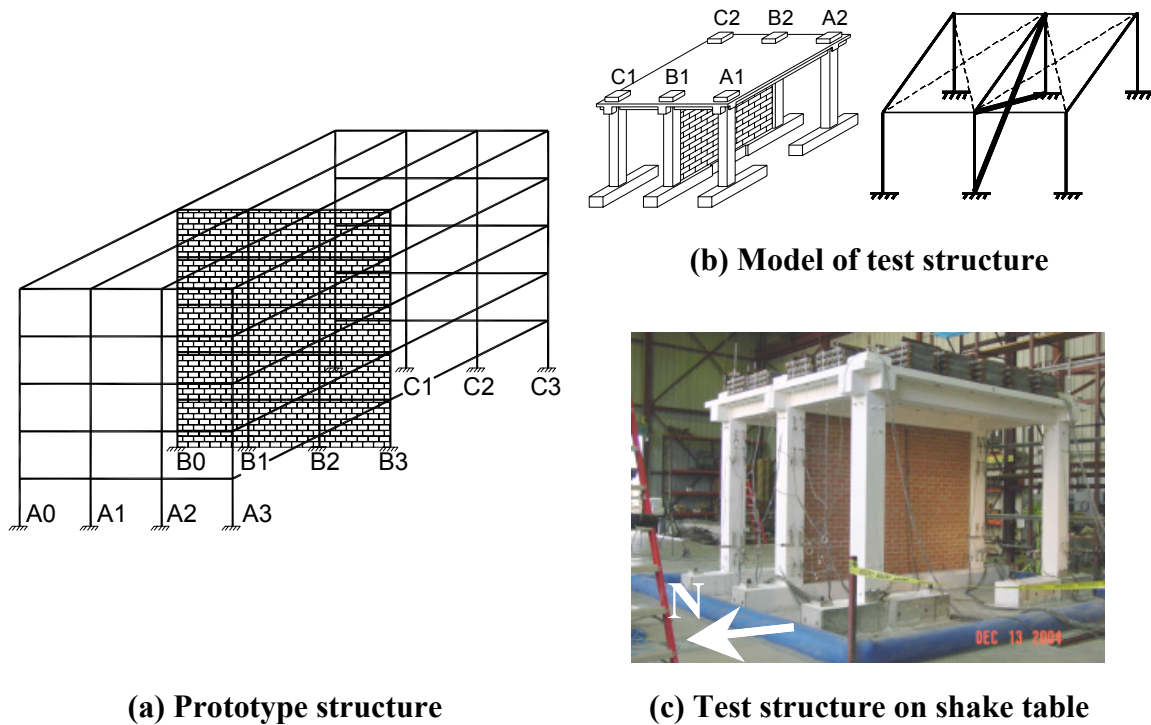


Fig. 1.1 Development of shake-table test structure.

In the pseudo-dynamic experiment, two separate RC frames are tested simultaneously. One frame is bare and the other infilled with the URM wall, corresponding respectively to frames A1–A2 and B1–B2, as illustrated in Figure 1.2. While the two frames constitute the response of the physical specimens in the pseudo-dynamic experiment, the third frame (C1–C2 in Fig. 1.2) response is obtained from the symmetry of the test structure, and the RC slab connecting the three frames is simulated numerically, making use of the substructuring technique. The development and results of the pseudo-dynamic experiments are out of the scope of this report. Full details of these experiments are documented in (Elkhoraihi and Mosalam 2007a, b).

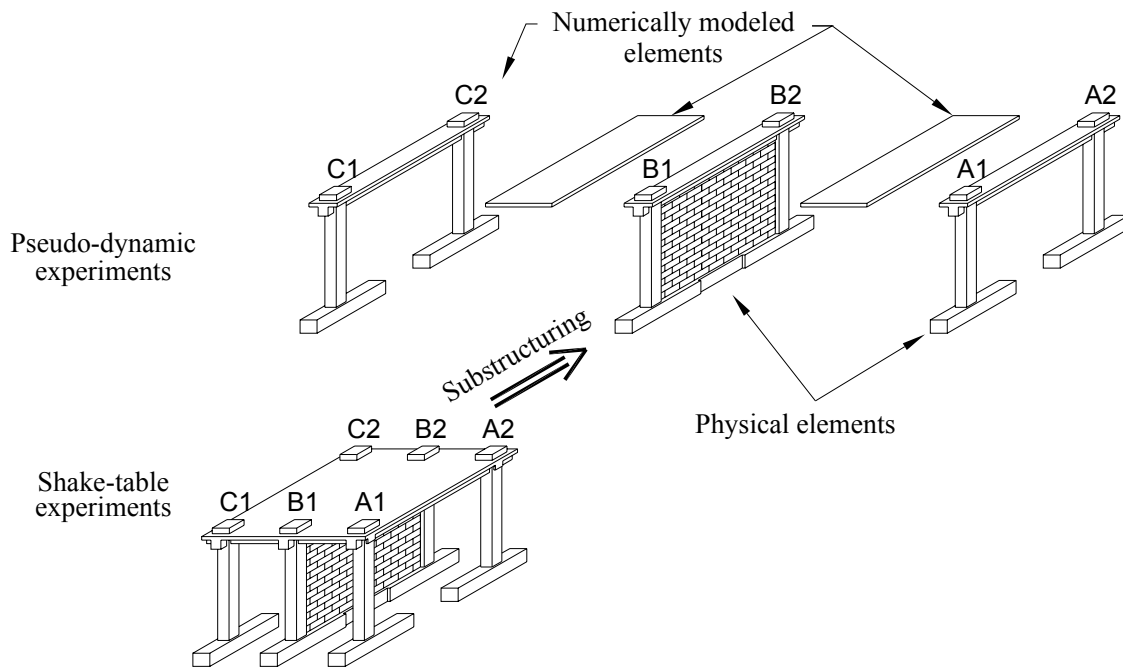


Fig. 1.2 Relationship between shake-table and pseudo-dynamic experiments.

1.2 BACKGROUND AND OBJECTIVES

When constructed in buildings with steel or RC moment frames, URM or lightly reinforced masonry infill walls are traditionally not considered as a part of the lateral load-resisting system. An argument for ignoring the effect of these infill walls is that such walls typically do not offer much displacement capacity, and in an event of significant lateral demands, the infill wall would disintegrate, whereas the original lateral load-resisting system acts as intended in the design assumptions and processes. The problem, however, is that on one hand such a simplified design approach does not predict the level at which the damage in the URM infill wall occurs—this can be significant in terms of nonstructural damage—on the other hand it does not consider the global and local effects of having these stiff and brittle elements coupled with the primary lateral load-resisting system, e.g., the shift in the natural frequency of the structure, the overall change of structural behavior, and the increases in shear demand on the columns, in diaphragm demands, and in collector element forces.

Masonry wall infilled frames have been experimentally investigated for both in-plane and out-of-plane forces by many engineers and researchers. Most of these studies are focused on the behavior of single-frame single-bay URM infilled frames under monotonic or cyclic lateral loading. Some of these investigations, past and recent, are documented. (Benjamin and Williams

1958; Holmes 1963; Stafford-Smith 1968; Moghaddam and Dowling 1987; Dawe et al. 1989; (Mander et al. 1993; Mehrabi et al. 1994); Negro and Verzeletti 1996; Durrani and Haider 1996; Pires et al. 1998; and Fardis et al. 1999b). Studies of tests on multi-story multi-bay s can be found in Liauw and Kwan 1985a; Gergely et al. 1994; Mosalam 1996a, b; Mosalam et al. 1997a, b and 1998). These studies provide evaluations of (1) the importance of infill wall confinement from bounding frames, (2) the types of failure that can be observed in the infill and/or the bounding frame members, (3) the stiffness and strength of the infilled frames, and (4) the degradation of strength upon load reversals. Since these experimental investigations are predominantly performed using static, quasi-static, or pseudo-dynamic loading, it is not clear how well these experimental data represent the dynamic performance of the framed structural system, e.g., damping characteristics, when masonry infill walls are introduced and the entire system is subjected to true earthquake loading.

Limited data exist on the dynamic properties of masonry wall infilled frames, since very few shake-table experiments are performed on masonry infilled structures. Fardis et al. (1999a) report on the shake-table test performed on single-bay two-story RC frames with eccentric (asymmetric in plan) masonry infill walls subjected to bidirectional ground accelerations. Their study focused on the effects of the eccentricity on the displacement demands on the corner columns. They also report that the infill panels survived out-of-plane peak accelerations of 0.6g at the base of the test structure or 1.3–1.75g at their mid-height. Zarnic et al. (2001) report on two shake-table tests performed on $\frac{1}{4}$ -scale one- and two-story RC frames with strong-block weak-mortar masonry infill walls subjected to unidirectional sinusoidal motion at the base of the test structure. Dolce et al. (2005) report shake-table tests performed on $\frac{1}{3}$ -scale three-story two-bay RC plane frames without infill walls, with masonry infill wall, and with two different types of energy-dissipating and re-centering braces. Their study compares the overall response and the dynamic properties of the tested three frames when subjected to a sequence of artificially generated accelerograms with increasing intensity.

The dynamic experiments discussed in the previous paragraph are generally performed on small-scale models limited by the size limitations of the available shake tables, and are focused on other aspects of the problem, e.g., torsional effects due to eccentric infill walls. The current shake-table experimental investigation is conducted to study the dynamic performance of a symmetric large-scale RC frame structure with URM infill wall subjected to real ground motions. The study focuses on evaluating the effects of the URM infill wall on the surrounding

structural elements, namely the RC slab and the RC columns. Moreover, since the two exterior frames have no infill walls (bare frames) and the interior (middle) frame is infilled with URM infill wall, quantifying the redistribution of lateral forces between these frames before and after infill wall damage and eventual collapse is an important objective of the study. The current study is unique in this aspect, and also serves as a benchmark for parallel experimental studies on pseudo-dynamic testing of similar RC structural systems with and without URM infill walls.

The shake-table and pseudo-dynamic experimental investigations serve the purpose of validating finite element (FE) models of the RC frame structures with URM infill walls and in calibrating analytical models being developed using the Open System for Earthquake Engineering Simulation (OpenSees) (Mazzoni et al. 2006). The objectives of these computational modeling efforts are (1) to develop FE models of the pseudo-dynamic and shake-table test structures as tools for further numerical simulations including different loading configurations, (2) to enable accurate representation of the in-plane and out-of-plane behaviors of URM infill walls, and (3) to refine the modeling techniques of hysteretic response and strength and stiffness degradation in elements of RC moment frames interacting with URM infill walls. Under extreme loading conditions, the experimental data are intended to validate numerical algorithms being developed for local failure criteria in brittle and ductile modes with an ultimate objective of automatic element removal for modeling the progressive collapse of RC frame structures with and without URM infill walls (Talaat and Mosalam 2006, 2007a (forthcoming)). Moreover, the data gathered from the numerical simulations using the FE models of the frames with URM infill walls are utilized to establish a framework for practical reliability analyses and performance evaluation of RC buildings with URM infill walls subjected to bidirectional earthquake loading.

1.3 OUTLINE OF REPORT

The overall study program of the research project is shown in Figure 1.3. This report mainly focuses on the shaded boxes in this figure denoted by numbers (1), (2), (4–6), (10), (14), and (16). The selection of the prototype structure and its relationship with the shake-table test structure are discussed in Chapter 2. The design, construction, and instrumentation of the shake-table test structure are discussed in Chapter 3. Chapter 4 focuses on the results of the preliminary system identification and material testing prior to the shake-table experiments. The selection of

shake-table motions from real ground-motions and their scaling and sequence of application during the shake-table experiments are covered in Chapter 5. The results of the shake-table experiments in terms of local and global behavioral observations of the test structure, the damage sequence and collapse mechanisms, and the interaction between the RC frames, RC slab, and the URM infill wall during different levels of testing are discussed in Chapter 6. The benefits and limitations of different modeling approaches, from simple strut models to elaborate strut and tie (SAT) and FE models to represent the URM infill walls in buildings, are discussed in Chapter 7. Moreover, this chapter includes comparisons between the results from the analytical simulations and those from the pseudo-dynamic and shake-table experiments. Reliability analyses and fragility functions considering the effects of bidirectional seismic loading on the URM infill walls for a case study RC building are described in Chapter 8. Finally, a summary of the findings, conclusions, and future extensions are presented in Chapter 9. The pseudo-dynamic experiments and the progressive collapse modeling of the infill walls constitute ongoing research and will be discussed in forthcoming reports by Elkhoraibi and Mosalam and Talaat and Mosalam.

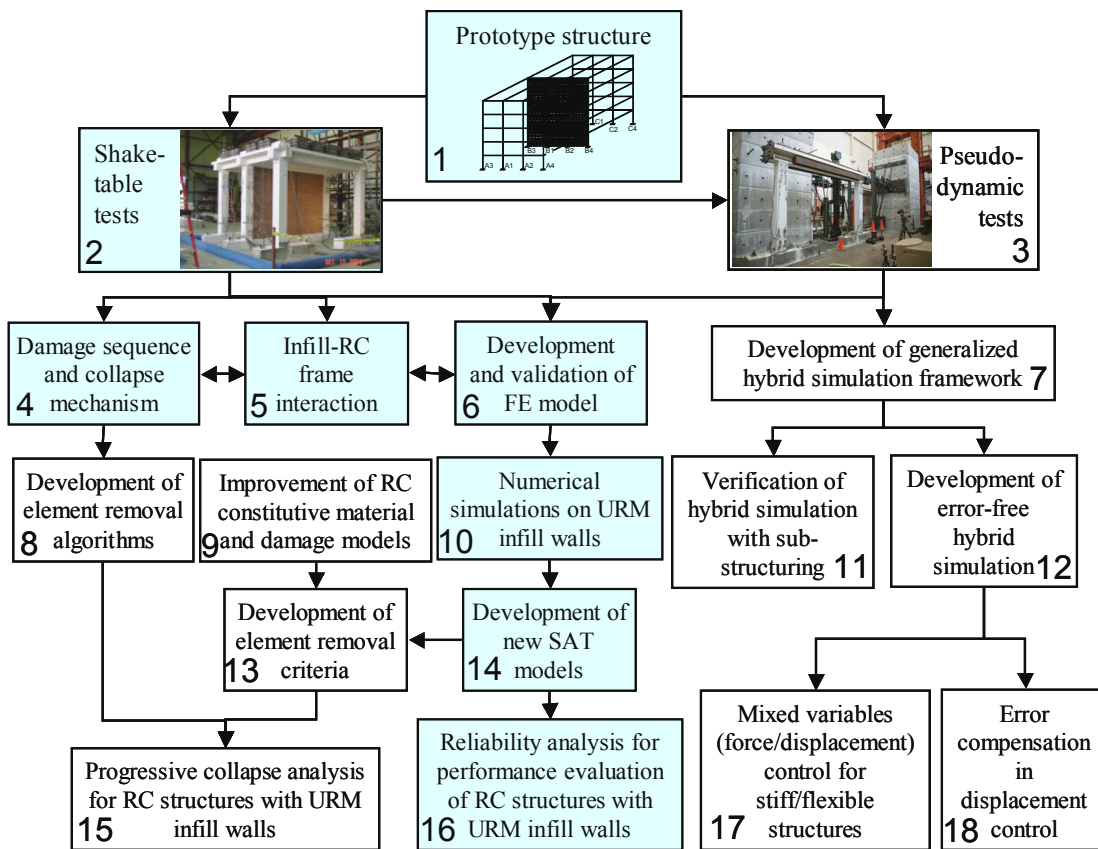


Fig. 1.3 Overall study program on RC building systems with URM infill walls.

1.4 REPORT CONTRIBUTIONS

The main contributions of this report are summarized as follows:

1. Development and execution of several shake-table experiments on three-dimensional (3D) RC frame structure with and without URM infill wall and methodical data analysis leading to quantification of the dynamic effects of the URM infill wall on the RC frame structure.
2. Generation of a 3D FE model validated using the experimental results as a tool for further analysis and numerical simulations of structures containing URM infill walls subjected to different loading conditions.
3. Establishing a framework for reliability analyses of buildings containing URM infill walls including the effects of bidirectional (in-plane and out-of-plane) ground motions and obtaining generalized fragility functions (i.e., accounting for different limit states) for RC buildings with URM infill walls.
4. Developing a practical 3D SAT model that accounts for the mechanical behavior and modes of failure for URM infill walls subjected to bidirectional (in-plane and out-of-plane) loading.

2 Prototype Structure

In this chapter, a hypothetical five-story three-bay by two-bay RC building containing URM infill walls is defined as the prototype structure of the presented research study. The first-story interior bays along the three-bay direction of this prototype structure are considered as the prototype substructure, which is the basis for the design of the shake-table test structure. Considering a computational model of the prototype structure built using the computational platform OpenSees, post-tensioning forces of the columns and additional masses to the RC slab of the first story for the shake-table test structure are defined to make the global response of the test structure match that of the prototype substructure. The computational model of the prototype structure is also used to quantify the effects of the higher modes on the response of the prototype substructure.

2.1 INTRODUCTION

The selection of the configuration of the prototype structure is done considering the feasibility and objectives of the shake-table experiment on a one-story substructure of the prototype structure. Different numbers of stories for the prototype structure are considered, and the shear demand on the first-story URM infill walls and their surrounding frames are estimated based on simplified code-based linear studies. From these preliminary studies, a five-story prototype structure is deemed adequate to generate enough lateral demand to ensure the failure of the URM infill wall during the shake-table experiment and to allow for defining a substructure for the shake-table experiment that is not significantly affected by higher modes of the structure or the overturning moments due to the height of the structure.

The prototype five-story moment-resisting frame structure is designed based on the requirements of the American Concrete Institute (ACI318, 2002) and the National Earthquake Hazards Reduction Program (NEHRP) recommendations (Building Seismic Safety Council

2000) in seismic regions with its exterior columns as the primary lateral load-resisting system. Although it is more common to have masonry walls on the perimeter of buildings, in this study, the URM infill walls are assumed to exist in the middle frames for two practical reasons. First, having two walls on the perimeter of the test structure would have required about twice as much shear force to damage the walls, thus exceeding the capacity of the available shake table. Second, the failure of the two URM infill walls on the perimeter would not have been simultaneous because of the inherent material and construction variability that would have caused a significant shift in the center of rigidity of the test structure and would have produced large torsional demands on the structure, leading to loading patterns that are beyond the scope of the intended experimental study.

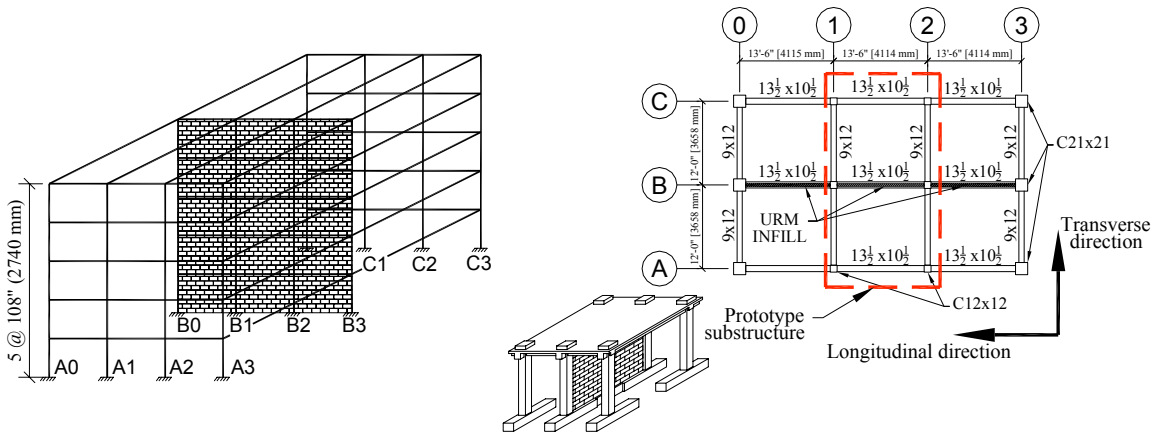


Fig. 2.1 Prototype structure ($\frac{3}{4}$ -scaled) (1" = 25.4 mm).

Due to the limited size of the available shake table, the prototype structure is scaled to 75% of its original design size. The typical floor plan and specifics of the $\frac{3}{4}$ -scaled prototype building are shown in 2.1. One of the implications of this reduced-scale configuration is that areas are reduced by the square of the length scale, i.e., reduced to 56.25% of the original areas. For satisfying the similitude requirements (Sabnis et al. 1983), the forces in the model are also reduced by the square of the length scale from those of the prototype to produce the same “elastic” stress and strain levels (using the same materials for the model and prototype structures, i.e., same modulus of elasticity) in both the model and the prototype configurations. Therefore, with elementary dimensional analysis, the distributed loads (force per unit area) on the scaled prototype structure are the same as those on the original (unscaled) prototype structure. Accordingly the adopted dead load on the scaled prototype structure is 110 psf (5270 Pa) on each floor and 90 psf (4310 Pa) on the roof, and the live load is 50 psf (2390 Pa) on each floor and 10

psf (480 Pa) on the roof. From this point on, the discussions refer to the 75%-scaled prototype structure as the prototype.

Table 2.1 Member sizes and reinforcement details of prototype substructure.

Structural Element	Dimensions	Main Reinforcement	Transverse Reinforcement
Slab	3¾" (95 mm) thick	#3 (M10) top and bottom @ 12" (305 mm) o.c. each way	None
Columns	12"×12" (305 mm×305 mm)	8-#6 (19 mm) diameter and 1¼" (32 mm) diameter post-tensioning rods	#3@3¾" (M10@95 mm) closed ties over 24" (610 mm) from faces of joints and #3@6" closed ties (M10@152 mm) elsewhere
Longitudinal direction beams (single span)	10½"×13½" (267 mm×343 mm)	3-#6 (19 mm) diameter top and bottom	#3@2¾" (M10@70 mm) closed ties over 28" (711 mm) from face of beam-column joint and #3@8" (M10@203 mm) elsewhere
Transverse direction beams (double span)	12"×9" (305 mm×229 mm)	2-#6 (19 mm) diameter top and bottom	#3@12" (M10@305 mm) closed stirrups
Footings	14"×18" (356 mm×457 mm)	4-#7 (22 mm) diameter top and bottom	#3@4" (M10@102 mm) closed stirrups
Masonry wall	4" (102 mm) thick	None	None

The prototype substructure is selected as the middle bays of the first story of the prototype building as defined by the dashed box in Figure 2.1. Although typically the exterior frames are designed and detailed as a part of the primary lateral load-resisting system the middle bays are also detailed such that they would endure the same displacement demands in an earthquake event and accordingly maintain their axial load-carrying capacity. The structural configurations (member sizes and reinforcements) of the different members of the prototype substructure are summarized in 2.1.

2.2 TEST STRUCTURE

The test structure, shown in Figure 2.2, is selected to represent the prototype substructure described in the previous section. It consists of three RC moment frames and the URM infill wall constructed in the interior (middle) frame. The RC frames are bolted through their footings to the shake table and connected from the top by the RC slab.

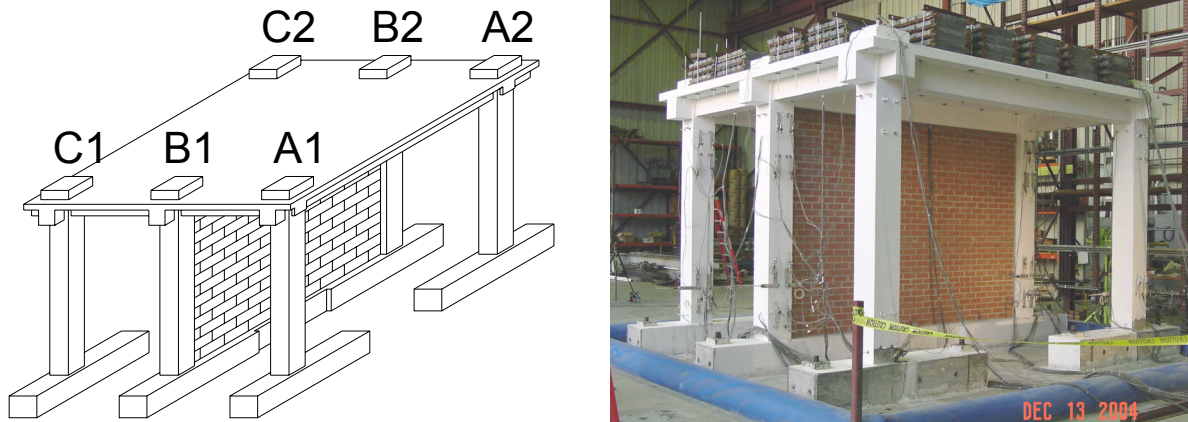


Fig. 2.2 Test structure.

Since in this study the test structure is only subjected to the ground motion in the longitudinal direction (parallel to the URM infill wall in Fig. 2.1 for designations of the longitudinal and the transverse directions), the spacing of the frames in the transverse direction is reduced from 13'-6" (4.11 m) to 6'-0" (1.83 m) to fit the test structure on the shake table. This implies that the RC slabs in the test structure behave under gravity loads as one-way slabs rather than two-way slabs in the prototype substructure. However, under lateral load, this reduction of frame spacing is expected to have a minimal effect because the RC slabs in both the prototype substructure and the test structure are expected to behave as rigid diaphragms. The beam and column sizes for the test structure are the same as in the prototype substructure; see Table 2.1. Additional masses are considered on the test structure such that the base-shear demand on the test structure matches that of the prototype substructure as determined using OpenSees modeling (refer to Section 2.5). Moreover, concentric post-tensioning rods are added to the columns of the test structure to match the levels of axial forces on the RC columns of the test structure with those of the prototype substructure (refer to Section 2.4).

2.3 COMPUTATIONAL MODELING

In order to determine the boundary conditions of the selected test structure, an analytical model of the prototype building is constructed using OpenSees. Beams and columns in the computational model are represented by *nonlinearBeamColumn* element in OpenSees, which is based on force formulation, and considers the spread of plasticity along the length of the element. Cross sections are defined using fiber discretization with distinct layers for longitudinal reinforcement. Concrete material is modeled using *Concrete01*, which is a uniaxial concrete material object with degraded linear unloading/reloading stiffness. Confining effect due to the prescribed transverse reinforcement is accounted for using confined concrete properties for core concrete material as suggested by Mander et al. (1988a,b). Steel reinforcing bars are modeled using *Steel01*, a uniaxial bilinear material object with kinematic hardening. The adopted values for concrete material parameters in different members and for steel material parameters of reinforcing bars are shown in Tables 2.2 and 2.3, respectively. These values are based on the uniaxial compression tests performed for concrete and the mill certification of the used #6 (19 mm) steel bars. The column-footing joints are modeled using the recommendations of Federal Emergency Management Agency (FEMA 356, 2000) by a trilinear moment-rotation relationship as defined in Table 2.4. The beam-column joints are modeled as rigid joints, although the column-footing joints do not to reflect the observed experimental results discussed in Chapter 6. The masonry infill is modeled using equivalent compression-only diagonal struts with properties as defined in Table 2.5.

Table 2.2 Concrete model properties.

<i>Concrete01</i>	Footing	Beams	Column cover	Column core	
f_{co}, f_{cc} [ksi (MPa)]	4.98 (34.4)	5.56 (38.4)	5.39 (37.2)	6.53 (45.0)	
$\epsilon_{co}, \epsilon_{cc}$	0.002	0.002	0.002	0.004	
f_{cu} [ksi (MPa)]	0.00	0.00	0.00	1.00 (6.90)	
ϵ_{cu}	0.006	0.006	0.006	0.020	

Table 2.3 Steel model properties.

<i>Steel01</i>	Reinforcing bars	
f_y [ksi (MPa)]	66.5 (458)	
E_s [ksi (GPa)]	29000 (200)	
$\epsilon_y = f_y / E_s$	0.00229	
α (strain-hardening ratio)	0.01	

Table 2.4 Column-footing joint model parameters.

M_{cr} [kip-in. (kN-m)]	265 (29.9)	
θ_{cr} (rad)	0.002	
M_y [kip-in. (kN-m)]	1150 (130)	
θ_y (rad)	0.015	
M_p [kip-in. (kN-m)]	1400 (158)	
θ_p (rad)	0.030	

Table 2.5 Masonry strut parameters.

f_{mo} [ksi (MPa)]	2.46 (17.0)	
ϵ_{mo}	0.00278	
f_{mu} [ksi (MPa)]	0.289 (1.99)	
ϵ_{mu}	0.00406	
Area [in. ² (cm ²)]	34.6 (223)	

Using the OpenSees computational model, nonlinear time-history analyses of the prototype structure subjected to different levels of the selected ground motion (refer to Chapter 5) are performed. The time step chosen for these analyses is 0.005 sec. The algorithm implemented in these nonlinear analyses to advance to the next time step is Newton Line Search (Crisfield 1991). The integrator used is the Newmark algorithm with well-known numerical integration parameters $\gamma = 0.5$ and $\beta = 0.25$ (Chopra 2001). Five percent mass proportional numerical damping is assumed in the computational model. The iterative solution convergence is tested based on the residual energy with tolerance of 10^{-12} kip-in. (1.1×10^{-11} kN-m). The details and references for the analysis and solution parameters described above can be found in Mazzoni

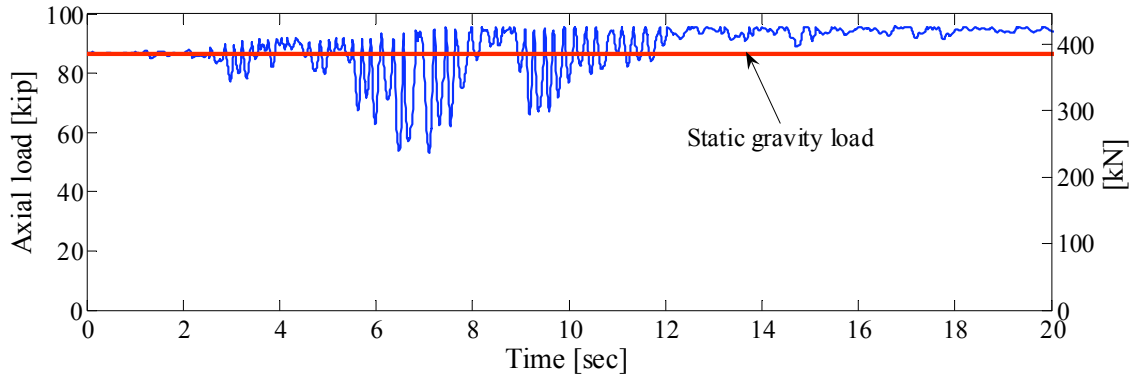
et al. (2006). Analyzing the results, the axial load and base shear affecting the selected prototype substructure are determined for each level of the input ground motions.

With the same assumptions as the prototype structure, an OpenSees computational model of the test structure is also analyzed and the required additional masses are determined for the test structure. This determination is based on matching the computationally-determined base shear of the test structure to that of the prototype substructure when subjected to the design-level ground motion, refer to Section 2.5. Moreover, the results of the computational models for both the prototype and the test structures are used to determine the required amount of columns post-tensioning forces in the test structure as discussed in the following section.

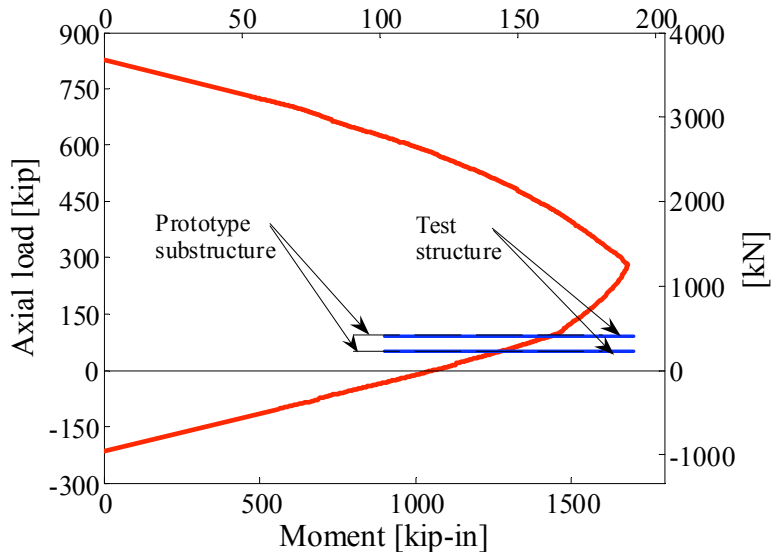
2.4 EFFECT OF COLUMN AXIAL LOAD

In order to explore the effects of the columns axial loads due to the weight of the upper stories in the prototype substructure, the range of change in the axial force during each level of the ground motion is examined and superposed on the moment-axial interaction diagram for the middle columns (B1 and B2 in Fig. 2.2). An example of such results for the design-level ground motion is shown in Figure 2.3. The static axial force due to gravity only on the column caused by the upper-story dead and live loads is 86.8 kips (386 kN) corresponding to 1420 kip-in. (160 kN-m) moment capacity for the column cross section. During the design-level ground motion, the axial load ranges from 49.5 kips (220 kN) to 96.5 kips (429 kN), as can be observed from Figure 2.3(a), and accordingly the corresponding moment capacity of the cross section ranges from 1270 kip-in. (144 kN-m) to 1450 kip-in. (164 kN-m). Comparing this variation with the moment capacity of the cross section at zero axial force, namely 1060 kip-in. (120 kN-m), it is concluded that the increase in the axial load of the column has significant effects on its flexural capacity (from 20% to 37% increase for gravity plus earthquake loadings and 34% increase for gravity loading only) of the cross section. To accommodate this observation, the static columns axial loads due to the weight of the upper stories of the prototype structure are applied to the columns of the test structure in the form of unbonded concentric post-tensioning rods in addition to the axial loads caused by the additional masses on the RC slab. The post-tensioning loads applied on the exterior columns (A1, A2, C1, and C2 in Fig. 2.2) are 32.6 kips (145 kN) and on the interior columns (B1 and B2 in Fig. 2.2) are 65.2 kips (290 kN). The resulting range of change in the axial load of the columns corresponding to the design-level ground motion for the test structure

is also obtained using the OpenSees computational model and is shown in Figure 2.3. This range for the test structure with the post-tensioning very closely matches that for the prototype substructure.



(a) Time history
[kN-m]



(b) Moment-axial interaction diagram

Fig. 2.3 Axial load change of middle columns (B1 and B2) in prototype substructure and test structure during design-level ground motion.

2.5 EFFECT OF LATERAL LOADING

A comparison of the responses of the first-story substructure of the prototype building and those of the test structure when subjected to different levels of the selected input ground motion is performed using nonlinear time-history analyses. For the prototype substructure, the displacement and base-shear response is obtained directly from the computational model of the whole prototype building, shown in Figure 2.1. The displacements are determined at the first-

floor level and the base-shear forces are determined by the sum of the column shear forces and the horizontal components of the force in the compression-only diagonal struts in the prototype substructure, indicated in Figure 2.1. The hysteretic energy is evaluated as the total accumulated area under the base-shear versus displacement plots. The base shear versus the first-story drift plots and the hysteretic energy time-history plots from these analyses are presented in Figure 2.4 for different ground motion levels of the Northridge earthquake, Tarzana (TAR) recording (refer to Chapter 5 for ground motion designations). Moreover, the plots for the maximum base shear versus its corresponding first-story drift and maximum first-story drift versus its corresponding base shear for both the prototype substructure and the test structure for different levels of the Northridge earthquake are shown in Figure 2.5. The cumulative hysteretic energy plots for consecutive runs at the applied ground motion levels are also compared for both the prototype substructure and the test structure in Figure 2.6. These results show good agreement between all the responses to a reasonable extent, justifying decisions and approximations made in the design and configuration of the test structure.

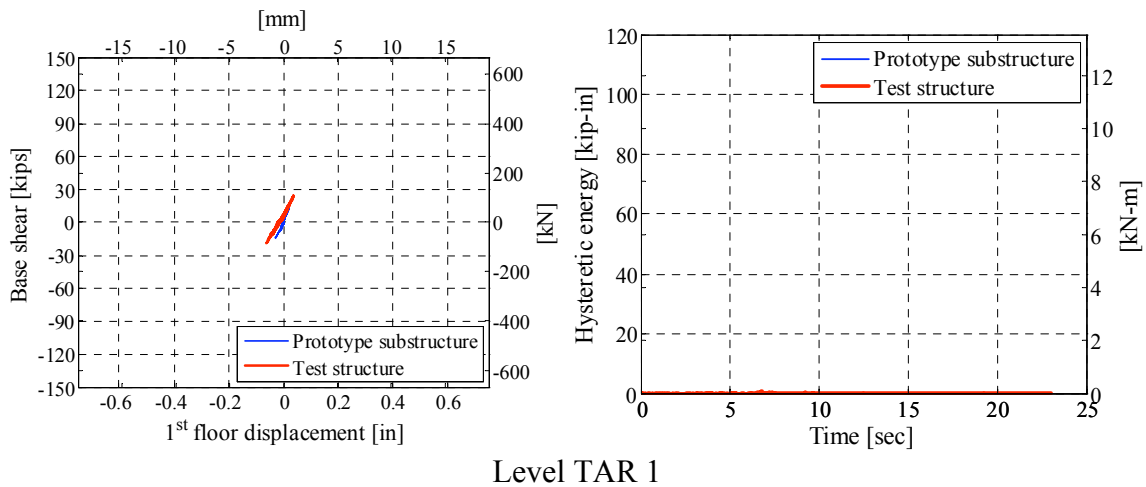
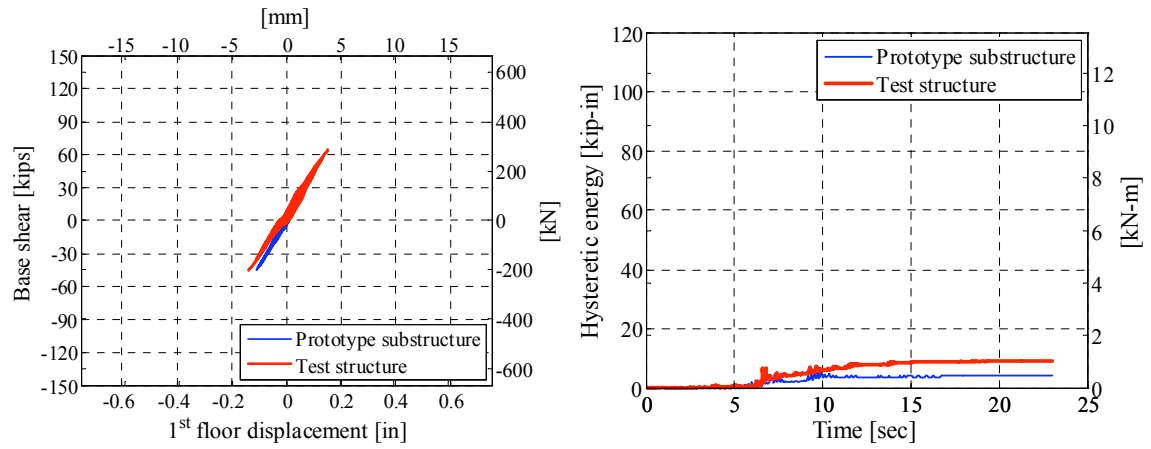
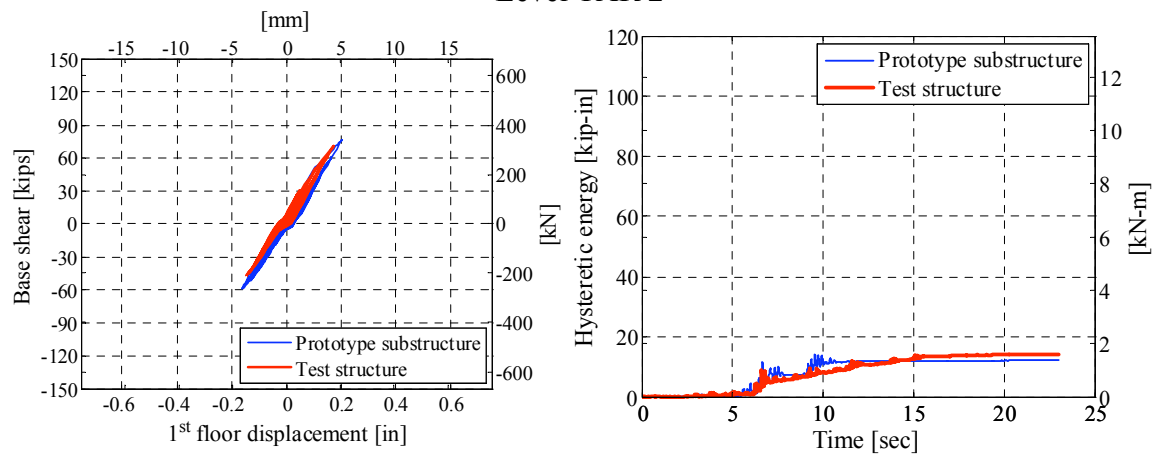


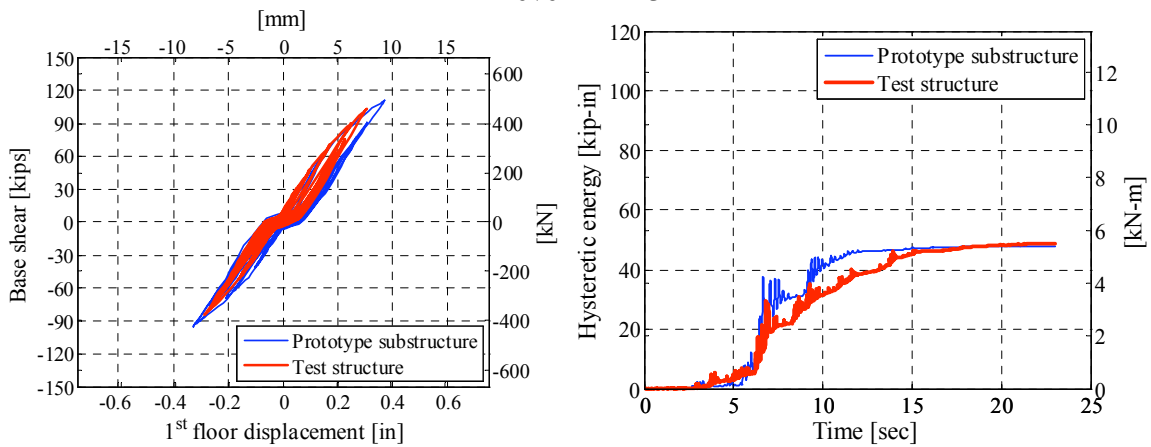
Fig. 2.4 Comparison between responses of prototype substructure and test structure.



Level TAR 2



Level TAR 3



Level TAR 4

Fig. 2.4—Continued

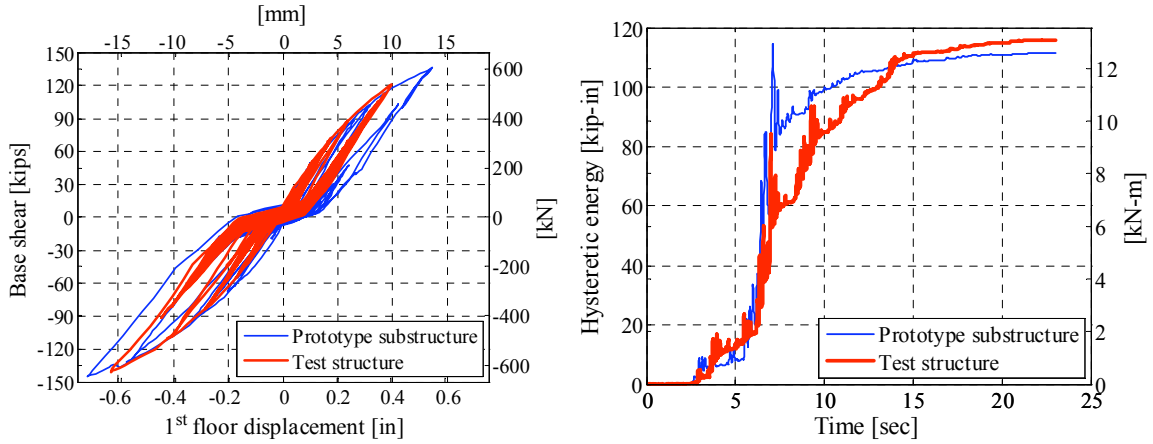


Fig. 2.4—Continued

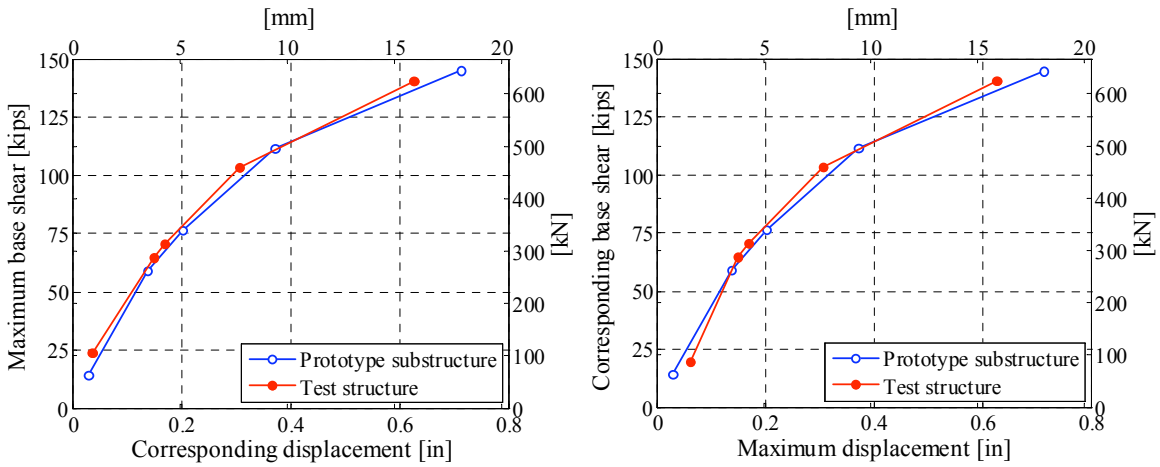


Fig. 2.5 Comparison between peak responses of prototype substructure and test structure.

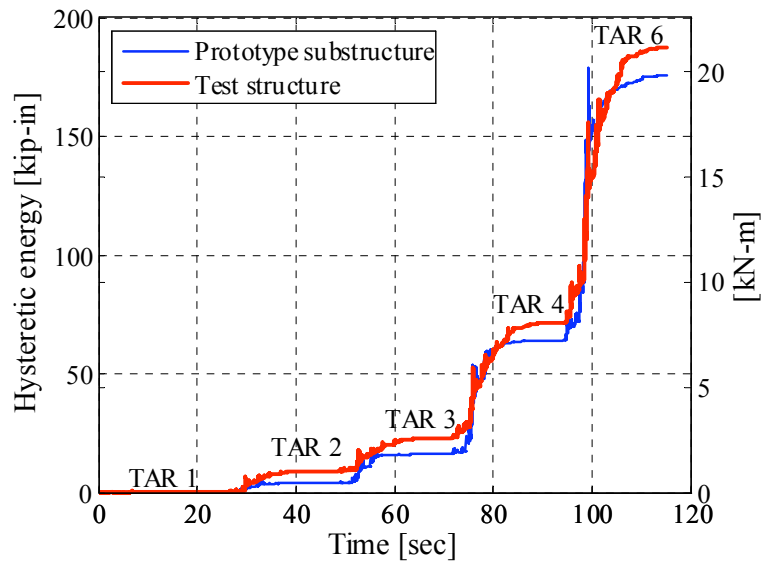


Fig. 2.6 Comparison between cumulative hysteretic energy plots for prototype substructure and test structure.

As mentioned earlier, by providing additional masses and post-tensioning in the test structure, an acceptable match between the responses of the prototype substructure and the test structure is achieved. The shortcomings however, are due to the effects of the overturning moment and higher mode effects (addressed in the next section) in the prototype structure. In general, the overturning moments have considerable role on the axial forces of the columns located on the perimeter of the building. These effects are less significant when one considers the interior columns. Figure 2.7 shows the variation of the axial loads in the columns versus the overturning moments for perimeter column (A0 in Fig. 2.1) and interior column (A1 in Fig. 2.1) in the prototype structure when subjected to the design-level ground motion. It can be observed that the axial force of the column A0 changes almost linearly with the increase of the overturning moment to more than 175%, whereas the axial force in column A1 changes merely 15% and is much less sensitive to the variation of the overturning moments.

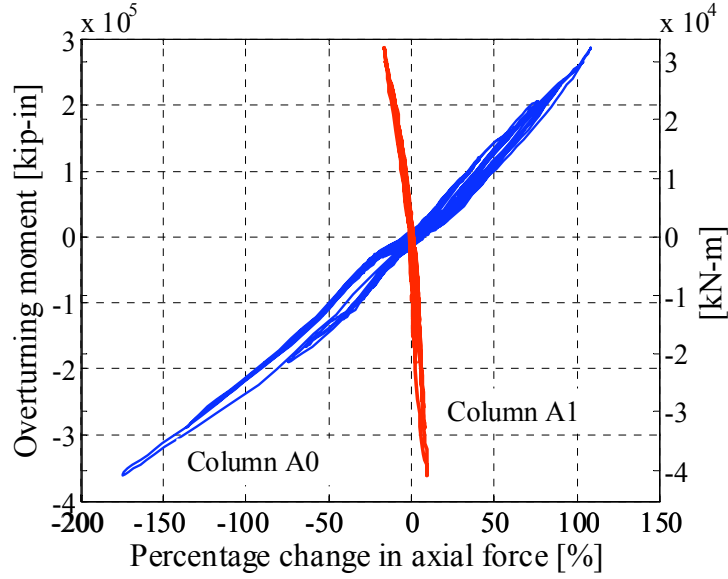


Fig. 2.7 Effect of overturning moments on column axial loads of prototype structure.

2.6 MODAL ANALYSIS OF PROTOTYPE BUILDING

Modal analysis (Chopra 2001) of the prototype building is performed to investigate the effects of higher modes on the response of the prototype substructure. Idealizing the prototype structure as a lumped-mass system, the governing equations of motion for the prototype structure subjected to the ground motion $\ddot{u}_g(t)$ can be expressed as

$$\mathbf{M} \ddot{\mathbf{u}}(t) + \mathbf{C} \dot{\mathbf{u}}(t) + \mathbf{K} \mathbf{u}(t) = -\mathbf{M} \mathbf{1} \ddot{u}_g(t) \quad (2.1)$$

where \mathbf{M} , \mathbf{C} , and \mathbf{K} are mass, damping, and stiffness matrices, respectively, $\mathbf{u}(t)$, $\dot{\mathbf{u}}(t)$, $\ddot{\mathbf{u}}(t)$ are displacement, velocity, and acceleration vectors, respectively, and $\mathbf{1}$ is the ground motion influence vector. The displacement vector $\mathbf{u}(t)$ can be expressed as the superposition of the modal contributions as shown below

$$\mathbf{u}(t) = \sum \mathbf{u}_n(t) = \sum \boldsymbol{\phi}_n q_n(t) \quad (2.2)$$

where $\mathbf{u}_n(t)$ is the contribution of the n^{th} mode to the displacement vector $\mathbf{u}(t)$ and $\boldsymbol{\phi}_n$ and $q_n(t)$ are the shape and the normal coordinates of the n^{th} mode, respectively. The maximum contribution of the n^{th} mode to the base shear of the structure V_{bn} can be expressed as

$$V_{bn} = M_n^* S A_n \quad (2.3)$$

where M_n^* is the effective modal mass of the n^{th} mode and $S A_n$ is the spectral acceleration corresponding to the natural frequency of the n^{th} mode. Following the standard procedure for

modal response spectrum analysis (Chopra 2001), the maximum contribution of the n^{th} mode to the displacement vector \mathbf{u}_n and V_{bn} can be obtained for a given ground motion or design spectra.

For the prototype building, the effects of the first five modes (Fig. 2.8) in the direction of the input ground motion are investigated. To explore the effects of higher modes on the prototype structure, a modal response spectrum analysis for the prototype structure subjected to the NEHRP design spectrum (Building Seismic Safety Council 2001) is performed. The effective modal mass M_n^* , the maximum modal contribution to the base shear V_{bn} , and the maximum modal contribution to the first-story displacement u_{1n} are shown in Table 2.6 for each of the first five modes. Moreover, this table includes the peak responses for the base shear and first-story displacement obtained using the square root of the sum of squares (SRSS) combination rule (Chopra 2001) for the first five modes. It can be observed that the ratio of the second mode to the first-mode response is about 9% for the base shear and about 6% for the first-story story drift. These ratios are even smaller for the higher modes, suggesting that the first-mode response is by far governing the total response of the prototype structure (representing 99.6% and 99.8% of the peak base shear and the peak first-story displacement, respectively, based on the SRSS combination,). Accordingly, the effects of the higher modes are neglected when comparing the obtained test structure results and observations to the prototype substructure.

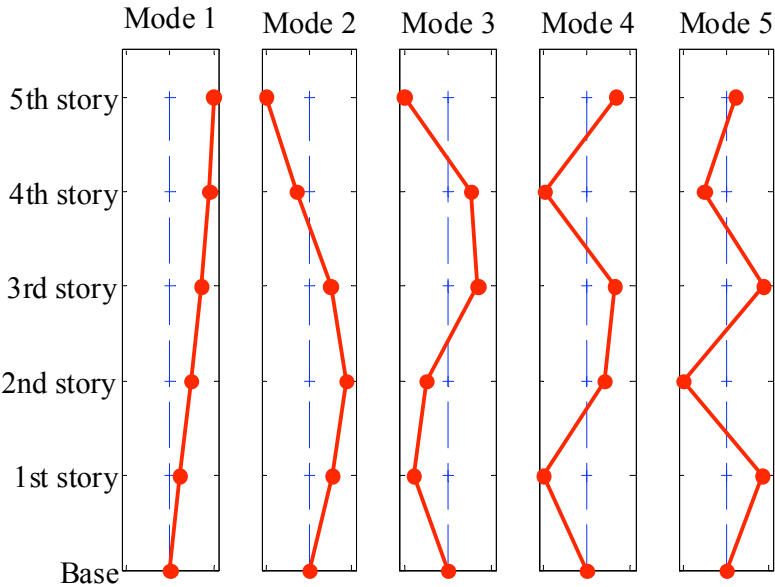


Fig. 2.8 First five mode shapes of prototype structure.

Table 2.6 Response spectrum analysis for prototype structure subjected to NEHRP design spectrum.

Mode	Period (sec)	M_n^*	SA_n (g)	V_{bn} [kips (kN)]	u_{1n} [in. (mm)]
1	0.239	1.166	1.070	482 (2140)	0.1608 (4.084)
2	0.069	0.143	0.800	44 (196)	0.0096 (0.244)
3	0.026	0.056	0.580	12 (53)	0.0009 (0.023)
4	0.025	0.029	0.580	7 (31)	0.0007 (0.018)
5	0.020	0.014	0.580	3 (13)	0.0002 (0.005)
Peak response (SRSS combination)				484 (2150)	0.1611 (4.092)

2.7 SUMMARY

A hypothetical prototype structure with RC frames and URM infill wall introduced into one of the RC frames is considered. The first-story interior frames of the prototype structure are selected as the focus substructure. A test structure representing the selected prototype substructure is proposed, and the relationship between its demand parameters and those of the prototype substructure is established using OpenSees modeling of the prototype and the test structures. The effect of column axial forces on the prototype substructure is discussed, and the post-tensioning forces for the columns of the test structure are determined to compensate for those effects. Additional masses are determined for the test structure to match its base-shear response to that of the prototype substructure when subjected to a series of ground motions. The effects of the overturning moment due to the lateral forces on the upper stories, and the effects of the higher mode contributions on the prototype substructure are also discussed and found to be negligible for the considered prototype substructure.

3 Development of the Test Structure

The development of the shake-table test structure and its experimental configuration are discussed in this chapter, including the specifics of the design, construction details, and final dimensions of the test structure. The characteristics and limitations of the shake table used and the results of its fidelity tests performed while the table is not loaded, i.e., prior to placing the test structure on it, are presented. The construction sequence, transporting of the test structure to the shake table, the arrangement of additional masses, and the instrumentation of the test structure are described in detail.

3.1 DESIGN ASPECTS

The test structure is designed to represent the $\frac{3}{4}$ -scaled prototype substructure described in Chapter 2, Figure 2.1. The overall dimensions of the test structure are 16'-0"×14'-6" (4.88 m×4.42 m) in plan and 11'-3" (3.43 m) in height. The center-to-center span of each frame is 13'-6" (4.11 m) and the frames are 6'-0" (1.83 m) apart. The frames are connected using a 3- $\frac{3}{4}$ " (95 mm) thick RC slab with #3 (10 mm dia.) reinforcing bars top and bottom at 12" (305 mm) on center each way. Column cross sections are 12"×12" (305 mm×305 mm) with 8-#6 (19 mm dia.) longitudinal reinforcing bars and Grade 150 unbounded 1- $\frac{1}{4}$ " (32 mm dia.) post-tensioning central rods to apply column axial loads representing the upper stories of the prototype building. The transverse steel reinforcements of the columns consist of #3 at 3 $\frac{3}{4}$ " (10 mm dia. at 95 mm) closed ties over 24" (610 mm) from the face of the joints and #3 at 6" (10 mm dia. at 152 mm) closed ties elsewhere. Long direction single-span beam cross sections are 10 $\frac{1}{2}$ "×13 $\frac{1}{2}$ " (267 mm×343 mm) with 3-#6 (19 mm dia.) top and bottom longitudinal reinforcing bars. Beam transverse steel is #3 at 2 $\frac{3}{4}$ " (10 mm dia. at 70 mm) closed stirrups over 28" (711 mm) from the face of the beam-column joint and #3 at 8" (10 mm dia. at 203 mm) closed stirrups elsewhere.

Short-direction double-span beam cross sections are 12"×9" (305 mm×229 mm) with 2-#6 (19 mm dia.) longitudinal top and bottom reinforcing bars and #3 at 12" (10 mm dia. at 305 mm) closed stirrups as transverse steel reinforcement. Foundation cross sections are 14"×18" (356 mm×457 mm) with 4-#7 (22 mm dia.) longitudinal top and bottom reinforcing bars and #3 at 4" (10 mm dia. at 102 mm) closed stirrups as transverse steel reinforcement. The concrete cover is 3/4" (19 mm) everywhere. The reinforcement is specified as ASTM A615 Grade 60. The specified 28-day compressive strength of the standard concrete cylinder per ASTM C 837-99 is 4.5 ksi (31 MPa). The masonry wall is made of clay bricks with modular size of 4"×8"×2²/₃" (102 mm×203 mm×68 mm) and ASTM C270 Type N mortar. The measured average 28-day compressive strength of the standard masonry prism per ASTM C1314 is 2.46 ksi (17 MPa). The complete construction drawings of the test structure are shown in Figures 2.3(a)–(e).

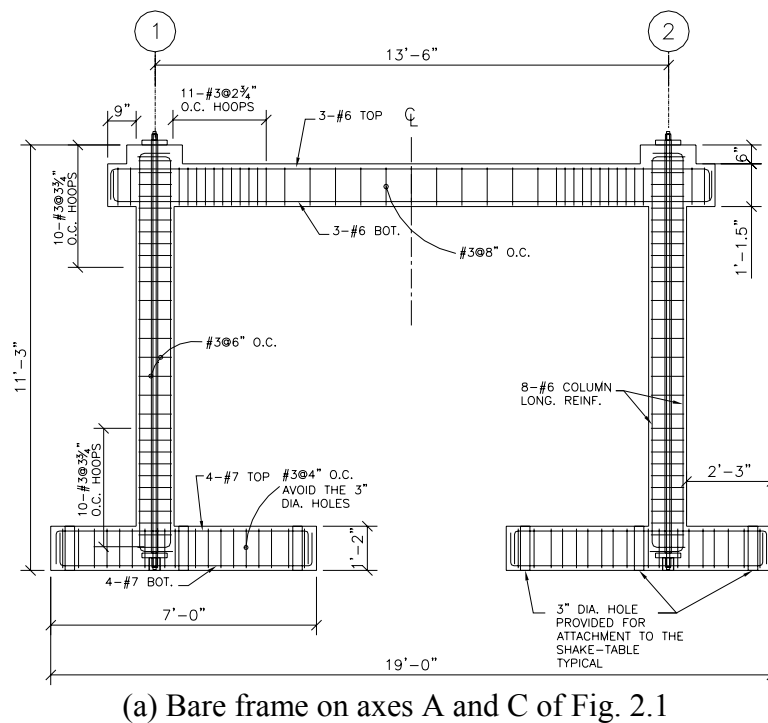
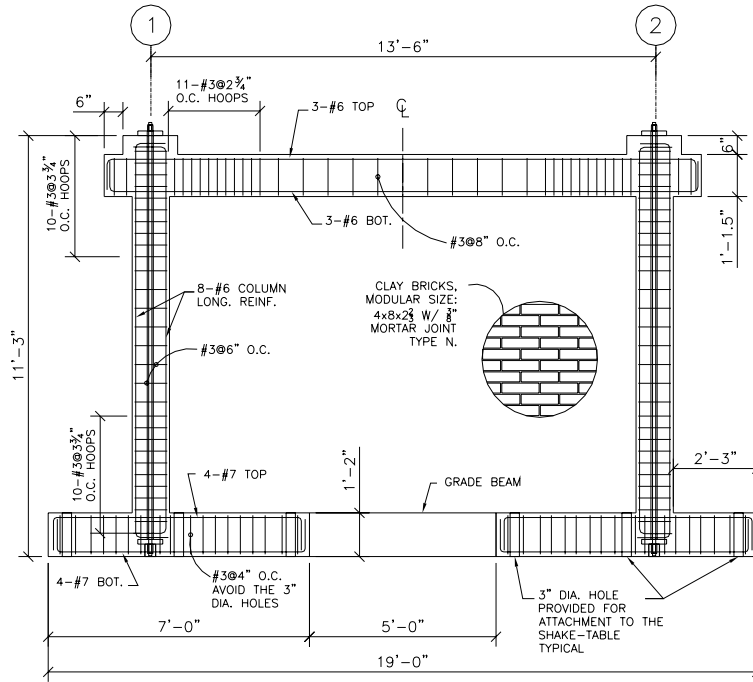
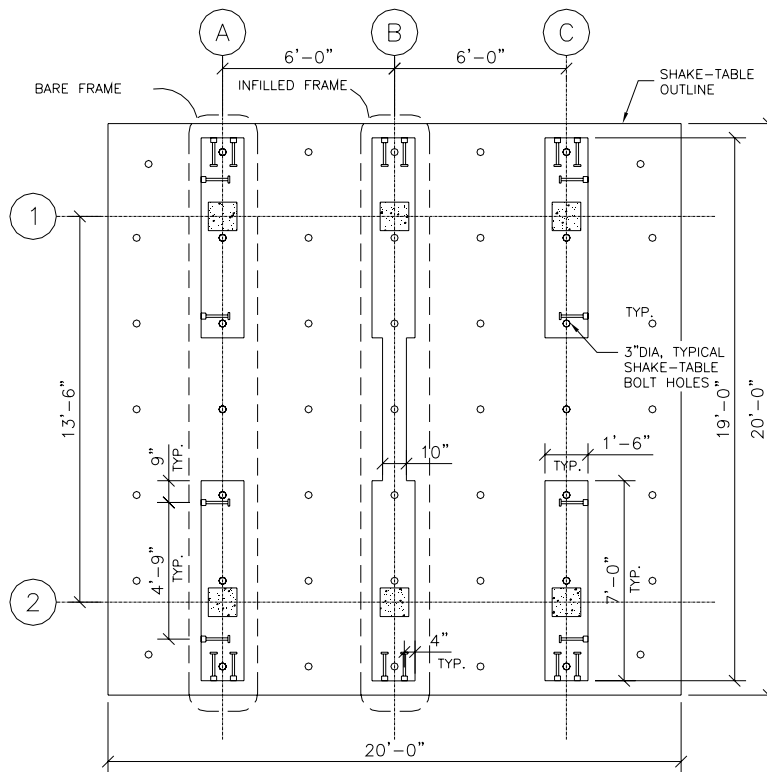


Fig. 3.1 Construction drawings and details of test structure.

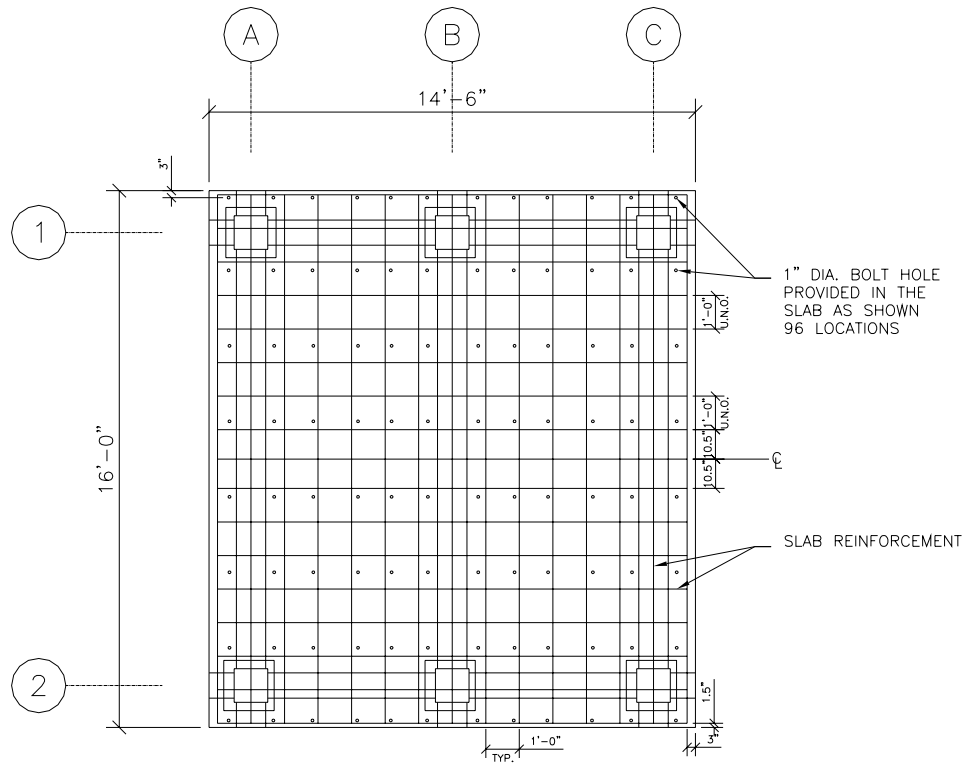


(b) Infilled frame on axis B of Fig. 2.1



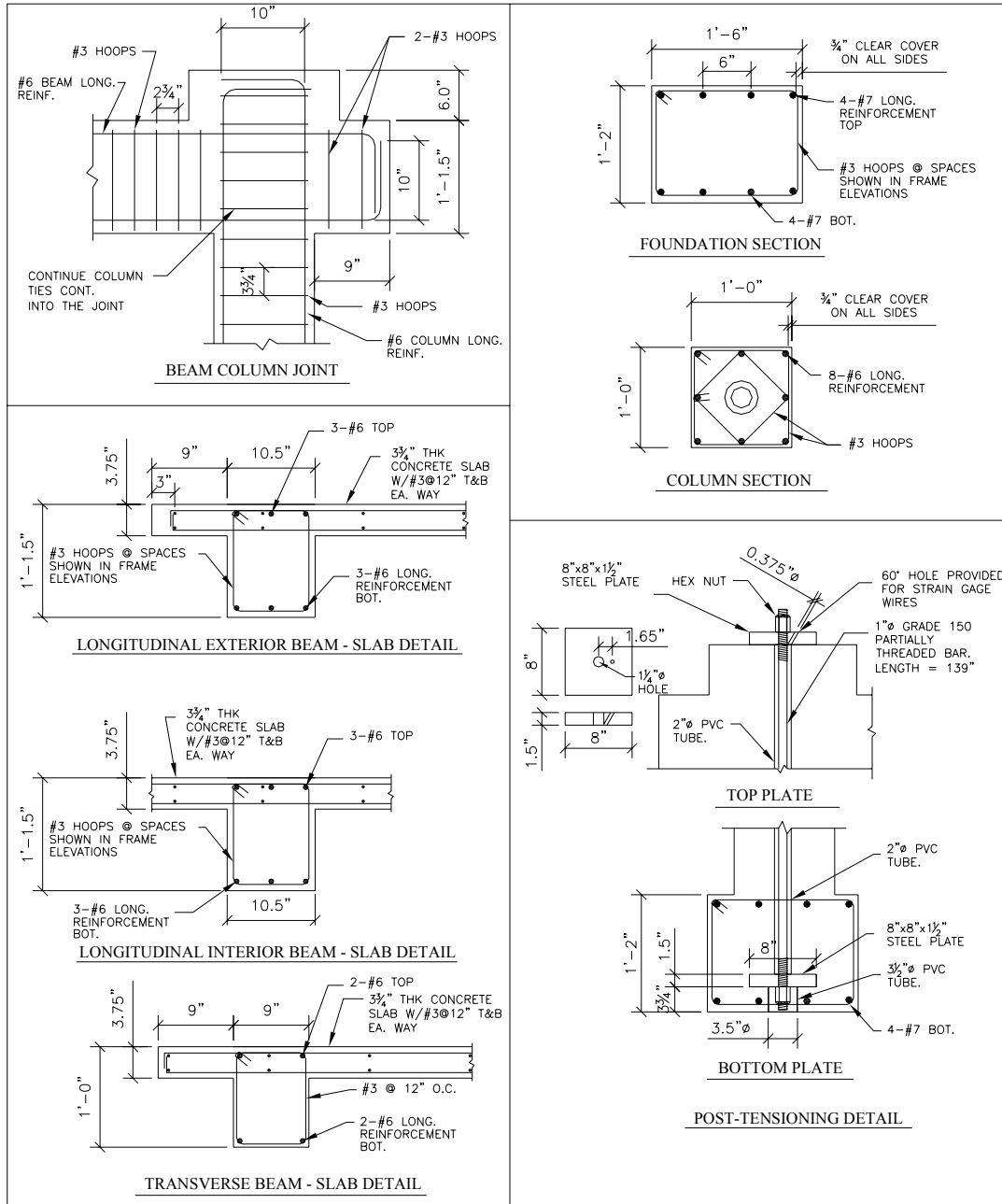
(c) Floor plan

Fig. 3.1—Continued



(d) RC slab reinforcement

Fig. 3.1—Continued



(e) Details

Fig. 3.1—Continued

3.2 CONSTRUCTION PROCESS

The test structure was constructed off the shake table by professional contractors. This was dictated by the expected somewhat long time for the construction stages of the test structure and the scheduling constraints of the shake-table usage. Following common practice, the concrete

was placed in three stages having two cold joints at the tops and the bottoms of the columns. The cold joints were roughened and cleaned before each new concrete placement. A total of thirty concrete test cylinders were prepared during each phase of construction to be tested during various stages of the project. Figure 3.2 shows photographs of different milestones of the construction process of the test structure, including transporting the test structure to the shake table.

For transporting the test structure, a stiff steel frame was assembled and attached through pre-installed embedded bolts in the foundation of the test structure. Furthermore, to prevent damage during the transportation, the test structure was braced (V bracing) using steel angle members spanning from the top slab to the middle of the supporting stiff steel frame. The test structure was then lifted through the formwork using hydraulic jacks, and rollers were placed under the supporting steel frame. The whole assembly was then towed inside the shake-table building and onto the table with utmost care to avoid any damage to the test structure. The test structure was then grouted and post-tensioned to the shake table using two high-strength (Grade 150) 1" (25.4 mm) diameter rods per column footing, and the supporting steel frame and steel braces were removed. The post-tensioning rods directly under the URM infill wall were recessed to avoid interference with the URM wall construction.

Once the test structure was secured to the shake table, professional masons constructed the URM infill wall in the middle frame. The work sequence described was designed to avoid moving the structure with the URM infill wall to eliminate any possibility for micro-cracks to develop in the brittle URM infill wall. Upon completion of the construction of the URM infill wall, a month of curing time was allowed before the start of the experiments. This time was utilized to install the required instrumentation and addition of the masses as described in the following sections.



(a) Construction of foundation



(b) Formwork for columns



(c) Formwork and construction of beams and slab



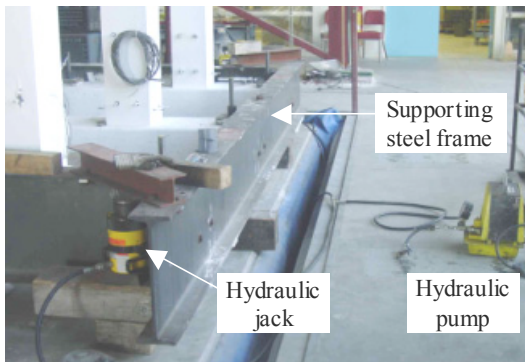
(d) Slab and beam reinforcement



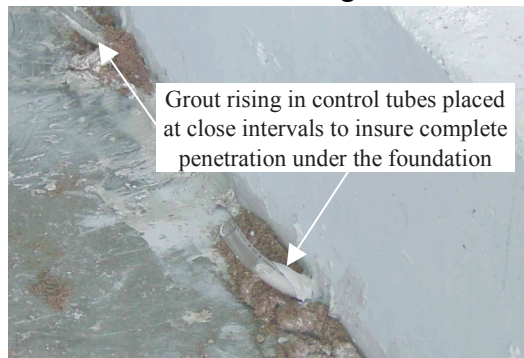
(e) Test structure after stripping forms



(f) Transporting test structure into shake-table building



(g) Lifting test structure to complete its grouting to shake table



(h) Grouting of test structure on shake table

Fig. 3.2 Construction of test structure.



(i) Construction of URM infill wall



(j) Test structure after completion of URM infill wall

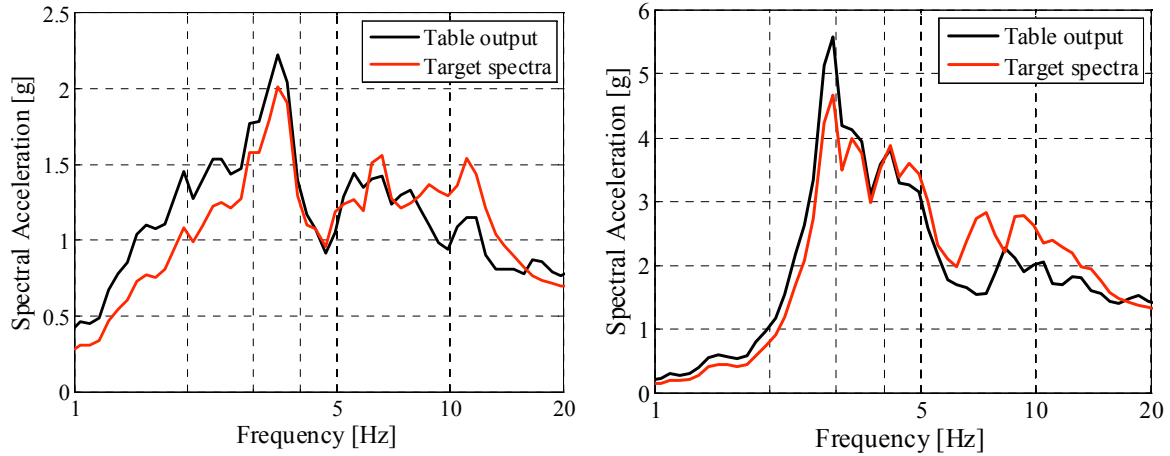
Fig. 3.2—Continued

3.3 SHAKE-TABLE FACILITY AND FIDELITY TESTS

The following description of the shake-table facility used at the Richmond Field Station of the University of California, Berkeley, is extracted from the Earthquake Engineering Research Center website at <http://eerc.berkeley.edu> where further details may be obtained. The heavily reinforced (with ordinary reinforcement and with post-tensioning tendons) concrete shake table has a size of 20'×20' (6.1 m×6.1 m). It is configured to produce three translational and three rotational components of motion along and about the vertical axis and two horizontal axes. These six degrees of freedom (DOF) can be programmed to reproduce any waveforms within the capacities of force, velocity, displacement, and frequency of the system. In this study, only unidirectional translation in the horizontal direction parallel to the URM infill wall plane is considered. The shake table can subject test structures weighing up to 100,000 lbs (445 kN), the same weight as the table itself, to horizontal accelerations of 150% the acceleration of gravity (1.5g). The maximum displacement of the shake table in the horizontal directions is limited to the gap that separates the shake table from the laboratory floor (5" (127 mm)). The maximum vertical displacement is limited to the stroke of the vertical actuators (8" (203 mm)). The maximum velocity of the table is limited by its hydraulic system and it is suggested to limit the maximum velocity to about 30 in./sec (762 mm/sec). The table is designed to be stiff enough to have a natural frequency greater than 20 Hz, behaving essentially as a rigid body in the typical operating range of 0-10 Hz. In operation, the air in the pit beneath the shake table is pressurized such that the total weight of the table and the test structure is balanced by the difference in air pressure in the pit and the ambient air pressure.

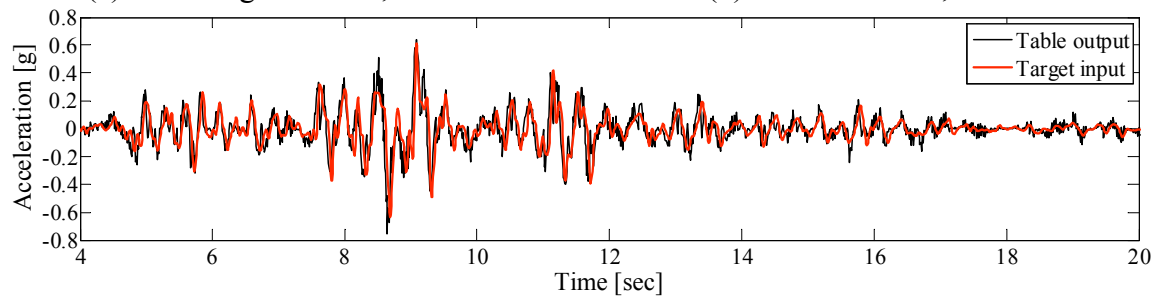
Eight hydraulic actuators, with a capacity of 75,000-lb (330-kN) each, drive the shake table horizontally and are attached to stiffened parts of the table from underneath. The actuators are long and have swivel joints at each end so they can rotate to accommodate the components of motion perpendicular to their direction of extension. The long length of the actuators helps to decouple the horizontal and vertical components of motion, with further decoupling accomplished in the control system. An MTS model 469 controller performs the primary control of the shake table. The controller provides for closed-loop control of motion on translational and rotational DOF. It is designed so that each of these 6 DOF can be programmed individually to run concurrently. Earthquake records of displacement are used in programming and controlling the shake-table motions.

In order to gain a measured confidence in the performance of the shake table, before installing the test structure, the selected input ground motions in the present study were run on the unloaded shake table and the acceleration response was measured at the center of the table and compared to the target motions. Figures 3.3(a) and (b) compare the shake-table and target acceleration response spectra for Northridge Tarzana, level 4, and Düzce Lamont, level 7, ground motions, respectively. The details of these selected ground motions and their intensity levels are discussed in Chapter 5. In the expected first-mode frequency range of the test structure, 7.5 Hz for the as-built, i.e., before any damage, infilled test structure to about 1.0 Hz for the extensively damaged test structure, the match between the shake-table output and the target spectra is deemed acceptable. Since the main objective of this study is to evaluate the response of the test structure due to ground motions representative of the design spectra rather than any specific actual ground motion, the shake-table output signals are used in determining the scale factors to match the design spectra (refer to Chapter 5 for details), and also these output signals are used in post-experiment computational analyses (refer to Chapter 7 for details). For completeness, the actual time history of the input and output signals of the shake table for the same level discussed above are shown in Figures 3.3(c)–(d), indicating that while the shake-table output follows the input acceleration closely, the outcome contains significant noise and sometimes does not achieve all the peaks in the input acceleration time history. The input and output of the loaded shake table (with the test structure installed) are presented and compared in the time and frequency domains in Chapter 5. The filtering process to reduce the noise is also discussed in detail in that chapter.

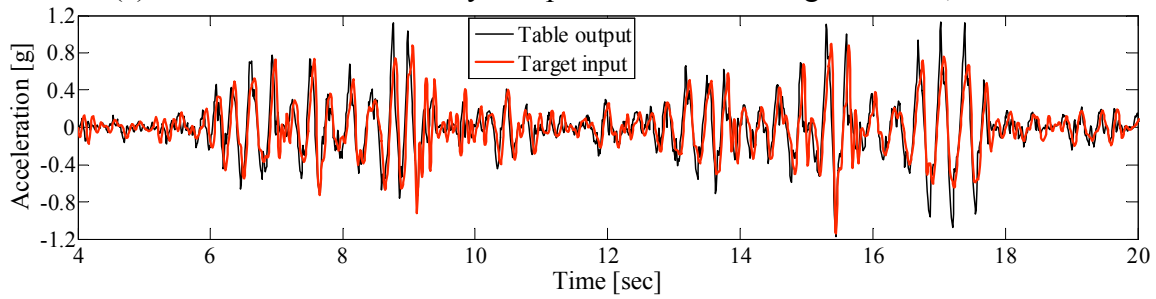


(a) Northridge Tarzana, level 4

(b) Düzce Lamont, level 7



(c) Acceleration time-history comparison for Northridge Tarzana, level 4



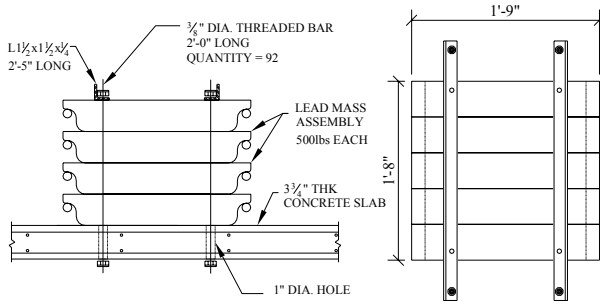
(d) Acceleration time-history comparison for Düzce Lamont, level 7

Fig. 3.3 Fidelity test for empty shake table before experiments.

3.4 ADDITIONAL MASS ARRANGEMENT

A total of 72.0 kips (320 kN) uniformly distributed weight is added to the RC slab of the test structure in the form of stacked lead ingots bolted to the slab using $\frac{3}{8}$ " (10 mm) diameter high-strength rods. The purpose of these added masses and the computational models used to estimate their values are discussed in Chapter 2. Due to potential health hazards related to lead particles, the utmost care was taken in handling the lead ingots, and the work was performed under the supervision of the University of California Environmental, Health and Safety office. The lead ingots are stacked in groups of 3 and 4 (1500 lbs (6.67 kN) and 2000 lbs (8.90 kN), respectively)

on the ground and placed on the roof of the test structure stack by stack in a symmetrical order to avoid asymmetric loading of the RC beams and slab. After tightening the $\frac{3}{8}$ " diameter high-strength rods to 70% their tensile strength using a torque wrench, static tests are performed by placing a hydraulic jack between a few pairs of the stacked lead ingots at different locations on the RC slab and by applying horizontal force pushing the ingots apart from each other while measuring the relative displacement between them. These tests confirm that the friction forces between the slab and the lead ingots are large enough to accommodate up to 4.0g lateral acceleration at the slab level. At a horizontal force equal to about four times the weight of the stacked lead ingots, they begin to slide on the RC slab, but no relative slip was observed between the lead ingots themselves. Mass assembly details, photographs of the placement and handling of the lead stacks, placement and arrangement details, and the final state of the structure after the completion of the mass-stacking procedure are shown in Figures 3.4(a)–(f), respectively.



(a) Details for lead assembly and attachment to RC slab of test structure



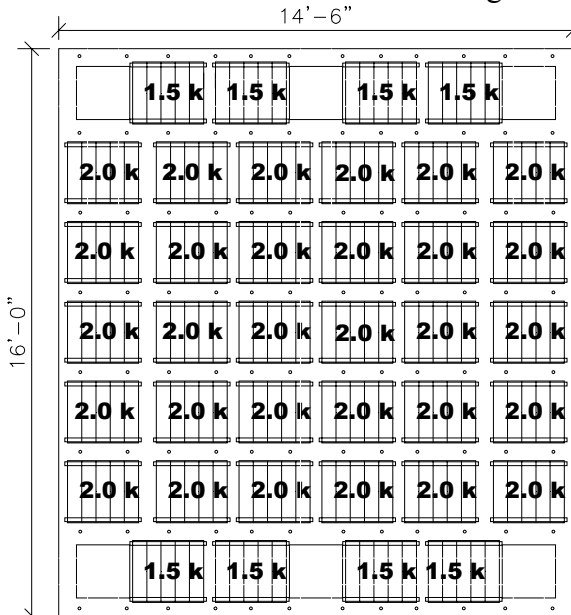
(b) Lead ingots attached to RC slab of test structure



(c) Steel tong designed and constructed to facilitate safe transfer of lead ingots



(d) Positioning lead assembly on prescribed locations using crane



(e) Distribution of weight on RC slab of test structure (plan view)



(f) Test structure after completion of mass-stacking procedure (top view)

Fig. 3.4 Additional mass arrangement and details.

3.5 INSTRUMENTATION

The experimental setup is instrumented to provide data for the evaluation of the global and local behavior of the test structure. Three types of instruments are used: (1) accelerometers, (2) displacement transducers, and (3) strain gages. Examples of the use and setup of these instruments are shown in Figures 3.5(a)–(f). Detailed drawings for the exact locations and configurations of all instruments are shown in Appendix A.

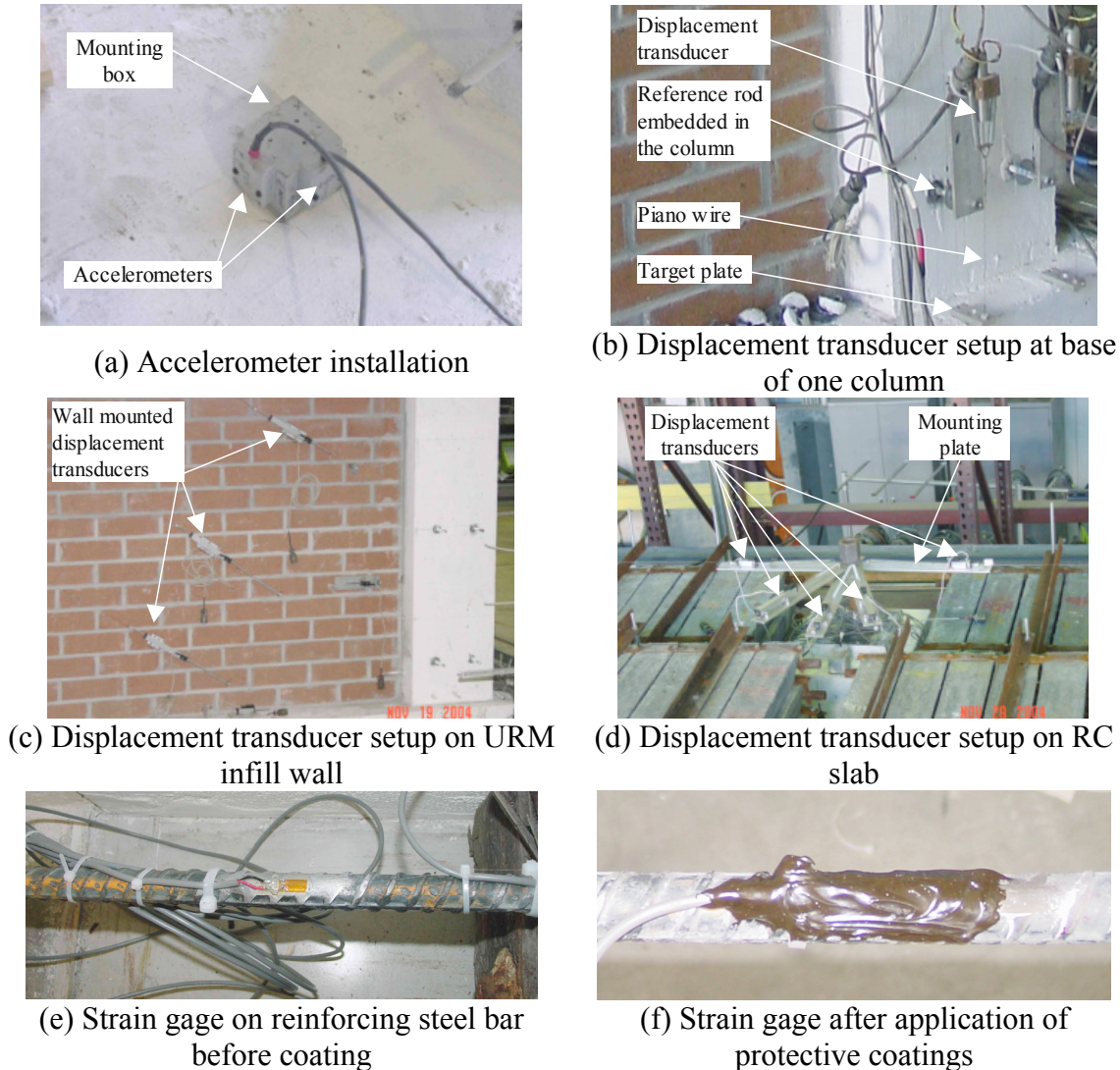


Fig. 3.5 Samples of different instrumentation used on test structure.

To measure the floor acceleration in three directions (vertical and two horizontal), 11 accelerometers are installed on the floor level (see Fig. A-1) as follows: in the longitudinal direction, parallel to the URM infill wall, 7 accelerometers, one-per-column and one at the

middle of the beam in frame B; in the transverse direction, 3 accelerometers on the diagonal of the slab on opposite corners and at the center; and in the vertical direction, one at the middle of the beam in frame B. Added to these are 3 more accelerometers at the base of the URM infill wall on the foundation (one in each direction) and 8 accelerometers built in the actuators underneath the shake table (one each per horizontal and vertical actuator).

To measure the global displacements of the shake table and the test structure with respect to the fixed frame of reference, eight displacement transducers (wire potentiometers) are used. Five of these measured the displacement of the floor (three in the longitudinal direction and two in the transverse), and the remaining three measured the displacements of the shake table (two in the longitudinal direction and one in the transverse).

To measure local displacements and rotations, a total of 75 displacement transducers (linear variable differential transducers, LVDTs) are utilized during the experiments. Nine were installed in the plane of the slab; 14 installed in the plane of the URM infill wall measuring the diagonal deformation, sliding, and opening with respect to the bounding frame; four for measuring the diagonal displacements of the frames; and the rest installed on four of the columns (12 per column) to measure the rotations and average curvatures along the length of the column (see Fig. A-2).

A total of 78 strain gages out of more than 150 strain gages installed on the reinforcing bars throughout the test structure are used during each run of the shake table (see Figs. A-3–A-4), since the total number of the installed instruments exceeded total data channels available in the data-acquisition system, namely 192 channels. In other words, almost twice the strain gages as those used in any single test are mounted in the reinforcing bars of the test structures. It should be noted that in Figures A-3–A-4, only the strain gages that are used during the shake-table experiments are numbered. Because some of the strain gages were damaged during the earlier test runs, this redundancy of strain gaging is very important in such large-scale shake-table experiments with multiple phases where alternative gages are selected and monitored in subsequent test runs. The post-tensioning rods are also gaged and monitored during all test runs to assess the change of the post-tensioning forces, i.e., the change of the axial loads in the columns.

3.6 SUMMARY

The specifics of the test structure including geometry, reinforcement configurations, and construction details are presented. The shake-table hardware and control system and the results of fidelity tests on the ability of the shake table to reproduce target ground motions are briefly discussed. It is concluded that the table performance is satisfactory within the expected frequency range of the test structure. The construction sequence, the procedure of transporting the test structure and mounting it on the shake table, the additional mass distribution and attachment, and the instrumentation of the test structure are described in detail. The reader is referred to Appendix A for the exact locations and orientations of all instruments used in the shake-table experiments.

4 Preliminary System Identification

This chapter deals with the results of the component and system tests performed before the start of the actual shake-table experiments involving the application of earthquake records. The component tests include standard concrete compression tests and concrete split tension tests on concrete cylinders fabricated during the construction of the test structure. These component tests also include masonry compression, shear and bending tests performed on masonry prisms and masonry panels constructed at the same time as the URM infill wall in the test structure. The system tests are a series of pull-back (snap-back) tests on the test structure at different stages of completion of the test structure configuration, namely before and after building the URM infill wall and after the placement of additional mass on the test structure. The results of these preliminary tests are used to gather the required data for calibrating and validating analytical models of the test structure as discussed in Chapter 7 and to document the state of the test structure at the beginning of the shake-table experiments as a point of reference when discussing the results of these experiments in Chapter 6.

4.1 COMPONENT TESTS

4.1.1 Concrete Cylinder Compression Tests

A total of 30 test cylinders are prepared after each concrete placement for foundation, columns, and beams and slab in accordance with ASTM C 837-99. The cylinders are kept in the same environmental conditions as the test structure. Three uniaxial compression tests are performed for each patch of concrete at different times to monitor the strength gain with time, the last of which was performed on the day before the start of the shake-table experiments. Mean values and the coefficient of variation (COV) of each test group are reported in Tables 4.1 and 4.2, respectively. It can be observed that the compressive strength of the concrete on the day of the

test is on average 22% higher than its 28-day compressive strength. No clear conclusion can be made on the COV for the test results due to the small sample size, namely three for each reported value. However, based on the results in Table 4.2 and for the purpose of practical reliability analyses as in Chapter 8, one may consider a mean value of the COV of the concrete compressive strength of 4.5%. The test setup and the resulting relationship of the mean strength-gain with time for the used concrete are shown in Figure 4.1. The mean strength values obtained at the time of the shake-table test are used in the computational modeling of the test structure (Chapter 7) and for system identification purposes (Chapter 6).

Table 4.1 Mean uniaxial concrete compression test results.

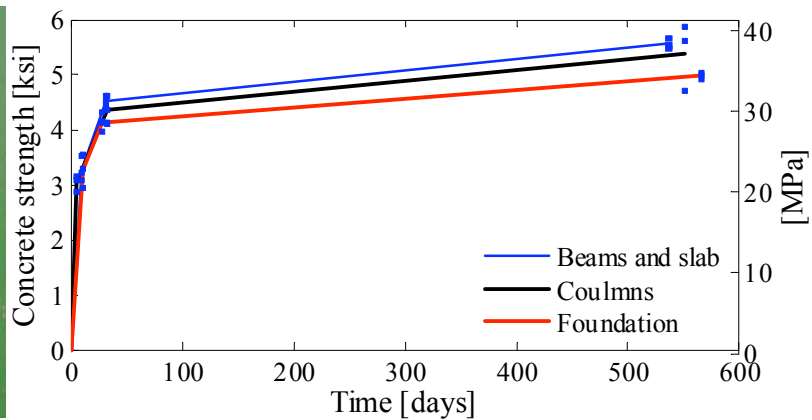
Structural element	First group [ksi (MPa)]	Second group [ksi (MPa)]	Third group (start of shake-table experiments) [ksi (MPa)]
Foundation	3.27 (22.5)@11 day	4.15 (28.6)@28 day	4.98 (34.3)@567 day
Columns	3.04 (20.9)@5 day	4.36 (30.1)@33 day	5.40 (37.2)@552 day
Beams and slab	3.28 (22.6)@10 day	4.53 (31.2)@32 day	5.56 (38.3)@538 day

Table 4.2 COV of uniaxial concrete compression test results.

Structural element	First group (%)	Second group (%)	Third group (start of shake-table experiments) (%)
Foundation	7.6@11 day	5.6@28 day	1.1@567 day
Columns	4.0@5 day	4.6@33 day	9.1@552 day
Beams and slab	5.4@10 day	1.6@32 day	1.4@538 day



(a) Test setup



(b) Concrete compressive strength-gain with time

Fig. 4.1 Concrete compressive strength test.

4.1.2 Concrete Cylinder Split Tension Tests

Concrete cylinder split tension tests are performed on three concrete cylinders constructed using the columns concrete batch. The tests are carried out at the start of the shake-table experiments. The split tension tests conform to ASTM C496 and are used to identify the tensile strength of concrete cylinders as defined in Equation 4.1.

$$f_{ct} = \frac{2P}{\pi l d} \quad (4.1)$$

where P is the maximum load at failure, l and d are the length and diameter of the cylindrical specimen, respectively. The failure is sudden, with a vertical splitting crack across the section of the specimen. The individual results as well as their mean value and COV are summarized in Table 4.3. The mean value of the tensile splitting strength of concrete (about 8% of the compressive strength) is used for the computational modeling of the test structure as described in Chapter 7.

Table 4.3 Concrete split tension tests.

Specimen	Maximum load [kips (kN)]	f_{ct} [psi (MPa)]
1	48.8 (217)	431 (2.97)
2	50.4 (224)	446 (3.08)
3	46.5 (207)	411 (2.83)
Mean	48.6 (216)	429 (2.96)
COV	3.3%	



Fig. 4.2 Concrete split tension test setup.

4.1.3 Masonry Compression Tests

Three masonry prisms are constructed at the time of the construction of the URM infill wall according to the requirements of the ASTM C 1314. The prisms are capped and secured to two steel plates on top and bottom using Hydrocal gypsum cement, and tested under uniaxial compression 28 days after the wall construction. Both the axial load and the axial displacement (measured between the two steel plates) of the masonry prisms are recorded during these axial compression tests. Figure 4.3 shows the configuration of the masonry prism tests as well as the typical failure mode consisting of vertical splitting and crushing. The stress-strain curves for the

three prisms are shown in Figure 4.4 with the individual results, as well as their mean values and COV, summarized in Table 4.4. In this table f_{mo} , E_m , ϵ_{mo} , and ϵ_{mu} indicate the compressive strength of the masonry, the modulus of elasticity measured as the secant modulus at 75% of the compressive strength, and strain corresponding to maximum compressive stress and ultimate strain of masonry corresponding to the residual stress value of $f_{mu} = 0.15f_{mo}$, respectively, as shown in the insert of Table 4.4.

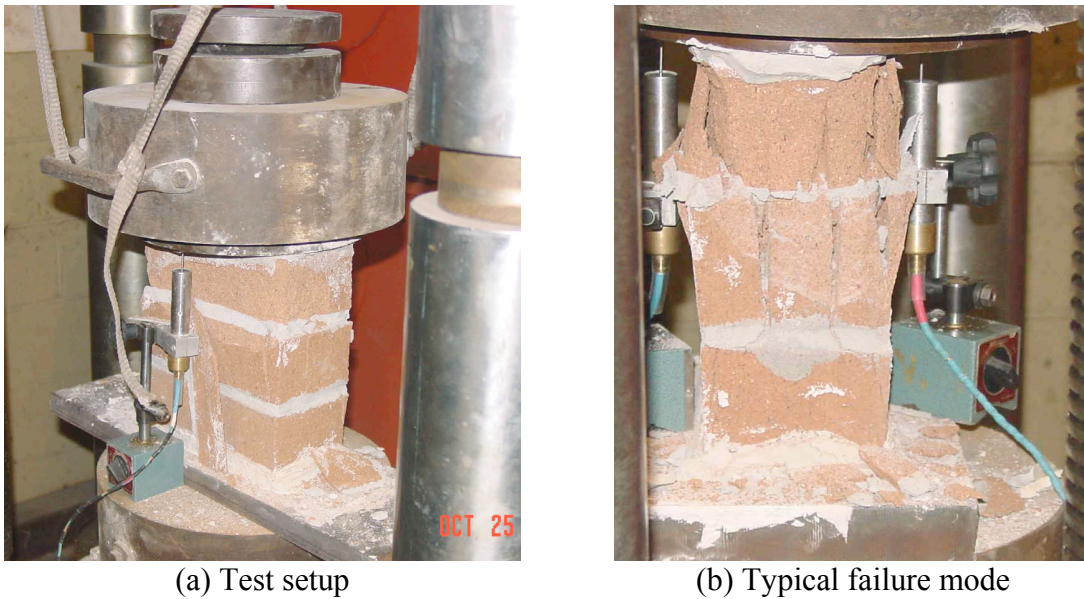


Fig. 4.3 Masonry prism tests.

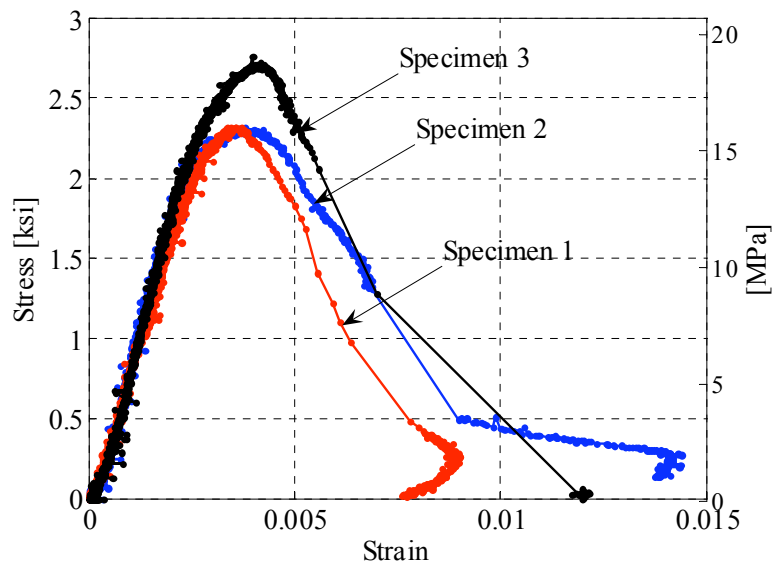
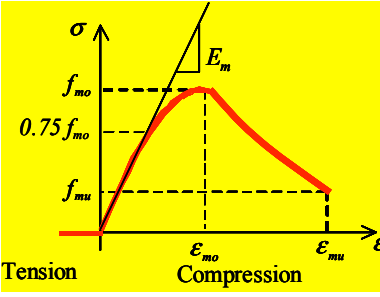


Fig. 4.4 28-day compression stress-strain curves for masonry prisms.

Table 4.4 28-day uniaxial compression test results for masonry prisms.

Specimen	f_{mo} [ksi (MPa)]	E_m [ksi (GPa)]	ϵ_{mo}	ϵ_{mu}
1	2.31 (16.0)	948 (6.54)	0.0038	0.0120
2	2.31 (16.0)	812 (5.60)	0.0035	0.0086
3	2.76 (19.0)	935 (6.45)	0.0040	0.0120
Mean	2.46 (17.0)	898 (6.19)	0.0038	0.0109
COV	10%	8.3%	6.1%	18%



4.1.4 Masonry Diagonal Tension (Shear) Tests

In order to determine the shear strength of masonry, diagonal tension (shear) tests in accordance with ASTM E519 are performed on three specimens. The used specimens are 2'-5½"×2'-5½" (75 cm×75 cm) instead of the usual 4'×4' (122 cm×122 cm) as specified in ASTM E519 in order to facilitate the construction and handling of the specimens. This reduction in size is suggested and allowed by ASTM E519. The specimens are loaded in compression along the diagonal, and the applied load and its corresponding vertical and horizontal deformations (along the diagonals) are recorded. The loading causes almost diagonal cracking (vertical splitting in the testing position) along an axis parallel to the direction of loading corresponding to a rapid drop in the load-carrying capacity of the specimen. The force-deformation plots corresponding to the vertical and horizontal diagonal deformations of the three tested specimens are shown in Figures 4.5 (a) and (b), respectively. From these plots, note that the horizontal deformation (corresponding to the crack opening of the vertical splitting cracks) is one order of magnitude higher than the vertical deformation.

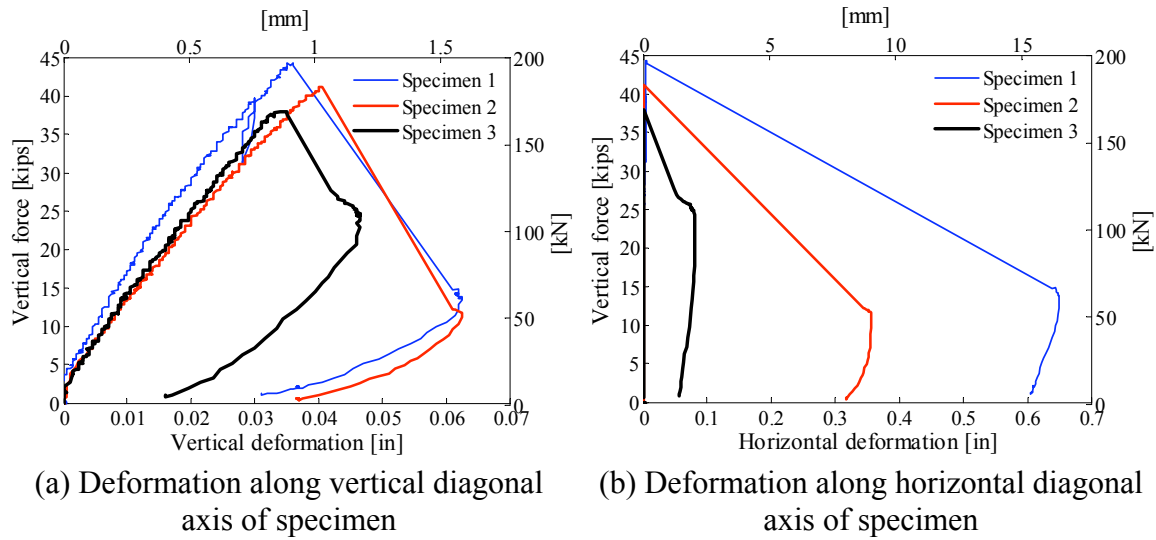


Fig. 4.5 Diagonal force-deformation plots for masonry shear tests.

The shear strength of the masonry f_v is obtained using Equation 4.2.

$$f_v = \frac{P}{A_{eff}} \quad (4.2)$$

where P is the applied peak compressive diagonal force on the specimen and A_{eff} is the gross sectional area of the specimen along its diagonal direction calculated as $\sqrt{2} h t$ where h and t are the side length and thickness of the square specimen, respectively. The applied peak compressive force and its corresponding shear strength for the three specimens as well as the mean value (about 11% of the masonry compressive strength) and COV are presented in Table 4.5. The test setup and a typical failure mode are shown in Figure 4.6.

Table 4.5 Masonry shear test results.

Specimen	Peak compressive load [kips (kN)]	Shear strength [psi (MPa)]
1	44.2 (197)	283 (1.95)
2	41.1 (183)	263 (1.81)
3	38.0 (169)	243 (1.68)
Mean	41.1 (183)	263 (1.81)
COV	7.6%	

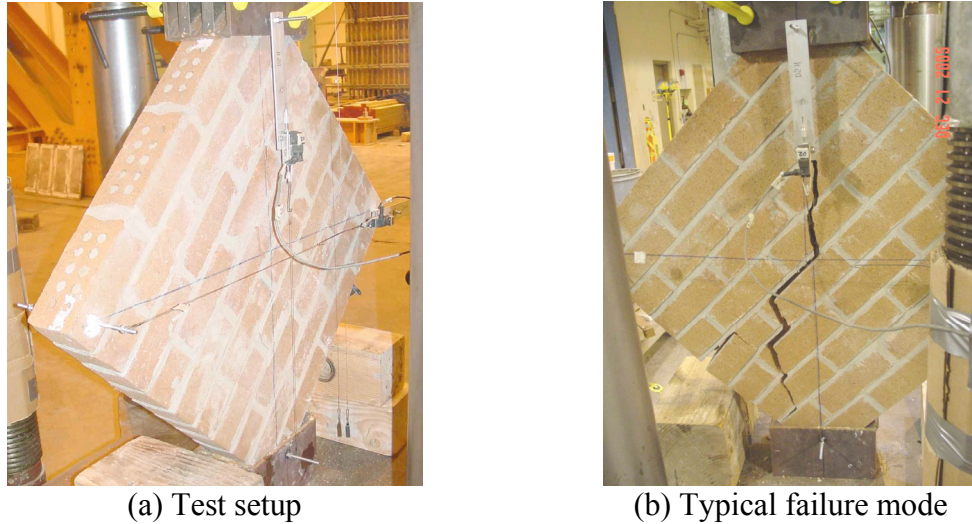


Fig. 4.6 Masonry diagonal tension (shear) test.

4.1.5 Masonry Bending Test

To determine the tensile strength of the masonry assembly, a bending test on 2'-5½"×2'-5½" (75 cm×75 cm) specimen is performed. The test setup is such that the middle third of the span of the specimen is subjected to pure bending moment (i.e., no shear) as shown in Figure 4.7(a). Assuming an elastic-brittle behavior for masonry in tension, the tensile strength of the masonry assembly can be calculated from Equation 4.3:

$$f_t = \frac{M}{S} = \frac{P L / 6}{b t^2 / 6} \quad (4.3)$$

where M is the applied bending moment, S is the section modulus, P is the total applied peak vertical load, L is the span, and b and t are the width and thickness of the specimen, respectively. The total applied peak vertical load recorded during the test is $P = 978$ lbs (4.35 kN) which corresponds to $f_t = 69.5$ psi (479 kPa) representing only 3% of the masonry compressive strength and 26% of its shear strength. This relatively low value, compared to those in more homogeneous materials, such as concrete, is attributed to the mode of failure of the masonry composite (two-phase) material (Lourenço 1996), in Figure 4.7(b), which is dominated by a single vertical crack along the weak plane of the mortar-brick interface.



(a) Test setup

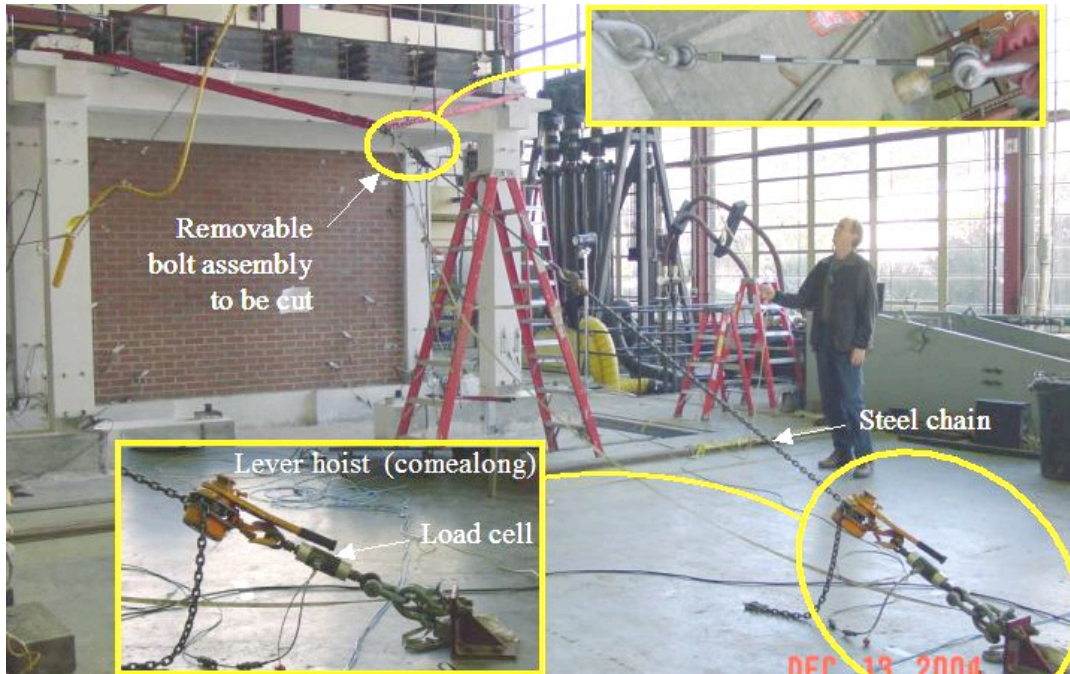


(b) Typical failure mode

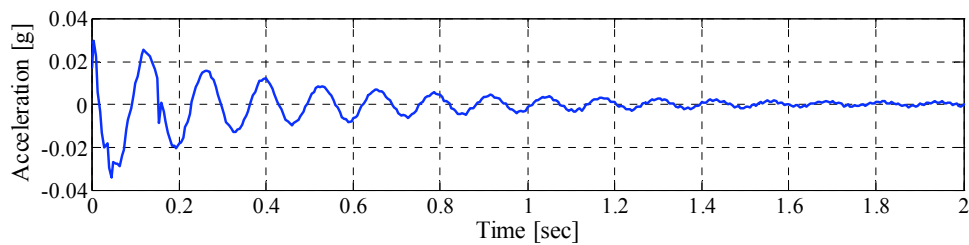
Fig. 4.7 Masonry bending test.

4.2 SNAP-BACK TESTS

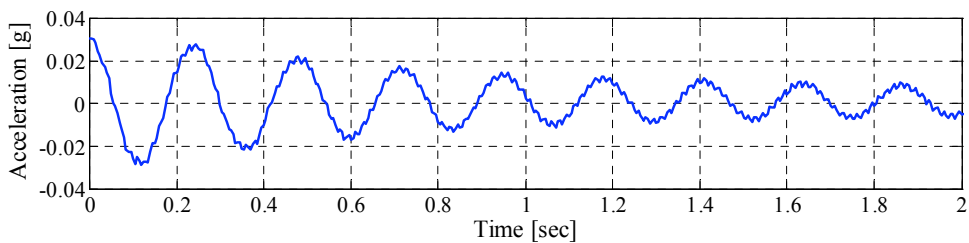
Pull-back (snap-back) tests are performed on the test structure before and after the URM infill wall construction to determine the stiffness, natural frequency, and damping ratio of the structural system before starting the shake-table experiments. These tests are separately conducted for both the longitudinal (north-south) and transverse (east-west) directions of the test structure. It is to be noted that the torsional response of this symmetric test structure is not of interest; therefore, asymmetric snap-back tests of the longitudinal and transverse directions are not considered in this study. For each test, the structure is pulled in one direction by applying 3–8 kips (13–36 kN) lateral force, depending on the stiffness of the test structure, using lever hoist (come-along), and then released suddenly to allow free vibration. The floor acceleration and displacements are measured during both the loading (pulling) phase and the free vibration phase of the test. The force-displacement results of the pull test are used to obtain an estimate of the stiffness of the test structure. The floor acceleration responses during the free vibration after releasing the pulling force, both in the time and frequency domains, are analyzed and used to estimate the natural period of vibration of the test structure and the corresponding damping ratio. A typical configuration and sample test results of the snap-back test is shown in Figure 4.8. The results in this figure refer to the second snap-back test in the north-south and east-west directions after building the URM infill wall, post-tensioning of the columns, and installation of additional mass on the RC slab. The complete results of the snap-back tests are presented in Appendix B.



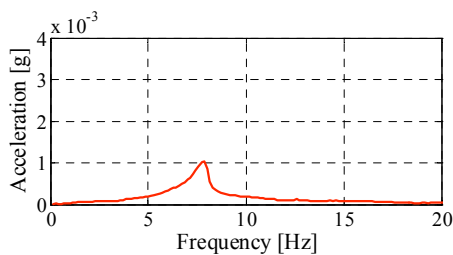
(a) Test configuration



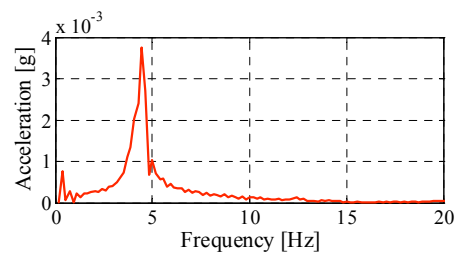
(b) North-south acceleration time history at RC slab level



(c) East-west acceleration time history at RC slab level



(d) North-south acceleration frequency response at RC slab level



(e) East-west acceleration frequency response at RC slab level

Fig. 4.8 Snap-back test configuration and sample results after building URM infill wall.

The mean and COV of the snap-back test results are tabulated in Tables 4.6 and 4.7, respectively. From these results, several conclusions can be made about the effect of adding the URM infill wall and post-tensioning of the columns on the overall stiffness, natural period, and damping ratio of the test structure in the north-south (longitudinal) and east-west (transverse) directions. Considering the response of the test structure in the north-south direction, it is observed that the addition of the URM infill wall increases the stiffness of the test structure by 380% while causing a 33% increase in the damping ratio with respect to the state of the structure before building the URM infill wall and post-tensioning of the columns. Considering the response in the east-west direction, it is observed that post-tensioning of the columns alone (assuming that the URM infill wall has negligible effects in the transverse direction) resulted in a 25% increase in the stiffness with a negligible change in the damping ratio. The addition of the mass does not affect the stiffness of the structure (1% change in the north-south direction). However, this added mass causes a 20% increase in the damping ratio of the test structure in the north-south direction, possibly due to the increase in the axial force on the URM infill wall enhancing the friction forces along the interface between the URM infill wall and the RC beam. The results obtained for the stiffness and the natural period show small variation between the different tests in both directions with COV ranging from 1.8% to 6.9%. On the other hand, the results for the damping ratio suggest more variability, with COV as high as 24%. These results underscore the importance of considering the uncertainty in the damping ratio of the test structure when performing reliability analyses.

Table 4.6 Mean of snap-back test results (see Fig. 1.1(c) for orientation of north (N) direction).

Conditions of test structure at time of snap-back test	North-south direction			East-west direction		
	Natural period (sec)	Damping ratio (%)	Stiffness [kips/in. [kN/mm]]	Natural period (sec)	Damping ratio (%)	Stiffness [kips/in. [kN/mm]]
Before building wall No additional mass	0.135	4.30	113 (19.8)	0.134	4.40	134 (23.5)
After building wall Columns post-tensioned No additional mass	0.055	5.70	426 (74.5)	0.122	4.30	167 (29.3)
After building wall Columns post-tensioned With additional mass	0.134	6.85	431 (75.5)	0.232	4.25	-

Table 4.7 COV of snap-back test results (see Fig. 1.1(c) for orientation of north (N) direction).

Conditions of test structure at time of snap-back test	North-south direction				East-west direction			
	Number of tests	Natural period	Damping ratio	Stiffness	Number of tests	Natural period	Damping ratio	Stiffness
Before building wall No additional mass	3	2.6%	4.9%	5.0%	3	2.2%	10%	1.7%
After building wall Columns post-tensioned No additional mass	3	1.8%	2.4%	2.1%	3	3.6%	10%	6.9%
After building wall Columns post-tensioned With additional mass	4	4.1%	19%	5.9%	2	4.5%	24%	-

4.3 SUMMARY

The mean and COV of the compressive strength of concrete used in the construction of the test structure are determined at different times. Moreover, the mean and COV of the tensile strength of concrete are estimated using the results of concrete split tension tests. Masonry prisms and panels are constructed with the same material and workmanship of the URM infill wall in the test structure. Uniaxial compression tests, masonry diagonal tension (shear) tests, and a bending test are performed on the masonry specimens and the mean and COV values for the compressive, shear, and tensile strength of masonry are reported. A series of snap-back tests are performed on the test structure before and after construction of the URM infill wall and post-tensioning of the columns, and after addition of the mass. From those snap-back test, the dynamic properties (natural period and damping ratio) and the overall stiffness of the test structure in both the north-south (longitudinal, parallel to the URM infill wall) and east-west (transverse, perpendicular to the URM infill wall) directions before the start of the shake-table experiments are determined. Sample results and discussions of these snap-back tests are presented and the reader is referred to Appendix B for the complete set of results.

5 Ground Motions and Experimental Stages

The process of selecting the ground motion for the shake-table experiments is outlined in this chapter. The specifics of each of the selected ground motions in the presented study, signal processing and filtering applied to each ground motion, and design spectra and scale factors used to produce different levels of intensity are also presented. The selected and scaled ground motions are fed as input signals to the shake-table control system. The recorded output motions of the shake table without (i.e., empty table) and with the test structure (i.e., loaded table) are compared in the time and frequency domains to the input ground motions. The shake-table experiments are organized in three distinct stages based on the damage state and configuration of the test structure. These stages and the sequence of loading in each stage are also discussed in this chapter, and abbreviated designations for each level are defined. These abbreviations are used in Chapters 6 and 7.

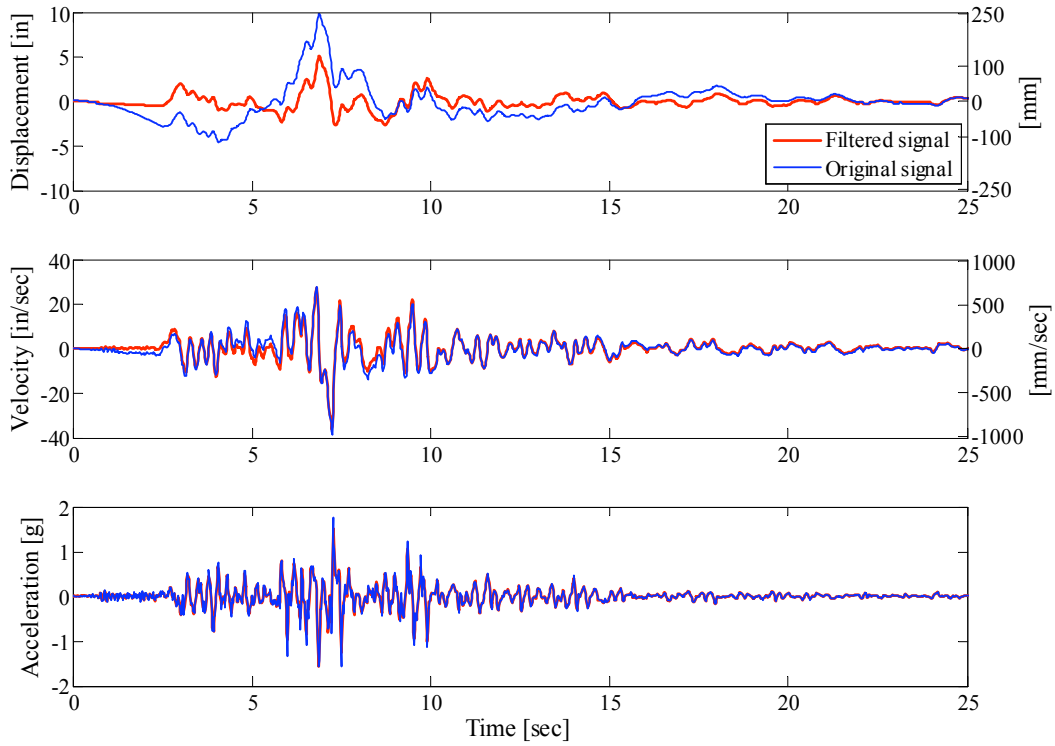
5.1 GROUND MOTION SELECTION

Ground motions with high amplitudes of spectral acceleration in the expected frequency range of the shake-table test structure are considered such that their peak displacement, velocity, and acceleration do not exceed the physical limits of the shake table. See Chapter 3 for a discussion of these limits. Because of the expected changes in the state of the test structure due to structural damages, three different ground motions are selected as the input motions for the shake-table experiments. These ground motions correspond to the Northridge (California, 1994), Düzce (Turkey, 1999), and Loma Prieta (California, 1989) earthquakes and are obtained from the Pacific Earthquake Engineering Research (PEER) Center strong motion database at <http://peer.berkeley.edu/smcat/>. These ground motions are intended to be applied as unidirectional motions in the direction parallel to the URM infill wall of the test structure,

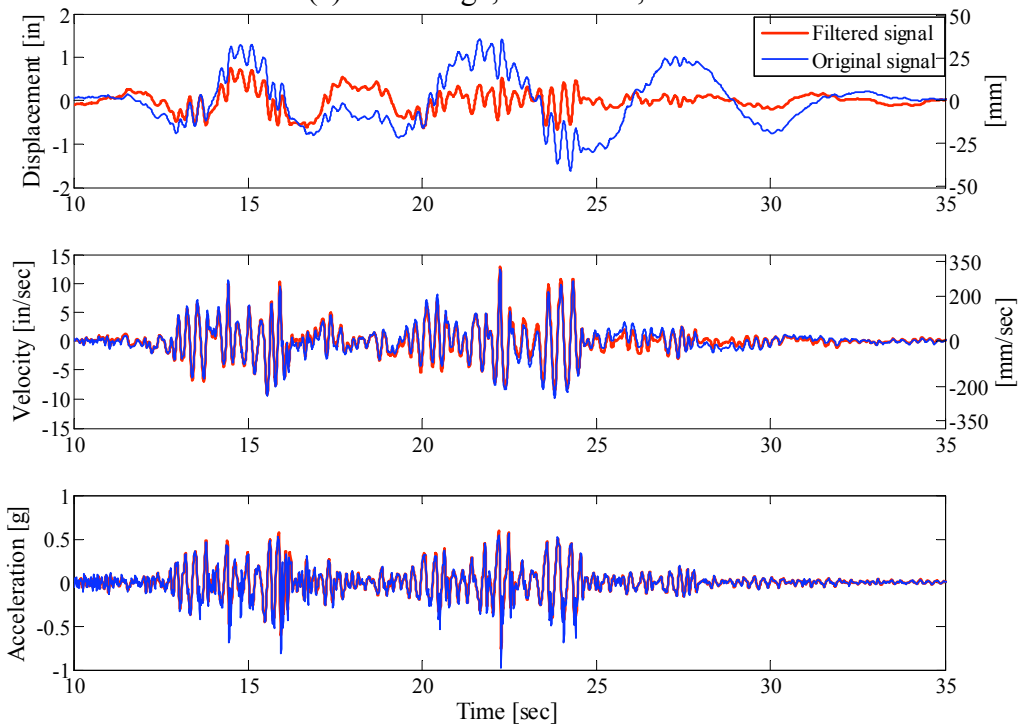
namely the north-south (longitudinal) direction. The ground motion records are compressed in time by a $\sqrt{3/4}$ factor to satisfy the similitude requirements (Sabnis et al. 1983) and to account for the reduced-length scale (3/4) of the test structure. In this way the relationship between the frequency content of the compressed record and the natural period of the undamaged reduced scale test structure is maintained with respect to that of the original record and the test structure without scaling (Sabnis et al. 1983). The ground motion signals are also filtered using a trapezoidal band-pass filter with cut-off frequencies of 0.2 and 15 Hz and corner frequencies of 0.25 and 12 Hz to eliminate the high-frequency content outside the performance range of the shake table and the low-frequency content that correspond to large displacements exceeding the displacement limits of the shake table. The displacement, velocity, and acceleration records of the selected three ground motions before and after filtering (both compressed in time) are shown in Figures 5.1(a)–(c). The acceleration response spectra of these three ground motions before and after filtering are also compared in Figure 5.2. The specifics of the ground motions and their kinematic characteristics before and after filtering are described in Table 5.1. In this table, PGA, PGV, and PGD refer to peak ground acceleration, velocity, and displacement, respectively. It is observed that the application of the described trapezoidal band-pass filter reduces the peak displacement and acceleration by as much as 54% and 21%, respectively, while it does not significantly affect the velocity of the motion or its frequency content in the unfiltered range.

Table 5.1 Ground motion specifications.

Ground motion	Station	Direction	Original signals			Filtered signals		
			PGA (g)	PGV [in./sec (mm/sec)]	PGD [in. (mm)]	PGA (g)	PGV [in./sec (mm/sec)]	PGD [in. (mm)]
Northridge, CA, 1994	Tarzana	090	1.78	38.7 (983)	9.81 (249)	1.57	36.2 (920)	5.13 (130)
Düzce, Turkey, 1999	Lamont	N	0.97	12.4 (316)	1.62 (41.1)	0.762	13.0 (329)	0.750 (19.1)
Loma Prieta, CA, 1989	Bran	000	0.45	17.5 (444)	2.47 (62.8)	0.426	17.4 (443)	2.28 (57.9)

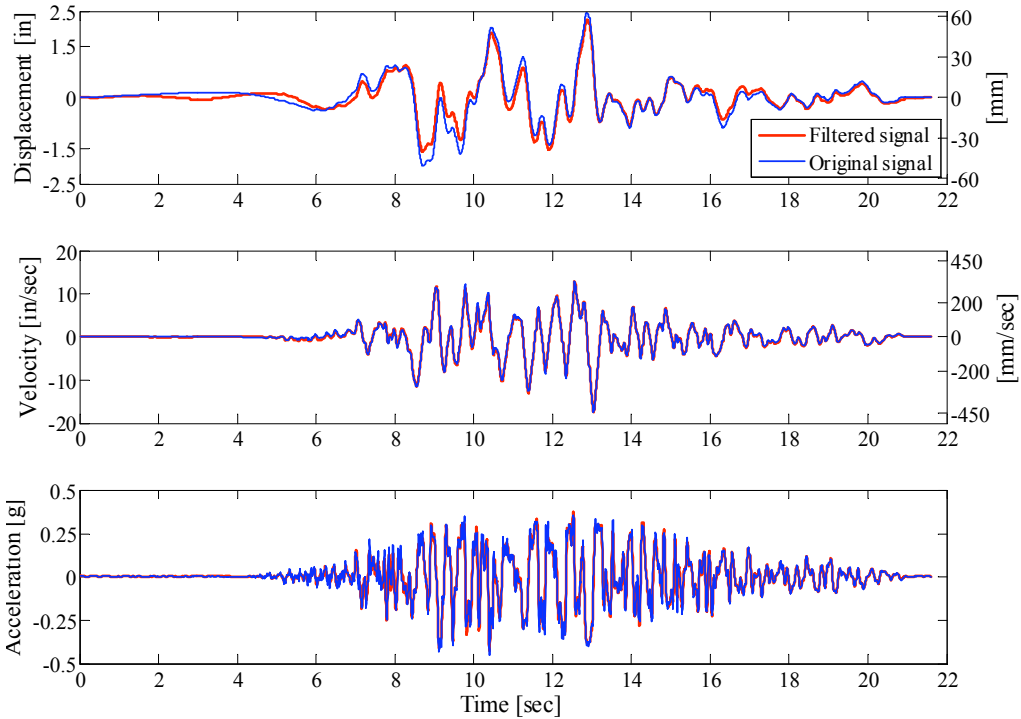


(a) Northridge, California, 1994



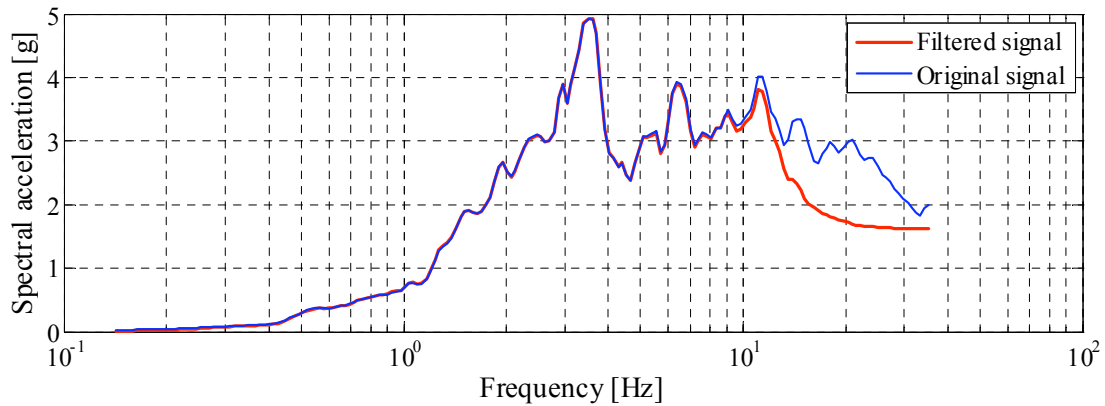
(b) Düzce, Turkey, 1999

Fig. 5.1 Time-domain comparisons for original and filtered shake-table input signals.



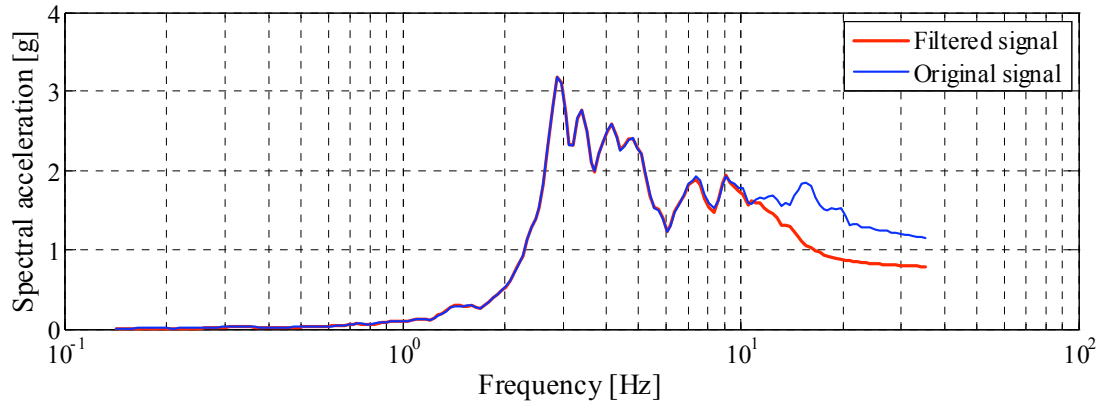
(c) Loma Prieta, California, 1989

Fig. 5.1—Continued

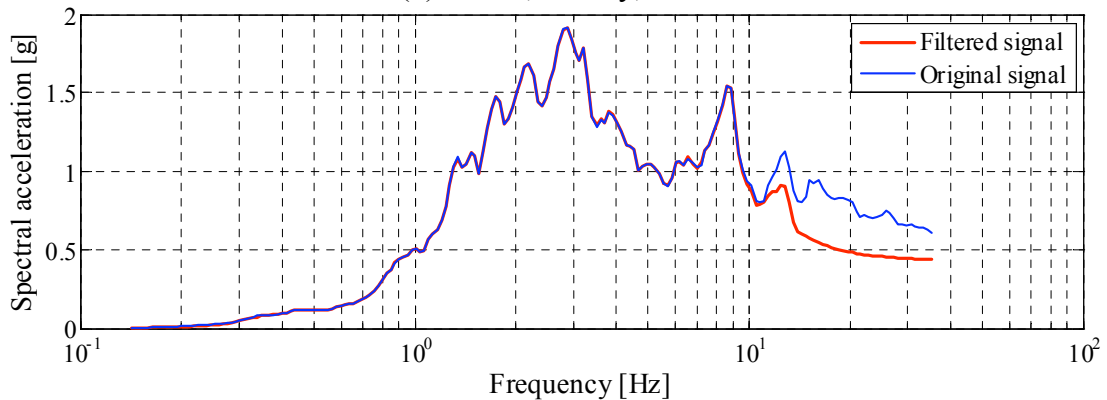


(a) Northridge, California, 1994

Fig. 5.2 Frequency-domain comparisons for original and filtered shake-table input signals.



(b) Düzce, Turkey, 1999



(c) Loma Prieta, California, 1989

Fig. 5.2—Continued

5.2 SHAKE-TABLE OUTPUT MOTIONS

The displacement time history of the selected scaled (compressed) and filtered ground motions discussed in the previous section are fed as input signals to the shake-table control system. The test structure, however, is subjected to the actual output of the shake table as measured at the test structure footings. As an example, the input and output displacement, velocity, and acceleration time histories of the design-level ground motion for the Northridge earthquake are compared in Figure 5.3. For this ground motion, the acceleration response spectra of the input and output motions are presented in Figure 5.4. The details of this design level and other intensity levels for each ground motion, as well as their corresponding scale factors, are discussed in the next section.

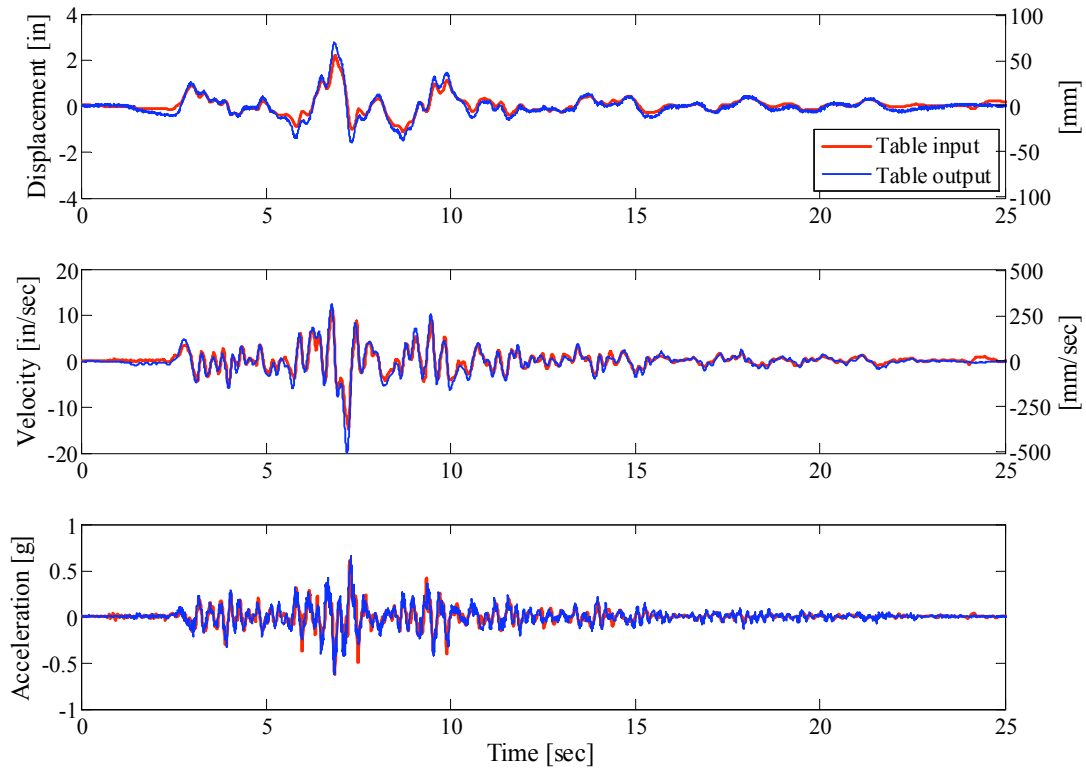


Fig. 5.3 Time-domain shake-table input and output comparisons for design level of Northridge earthquake.

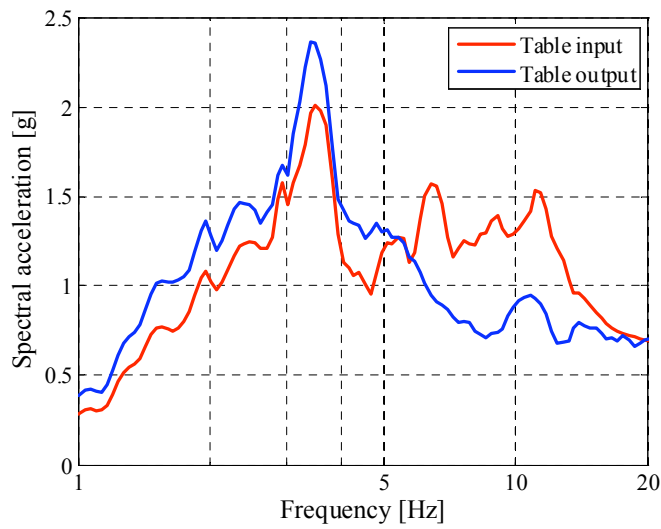


Fig. 5.4 Frequency-domain shake-table input and output comparison for design level of Northridge earthquake.

It is observed that although in the time domain the displacement, velocity, and acceleration of the shake table follow the command signal reasonably well, in the frequency domain the performance of the shake table is less than ideal, overestimating the response by 18% at 3.5 Hz and underestimating it by 30% at 10 Hz. The deficiency in the table performance at higher frequencies is primarily due to the interaction between the test structure and the shake table itself, which is a known difficulty when large and relatively stiff structures are installed on the shake table. To alleviate the effects of this difficulty in the presented study, instead of the input ground motions, the output of the shake table is used to determine the scale factors necessary for intensity levels, discussed in the following section, and as input motions to the computational models, discussed in Chapter 7. It is worth noting that the application of the actual prescribed input ground motions during the shake-table experiments did not offer any significant value or insight toward the realization of the goals of the study which is intended to be generic in nature and not for a specific structure or a particular ground excitation.

5.3 DESIGN SPECTRA AND INTENSITY LEVELS

The ground motions discussed in the previous sections are scaled to generate different levels of intensity (seismic hazards) as expressed in Table 5.2. The scaling is based on the average spectral acceleration of the selected ground motions and the NEHRP (Building Seismic Safety Council 2000) design spectra for a class D site with mapped spectral response accelerations at 1 sec, $S_1 = 0.65g$ and at short periods, $S_s = 1.60g$ with 5% damping within the range that the period of the test structure is expected to vary during the shake-table experiments. For the Northridge and Düzce ground motions, this range is estimated from the period of the undamaged infilled test structure to the period of the test structure after removal of the infill wall (between 0.15 sec–0.28 sec). For the Loma Prieta ground motion, this range is estimated between 0.44 sec–0.6 sec to reflect the damaged state of the bare (i.e., without URM infill wall) test structure. The scaled spectra of the three selected (original input) ground motions, i.e., before filtering, and the design spectra are shown in Figure 5.5. In this figure, the natural period of the test structure corresponding to important milestones of the shake-table experiments are indicated. The state of the test structure at these milestone events is discussed in detail in Chapter 6. Moreover, Figure 5.5 identifies the frequency ranges of the three stages of the shake-table experiments discussed in the following section.

Table 5.2 Scale factors for different levels of input ground motions.

Level	1	2	3	4	6	7	8	9
Northridge, CA, 1994 (TAR)	0.049	0.171	0.230	0.393	0.590	-	-	-
Düzce, Turkey, 1999 (DUZ)	-	-	-	-	-	1.498	1.997	2.528
Loma Prieta, CA, 1989 (LomaPr)	-	0.314	0.439	0.670	1.007	1.513	1.945	2.193

Level 1 is selected as a very small amplitude motion to check the performance of the shake table and data-acquisition system. Levels TAR 2 and TAR 3 are selected as low-intensity levels. Levels 4 and 6* correspond to design and maximum considered earthquake (MCE) spectra, respectively. Levels 7, 8, and 9 are selected to achieve higher demands on the test structure up to the limits of the shake table.

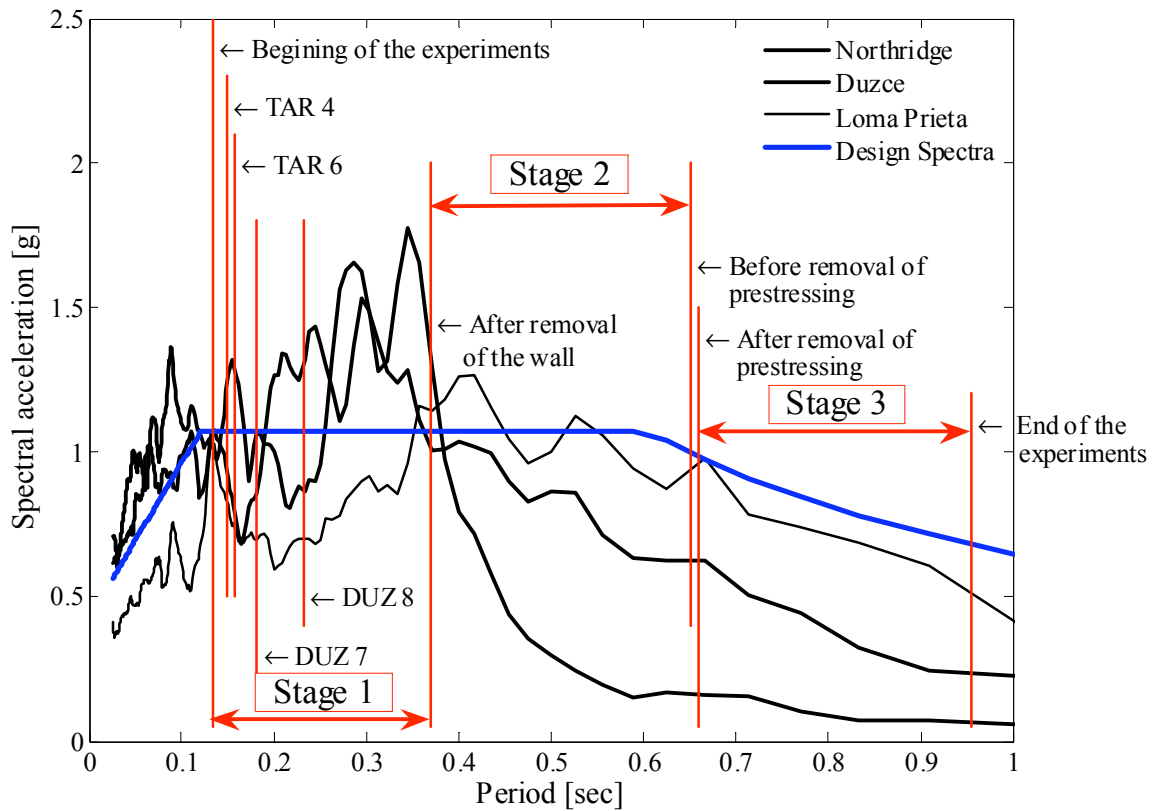


Fig. 5.5 Five percent damping response spectra for selected ground motions.

*During the last stages of planning for the sequence of ground motion, level TAR 5 with PGA of 0.49g was deemed redundant and was not used for the actual experiments.

5.4 STAGES OF EXPERIMENTS AND SEQUENCE OF LOADING

The shake-table experiments are performed in three distinct stages. For stage one, the intact test structure with the URM infill wall is subjected to a sequence of ground motions starting from Northridge, Tarzana level 1 to 6 (designated TAR 1–TAR 6) and Düzce levels 7, 8, and 7 again (designated by DUZ 7, DUZ 8, and DUZ 7-2). Due to the stiff URM infill wall, before the occurrence of any significant damage (up to TAR 6), as discussed in Chapter 6, the lateral behavior is governed by this high stiffness of the URM infill wall. This is not the case after the displacement demand on the URM infill wall exceeds its deformation capacity (refer to Chapter 6) and the wall practically disintegrates (at DUZ 7-2). A transitional phase can be defined in between, i.e., for DUZ 7 and DUZ 8, where the overall behavior is dictated by the level of damage of the URM infill wall and the interaction between the wall and the bounding RC frame.

Stage two of the shake-table experiments is performed after the complete collapse and removal of the URM infill wall. The goal of this stage is to better isolate the effects of the URM infill wall on the tested structural system through comparisons with the results of stage one. Toward this goal, the same sequence of ground motions as stage one is applied to the test structure with the addition of level DUZ 9 (replacing the repetition of DUZ 7, i.e., DUZ 7-2, in stage one) where the physical limitations of the shake table are reached. These motions are designated AWR-TAR 1–AWR-TAR 6 and AWR-DUZ 7–AWR-DUZ 9. Note that AWR stands for “After Wall Removal.” Because a large shift in the natural frequency of the test structure occurs at the end of this loading sequence, a different ground motion with high amplitudes of spectral acceleration in the expected lower-frequency range of the damaged bare test structure is needed to match the design spectra. As shown in Figure 5.5, Loma Prieta ground motion is suitable for this purpose. The test structure is then subjected to Loma Prieta Levels 2 and 6–9 designated LomaPr 2 and LomaPr 6 to LomaPr 9, respectively.

The final stage of the shake-table experiments, namely stage three, is performed to investigate the incipient collapse mechanism of the test structure without the URM infill wall. In order to achieve this goal, the concentric post-tensioning forces in the columns are released by loosening the anchorages of the post-tensioning rods. This is decided after observing that these rods behave as self-centering systems, preventing collapse of the test structure. In this final stage, the test structure is subjected only to the Loma Prieta ground motion sequence.

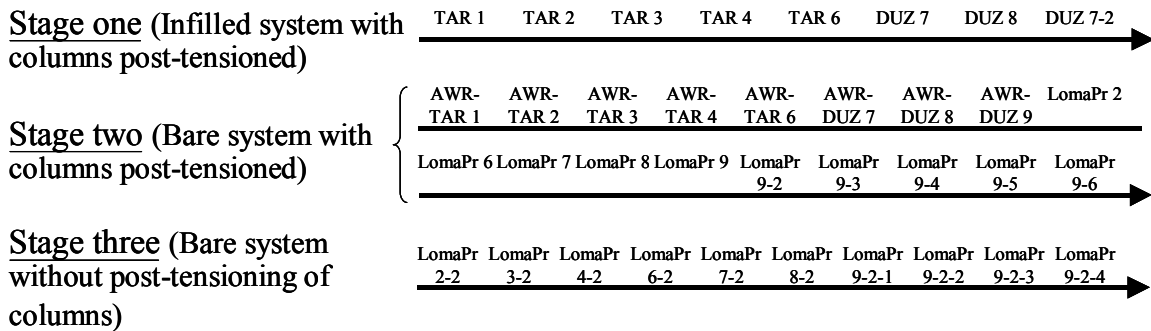


Fig. 5.6 Complete testing sequence of shake-table experiments.

It should be noted that for stages two and three of the shake-table experiments, Loma Prieta ground motion is repeated several times to induce more damage to the test structure. For stage two this is indicated by the repetition number following the designation for each ground motion and its level indicated in Table 5.2. For example, LomaPr 9-6 designates the sixth repetition of LomaPr 9. For stage three, the second designation “2” is introduced to distinguish these runs from those in stage two of the same level. Then, the repetition number, if any, is introduced as the third designation in the run name; e.g., LomaPr 9-2-3 indicates the third repetition of LomaPr 9 for stage three. The complete testing sequence is illustrated by Figure 5.6.

5.5 SUMMARY

Three different ground motions are selected for the shake-table experiments and compressed in time and filtered to offset the scaling of the test structure and to eliminate the frequency content outside the performance range of the shake-table control system. The characteristics of the original and filtered signals in the time and frequency domains are presented. The performance of the shake table is discussed and the input and output signals from the shake table are compared. It is concluded that the output of the shake table should be used for the purpose of scaling to generate different intensity levels and for future computational analyses. The ground motions are scaled with reference to the NEHRP design spectra to represent different intensity levels for the shake-table experiment. Three distinct stages of the shake-table experiments are defined and their objectives are discussed. Finally, the complete sequence of loading for the three stages of the shake-table experiments is presented.

6 Experimental Results and Discussions

This chapter summarizes the results of the shake-table experiments. First, the methodology used to evaluate the dynamic properties and internal forces in the test structure using the data obtained during the experiments from the instrumentation devices is discussed. Then, the results of the experiments are presented for the three different stages of the study discussed in Chapter 5. The global and local responses of the test structure during stage one of the experiments are examined and discussed in detail. The interaction between the URM infill wall and the RC frames, and the redistribution of forces with the progression of damage in the test structure are quantified. The results of stages two and three are also discussed, and the damage sequence in the test structure and the effects of the concentric post-tensioning rods of the columns are demonstrated. For comparison purposes, changes in the key dynamic properties of the test structure, e.g., natural period and damping ratio, are summarized and presented for all three stages of the shake-table experiments.

6.1 SHAKE-TABLE EXPERIMENTAL DATA

The raw data from instruments (Chapter 3) installed on the shake table and the test structure are recorded during each shake-table run and stored as a data matrix in the output file from the shake-table data-acquisition system. Each row of this data matrix corresponds to an instant of time (200 rows per sec at sampling rate of 200 Hz) and each column of this data matrix corresponds to an instrumentation channel (192 columns per each run). For a total of 37 runs in the three stages of the shake-table experiments, these 37 data matrices constitute a very large amount of data, which are analyzed and interpreted in this chapter. The complete raw data gathered during the shake-table experiments are organized and stored on the Network for Earthquake Engineering Simulation (NEES) central data repository at <https://central.nees.org/> to

be made available to the earthquake engineering research community. Nevertheless, small subsets of the raw data matrices are graphically represented in Appendix C for a selectively chosen number of shake-table runs, namely levels TAR 4, TAR 6, DUZ 7, DUZ 8, AWR-TAR 6, AWR-DUZ 7, LomaPr 9, and LomaPr 9-2-1 (see Fig. 5.6).

6.2 SYSTEM IDENTIFICATION

Figure 6.1 shows the methodology used to determine the base shear and distribution of forces in different elements of the test structure, as well as the mean damping coefficient c and the mean stiffness k of the test structure, during each run of the shake-table experiments. To estimate the mean damping coefficient \hat{c} and the mean stiffness \hat{k} , the test structure is idealized as a single-degree-of-freedom (SDOF) system with the mid-floor displacement as the governing degree of freedom (DOF). The total floor acceleration \ddot{u}' is calculated by taking the weighted average of the measured accelerations on the floor. Dividing the floor into three strips consistent with the tributary area of each of the three frames and designating the mass and the measured total acceleration associated with the i^{th} strip as m_i and \ddot{u}_i' , respectively, the total floor acceleration is obtained from Equation 6.1. The total inertial force acting on the structure F_I is subsequently determined using Equation 6.2.

$$\ddot{u}' = \frac{\sum_{i=1}^3 m_i \ddot{u}_i'}{\sum_{i=1}^3 m_i} \quad (6.1)$$

$$F_I = \left(\sum_{i=1}^3 m_i \right) \ddot{u}' \quad (6.2)$$

The acceleration of the floor relative to the shake table \ddot{u} is calculated by subtracting the recorded table acceleration \ddot{u}_g from the total acceleration of the floor \ddot{u}' . The corresponding relative velocity \dot{u} and displacement u are then determined by respective single and double integrations of the relative acceleration in time. It should be noted that the relative displacements are also directly measured using wire potentiometers installed on the test structure, as described in Chapter 3. The relative displacements obtained from wire potentiometers are very close to the values obtained from the accelerometers by double integration. As a representative example, the displacements obtained from double integrating the measurements of the accelerometers and

those from the wire potentiometers are compared for level DUZ 8 in Figure 6.2. In general, the results from the wire potentiometers are considered more direct measurements and are used where the displacements are the target response quantities without further post-processing. However, the displacement and velocity values obtained from integrating the measurements of the accelerometers are less noisy and are consistent with the determined inertial forces (Eq. 6.2) in the test structure. Therefore, the relative displacement and velocity obtained from the integration of the accelerometer results are used in calculation of other quantities, e.g., damping coefficient, dissipated energy, etc.

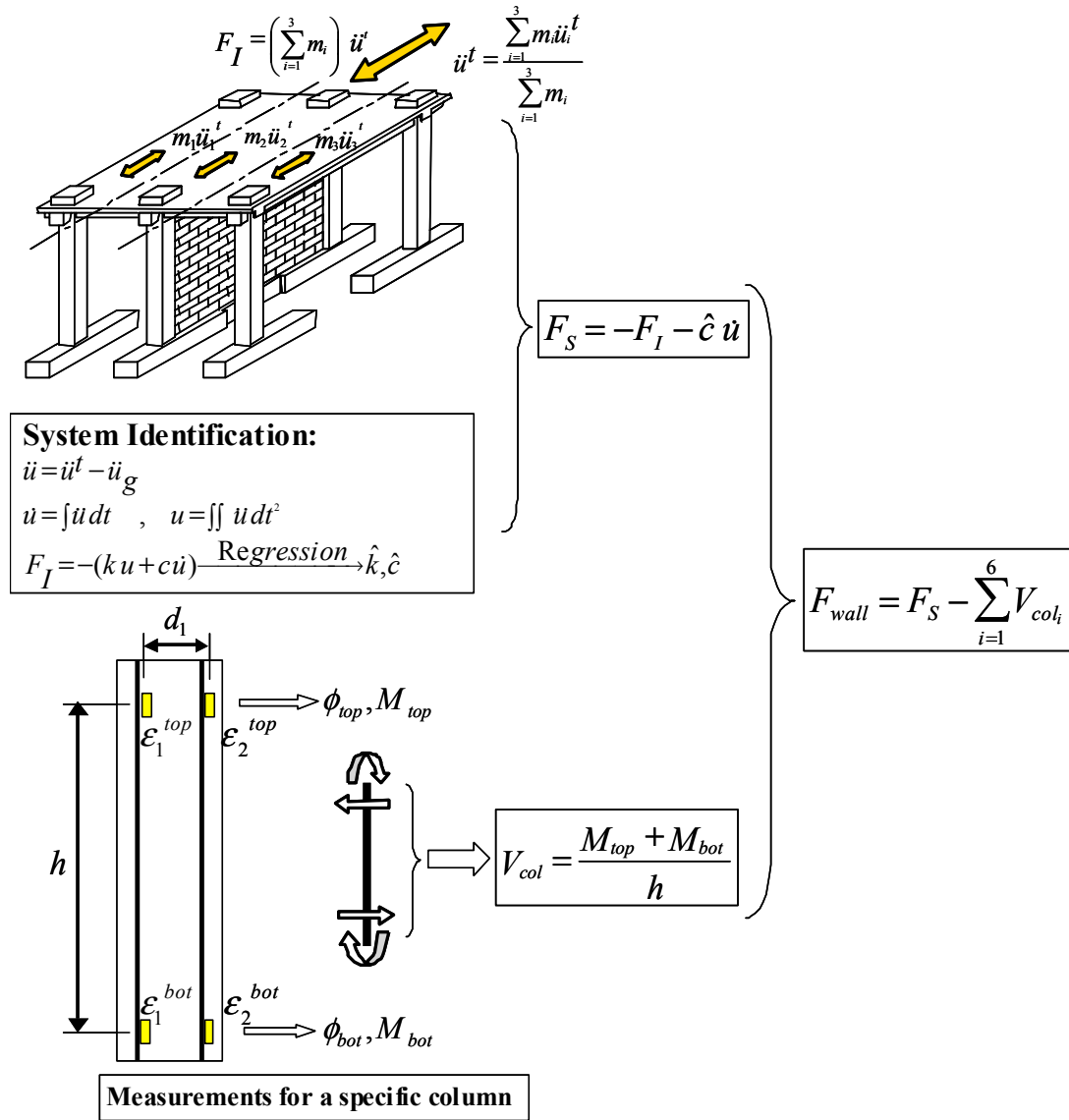


Fig. 6.1 System identification and column shear force calculation in test structure.

The dynamic equilibrium equation for the idealized SDOF system is written as $F_I + F_D + F_S = 0$ at each instant of time. With the assumption of viscous damping, $F_D = c \dot{u}$ is the damping force and $F_S = k u$ is the restoring force of the test structure. Assuming a constant mean damping coefficient c , and a constant mean stiffness k over the duration of each shake-table run, the least-square estimates of the mean damping coefficient \hat{c} and mean stiffness \hat{k} are obtained using the regression function $F_I = -(k u + c \dot{u})$ in the vector space of (u, \dot{u}) considering all the data points in the duration of each shake-table run. Using the estimated value of the mean damping coefficient, the restoring force in the test structure is calculated from the dynamic equilibrium, i.e., $F_S = -F_I - \hat{c}\dot{u}$. In the sequel, this force is referred to as the *total restoring force* of the test structure.

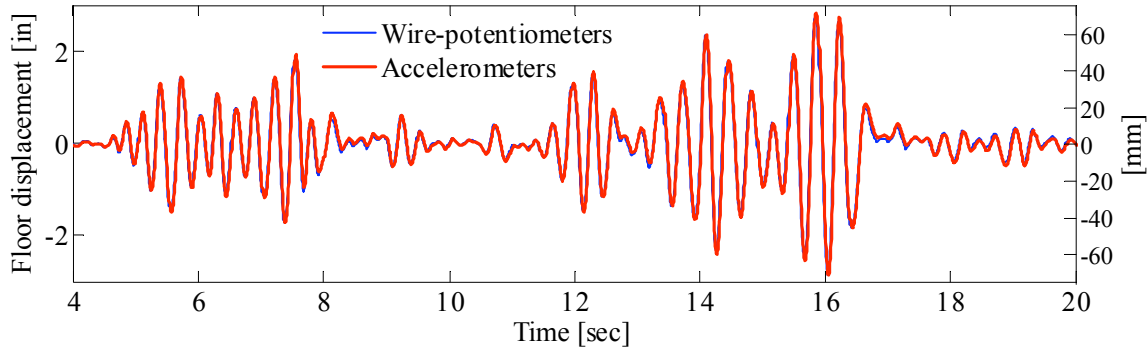


Fig. 6.2 Comparison between partial time history of relative floor displacement obtained from wire potentiometers and accelerometers by double integration during level DUZ 8.

The portion of the total restoring force carried by each column is calculated using the data from the strain gages located at the top and bottom cross sections of each column. By making the Bernoulli assumption of plane-section-remains-plane at those locations and knowing the geometric dimensions, cross-section curvature can be found as $\phi = \frac{\epsilon_1 - \epsilon_2}{d_1}$, where d_1 is the distance between the two strain-gages in the cross section (Fig. 6.1). Using the measured strains, calculated curvature, and assumed constitutive relationships for the reinforcing bars and concrete, the bending moments at each end of the column segment between the two pairs of the strain-gages can be obtained by straightforward cross-section analysis. From the equilibrium of the column segment, column shear can be found using Equation 6.3.

$$V_{col} = \frac{M_{top} + M_{bot}}{h} \quad (6.3)$$

where M_{top} , M_{bot} , and h are defined in Figure 6.1.

For the middle frame columns (B1–B2 in Fig. 2.2) where there is contact between the URM infill wall and the column, the equation for column shear force above the contact length is modified as in Equation 6.4, where $\alpha' h$ is the contact length between the URM infill wall and the column segment bounded by the two instrumented cross sections, and F'_{wall} is the horizontal component of the portion of the compression force in the URM infill wall that is being transferred to the column within the contact length αH , namely $\alpha' h$ as shown in Figure 6.3. Since the strain gages in the test structure are located at cross sections well above the column-footing joint and well below the column-beam joint, the values of both α' and F'_{wall} are relatively small and the second term of Equation 6.4 is neglected without significant loss of accuracy in the calculations of the shear forces of the middle columns.

$$V_{col} = \frac{M_{top} + M_{bot}}{h} - F'_{wall} \frac{\alpha'}{2} \quad (6.4)$$

Finally, the shear force in the URM infill wall F_{wall} is calculated as the total restoring force minus the sum of the shear forces in all six columns comprising the RC framing of the test structure (Fig. 6.1). The URM infill wall force is the horizontal force resisted by the infill wall and has an important role in understating how this URM infill wall contributes to the lateral load resistance of the test structure, one of the main goals of this study.

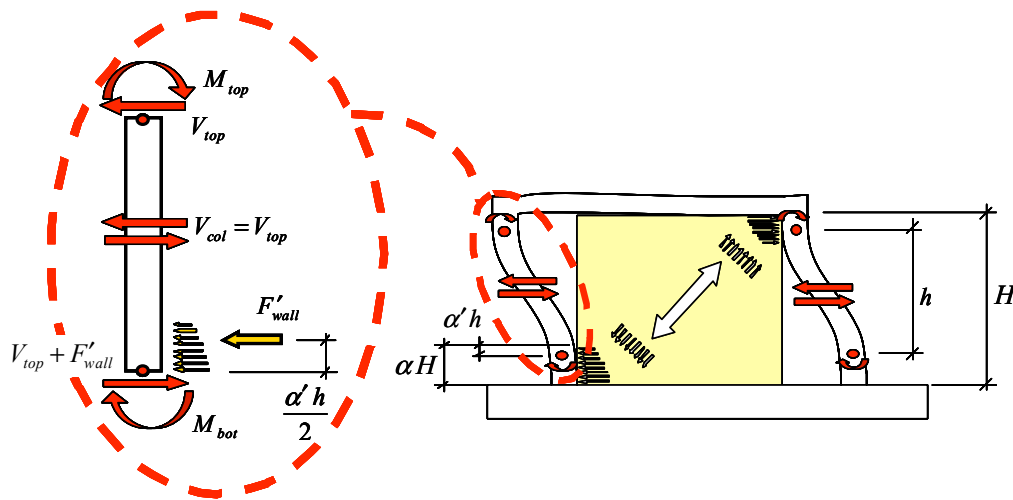


Fig. 6.3 Effect of contact between URM infill wall and columns in determining column shear force.

6.3 DISCUSSION OF STAGE ONE RESULTS

In this section, the results obtained during stage one of the experiments, where the test structure is infilled with URM wall in the middle RC frame, are discussed. The global responses of the test structure in terms of the overall drift, stiffness, and damping ratio as well as the local responses of the different elements of the test structure are quantified and discussed.

To investigate the global responses of the test structure and the extent of damage during one of the experiments, the changes of the force-deformation behavior of the test structure are emphasized first. This is represented by the base shear versus the floor displacement relationships. Subsequently, changes of the dynamic properties, e.g., natural period and damping ratio, are discussed.

The local responses of different elements of the test structure during stage one of the experiments are studied. In particular, the crack patterns and the load paths in the URM infill wall as well as its lateral strength and deformed shapes are illustrated. The distributions of base shear between the URM infill wall and the RC frames are discussed. The change in the demand shear forces on the RC slab, the effects of the accumulation of damage in the URM infill wall, and the redistribution of forces in the structural elements of the test structure are quantified.

6.3.1 Force-Deformation Behavior

The total base shear versus relative lateral displacement (with respect to fixed base) of the RC slab plots for selected test levels are presented in Figure 6.4. The lateral displacement in these plots is measured using the wire potentiometers installed on the floor and footing of the test structure, as described in Chapter 3. The total base shear is defined as the sum of the restoring and damping forces in the test structure, which from the equation of motion is equal to the total inertial force F_I as described in Section 6.2. In the presentation of results shown in Figure 6.4, the stiffness is estimated by the tangent stiffness of the loading branch evaluated to quantify the change in the force-deformation behavior during the experiments. During levels TAR 1 and TAR 2, there are no considerable changes in the stiffness of the test structure. The plot for level TAR 3 (Fig. 6.4(a)) shows slight reduction in stiffness (about 9% from 431 kips/in. (75.5 kN/mm) of the snap-back test results in Chapter 4) to about 391 kips/in. (68.4 kN/mm) without visible signs of damage in the test structure.

The response of the test structure in level TAR 4 (design level) as depicted in Fig. 6.4(b) shows some drop in the stiffness (about 15% reduction) with the overall behavior remaining almost linear. Close observation of the URM infill wall after the completion of TAR 4 reveals small visible cracks at the wall-column interfaces.

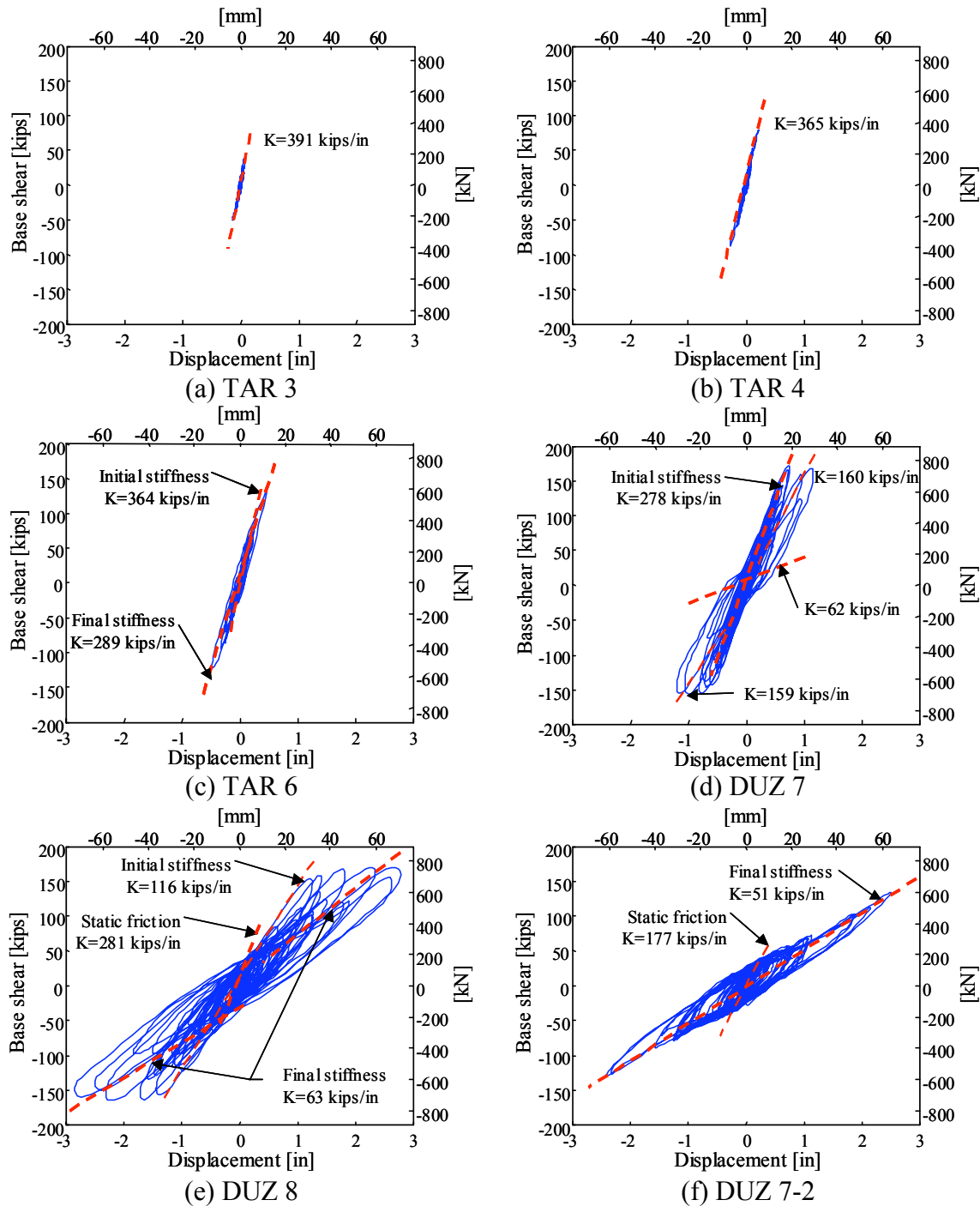


Fig. 6.4 Total base shear versus relative lateral displacement of RC slab for different test levels of stage one (1 kip/in. = 0.175 kN/mm).

Figure 6.4(c), corresponding to level TAR6, shows the first significant signs of damage. The stiffness of 364 kips/in. (63.7 kN/mm) in the initial motion shifts to 289 kips/in. (50.6 kN/mm) at the peak of the ground motion (21% shift). Observations after this test level suggest that some cracks are developing, especially along the column-wall interface, and some small vertical splitting cracks are observed in the mortar head joints at the URM infill wall corners. The maximum total base-shear force reached in this level is 136 kips (605 kN) corresponding to 144% of the total gravity load.

The response of the test structure during level DUZ 7 (Fig. 6.4(d)) shows the most significant change in the behavior of the structural system. The stiffness at the beginning of this level is 278 kips/in. (48.7 kN/mm). Significant URM infill wall cracks with clear pattern and load path definitions are formed during this test level. The crack pattern and load path are discussed in Section 6.3.5. The force-displacement behavior of the test structure at this point, i.e., after formation of these significant cracks, can be described by a bilinear relationship. For small relative lateral displacements (less than about 0.25" (6 mm)), the existing cracks on the URM infill wall open and close without engaging the different portions of the URM infill wall, resulting in an observed lateral stiffness of about 62 kips/in. (10.9 kN/mm). Once the cracks close for relative lateral displacement greater than about 0.25" (6 mm), the URM infill wall picks up the load by a compression strut action causing further damage in the URM infill wall and significant stiffness increase to about 160 kips/in. (28.0 kN/mm). The peak total base-shear force observed during all stages of the shake-table experiments, namely 170 kips (756 kN) corresponding to 180% of total gravity load, at relative lateral displacement of 0.75" (19.1 mm) is recorded during this level (DUZ 7) of the experiments and right before a major horizontal (along bed joint) crack in the URM infill wall is developed at about one third of the URM infill wall height from the bottom.

Figure 6.4(e) shows the gradual global disintegration of the URM infill wall as the test structure is cycled back and forth in level DUZ 8. The measured stiffness of the test structure at the beginning of this level is high, i.e., 281 kips/in. (49.2 kN/mm), for small displacements. Comparison of this stiffness and that of the previous run (278 kips/in. (48.7 kN/mm) for DUZ 7) suggests that at small force demands, the force transferred through the wall is not enough to overcome the static friction between the cracked surfaces. Accordingly, at such small forces, the URM infill wall acts as a whole panel increasing the apparent stiffness of the structural system. Once the force demands at the crack surfaces exceed the static friction (at about 25 kips (110 kN)

corresponding to 27% of the total gravity load), the cracked portions of the URM infill wall start to move with respect to each other and the stiffness reduces to that of the RC frames, including the intact portions of the URM infill wall, i.e., 116 kips/in. (20.3 kN/mm) as shown in Figure 6.4(e). Note that the stiffness of the test structure before constructing the URM infill wall (Table 4.6) is 113 kips/in. (19.8 kN/mm), so from this point on, the URM infill wall can be considered as structurally insignificant. As the test structure goes through large displacements, the RC frames start to accumulate damage mostly concentrated at the bases of the columns. The stiffness of the test structure at the end of this level is reduced to 63 kips/in. (11.0 kN/mm), i.e., only 56% of the initial stiffness of the test structure before constructing the URM infill wall, suggesting rather significant damage in the RC frames in addition to the collapse of the URM infill wall.

Finally, Figure 6.4(f) shows the results obtained from the repeated run of level DUZ 7, i.e., DUZ 7-2. Beyond the static friction at the beginning of the motion where the stiffness is high at a value of 177 kips/in. (31.0 kN/mm), the stiffness of the test structure is 51 kips/in. (8.9 kN/mm) at about 20% reduction from that at the end of DUZ 8 and representing only 45% of the initial stiffness of the test structure before constructing the URM infill wall.

Figure 6.5 shows a compilation of the changes in the “effective” stiffness of the test structure for all levels of testing in stage one plotted along with the measured initial stiffness of the test structure with and without the URM infill wall. This effective stiffness denotes the mean tangent stiffness of the loading branch obtained using linear regression between recorded lateral displacement and base shear when it exceeds the static friction at about 25 kips (110 kN), i.e., 27% of the total gravity load. It can be observed that the existence of the URM infill wall considerably increases the stiffness of the structural system. As the wall undergoes damage, the stiffness of the test structure reduces. This reduction occurs most rapidly during levels TAR 6, DUZ 7, and DUZ 8, suggesting the occurrence of significant disintegration of the URM infill wall in these levels. Note that the stiffness of the test structure reduces to a level less than that of the elastic structure without the URM infill wall, which is due to the damage at column-footing and beam-column joints in the RC frame structure. The damages in the RC frames are discussed in Section 6.3.7.

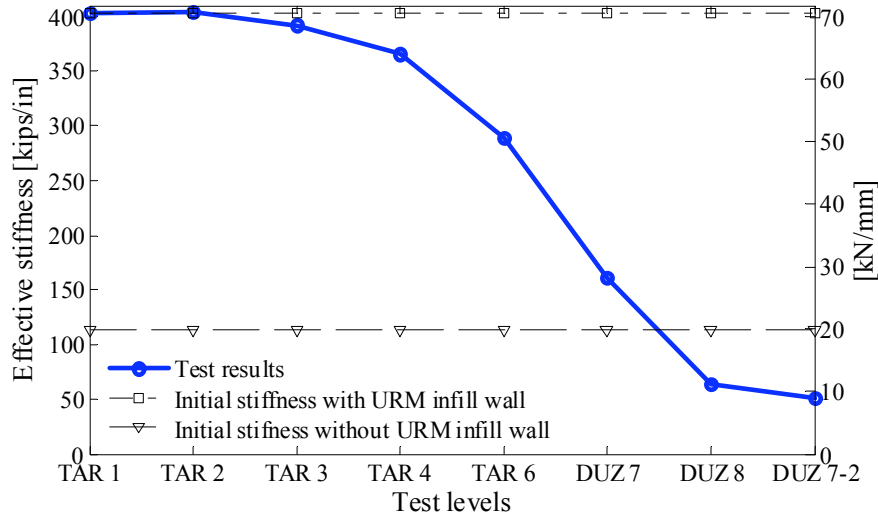


Fig. 6.5 Variation of effective stiffness during stage one of shake-table experiments.

6.3.2 Changes in Natural Period

The reduction in stiffness of the test structure corresponds to a significant elongation in the natural period of the test structure during different levels of the experiments. In order to identify and track changes in the natural period of the test structure as the experiments progress, a low-amplitude (about 0.07g) white-noise signal with approximately constant amplitude over the frequency range of 1–10 Hz is applied before each test run, and the resulting acceleration of the RC slab is studied in the frequency domain. The frequency corresponding to the peak amplitude of the frequency response is selected as the natural frequency of the test structure before each run. An example of these white-noise runs in the time and frequency domains corresponding to the white-noise run performed before level DUZ 7 is shown in Figures 6.6(a) and (b), respectively, where the natural frequency is estimated as 7.33 Hz. Because the white-noise tests are performed with very low amplitudes, it is possible that existing cracks opened during the strong motion of previous runs remain closed during the application of the white-noise signal. Accordingly, the test structure may appear stiffer than its actual conditions. In other words, the natural frequencies resulting from the white-noise data are expected to represent an upper bound for the natural frequency of the test structure during the application of the actual (strong) ground motion.

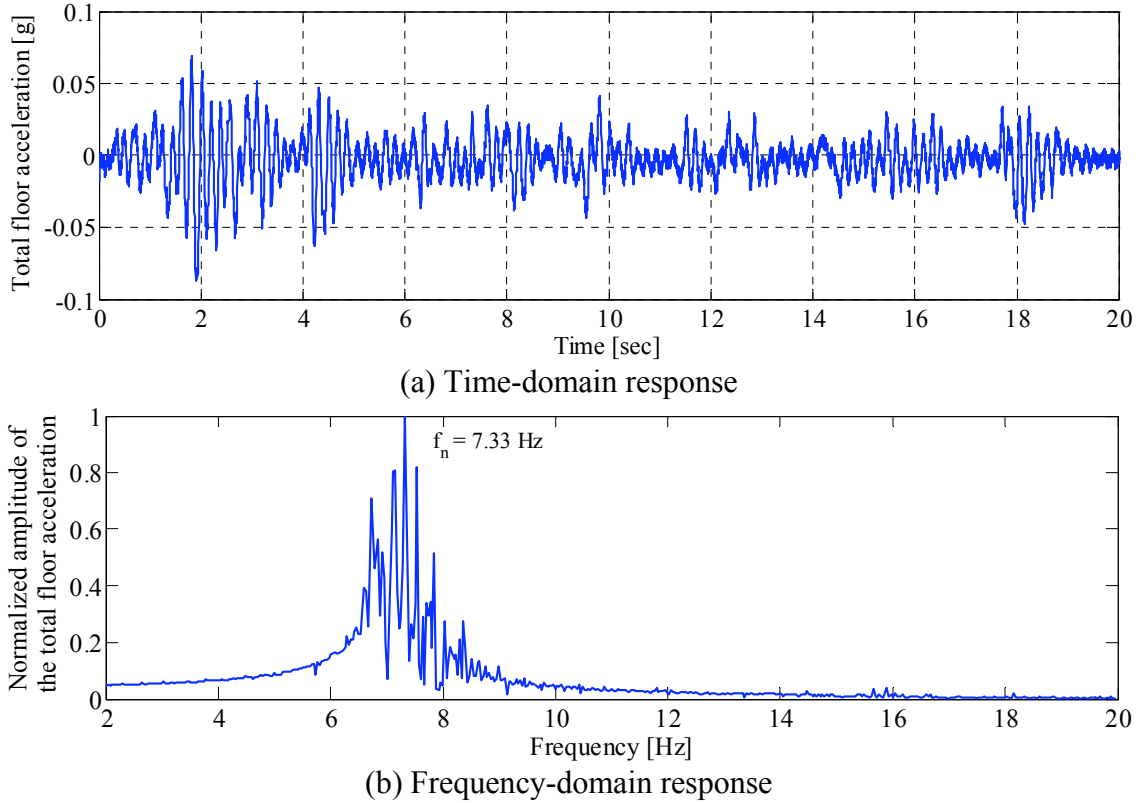


Fig. 6.6 Response of test structure to white-noise signal before level DUZ 7.

Alternatively, the transfer function of the test structure for the RC slab acceleration (output signal) given the acceleration of the base of the test structure (input signal) can be calculated as the ratio of the Fourier transform of the RC floor acceleration $A_{floor}(\omega)$ to the Fourier transform of the base acceleration $A_{base}(\omega)$ as measured by their respective accelerometers, Equation 6.5.

$$TF(\omega) = \frac{A_{floor}(\omega)}{A_{base}(\omega)} \quad (6.5)$$

The natural frequency of the test structure during each test level of the experiments can be defined as the frequency corresponding to the peak amplitude of the transfer function. Examples of these transfer functions in the frequency domain for levels TAR 6 and DUZ 7 are shown in Figures 6.7(a) and (b), respectively, where the natural frequencies are estimated as 6.75 Hz and 6.60 Hz, respectively. It is worth emphasizing that the natural frequency of the test structure obtained using the transfer functions is significantly lower than the upper-bound value obtained from the white-noise run between levels TAR 6 and DUZ 7, namely 7.33 Hz from Figure 6.6(b).

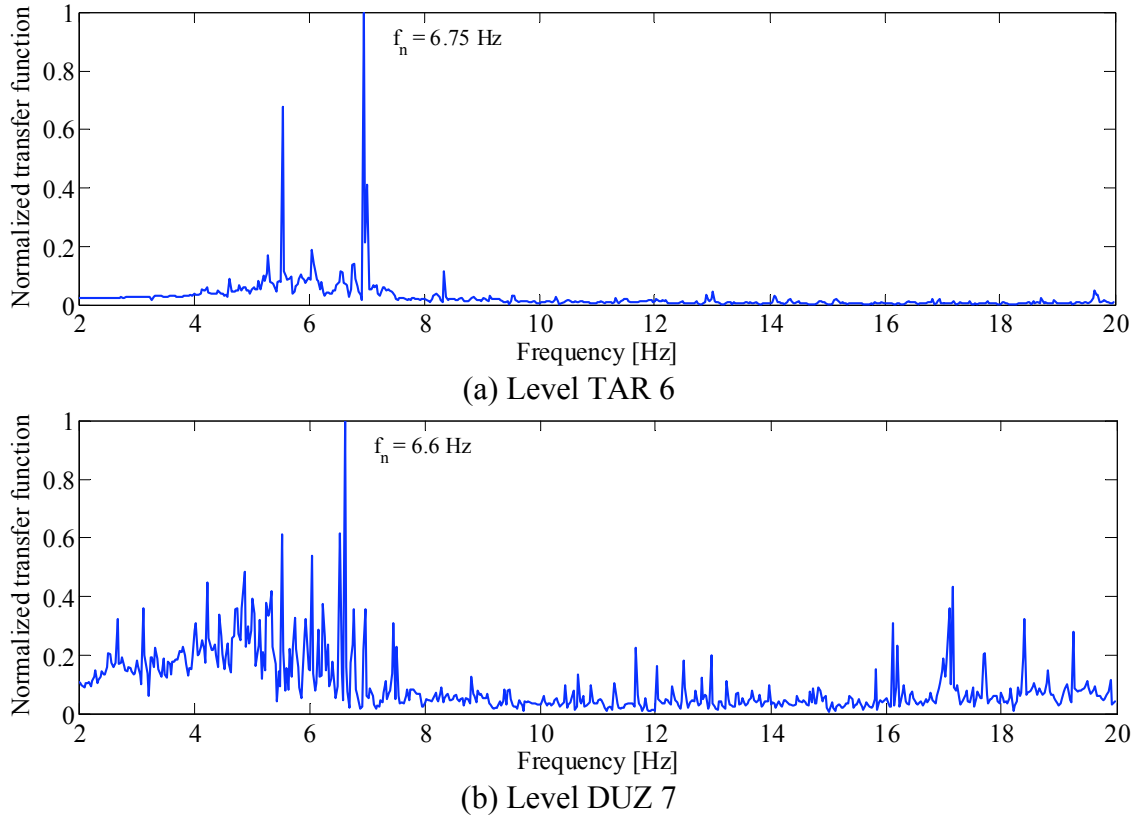


Fig. 6.7 Examples of transfer functions obtained for test structure.

Figure 6.8 demonstrates the change in the natural period (reciprocal of the natural frequency) of the test structure as the experiments progress determined using both the white-noise signals after each test run and the transfer functions of the test structure when subjected to the actual shake-table (ground motion) signals. It can be observed from the results based on the ground motion signals (judged to be more representative of the actual conditions of the test structure than the results from the white-noise signals) that there are significant elongations in the natural period of the test structure, from 0.147 sec during TAR 1 to 0.392 sec during DUZ 7-2, with a 167% increase as the URM infill wall and the RC frames accumulate damage during stage one of the experiments.

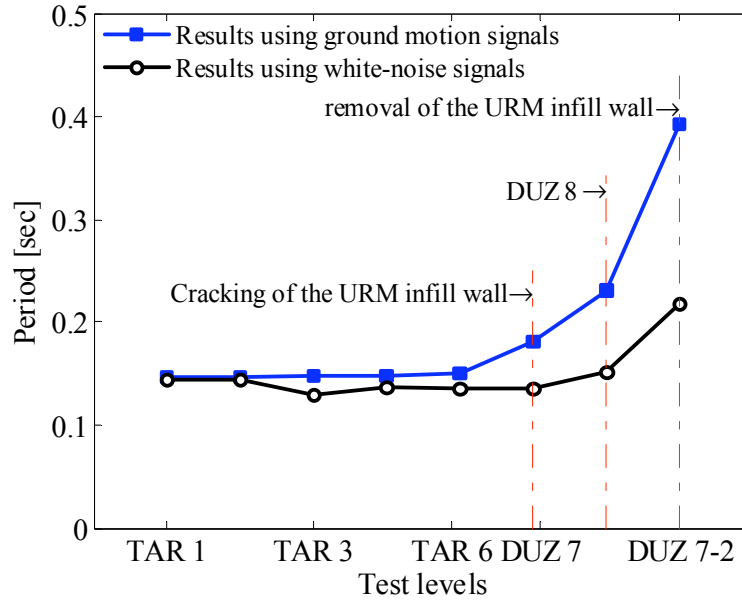


Fig. 6.8 Variation of natural period of test structure during stage one of experiments.

6.3.3 Changes in Damping Ratio

Another indicator of the change in the dynamic properties of the test structure due to the induced damage during the experiments is the change in the damping ratio. The mean damping coefficient c during each shake-table run is obtained with the regression procedure described earlier in this chapter, i.e., using its estimate \hat{c} (Fig. 6.9). It is observed that the highest values of the damping coefficient correspond to levels TAR 6 and DUZ 7 where the URM infill wall is most severely engaged in the structural response. The damping coefficient reduces by 51% during level DUZ 8 compared to level DUZ 7 due to the loss of the URM infill wall.

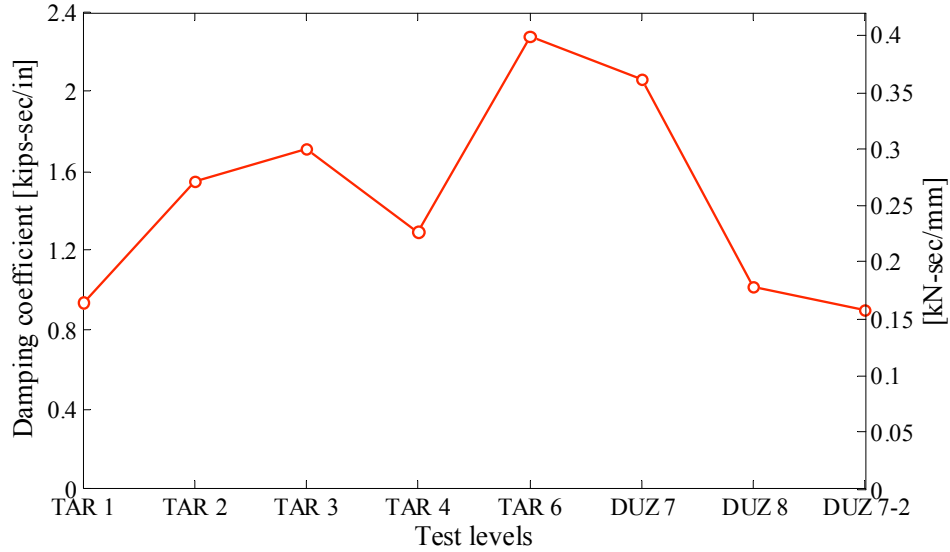


Fig. 6.9 Variation of damping coefficient estimate \hat{c} of test structure during stage one of experiments.

The damping ratio can be defined as $\zeta = \hat{c}/c_{cr}$ where $c_{cr} = 2m\omega_n = 4\pi m/T_n$ is the critical damping of the test structure, m is the total mass, ω_n is the natural circular frequency of the test structure and T_n is the natural period of the test structure. Alternatively, the equivalent damping ratio can be estimated as $1/4\pi$ times the ratio of the dissipated energy E_D to the maximum strain energy E_{So} in each cycle (Chopra 2001) as respectively expressed in Equations 6.6–6.7:

$$E_D = \int_{b: \text{beginning of a cycle}}^{e: \text{end of a cycle}} V_b du \quad (6.6)$$

$$E_{So} = \frac{1}{2} V_{bo} u_o \quad (6.7)$$

where V_b is the total base shear and u is the floor displacement determined from double integration of the relative floor acceleration \ddot{u} as previously defined, u_o is the peak displacement in each cycle, and V_{bo} is its corresponding total base shear. Each cycle, where the integration in Equation 6.6 is carried, can be defined between two local peak displacements in the time history of the floor displacement, and the value of the equivalent damping ratio can be estimated as the mean damping ratio over all the cycles during the length of each ground motion. However, instead of determining the damping ratio for each cycle, it is more practical to determine the sum of the energy values for both E_D and E_{So} over all cycles during each run and

subsequently determine the mean equivalent damping ratio directly as $1/4\pi$ times their ratio. This mode practical approach which avoids the complexity of determining the ends of each cycle is pursued here. The values of the total dissipated energy and the sum of the maximum strain energy over all cycles are evaluated and presented in Figure 6.10 for all test levels of stage one of the experiments. It should be noted that the energy dissipated in the test structure during level TAR 6 is one order of magnitude higher than that of level TAR 4, and energy dissipated in levels DUZ 7 and 8 are also about one order of magnitude higher than that of level TAR 6. The same observations may be made for the sum of maximum strain energy in all cycles during different levels of the experiments. The energy dissipation on its own may be interpreted as a measure of the damage in the test structure, while the sum of the maximum strain energy may be an indication of the intensity of the motion of the test structure. It should be noted that the point in Figure 6.10 where the total energy dissipation and the sum of maximum strain energies coincide (approximately at level TAR 6) corresponds to an equivalent damping ratio of $1/4\pi$, or about 8%. The damping ratios calculated before this point are less than 8% and those calculated after this point are more than 8% (Fig. 6.11).

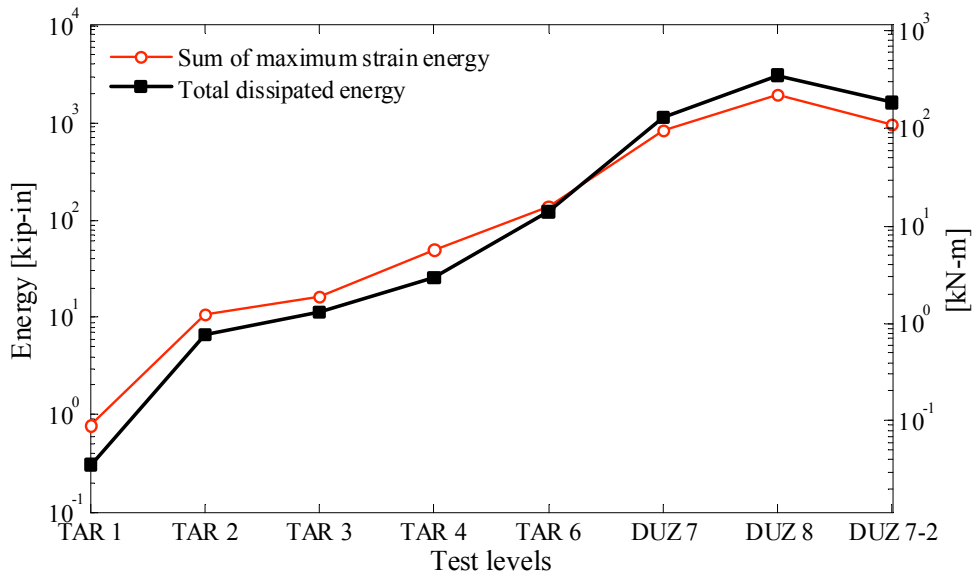


Fig. 6.10 Total dissipated energy and sum of maximum strain energy during stage one of experiments.

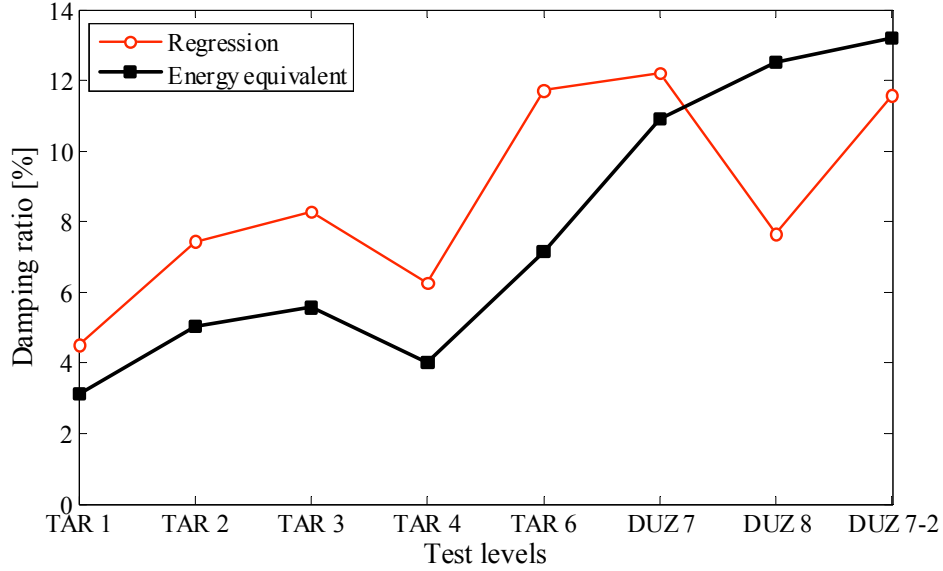


Fig. 6.11 Variation of mean damping ratio of test structure during stage one of experiments.

The resulting variations of the damping ratio ζ for different levels of shaking calculated using the regression and the energy equivalent methods is shown in Figure 6.11. It should be emphasized that while the regression method, assuming a linear response on average, limits the damping only to the velocity-related term in the equation of motion, the equivalent energy method includes both the viscous damping and the inelastic deformations as sources of dissipating energy. Therefore, both of these methods should be considered with their inherent limitations in mind. Since the regression is performed over all data points (loading and unloading including very small values) within each run, the estimate of stiffness \hat{k} is generally less than the actual stiffness of the test structure. The lower estimate of the stiffness in the regression function $F_l = -(\hat{c} \dot{u} + \hat{k} u)$ leads to an overestimation of the viscous damping coefficient in this method. In the equivalent energy method, however, when there is significant hysteretic energy dissipated in the test structure (Levels DUZ 8 and DUZ 7-2), a larger value of the equivalent damping ratio is obtained. It should also be noted that the large value of the damping ratio obtained using the regression method in level DUZ 7-2 with respect to level DUZ 8 is mainly due to the significant elongation in the natural period (associated with significant reduction of the effective stiffness) of the test structure (by 70%) during level DUZ 7-2 (Fig. 6.8). Both methods indicate smaller damping ratios (4%–6% on average) for the intact structure (levels TAR 1 through TAR 4) and large

damping ratios (11%–13% on average) where significant damage occurs in the test structure (levels TAR 6 through DUZ 7-2).

6.3.4 Variation of Structural Properties within Each Test Run

The structural properties of the test structure as discussed in previous sections are presented as mean values over the duration of each of the shake-table runs. It is important to understand that these properties vary during each of these durations of shaking. For a RC structure, the opening and closing of cracks, yielding of the reinforcing bars, and slippage between a reinforcing bar and the surrounding concrete constitute sources of this continuous variation of the structural properties. The addition of the URM infill wall brings further complexity because of the formation of cracks, mainly along the mortar joints, and opening and sliding along the interface between the URM infill wall and the bounding RC frame.

In an attempt to capture the change in the natural period, and stiffness and damping of the test structure during each of the shake-table runs, a small window of time (in this case 1.0 sec) is considered and incrementally moved along the time axis with an increment of 0.005 sec over the whole duration of the shaking. A frequency-domain analysis to determine the natural frequency and a time-domain regression analysis to determine the stiffness and the damping ratio, as described earlier in this chapter, are performed for each time window defined in this manner. The resulting period, damping ratio, and stiffness are then assigned to the mean time of the defined time window and is smoothed over 40 steps (0.2 sec). The time variations of the structural properties for different test levels are shown in Figure 6.12.

It can be observed that the natural period of the test structure remains almost constant during levels TAR 2 to TAR 6. During levels DUZ 7 and DUZ 8, the natural period elongates during the strong motion of the shaking with gradual variations. The variation of the damping ratio ζ of the test structure is related to two different sources. One is the change in the natural period of the test structure, as discussed earlier, and the other is the change in the damping coefficient c of the test structure. It is observed that the damping ratio remains almost constant during levels TAR 2 to TAR 4 at about 7% where there is small damage in the test structure. During levels TAR 6, DUZ 7, and DUZ 8, the damping ratio significantly increases during the strong motion portion of the shaking. This is both due to the elongation of the natural period due

to the reduction of the effective stiffness of the test structure and to the increase in the damping coefficient due to the accumulation of damage in the test structure.

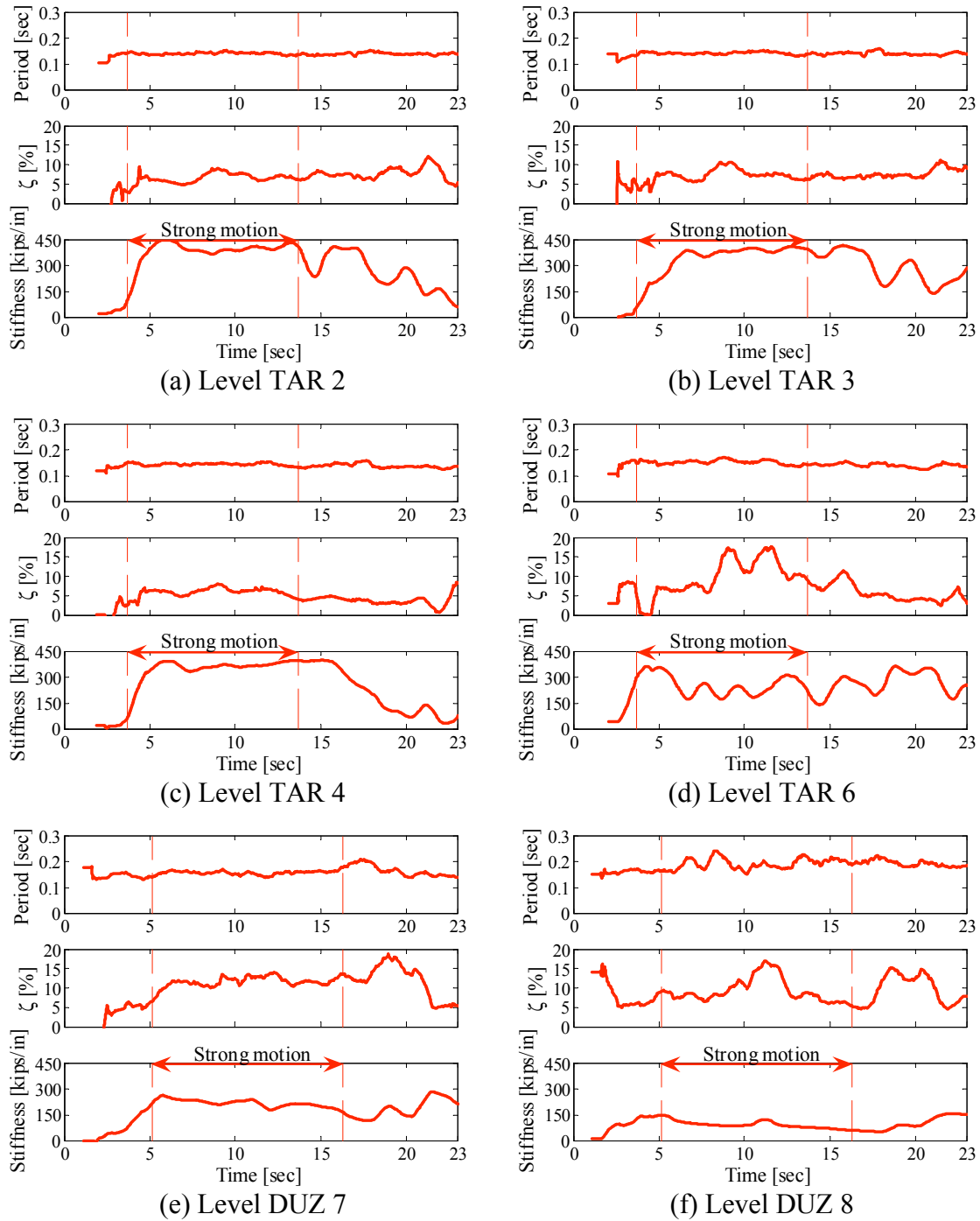


Fig. 6.12 Variation of structural properties of test structure(1 kip/in. = 0.175 kN/mm).

The stiffness of the test structure in the plots of Figure 6.12 is obtained from the regression analysis and is interpreted as the secant stiffness of the test structure. The stiffness values obtained by this method are not reliable when the amplitude of the motion is very small, due to limited resolution of the measurement devices. For the strong motion part of the shaking in levels TAR 2 to TAR 4, the secant stiffness is almost constant. This agrees with the earlier observation that the test structure remains almost elastic during these levels. During levels TAR 6, DUZ 7, and DUZ 8, the secant stiffness decreases gradually as the test structure accumulates damage during the strong motion parts of the shaking. The instantaneous variations in the secant stiffness observed during higher levels, especially TAR 6, are attributed to the bilinear behavior of the total base shear versus lateral displacement relationships, which take place at the strong motion part of the shaking.

6.3.5 URM Infill Wall

The main failure mode of the URM infill wall forms in level DUZ 7 and is characterized as large cracks at about 60° with the horizontal axis starting from the top corners of the wall and connecting with a long horizontal crack at the lower third of the wall to a series of approximately 45° cracks propagating into the opposite bottom corners along each of the wall diagonals. At the same time, early signs of corner crushing are observed at the top corners. The markings in Figure 6.13(a) show the observed crack pattern in the URM infill wall after DUZ 7. The sharp angle of cracking in the top part of the wall can be attributed to the weaker bond between the top mortar bed joint and the RC beam relative to the bond between the side mortar vertical joints and the RC columns. In level DUZ 8, partial collapse of the top corners and sides of the URM infill wall follows the formation of the crack pattern. The markings on Figure 6.13(b) and the photograph in Figure 6.13(c) show the final crack patterns on the URM infill wall at the end of level DUZ 8. Finally, in level DUZ 7-2 the loose portions of the URM infill wall collapse, leading to the observed damage state in Figure 6.13(d).

The shear force carried by the URM infill wall and the shear force carried by each column are calculated as described earlier in this chapter. The shear force carried by the RC frame structure is the sum of all the shear forces in its six columns. Figure 6.14 shows the portions of the total base shear resisted by the URM infill wall compared to those resisted by the three RC frames at the peaks of both the total base shear and the lateral floor displacement for all

testing levels. These histograms confirm that the behavior of the test structure is governed by the undamaged URM infill wall before level TAR 6. As the URM infill wall experiences damage, the RC frames resist larger portions of the applied load. At level DUZ 7-2, the infill wall is completely disintegrated and can be considered structurally insignificant, as the applied lateral load is carried almost entirely by the three RC frames.

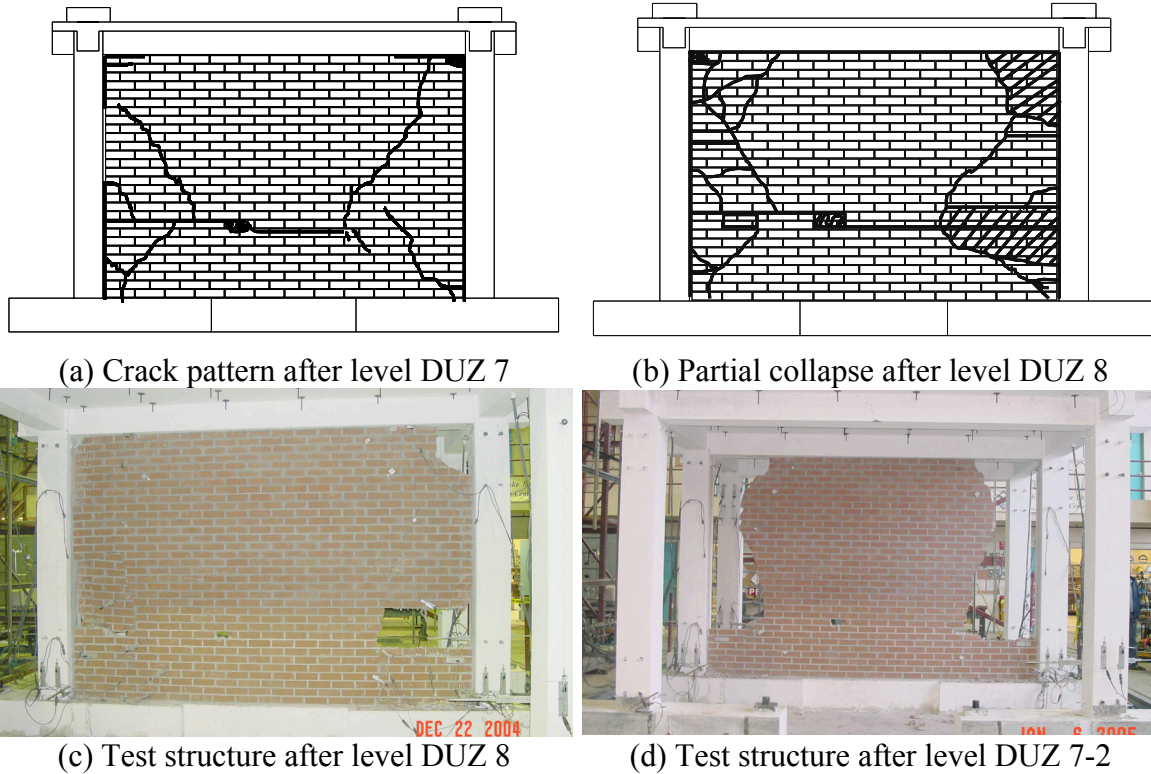
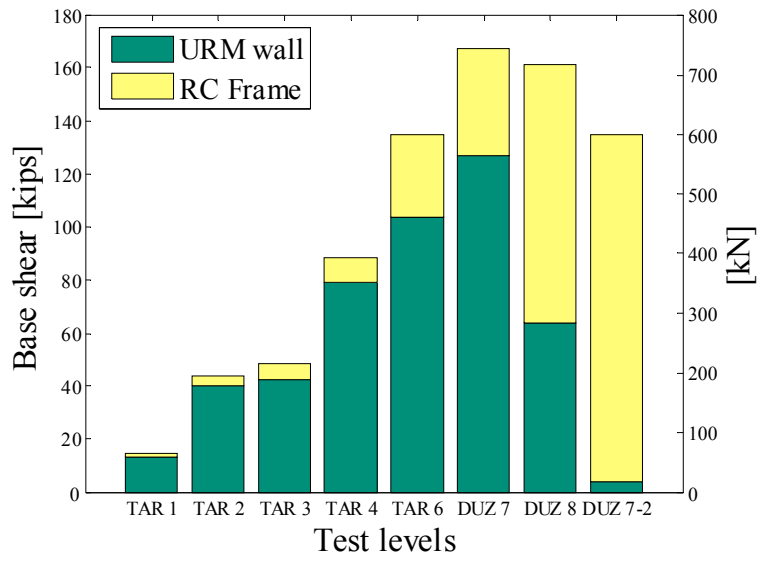
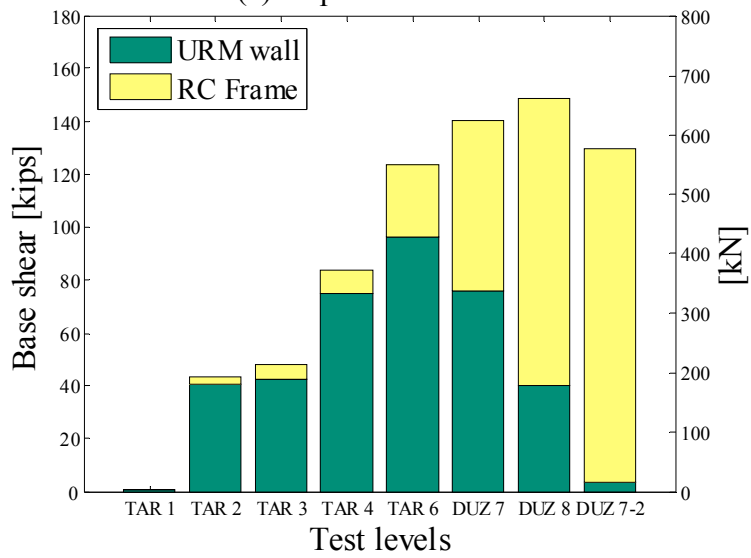


Fig. 6.13 Observed damage of URM infill wall.

The distinction between the force distributions for the peak base shear and the peak floor displacement in Figures 6.14(a) and (b), respectively, is made to emphasize the different states of the test structure at these different peak points, particularly for levels DUZ 7 and DUZ 8. During these two levels of shaking, the point of peak base shear takes place when the URM infill wall is still resisting a large portion of the applied lateral load at its incipient failure. On the other hand, the peak floor displacement takes place after the damage in the URM infill wall has occurred. As an example, the time histories of the shear force in the URM infill wall and the shear force carried by the RC frames are presented in Figures 6.15(a) and (b), respectively. In these figures, the corresponding floor displacements are also shown. From these figures, it is observed that the maximum base shear takes place at about 8.8 sec, while the maximum floor displacement occurs at about 17.4 sec following the occurrence of major wall cracking at about 15.4 sec.



(a) At peak base shear



(b) At peak displacement

Fig. 6.14 Effect of progression of damage on force distribution in test structure during stage one of experiments.

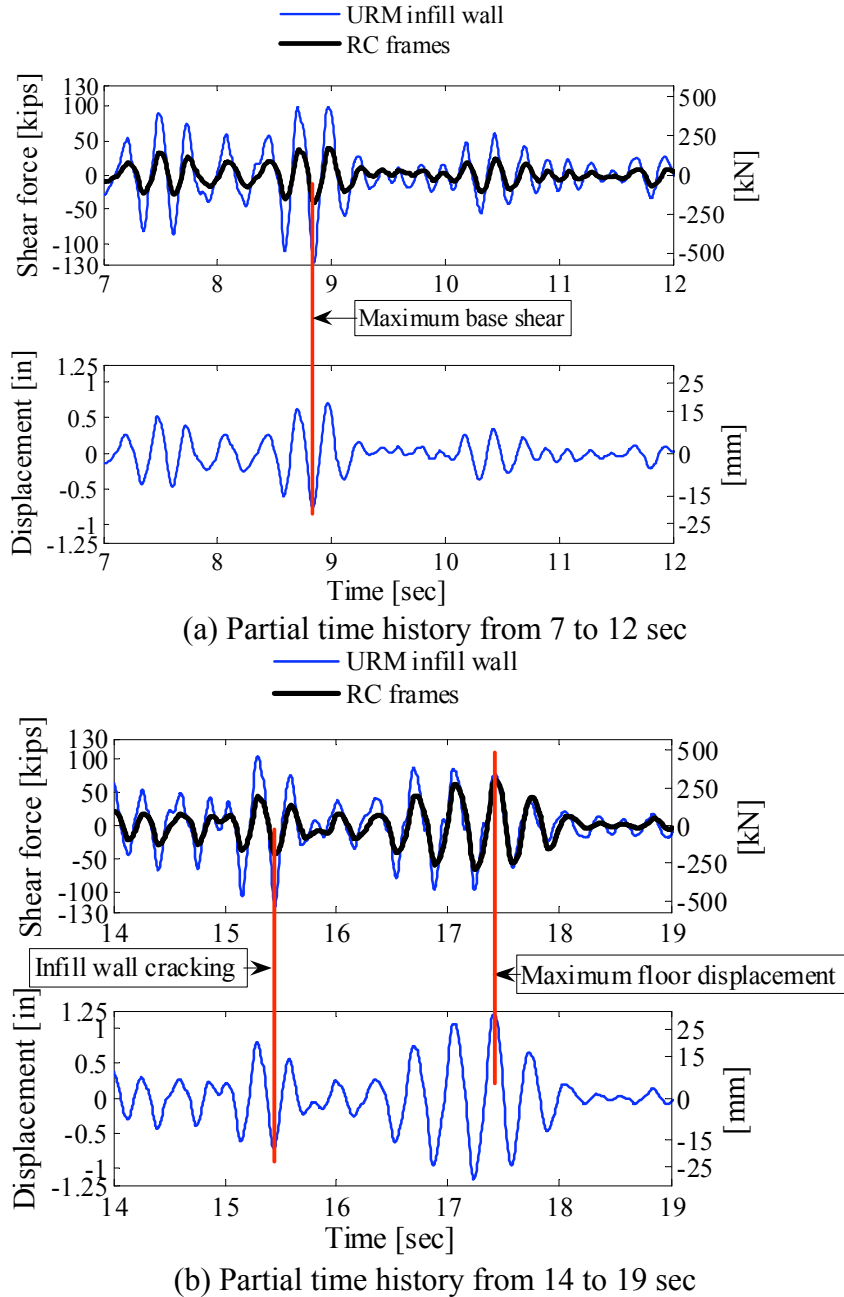


Fig. 6.15 Time histories of shear forces and displacements for level DUZ 7.

An important aspect of the response of the URM infill wall is represented by the shear force versus shear deformation in the plane of the URM infill wall. The shear deformations γ are determined using the diagonal measurements made in the plane of the URM infill wall as demonstrated in Figure 6.16. The shear force in the URM infill wall F_{wall} is estimated as discussed earlier in this chapter (see Fig. 6.1).

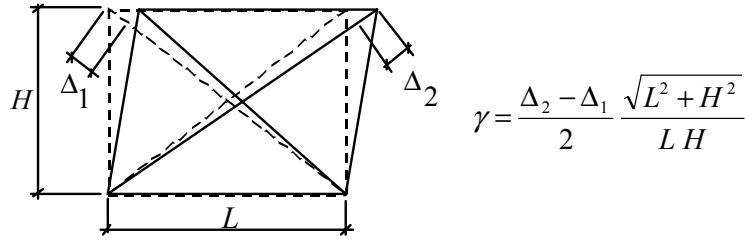
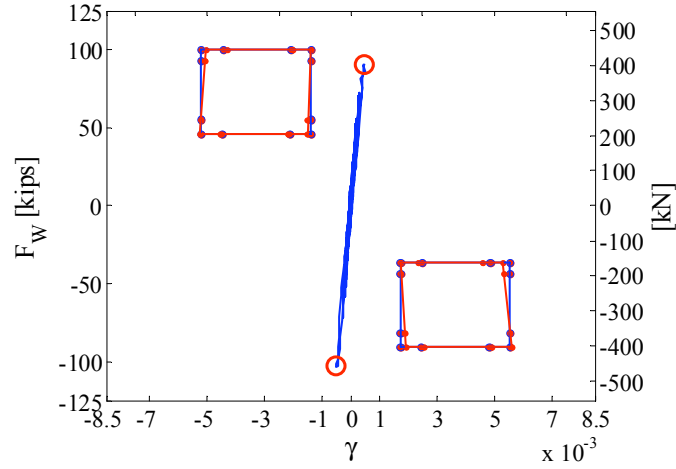
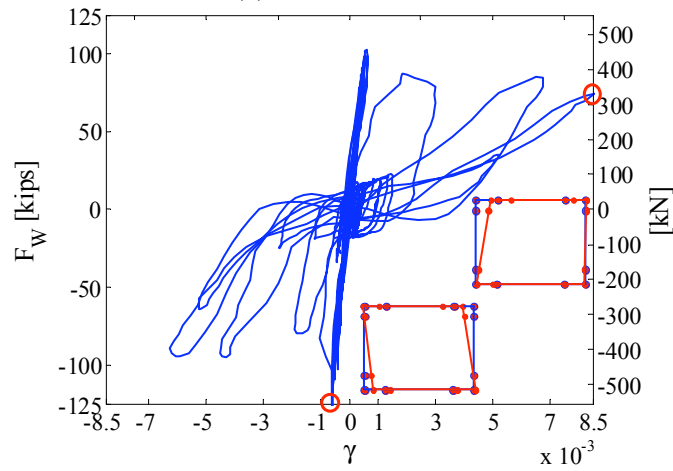


Fig. 6.16 Shear deformation of URM infill wall.



(a) Level TAR 6



(b) Level DUZ 7

Fig. 6.17 Shear force versus shear deformation of URM infill wall.

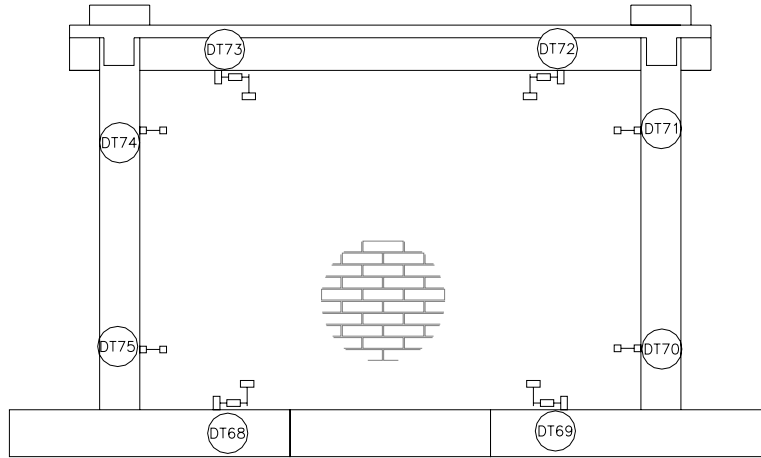
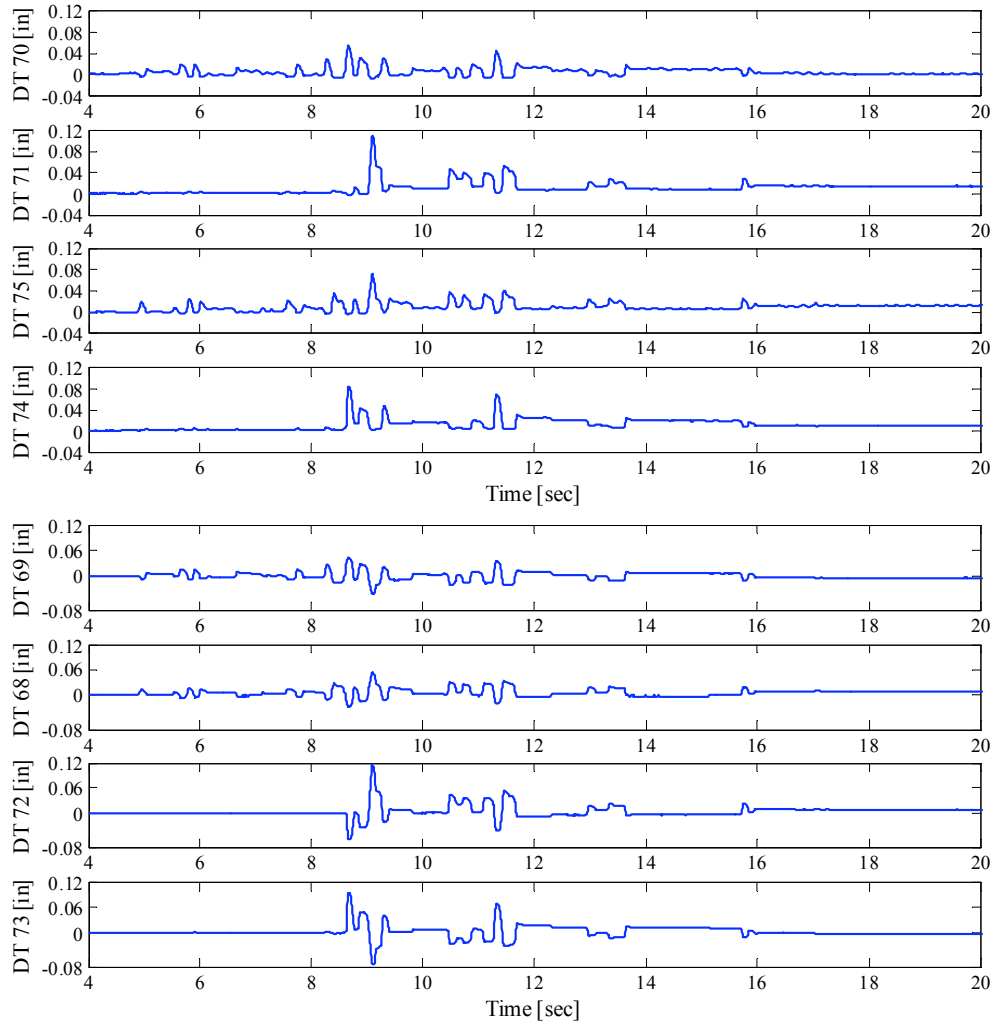


Fig. 6.18 Displacement transducers (DT) along URM infill wall / RC frame interface.

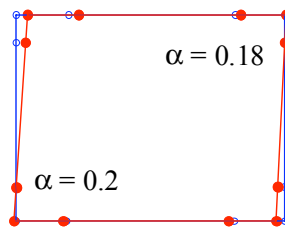
The shear force versus shear deformation relationship for the URM infill wall for levels TAR 6 and DUZ 7 are shown in Figures 6.17(a) and (b), respectively. In these figures, the deformed shapes of the URM infill wall at the indicated peak points (marked with open circles) are also superimposed. These deformed shapes are obtained from the interface deformation measurements (Fig. 6.18). Before cracking, i.e., level TAR 6, a linear shear force versus shear deformation relationship is obtained. After cracking, i.e., level DUZ 7, there is a rapid degradation of the shear stiffness of the URM infill wall due to significant increase of the shear deformation.

The exaggerated distorted shapes of the URM infill wall shown in Figure 6.17 are plotted relative to the adjacent RC frame members. The displacement transducers installed on the boundaries of the URM infill wall (Fig. 6.18) measure the opening and closing of the gaps (DT 70, DT 71, DT 74, and DT 75) and sliding (DT 68, DT 69, DT 72, and DT 73) between the URM infill wall and its bounding RC frame members. The same data can be used to estimate the contact length between the URM infill wall and the RC columns by assuming that the bending deformation of the URM infill wall is small relative to that of the RC frame (each side of the URM infill wall stays as a line). The results of such measurements for levels TAR 6 and DUZ 7 are shown in Figures 6.19 and 6.20, respectively. In these figures, α refers to the ratio of the length of the contact zone between the URM infill wall and the bounding RC frame and the height of the URM infill wall H as defined in Figure 6.3. From the calculation of α during different levels of the shake-table experiments, the following observations are made: (1) The value of α is not significantly different when compared between different levels of the shake-

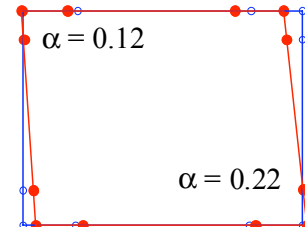
table experiments ($0.18 < \alpha < 0.22$). (2) The contact length α is generally higher at the base of the URM infill wall compared to its top due to less flexibility of the RC frame at its base compared to its beam-column joint and the increase in the lateral force transferred between the RC frame and the URM infill wall due to the added inertial force of the URM infill wall. (3) For design purposes a value of α at roughly 20% of the height of the URM infill wall may be used which also agrees with the formulation by FEMA 356 provisions (2000) and Liaw and Kwan (1985b), which for the RC frame in the test structure result in values of 0.19 and 0.20, respectively, discussed in Chapter 7.



(a) Time-history plots of identified transducers in Fig. 6.18

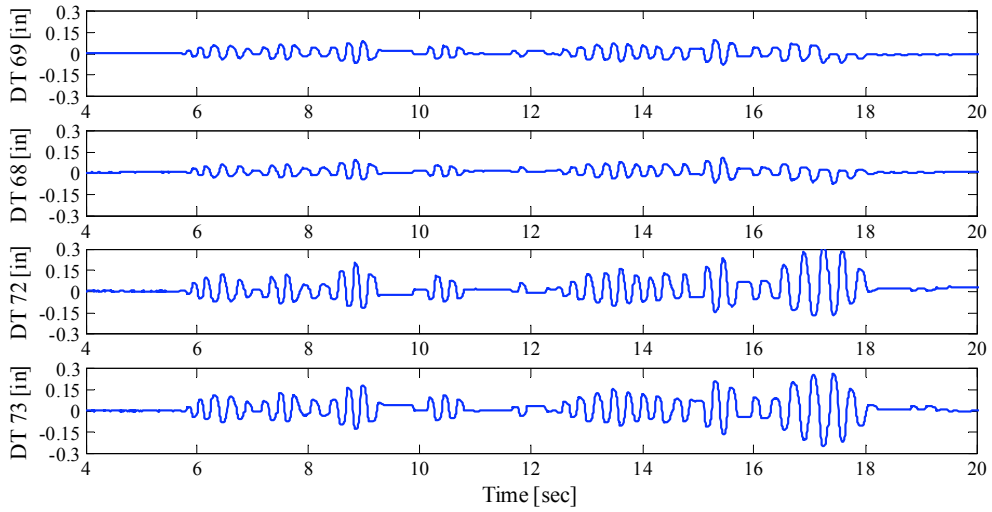
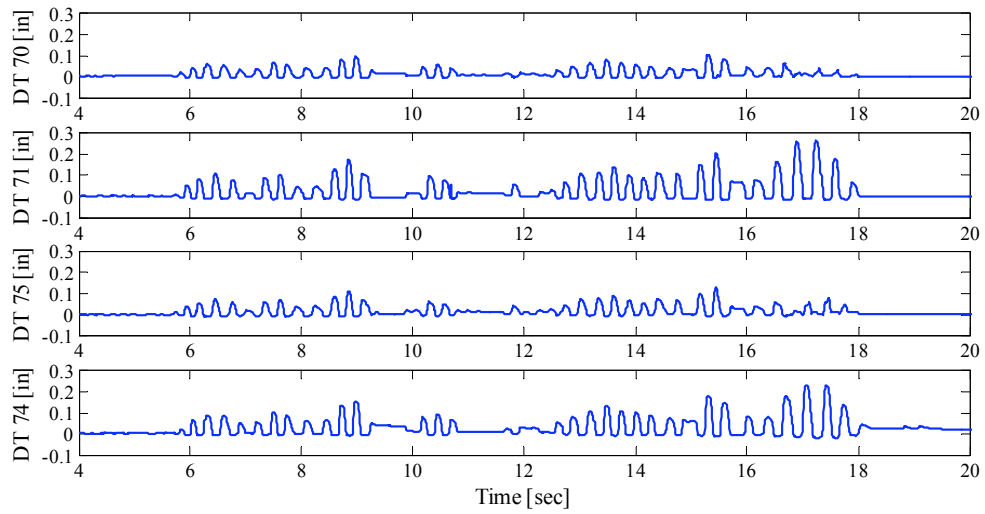


(b) At maximum shear deformation in URM infill wall

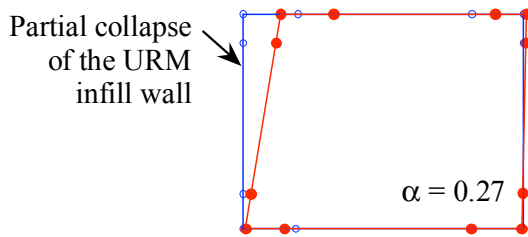


(c) At maximum shear force in URM infill wall

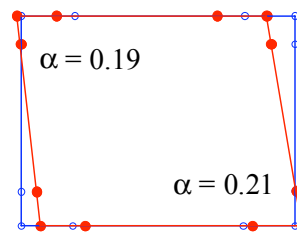
Fig. 6.19 Relative displacement between URM infill wall and bounding RC frame for level TAR 6 (1 in. = 25.4 mm).



(a) Time-history plots of identified transducers in Fig. 6.18



(b) At maximum shear deformation in URM infill wall



(c) At maximum shear force in URM infill wall

Fig. 6.20 Relative displacement between URM infill wall and bounding RC frame for level DUZ 7 (1 in. = 25.4 mm).

6.3.6 RC Slab

The 3³/₄" (95 mm) thick RC slab is supported on boundary beams from all sides and spans between the bare and infilled frames. In its plane, the RC slab acts as a diaphragm distributing the inertial force to the lateral-resisting elements of the test structure by deforming in shear and in-plane bending. The inertial force is generated by the acceleration of the mass at the slab level in the test structure. This mass consists of the tributary mass of the test structure itself and the added mass of the lead ingots. In the out-of-plane direction of the RC slab, it spans between the three RC frames. Since the aspect ratio of the RC slab is 2.25, the out-of-plane behavior of the RC slab is a one-way action. This is confirmed by observing the gravity-induced crack patterns on the RC slab after loading the lead ingots. The cracks run almost parallel to the long edges of the RC slab.

While the vertical force on the RC slab hardly changes during the experiments, the lateral inertial force acting on the RC slab and the resisting reactions from the supporting RC frames change dramatically as the test structure is subjected to different levels of shaking. Assuming a uniform distribution of the inertial force along the RC slab width (refer to the insert in Fig. 6.21(a)), i.e., normal to the shaking direction, the maximum shear in the RC slab can be estimated as stated in Equation 6.8, where V_b denotes the total inertial force at each instant of time, and V_A and V_C are the total shear forces resisted by the two bare frames on axes A and C, respectively, of Figure 2.2.

$$V_{s,\max} = \max \left\{ V_A, \frac{V_b}{2} - V_A, V_C, \frac{V_b}{2} - V_C \right\} \quad (6.8)$$

In order to investigate the change in the demand shear force in the RC slab, the following two extreme cases are considered.

1. Assuming that the infilled frame B is infinitely stiff compared to the two bare frames A and C, then frame B attracts all the inertial forces in the RC slab. It is implicit in this assumption that the RC slab is rigid in its plane relative to the frames. In this case, $V_B = V_b$ and $V_A = V_C = 0$, and the maximum shear in the RC slab is calculated as one half the total base shear.
2. Assuming that the URM infill wall is completely disintegrated and that the three frames A, B, and C have the same lateral stiffness, then the total base shear V_b is evenly distributed between the three frames, and the shear force in each frame is one third of the

total base shear. Accordingly, the maximum shear in the RC slab is calculated as one third of the total base shear.

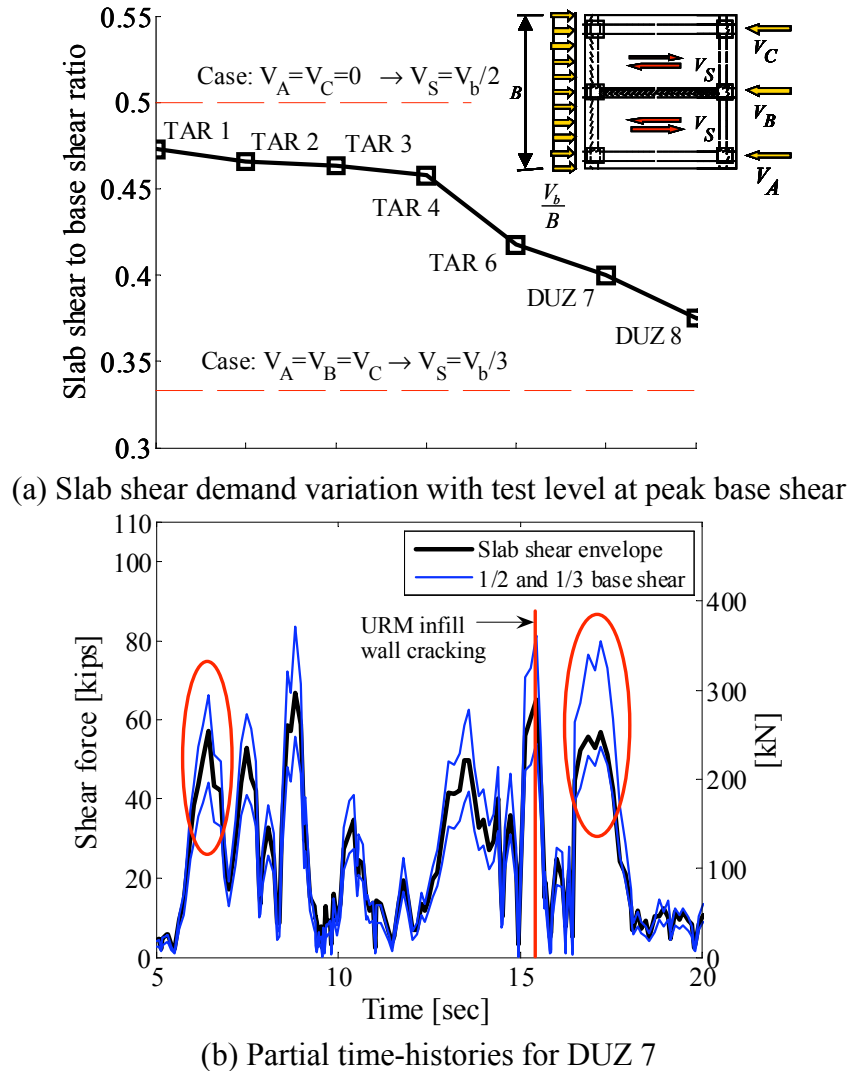


Fig. 6.21 Variation of shear demand in RC slab due to damage in URM infill wall.

Examining the above two extreme cases suggests that the existence of the URM infill wall increases the shear demands on the diaphragm. Figure 6.21(a) shows the ratio of the maximum slab shear to the total base shear corresponding to the maximum base shear in the test structure for different levels of shaking. As expected, the slab shear to base shear ratio reduces as the URM infill wall is damaged in higher levels of shaking. The time-history results from the experiments confirm this as well. Figure 6.21(b) shows the time-history plot of the maximum shear in the RC slab (absolute value) as well as the two limits of one half and one third of the base shear for level DUZ 7. As discussed previously, severe damage in the URM infill wall occurred during this level at time $t = 15.4$ sec. Comparing the slab shear forces for intervals of

time at the beginning of the motion (at about $t = 7.0$ sec and identified by a dashed ellipse in Fig. 6.21(b)) and toward the end of the motion (at about $t = 17.0$ sec and identified by a dashed ellipse in Fig. 6.21(b)) shows that the shear demand in the RC slab changes from close to the upper limit of one half the total base shear before the URM infill wall damage is close to the lower limit of one third the total base shear after the URM infill wall damage.

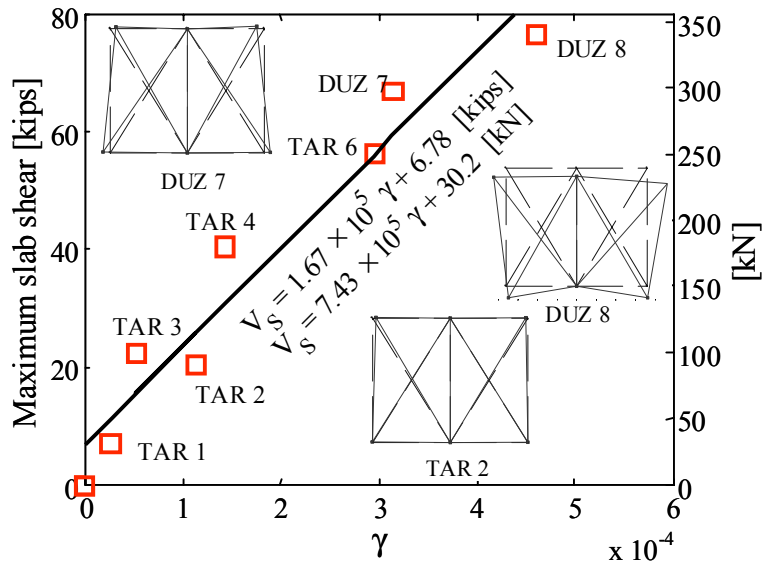
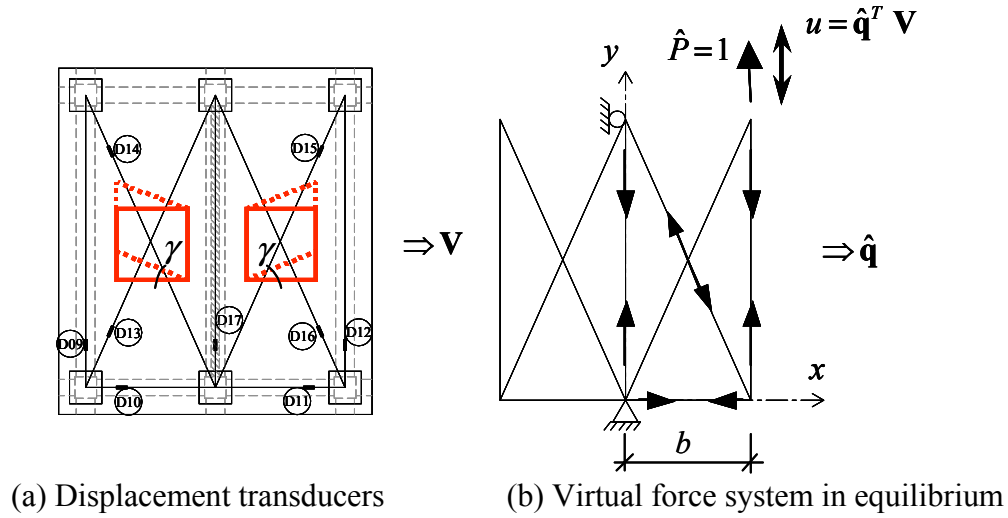
In order to measure the RC slab deformations, a set of displacement transducers are installed as shown in Figure 6.22(a). The transducers are arranged to form a virtual truss, which is statically determinate, such that the compatibility matrix \mathbf{A}_c can be inverted and the displacement of all nodes \mathbf{u} can be derived from the measured deformations of the truss elements \mathbf{V} as shown in Equation 6.9.

$$\mathbf{u} = \mathbf{A}_c^{-1} \mathbf{V} \quad (6.9)$$

In order to determine the displacement of each node, the local coordinate system xy as shown in Figure 6.22(b) is defined. Invoking the principle of virtual force (PVF) and applying a virtual force \hat{P} in the direction of the required displacement u and solving the statically determinate truss, the corresponding virtual internal forces satisfying equilibrium can be determined. Arranging the measured deformations and their corresponding virtual internal forces into vectors \mathbf{V} and $\hat{\mathbf{q}}$, respectively, the displacement u can be determined from Equation 6.10 with $\hat{P} = 1.0$. It should be noted that the new vector $\hat{\mathbf{q}}^T$ may also be interpreted as the row corresponding to the displacement u in \mathbf{A}_c^{-1} matrix.

$$\hat{P} u = \hat{\mathbf{q}}^T \mathbf{V} \quad (6.10)$$

All components of the nodal displacement vector \mathbf{u} may be individually determined from Equation 6.10. Alternatively, the \mathbf{A}_c^{-1} matrix may be assembled and the displacement vector \mathbf{u} directly evaluated from Equation 6.9. The shear deformation γ of the RC slab as shown in Figure 6.22(a) is calculated as the relative displacement along the edge and middle of the RC slab divided by the distance b as defined in Figure 6.22(b). It should be noted that using the PVF yields more accurate results compared to the approximate method used to estimate the shear deformations in the URM infill wall (see Fig. 6.16). While the approximate method is applicable to the URM infill wall, it is not suitable for the RC slab, since the shear deformation of the RC slab is an order of magnitude smaller than that of the URM infill wall; compare the values of γ in Figure 6.22(c) to those in Figure 6.17.



(c) RC slab shear stiffness

Fig. 6.22 Shear deformation of RC slab.

Figure 6.22(c) shows a plot of the maximum slab shear versus its corresponding shear deformation. Although it is observed during the experiments that the initial gravity-induced cracks become more visible with increase in the intensity of shaking, Figure 6.22(c) suggests that there is no significant drop in the shear stiffness of the RC slab. The slope of the fitted line through the data points (1.67×10^5 kips (7.43×10^5 kN)) is about one eighth of the elastic shear stiffness of the uncracked cross section of the RC slab ($GA = 1.3 \times 10^6$ kips (5.8×10^6 kN)), indicating that although the shear stiffness of the RC slab remains almost unchanged, its value is significantly reduced due to initial cracks caused by the gravity loads and possible shrinkage of concrete. Note that the deformed shapes plotted on the graph of Figure 6.22(c) are obtained using

the PVF as previously described and are greatly exaggerated (to the same scale of 250:1 for all plots). These deformations include the effects of both shear forces and bending moments in the plane of the RC slab.

6.3.7 RC Frames

In this section, the state of the RC frames and the damage sequence in the test structure during stage one of the experiments are discussed. The procedure to quantify section demands in the RC columns using the results of the strain gages installed on the reinforcing bars are also addressed, and sample results are presented. The summary of the section results obtained during stage one is presented in comparison with stages two and three results in Section 6.6.5.

6.3.7.1 Description of Damage

As mentioned earlier, up to level TAR 6 and the initial part (first 15 sec) of DUZ 7, the stiff URM infill wall carries most of the base shear, protecting the three RC frames. At incipient failure of the URM infill wall and after the major cracking occurs at time $t = 15.4$ sec of DUZ 7, there are large shear demands at the bases of the columns where there are contacts with the URM infill wall as well as large bending moment demands on the RC frames as the test structure undergoes larger displacements. Figure 6.23(a) shows the locations in the test structure where reinforcing bar yielding is recorded by the strain gages during level DUZ 7 after partial failure of the URM infill wall. It can be observed that all the yielding occurred in the middle infilled frame and that the bare frames are practically undamaged. The recorded maximum strain in the transverse reinforcing bars is about 0.003 (indicating yielding of the transverse reinforcement) at the base of column B2, confirming high column shear demand at this location. Figure 6.23(b) shows a photograph of the column-footing joint at the base of column B1 in the infilled frame taken after level DUZ 7. Cracking and initiation of spalling of concrete at the base of the infilled frame is observed, as seen in this figure, confirming the higher state of damage in the infilled frame during the experiments.

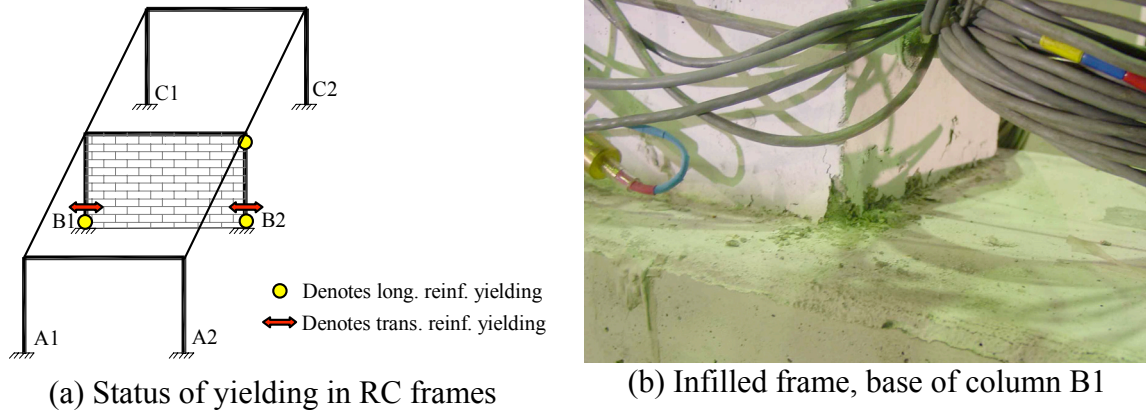


Fig. 6.23 Damage in RC frames after level DUZ 7.

As discussed before, during level DUZ 8 and the repeat of level DUZ 7, i.e., DUZ 7-2, the effect of the URM infill wall on the behavior of the test structure diminishes and the RC frames resist significant portions of the earthquake-induced forces. The high-force demands on the RC frames during these levels cause some damage in the form of local spalling and cracking in the beam-column and column-footing joints. The state of the test structure at the end of stage one of the shake-table experiments, i.e., after completing level DUZ 7-2, is shown in Figure 6.24. The photographs of the bases of columns C1 and B2 (Figs. 6.24(a) and (c)) show the typical state of damage at the bases of the bare and the infill RC frames, respectively, including concrete spalling and horizontal cracks at the column-footing joints. Figures 6.24(b) and (d) show the typical state of minor cracks at the beam-column joints in the bare and infilled RC frames, respectively.

Figure 6.24(e) identifies the locations in the test structure where reinforcing bar yielding is recorded by the strain gages during level DUZ 8 after partial collapse of the URM infill wall. It can be observed that yielding of longitudinal bars is recorded at all joints in the test structure. On the other hand, only the transverse reinforcing bars in the infilled RC frame at the column bases show signs of yielding due to the existence of the URM infill wall. The maximum yield strain recorded in the transverse reinforcing bars during level DUZ 8 is about 0.0022 at the base of column B2, which is 27% less than the strain recorded during level DUZ 7 due to the reduction in the interaction between the significantly damaged (partially collapsed) URM infill wall and the RC frame.

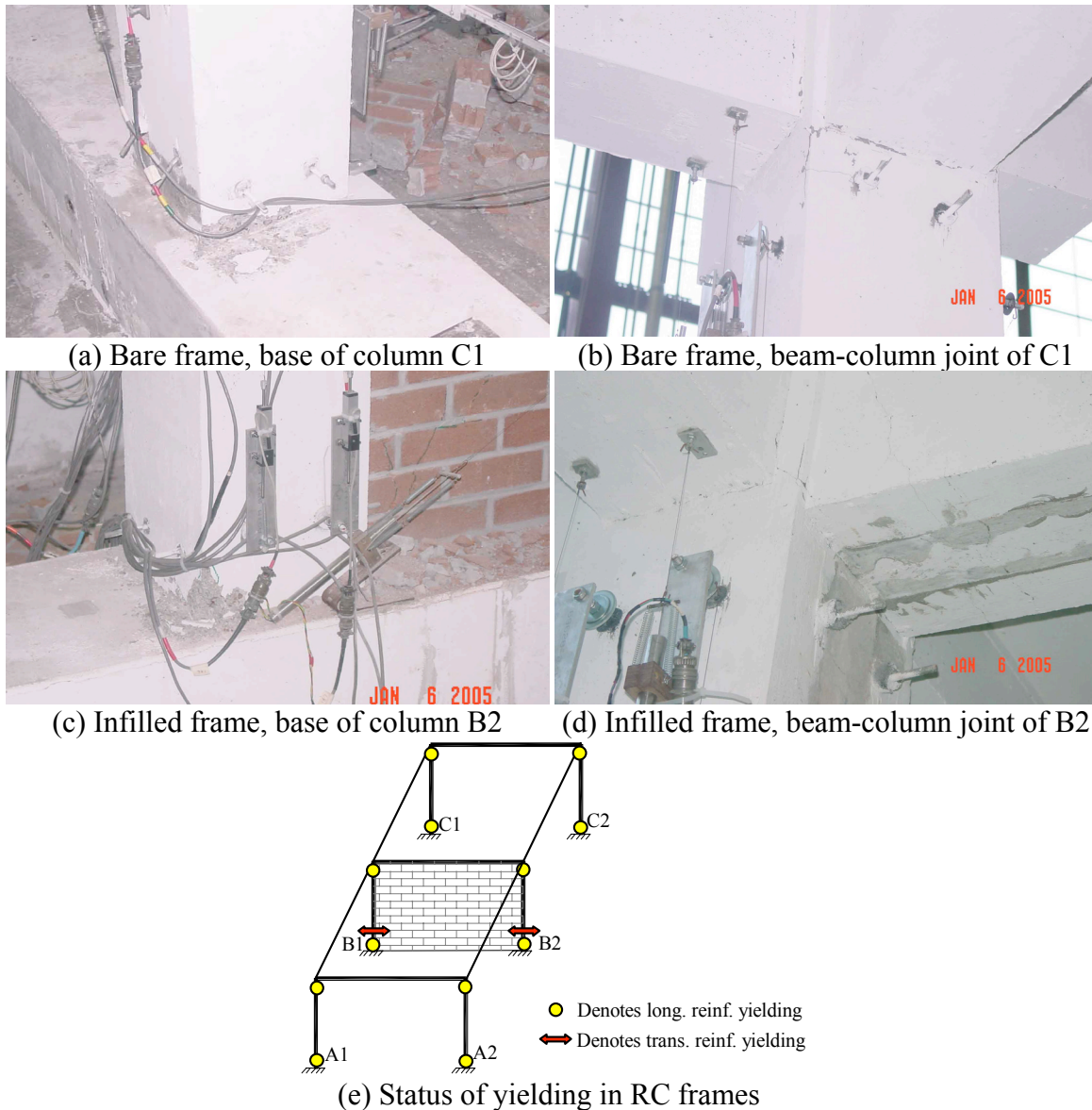


Fig. 6.24 Status in RC frames at end of stage one of experiments.

6.3.7.2 Section Response

In order to quantify the cross-section demands in the RC columns, standard section analysis is performed using the strain gage recordings from the longitudinal reinforcing bars available at different locations at the top and bottom of the columns. The step-by-step procedure to obtain section forces, namely bending moments and axial forces, is described in Figure 6.25 based on the following assumptions: (1) plane sections remain plane, i.e., a linear variation of strains across the column cross section is assumed, (2) concrete stress-strain relationship is assumed to conform to the Mander et al. (1988a,b) confined concrete model with uniaxial concrete

compression strength $f'_c = 5400$ psi (37.2 MPa) and neglected concrete tensile strength, (3) the reinforcing steel stress-strain relationship is assumed as elastic-perfectly plastic with steel yield stress $f_y = 66.5$ ksi (458 MPa) and elastic modulus $E_s = 29000$ ksi (200 GPa), (4) a perfect bond is assumed between the reinforcing steel and the surrounding concrete before cracking, and (5) the elastic stress-strain relationship for the unbonded post-tensioning rods is assumed with elastic modulus $E_{ps} = 27000$ ksi (186 GPa). The input parameters for the section analysis are the strains in the outside longitudinal reinforcing bars, namely ϵ_1 and ϵ_2 , and the strain measured in the unbonded post-tensioning rod ϵ_{ps} . These measured strains determine the strain distribution across the cross section of the column, e.g., ϵ_3 , ϵ_c and the depth of the compression zone c in the cross section. Once the strain in different components of the cross section are determined, their corresponding stresses and forces can be calculated using the assumptions above; finally by section equilibrium the section forces, namely bending moment M and axial force P are determined. The bending moment at other sections in the columns, e.g., at the column-footing joint, may be estimated by assuming a linear bending moment diagram for the columns. Examples of the strains measured at the base and top of the columns are shown in Appendix C. Figure 6.27(a) shows an example of the partial time history of the bending moment calculated at the base of column B1 during level DUZ 7.

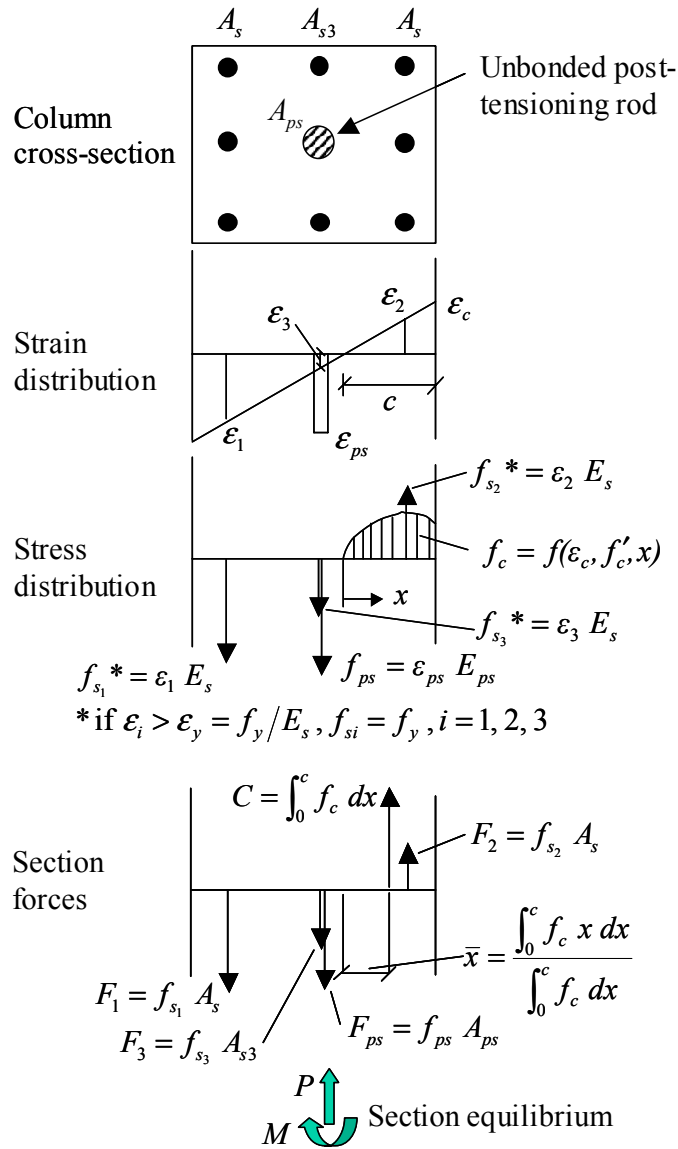


Fig. 6.25 Section analysis procedure in RC columns.

Another important cross-section parameter is the section rotation θ at the base and top of the columns. The cross-section rotation is estimated using the data from the displacement transducers located at the top and bottom of each column as shown in Figure 6.26. In this figure, u_1 and u_2 are the vertical displacements measured by the two displacement transducers at the same elevation defined by the distance d_1 , and d_2 is the horizontal distance between them. An example of the partial time history of the cross-section rotations at the base of column B1 during level DUZ 7 is shown in Figure 6.27(b).

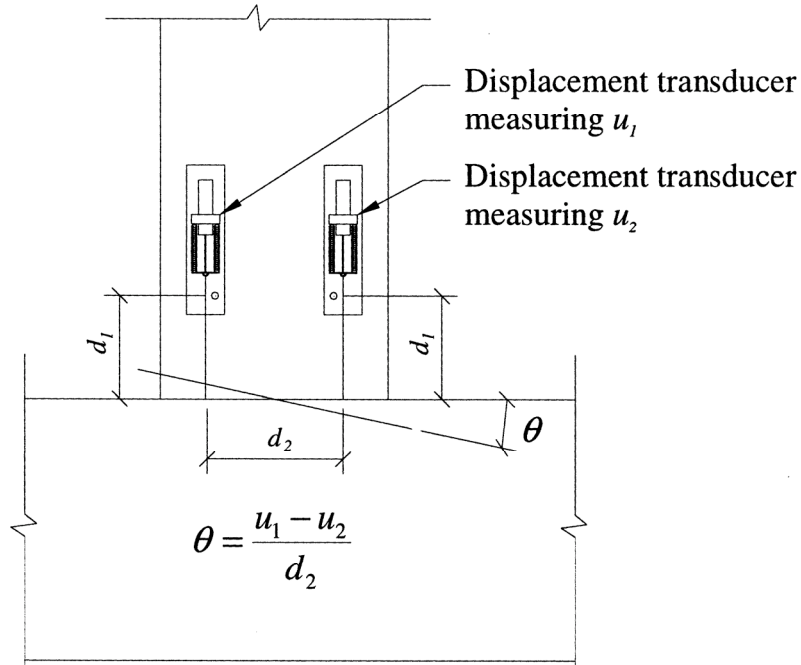


Fig. 6.26 Section rotation determination procedure in RC columns.

The maximum values of the bending moments and their corresponding rotations at the base and top of the RC columns during different levels of stage one of the experiments are reported and discussed for columns A2 and B1 in comparison with stages two and three results in Section 6.6.5. These values are obtained directly from the time histories and are indicated with open circles for column B1 during level DUZ 7 in Figures 6.27(a)–(b).

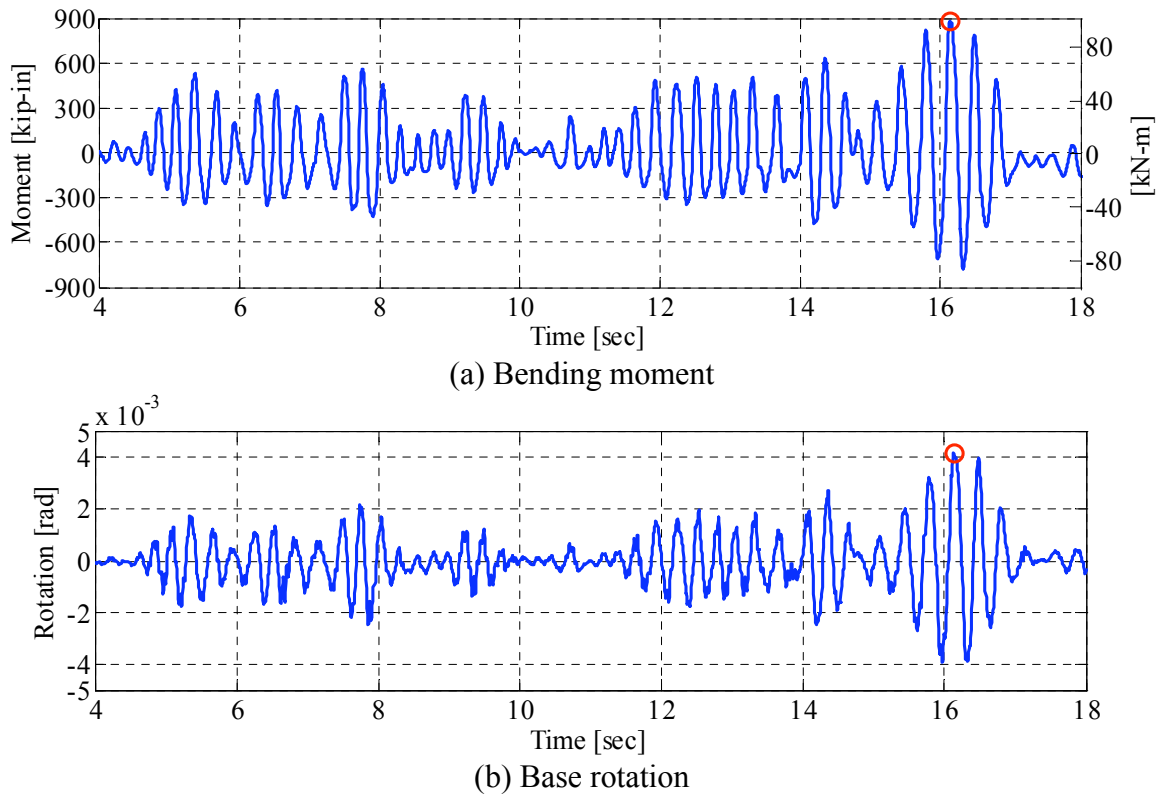


Fig. 6.27 Section response time-histories at base of column B1, level DUZ 7.

6.4 DISCUSSION OF STAGE TWO RESULTS

In this section the behavior of the test structure in terms of the observed damage and the change of the effective RC slab width during stage two of the experiments is described. The effects of the column post-tensioning rods on the test structure are also evaluated and quantified. Further discussion of the results obtained during stage two are presented in later sections in comparison with results from stages one and three of the experiments.

6.4.1 Damage in Test Structure

With the progress of the shake-table experiments in stage two, more spalling at the bases of the columns and the beam-column joints is observed. After the repeat of the stage one test protocol (with level DUZ 9 instead of DUZ 7-2), diagonal cracks are observed at the column-footing joints as shown in Figure 6.28(a). Some evidence of spalling and flexural cracking are also observed in the beam-column joints (Fig. 6.28(b)). At this point a Loma Prieta ground motion is

chosen to subject the test structure to higher demands according to the design spectra at the new (elongated) natural period of the test structure, as described in Chapter 5. Significant yielding of the gaged reinforcing bars is recorded for shaking beyond Loma Prieta level 7 (LomaPr 7). The most severe damage occurs with the propagation of diagonal cracks and cover spalling in the footings as shown in Figure 6.28(c). This observed damage softens the column-footing connection and in effect produces plastic hinges with large plastic rotations at the column bases. Significant damage at the beam-column joints in the form of diagonal cracking, longitudinal bar yielding, and concrete spalling is observed during level LomaPr 9 and its repeats as shown in Figure 6.28(d).

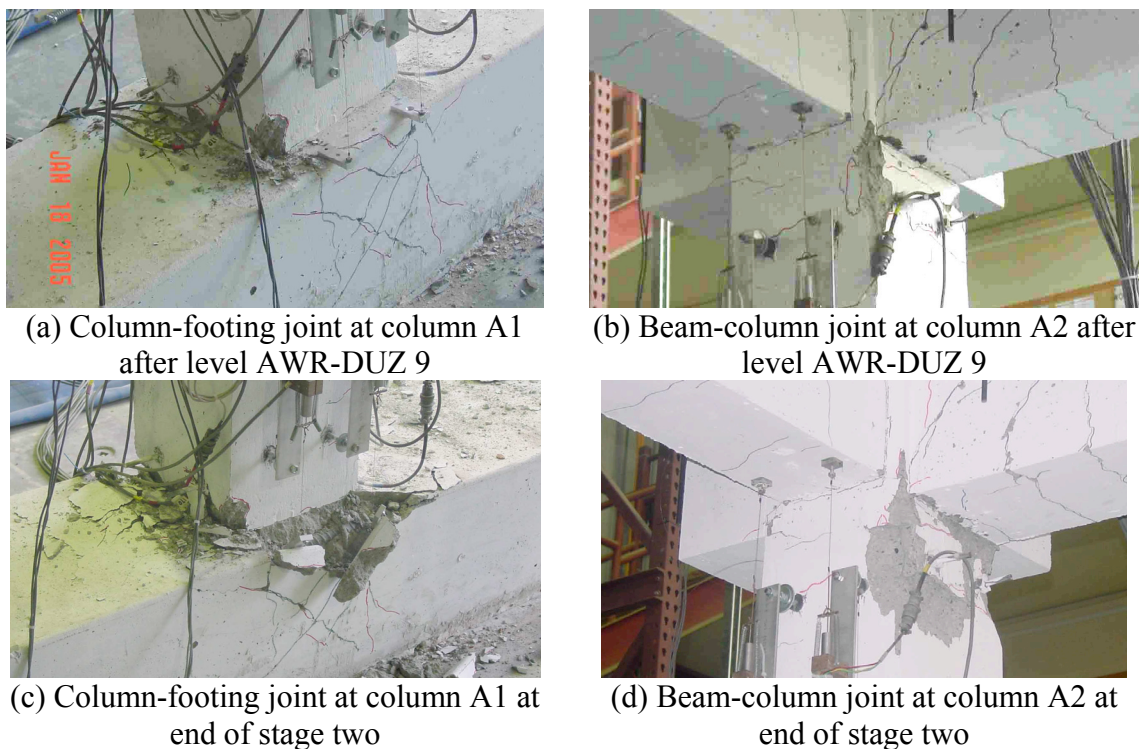


Fig. 6.28 Damage in RC frame joints during and after stage two of experiments.

6.4.2 Effective Slab Width

The effects of the URM infill wall on the effective width of the RC slab is investigated by considering the distribution of strain in the RC slab perpendicular to the floor longitudinal beams in stages one and two of the shake-table experiments. This distribution is shown in Figures 6.30(a)–(d) between axes A and B at 29 in. (740 mm) from the north edge of the RC slab (see middle insert of Fig. 6.30), where strain gage data are available at levels TAR 2, AWR-TAR 2, TAR 4, and AWR-TAR 4, respectively. The horizontal axis in this figure refers to the horizontal

distance of the strain gages from axis A. As an example, the partial time history of the strain gage recording for strain gage number 222 during level TAR 4 is shown in Figure 6.29. The strain distributions presented in Figure 6.30 are snapshots at the time corresponding to the maximum strain reading recorded during each run by strain gage number 222 located on axis A (see Appendix A for exact locations of strain gages). The values of the maximum strains recorded between the two axes used to normalize the strain distributions in these levels are also reported in Figure 6.30. Comparing the plots for levels TAR 2 and TAR 4 (with URM infill wall intact) and levels AWR-TAR 2 and AWR-TAR 4 (after removal of the URM infill wall), it is observed that: (1) the distribution of the strain in the section does not change with increase in the intensity of the ground motion, (2) the strain values are much higher (about 20 to 40 times) at levels after removal of the URM infill wall, (3) the strains are somewhat more evenly (less change of the strain values) distributed across the RC slab after removal of the URM infill wall as the maximum difference in strain values is about 90% with the URM infill wall and about 70% after its removal, and (4) the maximum strain shifts from axis A to axis B after the removal of the URM infill wall. This is because the URM infill wall prevents the middle frame beam (Axis B) from deforming vertically in flexure during stage one of the experiments. However, during stage two of the experiments, the middle frame is already more damaged than the exterior ones, as previously discussed, and therefore this middle frame deforms more than the exterior frames, e.g., the one on axis A, resulting in higher strain readings on axis B.

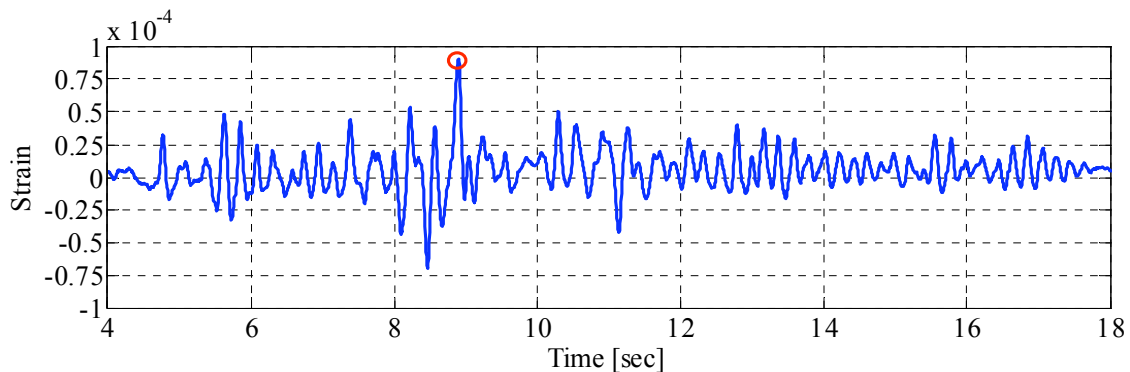


Fig. 6.29 Partial time history of strain gage number 222 during level TAR 4.

The observations based on the strain measurements discussed above lead to the following conclusions: (1) because the strain distribution does not change, the beam-slab section is behaving linearly at these low test levels as expected; (2) because of the large increase of the strain readings after removal of the URM infill wall, the RC frames do not participate fully in

resisting the lateral load when the URM infill wall is still intact, since this wall carries a significant portion of the lateral load as was demonstrated when discussing the force distribution in stage one of the experiments (Fig. 6.14), and (3) because of the more even strain distribution after the URM infill wall removal compared to that with the intact URM infill wall, the presence of stiff structural elements, i.e., the URM infill wall, reduces the effective RC slab width significantly. The third conclusion has implications in the design, since current design codes do not consider the effects of such stiff elements in determining the effective width of the RC slab under lateral loads. For the present test structure, the effective RC slab width based on ACI318-05 Section 8.10.2 is 20.25 in. (514 mm) from the center of the beam to each side for both cases before and after removal of the URM infill wall. While this code-based estimation of the effective RC slab width may be appropriate after removal of the URM infill wall, the significantly smaller strain measurements in levels TAR 2 and TAR 4 compared to those of levels AWR-TAR 2 and AWR_TAR 4 suggest that a smaller effective RC slab width may be used, perhaps in the order of the width of the beam measured from the center of the beam to each side, i.e., about 10 in. (250 mm) for the test structure, in the presence of very stiff lateral load-resisting elements as the RC-infilled frame with URM wall.

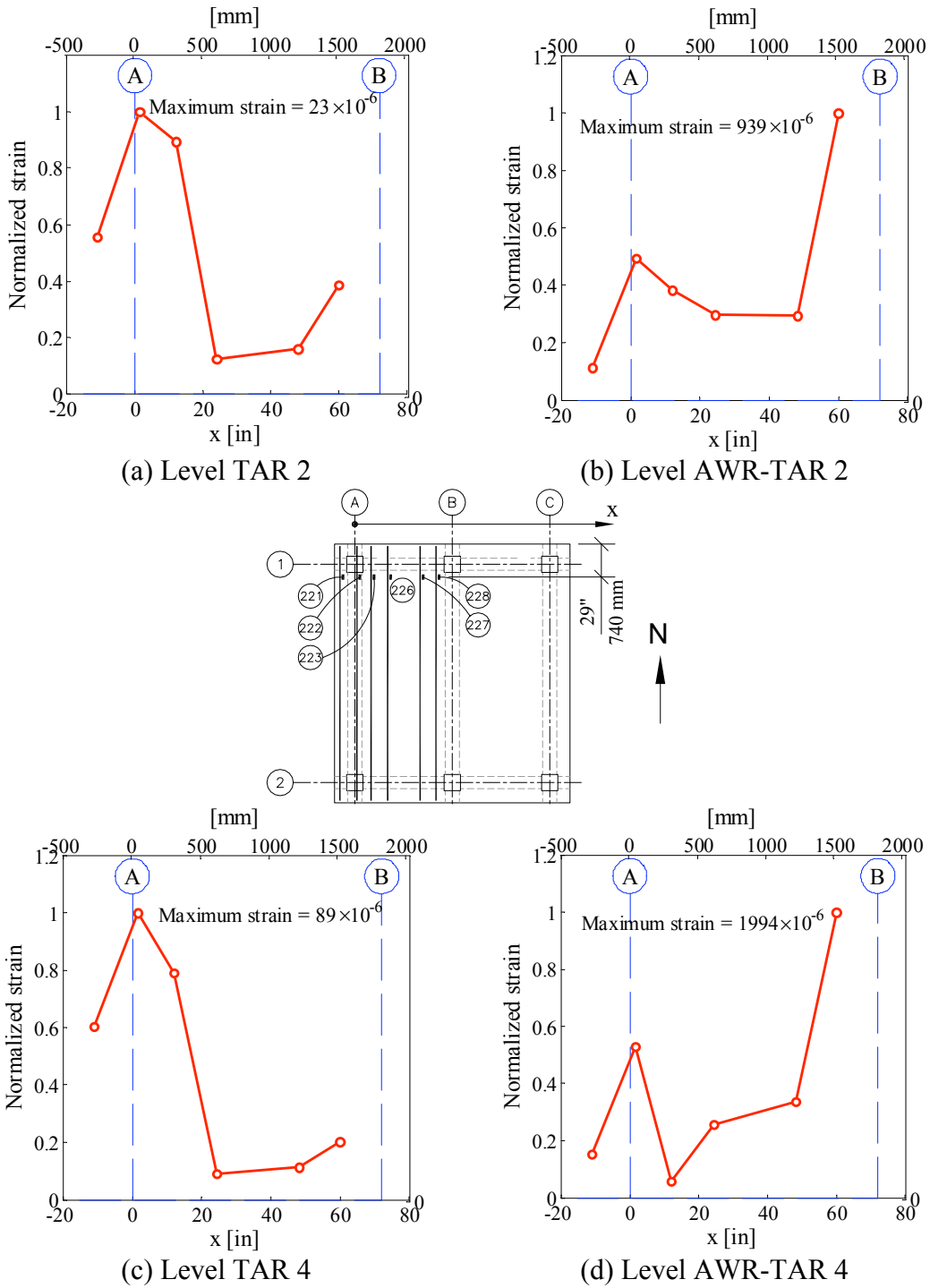


Fig. 6.30 Strain distribution in RC slab perpendicular to RC frames.

6.4.3 Effects of Post-Tensioning in Columns

At the end of stage two of the experiments, it is noted that although the deformations increase significantly due to the removal of the URM infill wall compared to those of stage one, the post-tensioning rods act as a self-centering system preventing the excessive degradation and permanent deformation in the bare test structure. The self-centering mechanism due to post-tensioning of the columns and its effects on the structural behavior are quantified in this section.

6.4.3.1 Measurements in Post-Tensioning Rods

As mentioned in Chapter 3, strain gages are installed on all post-tensioning rods except in column C2 for which a calibrated load cell is installed on top of the column. These instruments serve to monitor the variation of axial forces in the post-tensioning rods during the experiments. The recorded strain variation may be attributed to two sources, namely (1) elongation due to lateral displacement at the top of the columns and (2) bending of the post-tensioning rods. Assuming that the top of the column moves horizontally (does not drop as it undergoes side sway), the strain in the post-tensioning rod due to lateral displacement ϵ_{Δ} is calculated as shown in Equation 6.11.

$$\epsilon_{\Delta} = \frac{u \sin\left(\tan^{-1}\left(\frac{u}{L}\right)\right)}{L} \quad (6.11)$$

where L is the length of the rod and u is the relative lateral displacement of the top with respect to the bottom of the rod. Assuming that the rod stays elastic, the maximum strain in the post-tensioning rod due to bending moment ϵ_M is calculated as shown in Equation 6.12.

$$\epsilon_M = \frac{M_{ps}/S}{E_{ps}} = \frac{6E_{ps}I_{ps}u/I_{ps}}{L^2} \bigg/ \frac{I_{ps}}{r} = \frac{6ur}{L^2} \quad (6.12)$$

where M_{ps} is the fixed-end bending moment at the top or bottom section of the rod, I_{ps} is the cross-sectional moment of inertia of the rod, S is the section modulus of the rod, E_{ps} is the elastic modulus of the post-tensioning rod estimated as 27000 ksi (186 GPa), and r is the radius of the cross section of the rod. As an example, Figure 6.31 shows the actual recorded strain variation in the post-tensioning rod of column C1 during level LomaPr 9 as well as the strain corresponding to Equations 6.11–6.12. Comparison between the plots reveals that the actual

experimental strain peaks in tension, while ϵ_M (and lateral displacement) reaches its peak in both directions, suggesting that the source of strain variation in the post-tensioning rod is indeed elongation due to the lateral displacement and not bending in the rod itself. This is an important observation, since the strain due to bending would be affected by the location of the strain gage on the post-tensioning rod which is not precisely known due to possible turning of the unbonded rod when the post-tensioning force is applied.

Where strain gages are used, the axial force in the post-tensioning rods F is calculated from Equation 6.13.

$$F = E_{ps} \epsilon_{ps} A \quad (6.13)$$

where ϵ_{ps} is the measured strain and A is the cross-sectional area of the post-tensioning rod.

The benefit of the load cell installed on the post-tensioning rod of column C1 is that it allows for a direct measurement of the axial force in this column that can be used to confirm the results obtained from strain gages using Equation 6.13. Since the main source of the variation of axial force in the post-tensioning rods is the relative lateral displacement between the top and bottom of each column, it is expected due to the in-plane rigidity of the RC beams and slab that this variation would be consistent between the two columns of each frame. As an example, Figure 6.32 compares partial time-histories of the axial force variations in columns C1 and C2 during level LomaPr 9 which validates the strain gage measurements and the use of Equation 6.13.

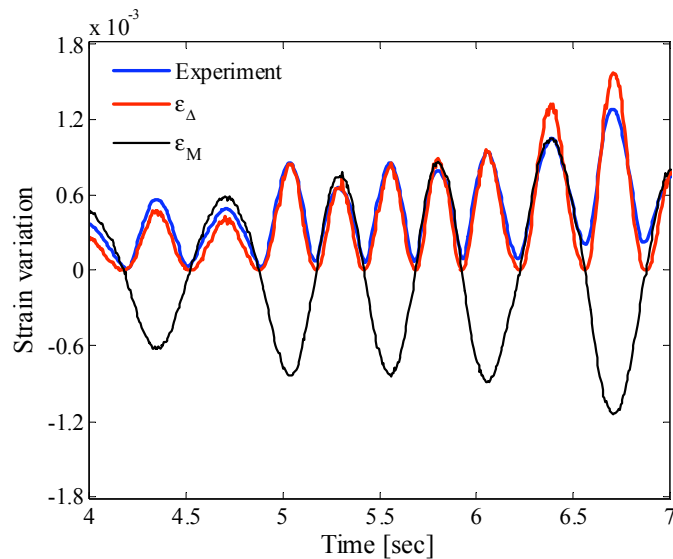


Fig. 6.31 Partial time history of strain variation for column C1 post-tensioning rod during level LomaPr 9 compared with theoretical strains per Eqs. 6.11–6.12.

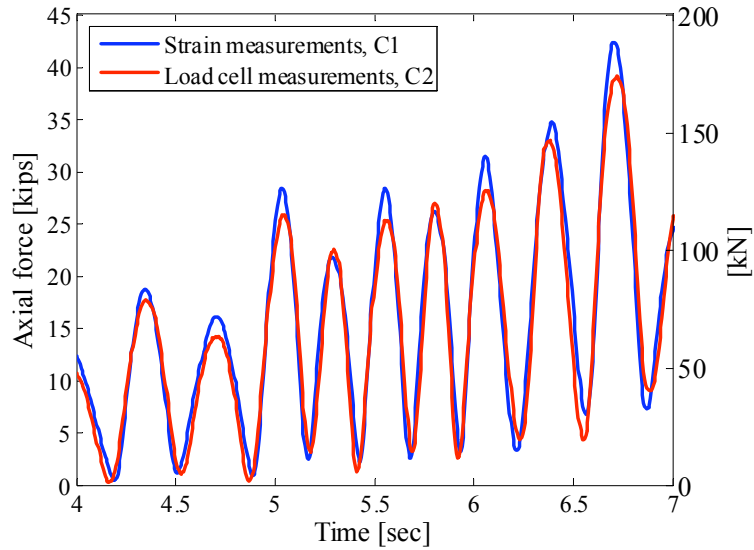


Fig. 6.32 Partial axial force variation time-histories of columns C1 and C2 during level LomaPr 9.

6.4.3.2 Variation of Axial Force in Post-Tensioning Rods

As described in the previous section, the variation of the axial force in the post-tensioning rods is closely related to the lateral displacement of their corresponding columns. Therefore, a significant change in the axial force of these rods is expected during levels with large displacement demands. As an example, the axial force variation of columns C1 and B1 are shown in Figure 6.33 during level LomaPr 9. During this level, maximum axial force increases from the initial post-tensioning forces of 65.2 kips (290kN) and 32.6 kips (145 kN) are 64 kips (280 kN) and 43 kips (190 kN), recorded for columns B1 and C1, respectively.

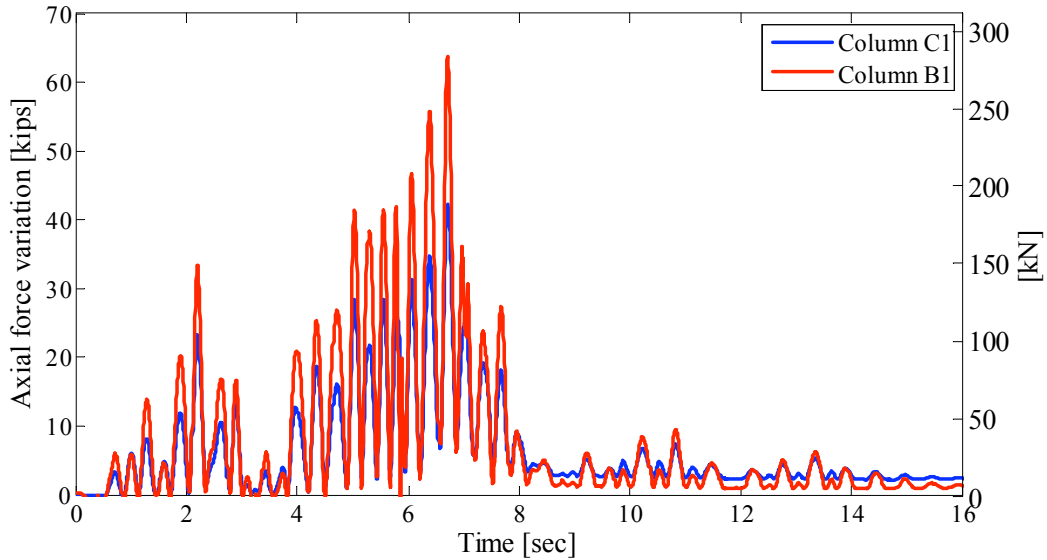


Fig. 6.33 Axial force variation time histories for post-tensioning rods during level LomaPr 9.

Figure 6.34 shows the mean and maximum values of the axial force in the post-tensioning rods observed during different levels of the experiments. Note that these forces include the initial post-tensioning force as described in Chapter 2. The maximum increases in the axial forces of the post-tensioning rods during stage one of the experiments are recorded at level DUZ 8 corresponding to 45% and 69% for columns B1 and C1, respectively. During stage two of the experiments, the maximum increases are recorded in level LomaPr 9 corresponding to 78% and 105% for columns B1 and C1, respectively. The gradual increases in the mean post-tensioning force (7% and 40% over 21 shake-table runs for columns B1 and C1, respectively) are attributed to the expansion of the concrete in the longitudinal direction of the columns due to cracking and accumulation of damage.

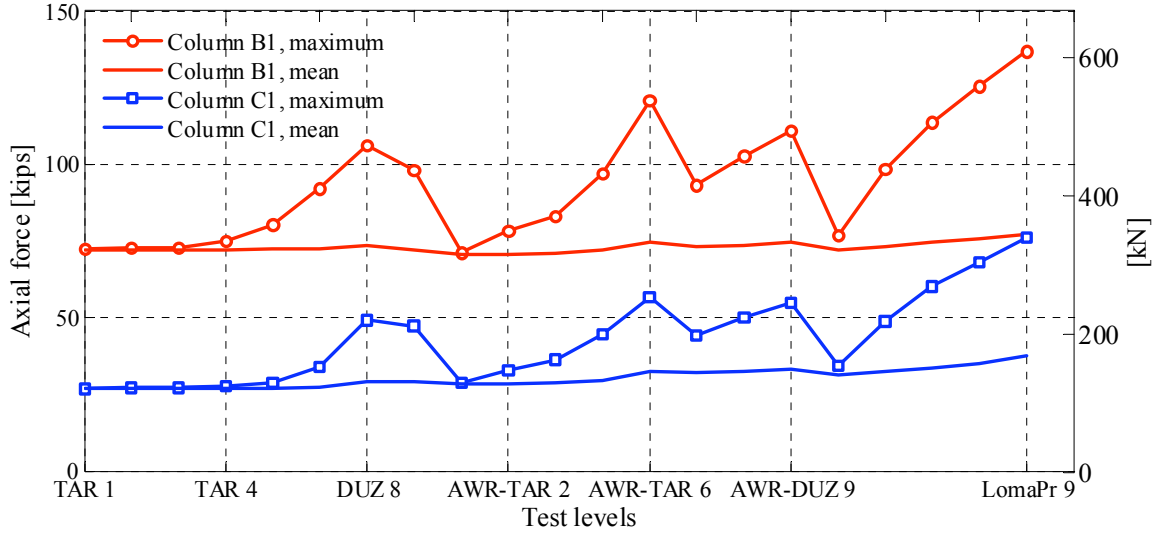


Fig. 6.34 Range of variation of column post-tensioning forces during different levels of shaking.

6.4.3.3 Self-Centering Force

The axial force F in the post-tensioning rods is always concentric with the column centerline. The horizontal component of this force is calculated as shown in Equation 6.14 and is referred to as the self-centering force F_r .

$$F_r = F \sin\left(\tan^{-1}\left(\frac{u}{L}\right)\right) \quad (6.14)$$

Figure 6.35 presents a plot of the total self-centering force calculated as the sum of the self-centering forces in all six columns of the test structure versus the lateral displacement at the RC slab level during level LomaPr 9. The maximum self-centering force observed during this level corresponds to 18.3 kips (81.4 kN) or 19% of the total gravity load (94.0 kips (418 kN)) not accounting for the post-tensioning loads in the columns. It is observed that the increase in the lateral displacement causes a nonlinear increase in the self-centering force in the opposite direction. The more the offset from the original state of the test structure, the more force opposing the motion is generated. This phenomenon helps in limiting the extent of the damage and the permanent deformation of the test structure during stage two of the experiments.

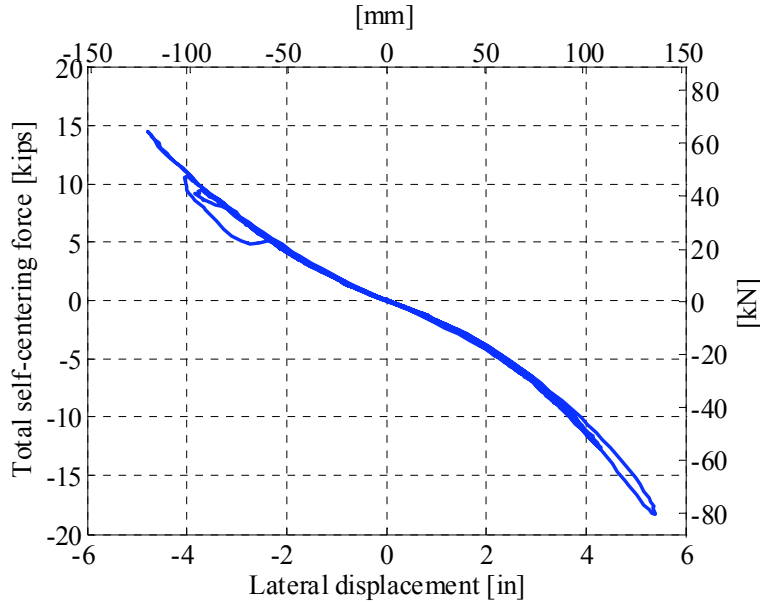


Fig. 6.35 Total self-centering force versus lateral displacement plot during level LomaPr. 9.

The total self-centering force is calculated for all levels of the shake-table experiments in stages one and two, and its minimum and maximum values are presented in Figure 6.36. It can be observed that the range of variation of the self-centering force during stage one of the experiments is limited to ± 6.9 kips (± 31 kN) or $\pm 7\%$ of the total gravity loads which may be deemed negligible in the lateral response of the test structure during this stage. This range increases from $\pm 7\%$ to almost $\pm 19\%$ of the total gravity loads in stage two of the experiments, thus affecting the lateral response of the test structure to a larger extent in stage two than in stage one. It should be noted that the apparent symmetry of the positive and negative changes in Figure 6.36 is due to the fact that the absolute value of the maximum and minimum floor displacements measured during each run are generally close and that these displacements originate the self-centering forces as discussed before.

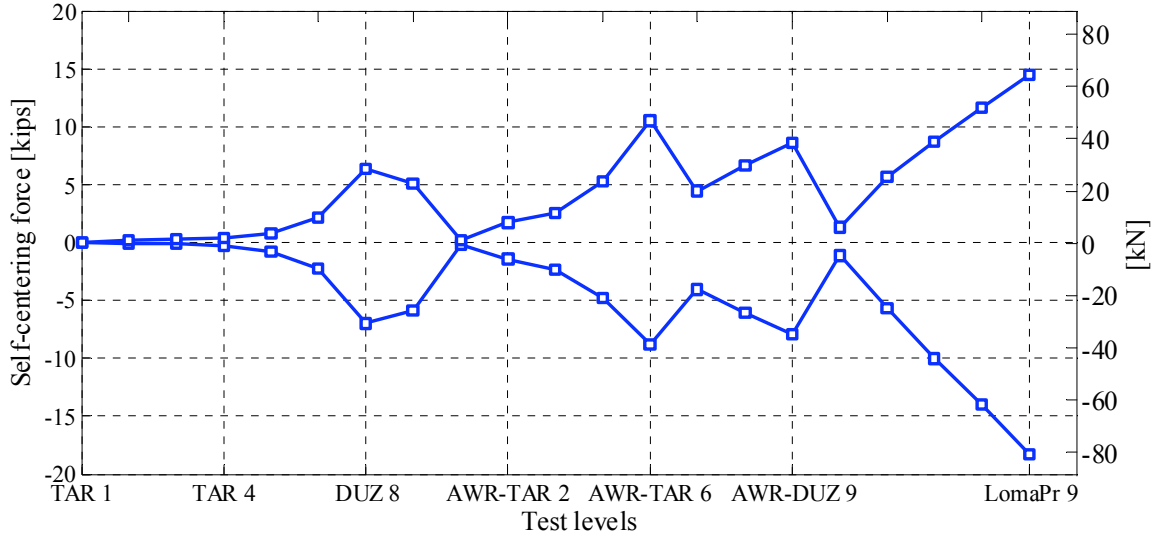


Fig. 6.36 Range of variation of total self-centering force during different levels of shaking.

6.5 DISCUSSION OF STAGE THREE RESULTS

Stage three (the final stage) of the shake-table experiments is performed to investigate the incipient collapse mechanism of the test structure without the URM infill wall. In order to achieve this goal, the post-tensioning rods in the columns are removed. In this final stage, the test structure is subjected only to the Loma Prieta ground motion sequence. Figures (a) and (b) show the typical state of the column-footing joints and beam-column joints, respectively, at the end of this stage. The development of the diagonal cracks in the footing and severe spalling of the concrete at the column-footing interface is shown in Figure 6.37(a). The effects of the described damage in the column-footing joints is the development of flexible hinges at the footings that cause the redistribution of forces in the RC frames and the increase in bending moment demands on the beam-column joints. The significant spalling of the concrete at the beam-column joints follows as can be observed from Figure 6.37(b). Large rotations at the joints exceeded the range of many of the measuring devices installed at the joints, and the excessive spalling of the concrete adversely affects the accuracy of many of the measuring devices. Therefore, the results on the local behavior of the joints in this stage of the experiments are limited compared to the other two stages. The maximum base shear is 120% of the total gravity loads, and the maximum drift ratio reached at this stage is 5.95% taking place in levels LomaPr 9-2-1 and LomaPr 8-2, respectively. The sequence of damage in the test structure observed during this stage suggests that the collapse mechanism for the test structure initiated from hinges forming at the column-

footing joints and progressing to the top of the columns at the beam-column joints resulting in a side-sway mechanism. The state of the test structure at the end of this stage is judged close to the collapse mechanism. Note that added loose safety chains (Fig. 6.38) are used to prevent complete collapse of the test structure at stage three of the experiment to prevent damaging the measurement instruments and shake-table hardware. More discussion on the results obtained during stage three of the experiments are presented in the next section and compared with the results obtained from stages one and two.

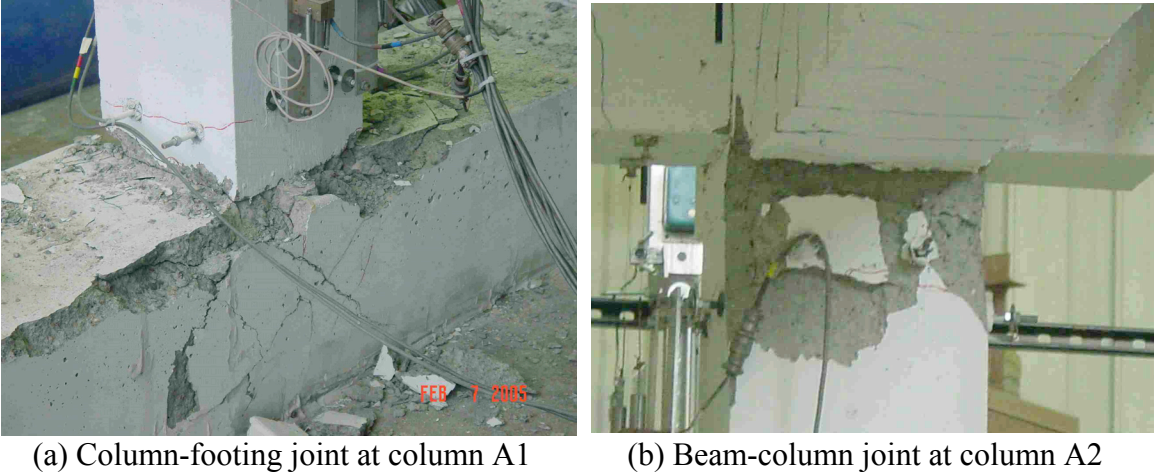


Fig. 6.37 Damage in RC frame joints after stage three of experiments.



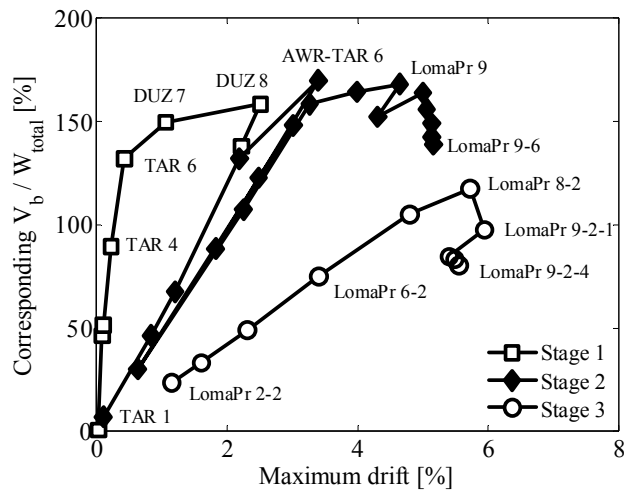
Fig. 6.38 State of test structure at end of stage three of experiments.

6.6 COMPARING RESULTS OF ALL THREE STAGES OF EXPERIMENTS

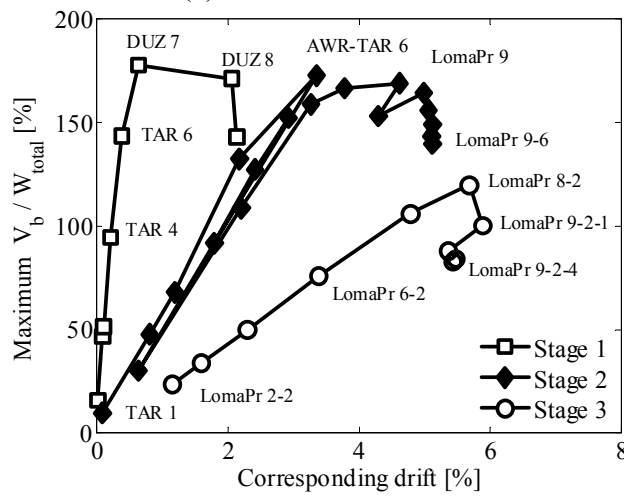
The global and local responses of the test structure during the three stages of the experiments are discussed in detail in previous sections. To gain a clearer perspective, the overall changes in the global dynamic properties of the test structure are compared here for the three stages of the shake-table experiments.

6.6.1 Force-Deformation

The maximum total base shear V_b normalized by the total gravity load W_{total} (94.0 kips (418 kN)) versus maximum drift percentage (top floor displacement with respect to fixed bottom normalized by the story height) at each level of testing is shown in Figure 6.39. The maximum base shear of 167 kips (743 kN), 177% of total gravity load, at level DUZ 8 of stage one corresponds to 0.61% drift in the test structure. However, the maximum drift in this stage is 2.51% corresponding to the base shear of 149 kips (663 kN), 158% of total gravity load in level DUZ 7-2, suggesting a significant decrease in the stiffness but not in the strength of the test structure.



(a) At maximum drift



(b) At maximum base shear

Fig. 6.39 Peak total base shear versus drift plots for different stages of shake-table experiments.

The maximum base shear of 162 kips (721 kN), 172% of total gravity load, at stage two after the removal of the URM infill wall occurs at 3.37% drift ratio during level AWR-TAR 6. The maximum drift ratio recorded in stage two is 5.18%, corresponding to base shear of 130 kips (579 kN), 138% of total gravity load, at level LomaPr 9-6, i.e., the sixth and last repetition of LomaPr 9. After the removal of the post-tensioning rods, the stiffness of the test structure is reduced even further. The maximum base shear of 113 kips (503 kN), 120% of total gravity load, in stage three corresponds to a drift ratio of 5.68% in level Loma Pr 8-2. Despite the increase in the intensity of the ground motion at level LomaPr 9 and its repeated runs, smaller values of the maximum base shear and the maximum drift ratio for the repeated runs (maximum

drift ratio for LomaPr 9-2-1 is 5.95% corresponding to base shear of 91.7 kips (408 kN), 97.5 % of the total gravity load) are reached. This is explained by noting the shape of the ground motion spectra (Fig. 5.5), where as the test structure softens the natural period of the test structure elongates, and the demand forces and displacements on the test structure decrease.

Figure 6.40 shows the effective stiffness as defined in Section 6.3.1 of the test structure normalized with respect to the stiffness of the test structure at the beginning of stage two of the experiments, 49 kip/in. (8.6 kN/mm), during stages two and three (for the stiffness variation in stage, see Fig. 6.5). It is observed that at the end of stage two, the test structure is still holding to 45% of its stiffness and at the end of stage three, the stiffness is reduced to only 22% of the stiffness at the beginning of stage two. The plot also suggests significant damage to the test structure during levels AWR-TAR 6 and LomaPr 9. It is also worth noting that there is a 22% reduction in the stiffness of the test structure due to the removal of the post-tensioning rods at the beginning of stage three compared to at the end of stage two.

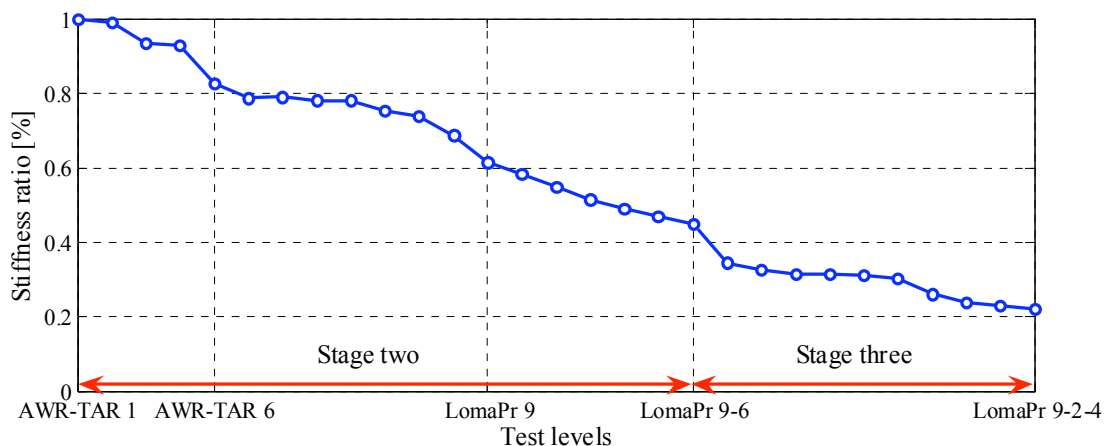


Fig. 6.40 Effective stiffness variation in test structure during stages two and three.

6.6.2 Natural Period

Figure 6.41 illustrates the variation of the natural period of the test structure as the different levels of the experiments progress. This figure is an extension of Figure 6.8 given for stage one only. These values are determined using both the white-noise signals and the ground motion signals. As explained previously, the white-noise signals are applied with very small amplitudes (about 0.07g) before each test level and are not necessarily evaluating the actual natural period of the test structure during the ground motion shaking. Two distinct jumps can be observed in the

natural period of the test structure using either signal: (1) 70% jump when the URM infill wall cracks and (2) 25% jump at the first significant shaking after removal of the post-tensioning rods (LomaPr 3-2) at the beginning of stage three of the experiments. It is observed that there is one level delay in detecting the increase in the natural period of the test structure when using the results of the white-noise tests, particularly for stage one of the experiments. The reason is that the amplitude of the white-noise signal is too small to cause the existing cracks to open. Therefore, the test structure vibrates under these white-noise signals without detecting the existence of the current cracks. When the next shaking level is applied, however, the previous cracks open (but not the current) and remain open for the subsequent white-noise signal.

During the course of all the experiments and based on the results of the actual shaking signals, the natural period of the test structure changes by a factor of about 6.5 from 0.147 sec to 0.955 sec. This significant change of the natural period emphasizes the change of the structural configuration (removal of the URM infill wall and removal of the columns post-tensioning) and the extent of the damage to the test structure.

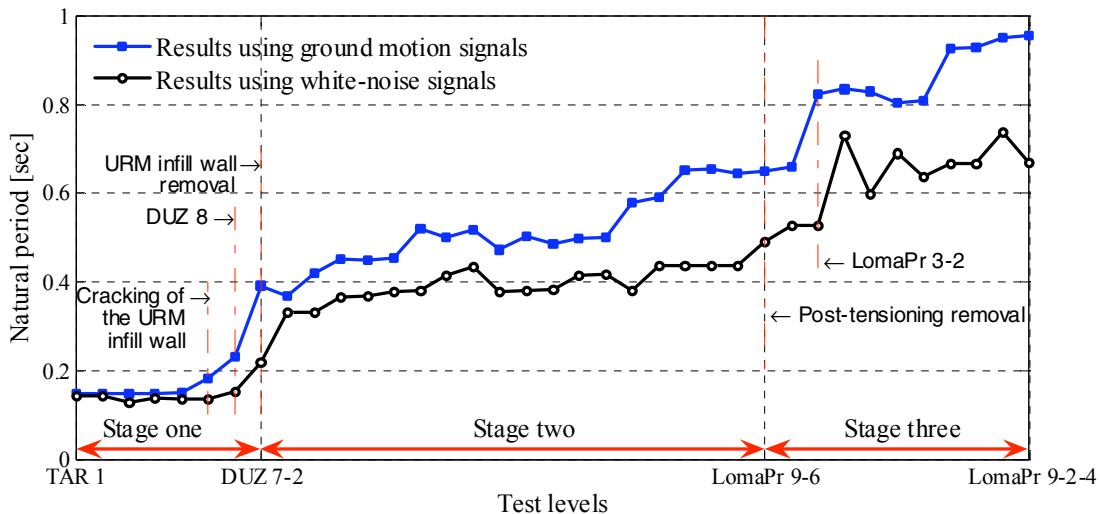


Fig. 6.41 Variation of natural period of test structure during shake-table experiments.

6.6.3 Damping Ratio

Figure 6.42 demonstrates the change in the mean damping ratio of the test structure during each shake-table run using the two approaches discussed early in this chapter. This figure is an extension of Figure 6.11 given for stage one only. It can be observed that the highest values of damping ratio (above 13%) are achieved during levels DUZ 8 and DUZ 7-2. The damping ratio is also high (between 8% and 10%) during the repeats of level LomaPr 9 in stages two and three

of the shake-table experiments when the most severe damage occurs in the RC frames. However, when the test structure is subjected to small-intensity ground motions (levels 1–4), the damping ratio ranges between 4%–6%, suggesting that the damping ratio is not independent of the intensity of shaking. The gradual increasing trend observed in the value of the damping ratio is attributed to the reduction in the stiffness of the test structure due to the inverse relationship between the damping ratio and the square root of the stiffness (Chopra 2001). The results obtained by the energy-equivalent damping method and the regression method are in closer agreement in stages two and three when compared to stage one results. Perhaps the reason is that after removal of the URM infill wall, there is no sudden shift in the stiffness of the test structure that limits the accuracy of the linear regression model. Since the energy equivalent formulation takes into account the energy dissipation in the structural system, it offers a more reliable estimate of damping for the equivalent linear system especially when subjected to strong motions and significant nonlinearity.

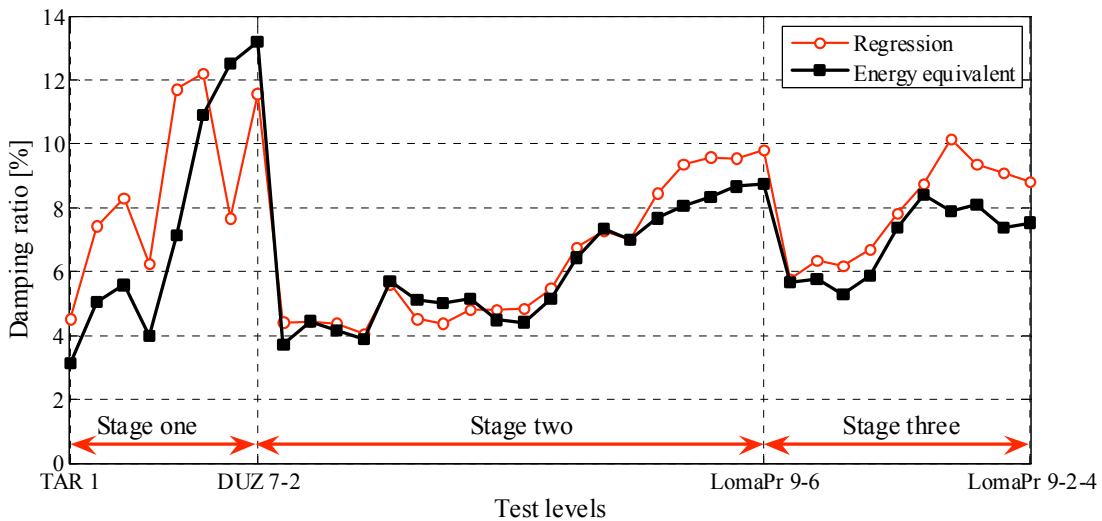


Fig. 6.42 Variation of mean damping ratio of test structure during shake-table experiments.

6.6.4 Residual Displacements

The residual displacement at the end of each run is determined by subtracting the mean of the first 100 displacement data points, i.e., first 0.5 sec at 200 Hz sampling rate, from the mean of the last 200 displacement data points, i.e., the last 1 sec of each run. The absolute value of the residual displacement for each run is presented in Figure 6.43. During stage one of the experiments (URM infilled test structure), the residual displacements are practically negligible

with peaks of 0.03 in (0.76 mm) at level DUZ 7 and 0.075 in. (1.9 mm) at level DUZ 7-2 (URM infill wall collapsed) corresponding to 0.028% and 0.069% drift ratios, respectively. During stage two of the experiments, the residual displacement within each run is still limited to a small peak value of 0.17 in. (4.3 mm) during the third repetition of Loma Prieta level 9 (LomaPr 9-3) corresponding to a 0.16% drift ratio. This is due to the self-centering effects of the post-tensioning rods as previously discussed. On the other hand, after removal of the post-tensioning rods in stage three of the experiments, large residual displacements are observed in the experiments with the peak value of 0.51 in. (12.9 mm) during level LomaPr 9-2-1 corresponding to a 0.47% drift ratio.

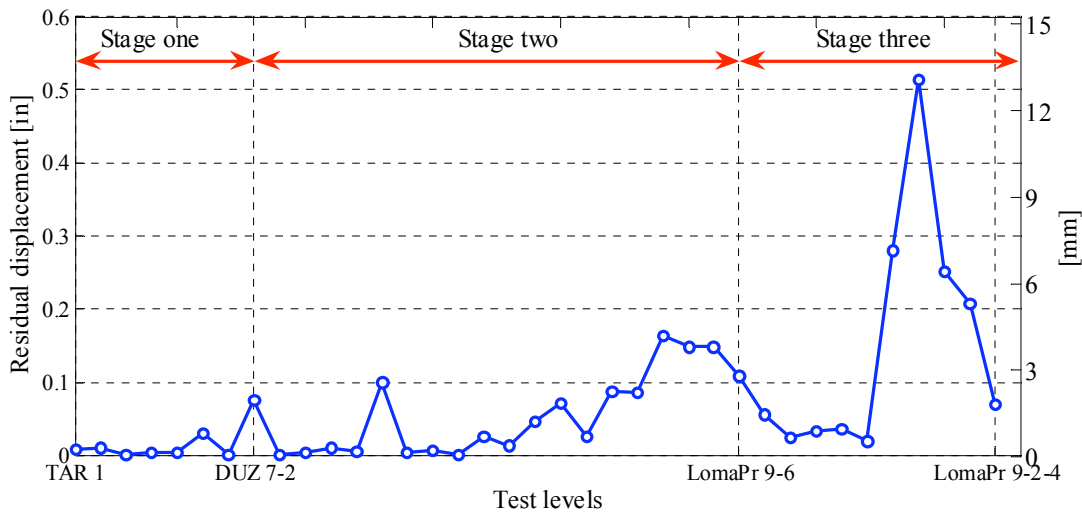


Fig. 6.43 Absolute value of residual displacement at RC floor slab during shake-table experiments.

Since the residual displacements within each shake-table run are evaluated for the state of the test structure at the end of the run with respect to the start of that run, cumulative and algebraic sums of these values result in the total residual displacement of the RC floor slab at the end of each shake-table run with respect to the start of the shake-table experiments. These total (cumulative) residual displacements are shown in Figure 6.44. The maximum residual displacement at the RC floor slab recorded is 0.95 in. (24.1 mm) corresponding to 0.88% residual drift ratio at the end of level LomaPr 6-2. The total residual displacement at the end of all the experiments is -0.39 in. (-9.9 mm) corresponding to 0.36% residual drift ratio. The change in the direction of the residual displacement is difficult to explain and perhaps not practically informative. However, it may be attributed to several factors such as the sequence of cracking in

the columns and joints in the test structure, the particular displacement history of each input ground motion, and the frequency content of these motions with respect to the changing natural period of the test structure.

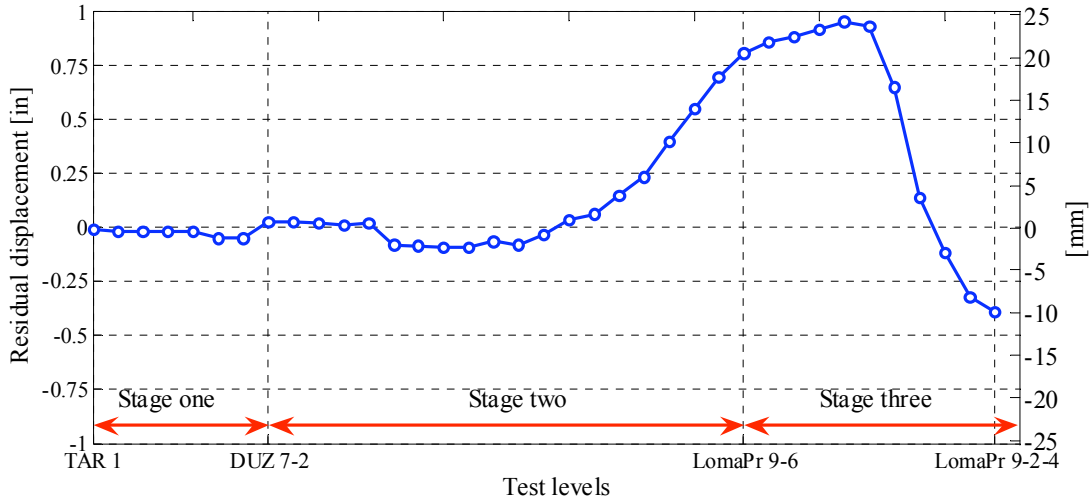


Fig. 6.44 Total cumulative residual displacement at RC floor slab of test structure.

6.6.5 Change of Demand Forces in RC Frame Joints

In this section the change in the demand forces in the RC frame beam-column and column-footing joints during the three stages of the shake-table experiments are discussed. The procedure to determine the bending moments and section rotations at the tops and bases of the columns were discussed in Section 6.3.7.2. The maximum values of the bending moments and their corresponding maximum section rotations obtained during different levels of the shake-table experiments are presented in this section in Figure 6.45. It should be noted that the maximum values of the section rotations do not necessarily occur at the same instants of time as the maximum values of the bending moments and may be higher than the actual values corresponding to these maximum bending moments. Moreover, the results of many instruments are used in the determination of these quantities and these results are not available for every level due to malfunctioning of one or more of these instruments, which leads to incomplete data.

The change in the demand forces is due to two important reasons: (1) The failure of the URM infill wall, removal of the post-tensioning rods, and the development of footing hinges reduce the stiffness of the test structure resulting in significant increases in its natural period as discussed in the previous sections. Therefore, the spectral demands on the test structure are reduced as can be observed from Figure 5.5, which represents the SDOF elastic spectral response

for 5% damping ratio. (2) The development of the hinges at the footings causes redistribution of forces in the RC frames by increasing the demands on the beam-column joints causing further spalling and yielding at the top cross sections of the RC columns.

Figures 6.45 (a) and (b) show the maximum base moment versus maximum base rotation for columns A2 and B1, respectively (Fig. 1.1(b)). These plots show a 43% and a 37% drop in moment demands at the bases of columns A2 and B1, respectively, for stage two results compared to stage one results, suggesting significant damage at the bases of the columns. Toward the end of stage two, the maximum base rotations are 0.037 rad for A2 and 0.049 rad for B1, with respective sustained maximum bending moments of 1000 kip-in. (113 kN-m) and 1340 kip-in. (151 kN-m), suggesting severe damage at the column-footing joints. Figures 6.45(c) and (d) show the maximum top moment versus the maximum top rotation for columns A2 and B1, respectively. These plots suggest significant increases (80% for columns A2 and 88% for column B1) in the bending moment demands on the beam-column joints for both columns for stage two results compared to the results of stage one of the shake-table experiments. The difference between the results for columns A2 and B1 suggests more severe damage at the base of column B1 due to higher bending moments recorded at the top of column B1 and more base rotation recorded for column B1.

During stage three of the experiments, it is observed that the maximum bending moments in the column-footing joints are further reduced, e.g., a 52% reduction for column A2 and a 14% reduction for column B1 in level LomaPr 7 compared to the same level in stage two as shown in Figures 6.45(a) and (b), respectively. This decrease in demand is primarily due to the shift in the natural period of the test structure and the resulting reduction in the spectral acceleration. Moreover, these bending moments occur at much higher base rotations, e.g., 170% and 120% higher base rotation in columns A2 and B1, respectively, for level LomaPr 7 when compared to the rotations measured at the same level during stage two of the experiments. Figure 6.45(c) suggests significant accumulation of damage in the beam-column joint of column A2 compared to stage two results, i.e., a 48% drop in the maximum bending moment and a 47% increase in the maximum rotation. The moment rotation plot for column B1 at its beam-column joint during stage three of the experiments is close to the results obtained for stage two as shown in Figure 6.45(d) suggesting no significant additional damage at this location during stage three. Moreover, for stage three of the experiments, the difference between the results for columns A2

and B1 suggests more damage at the base and consequently at the top of column A2 compared to column B1.

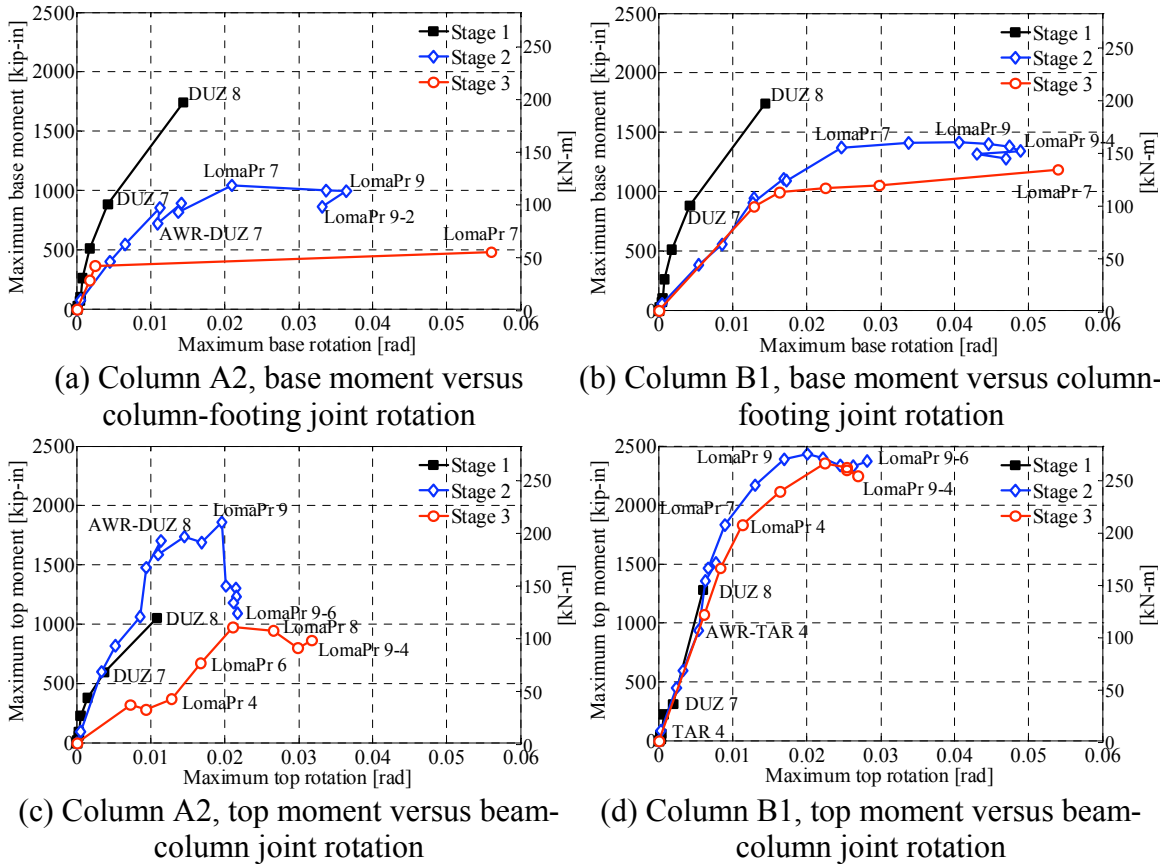


Fig. 6.45 Maximum moment versus maximum rotation at top and bottom of selected columns.

6.7 SUMMARY

The results of the shake-table experiments are presented in this chapter. The methodology used to determine the internal forces and the dynamic properties of the test structure during the experiments are described. The global and local responses of the test structure in all three stages of the shake-table experiment are presented.

For stage one of the experiments, variations of natural period, damping ratio, and stiffness of the test structure as quantitative representations of the accumulation of damage in the URM infill wall and the RC frames both within each run and between different shaking are discussed. Also discussed in detail are the load path and crack patterns in the URM infill wall, the distribution of forces between different elements of the test structure before and after

cracking of the URM infill wall, the deformed shape of the URM infill wall with respect to the bounding RC frame, and the contact length between the URM infill wall and the bounding RC frame members in stage one. Also at this stage, the variation of demand forces on the RC slab and frames due to the damage in the URM infill wall as well as the deformations of the RC slab are illustrated. Moreover, the damage sequence and the yielding locations of the reinforcing bars in the RC frames after high levels of shaking are discussed.

For stage two of the experiments, after removal of the URM infill wall, the state of the test structure and its progression of damage states are depicted. The effective RC slab width participating in the lateral load-resisting system is evaluated and compared for the scenarios before and after removal of the URM infill wall. The role of the post-tensioning rods in the ability of the test structure to sustain intense shaking is also discussed and the variation of the self-centering forces due to these rods is quantified. For stage three of the experiments, after removal of the post-tensioning rods, the state of the test structure and its progression of damage states and the collapse mechanism for the test structure are discussed.

Important engineering demand parameters such as maximum base shear and maximum drift as well as important properties of the test structure such as effective stiffness, natural period, and damping ratio are compared for all three stages of the experiments. The individual and cumulative variations of the residual displacements at the RC floor slab are also presented and discussed for all stages. The local responses in terms of the variations in the demand forces in the joints of the test structure due to the redistribution of forces and the elongation of the natural period of the test structure are presented for all stages of the experiments.

7 Computational Modeling of URM Infilled Frames

Modeling RC frame structures containing URM infill walls is a challenging problem and can be studied from two different points of view: first, by determining the failure mechanics and detailed behavior of each individual infill panel, and second, by studying the overall structural system response as it changes due to the engagement of the URM infill walls in the lateral response of the structure. This chapter is an attempt at the second approach, discussing ways of accurately considering URM infill walls within the larger RC structural system.

Perhaps the most precise models to properly consider the URM infill walls in the analysis of structures are based on finite element (FE) methods considering the individual bricks, mortar joints, and the interface conditions between the bricks, mortar, and the bounding frame (Mosalam 1996a). However, this detailed approach is computationally very expensive and practically not possible for the design of large structures. Alternatively, simpler models have been proposed to account for the strength and stiffness of URM infill walls by representing them as compression-only single diagonal struts or a set of struts in the form of parallel diagonal and off-diagonal struts (Holmes 1963; Stafford-Smith 1962, 1966; Thiruvengadam 1985; and Chrysostomou 1991). Typically, these simple models do not go beyond the elastic behavior of the URM infill wall and are not suitable for cyclic loading or the analysis of the structure past failure of the URM infill wall. Moreover, both aforementioned types of models for URM infill walls, detailed with FE models or simplified with compression-only struts, are limited in literature to two-dimensional configurations considering only the in-plane behavior of the URM infill walls. Accordingly, such models are not capable of accounting for the effects of the out-of-plane forces on the URM infill walls, cyclic degradation of the infill in one loading excursion due to the damage caused by the reverse loading excursion, and the strong coupling between the in-plane and the out-of-plane forces in the URM infill walls.

In this chapter, the traditional methods for determining the in-plane modes of failure of URM infill walls and their modeling using compression-only struts are briefly discussed. Two computational models of the shake-table test structure discussed in the previous chapters are constructed using two separate single-strut models to represent the URM infill wall. The strut properties in one model are determined based on the FEMA 356 provisions (2000). For the other model, the properties are calibrated and modified based on experimental results. The computational results are compared with the actual shake-table experimental results, discussed in Chapter 6, and the benefits and limitations of the single-strut model are discussed.

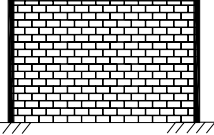
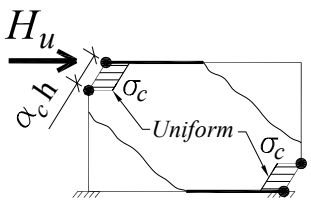
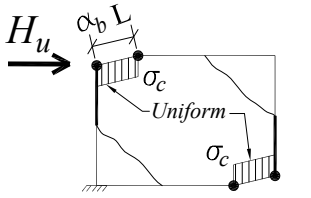
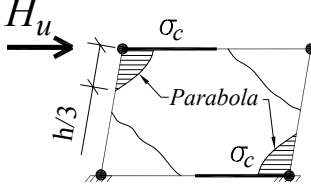
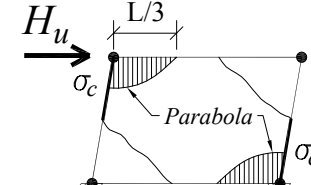
In order to fully understand the behavior of the URM infill walls, a FE model of the test structure is developed to serve as a tool for detailed numerical simulations of the test structure. The FE model is validated by comparing the response of the computational model with the pseudo-dynamic and the shake-table experimental results. It is reiterated that the actual pseudo-dynamic experiments (see Fig. 1.3) are not part of this report as stated in Chapter 1. Using the FE model, a series of numerical simulations are performed to investigate the interaction between the in-plane and the out-of-plane forces on the URM infill wall. Finally, a novel 3D strut and tie (SAT) model is proposed and developed for practical implementation and consideration of both the in-plane and the out-of-plane responses of URM infill walls and their interaction. The model is evaluated for a wide range of URM infill wall properties.

7.1 IN-PLANE FAILURE MODES OF URM INFILL WALLS

In-plane failure modes of URM infill walls are defined in terms of the type and sequence of damage among the elements of the infilled RC frame. Such damage is defined as corner and diagonal crushing of masonry; plastic hinge formation in columns, beam; or beam-column joints; and shear failure of the beam or columns. Using plastic analysis, the following four in-plane modes of failure for the URM infilled RC frames are introduced and formulated by Liauw and Kwan (1985b). These modes of failure and their estimated plastic capacities H_u and joint shear demands V_j are summarized in Table 7.1.

Mode 1, corner crushing with failure in columns and infill-beams connections: In this mode of failure, the compressive corner regions of the infill panels crush. Moreover, plastic hinges form at the loaded corners and at the columns near the compression zone of the panel and, where shear connectors, the infill-beam connections yield.

Table 7.1 In-plane modes of failure and their corresponding estimated capacities H_u and joint shear demands V_j of infilled systems.

Mode		Estimated capacity H_u and joint shear demand V_j (Liauw and Kwan 1985b)
1		$H_u = \sqrt{2 \frac{(M_{pj} + M_{pc})}{\sigma_c t h^2}} \sigma_c t h + s \left(L - \frac{h}{2} \right)$ $V_j = \frac{M_{pj} + M_{pc}}{\alpha_c h} + \sigma_c t \frac{\alpha_c h}{2}$
2		$H_u = \frac{1}{\tan \theta} \sqrt{2 \frac{(M_{pj} + M_{pb})}{\sigma_c t h^2}} \sigma_c t h + s \frac{h}{2} \tan \theta$ $V_j = \frac{M_{pj} + M_{pb}}{\alpha_b L} + \sigma_c t \frac{\alpha_b L}{2}$
3		$H_u = 4 \frac{M_{pj}}{h} + \sigma_c t \frac{h}{6} + s \left(L - \frac{h}{2} \right)$ $V_j = 4 \frac{M_{pj}}{h} + \sigma_c t \frac{h}{6}$
4		$H_u = 4 \frac{M_{pj}}{h} + \sigma_c t \frac{h}{6(\tan \theta)^2} + s \frac{h}{2 \tan \theta}$ $V_j = 4 \frac{M_{pj}}{h} \tan \theta + \sigma_c t \frac{h}{6 \tan \theta} + s \frac{h}{2}$

Mode 2, corner crushing with failure in beams and infill-columns connections: In this mode of failure, the compressive corner regions of the infill panels crush. Moreover, plastic hinges form at the loaded corners and at the beams near the compression zone of the panel and, where shear connectors, the infill-column connections yield.

Mode 3, diagonal crushing with failure in infill-beam connections: In this mode of failure, all plastic hinges form at the four beam-column joints. Moreover, where shear connectors, the infill-beam connections yield.

Mode 4, diagonal crushing with failure in infill-columns connections: In this mode of failure, all plastic hinges form at the four beam-column joints. Moreover, where shear connectors, the infill-columns connections yield.

The formulas in Table 7.1 utilize the following notations:

- H_u lateral frame capacity,
- M_{pb} plastic moment capacity of beam,
- M_{pc} plastic moment capacity of column,
- M_{pj} plastic moment capacity of beam-column joint,
- h story height,
- L span of infilled RC frame,
- t thickness of infill panel,
- s shear strength of interface connection,
- σ_c crushing stress of panel material, and
- θ angle between the diagonal of the infill panel and the horizontal axis.

The shear failure of the beam, column, or joint in the formulas in Table 7.1 must be checked independently and if the shear demand is higher than the corresponding shear capacity, the lateral frame capacity H_u must be reduced accordingly. The joint shear demand V_j due to each mode of failure can be calculated from statics (see Table 7.1) by determining the lengths from the loaded corner to the plastic hinges in the beams $\alpha_b L$ or the columns $\alpha_c h$ where α_b and α_c are determined from Equations 7.1 and 7.2, respectively.

$$\alpha_b = \sqrt{2 \frac{(M_{pj} + M_{pb})}{\sigma_c t h^2}} \tan \theta \quad (7.1)$$

$$\alpha_c = \sqrt{2 \frac{(M_{pj} + M_{pc})}{\sigma_c t h^2}} \quad (7.2)$$

For the infilled RC frame of the test structure, defined in Chapter 3, the geometric parameters are as follows: $h = 108$ in. (2740 mm), $L = 162$ in. (4110 mm), $t = 3.75$ in. (95.2 mm) and $\theta = 33.7^\circ$. The crushing stress σ_c is taken as $f'_m = 2.46$ ksi (17.0 MPa) and the shear strength of the interface connection between the URM infill wall and the RC frame members s is assumed to be zero at the sides of the URM infill wall, i.e., interfaces with the columns, and judged as one half the shear strength of masonry at the top and bottom edges, i.e., interfaces with

the beam and footing. These values are chosen based on expected low bond between the URM infill wall and the RC concrete frame on the sides and friction force due to high normal forces on the top and bottom interfaces caused by the gravity loads on the infilled RC frame of the test structure. The additional normal force on the bottom interface due to the weight of the URM infill wall is small compared to the gravity loads from the RC beam, RC slab, and additional weight on the slab. This additional weight is ignored in the determination of the shear strength of the bottom interface. The plastic hinge capacities of the RC beam M_{pb} and columns M_{pc} are calculated based on standard section analysis procedure (e.g., ACI 318-05) as 888 kip-in. (100 kN-m) and 1280 kip-in. (144 kN-m), respectively. The joint plastic hinge capacity is taken as the lower of the plastic capacities of the beam and the columns, i.e., 888 kip-in. (100 kN-m). The resulting estimated lateral frame capacities for the four modes identified in Table 7.1 are listed in Table 7.2. It is to be noted that the values of α_b and α_c are determined as 0.12 and 0.20, respectively. Using these values, the shear demand at the beam-column joint V_j corresponding to each mode of failure is determined as presented in Table 7.2. From these results, it follows that the mode governing the failure of the infilled RC frame is the third mode, although the first mode can not be entirely ruled out. It should be emphasized that the benefit of plastic analysis is in the determination of the failure mode and the corresponding estimated capacity value as an upper bound to the actual capacity of the infilled frame. In fact, compared to the results obtained from the shake-table experiment, discussed in Chapter 6, the capacity estimate is higher by a factor of 2.2. Also, the joint shear demand predicted for mode 3 is 64% higher than the joint shear capacity evaluated per ACI 318-05 section 21.5.3.1 as 121 kips (538 kN), which could lead to joint shear failure contradictory to the observed results presented in Chapter 6.

Table 7.2 Estimated lateral capacity of infilled RC frame of test structure based on plastic analysis.

	Mode 1	Mode 2	Mode 3	Mode 4
H_u [kips (kN)]	248 (1100)	272 (1210)	247 (1100)	407 (1810)
V_j [kips (kN)]	200 (890)	181 (805)	199 (885)	271 (1210)

The above failure modes are not reflected in the FEMA 356 provisions (2000). Instead, it is suggested that a detailed FE analysis may be performed to determine the strength and stiffness of the composite frame substructure. Alternatively, the stiffness of the infill panel is given by an

empirical formula, and the strength of the infill panel is determined based on the shear strength of the masonry panel across its net mortar cross section, suggesting a horizontal plane of failure. The FEMA 356 strut model is discussed in detail in the next section.

7.2 STRUT MODELS

In this section, two different strut models to represent URM infill walls in structures are discussed. A single-strut model offered by FEMA 356 provisions (2000) and a calibrated single-strut model are discussed in detail and used in the computational modeling of the test structure defined in Chapter 3. The results of the computational models are compared with those obtained from the shake-table experiments, and the benefits and limitations of these strut models are discussed.

7.2.1 Background

In order to represent URM infill walls within the larger structural systems, researchers have proposed properties of simple equivalent strut or struts replacing the infill wall in each frame (Holmes 1963; Stafford-Smith 1962, 1966; Thiruvengadam 1985; Chrysostomou 1991; Hamburger 1993; and El-Dakhkhni et al. 2003). Such strut models are proportioned to represent the stiffness and strength of the URM infilled RC frame assembly by matching experimental data, assuming some specific failure mode, or by calibrating the struts using a FE model of the infilled RC frame. The arrangement of the struts depends on the expected failure mode of the assembly. For example, to represent the failure modes discussed in the previous section and based on the crack patterns observed in many experiments performed on URM infilled RC frames (Manzouri and Shing 1995; Angel and Abrams 1994; and Buonopane and White 1999), the SAT models shown in Figure 7.1(a) are proposed. The typical compression-only strut to RC frame connection to ensure stability is also shown in this figure. These SAT assemblies may be made more elaborate or simplified depending on whether the local effects of the infill wall on the adjacent frame elements are considered. For example, by neglecting the tensile strength of the URM material, the tie elements may be omitted in modes 1 and 2. Another possible simplification for modes 3 and 4 is to represent the URM infill wall with a single diagonal or off-

diagonal strut. Simplified representations of the SAT models in Figure 7.1(a) are shown in Figure 7.1(b).

The choice of the geometric details of the SAT model for infilled RC frames is somewhat arbitrary and can be adjusted based on the experience of the designer and the balance between the practicality and the accuracy of the model. In general, the material properties of each horizontal strut or tie are obtained from the shear capacity of the interface between the mortar joint and the masonry units. Likewise, the material properties of the vertical struts and ties are obtained from the behavior of the masonry prisms in compression and tension. Similarly, the material properties of the diagonal struts and ties can be estimated from the diagonal compression and tension behavior of masonry assemblies. The area of each strut and tie can be chosen by a trial and error procedure such that the assembly has the same strength and stiffness as predicted by experiments or by FE analyses.

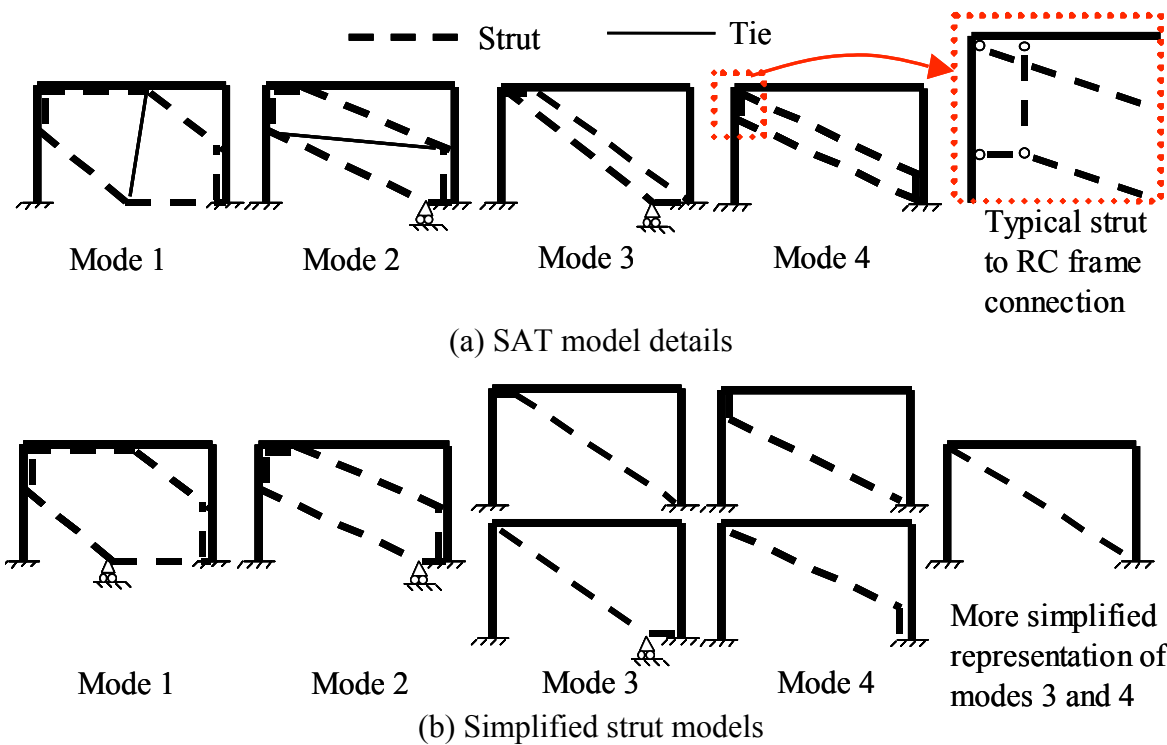


Fig. 7.1 SAT models for different in-plane failure modes of URM infilled RC frames.

7.2.2 Computational Modeling of Test Structure

In order to demonstrate the benefits and limitations of the strut models, a simple single-strut (compression-only) element is considered to represent the URM infill wall in an analytical model of the test structure described in Chapter 3. The analytical model is developed using OpenSees (Mazzoni et al. 2006). Beams and columns in the computational model are represented by *nonlinearBeamColumn* elements, which are based on force formulation, and consider the spread of plasticity along the length of each element. Cross sections are defined using fiber discretization with distinct fibers for reinforcement. Concrete material is modeled using *Concrete01*, which is a uniaxial concrete material object with degraded linear unloading/reloading stiffness. Steel reinforcing bars are modeled using *Steel01*, a uniaxial bilinear material object with kinematic hardening. The adopted values for concrete parameters of different members and steel parameters for reinforcing bars are shown in Tables 2.2 and 2.3, respectively, in Chapter 2. The column-footing joints are modeled using the provisions of FEMA 356 (2000) by a trilinear moment-rotation relationship as defined in Table 2.4. The beam-column joints are assumed to behave rigidly in stage one of the experiments. In order to determine the properties of the compression-only diagonal struts representing the URM infill wall, two different approaches are adopted. In the first approach, the FEMA model, the provisions of FEMA 356 (2000) are used to find the compression strut geometric and material properties. In the second approach, a calibrated model, a simple concrete-like material model is used for the strut material, which is calibrated based on the measured properties of masonry prisms, and the geometric properties of the strut are determined based on the observed stiffness of the URM infilled RC frame during the shake-table experiments. Figure 7.2 shows a schematic view of the OpenSees model.

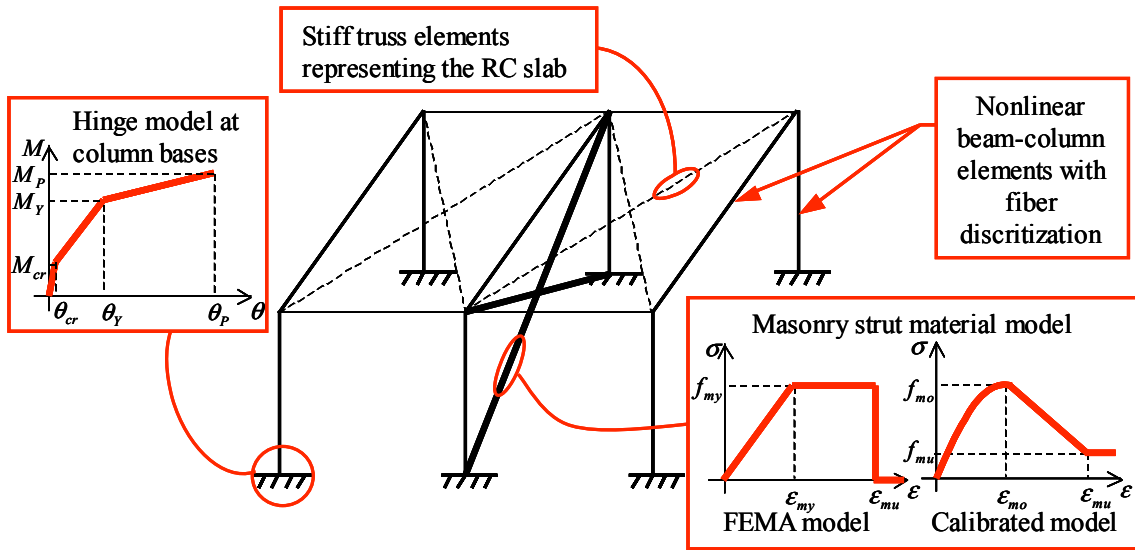


Fig. 7.2 OpenSees model with single strut for URM infill wall.

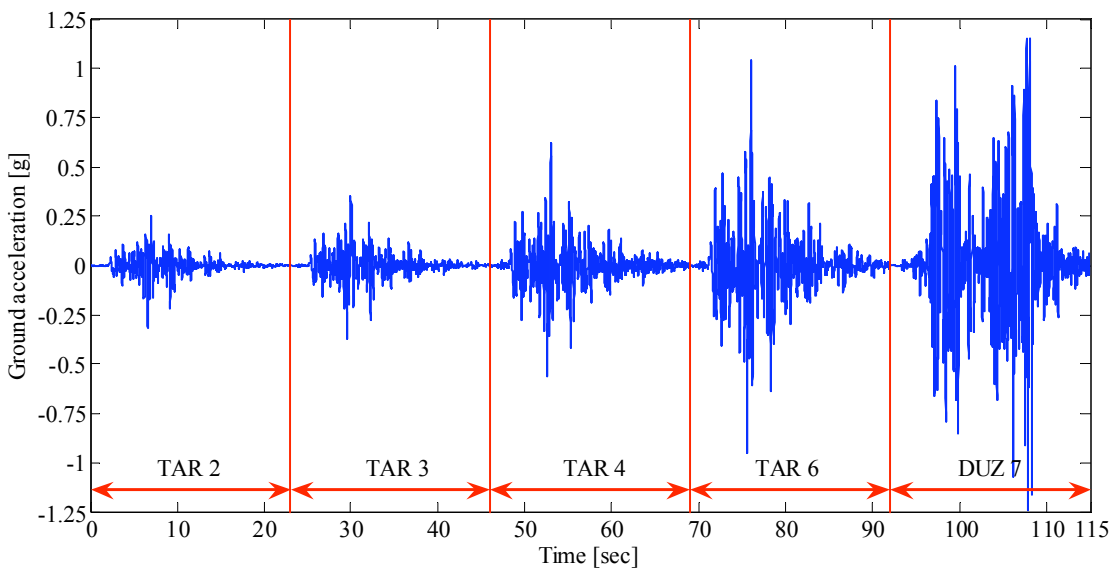


Fig. 7.3 Concatenated input ground (shake-table) motion for simulations.

The analytical model is subjected to the same sequence of ground motions discussed in Chapter 5 from levels TAR 2 to DUZ 7. These ground motions are measured acceleration time-histories recorded at the base of the test-structure during the shake-table experiments and concatenated one after the other as shown in Figure 7.3. As a reference, the time histories of base shear and RC floor slab displacement as observed in the shake-table experiments corresponding to the concatenated ground motions are presented in Figure 7.4. It should be noted that for each test level of this concatenated motion, the small motions at the beginning and end of the record are truncated such that the duration of each ground motion is limited to 23 sec which contains at

least 99.8% of the total energy of the ground motion where this total energy is estimated according to Trifunac and Brady (1975). This is conducted to synchronize recordings for different intensity levels of the same ground motion and to simplify the comparison between results of different runs. In order to include the effects of variation in the damping ratio between the shake-table runs, different damping ratios are adopted at different segments of the analysis to match the energy equivalent damping as discussed in Chapter 6.

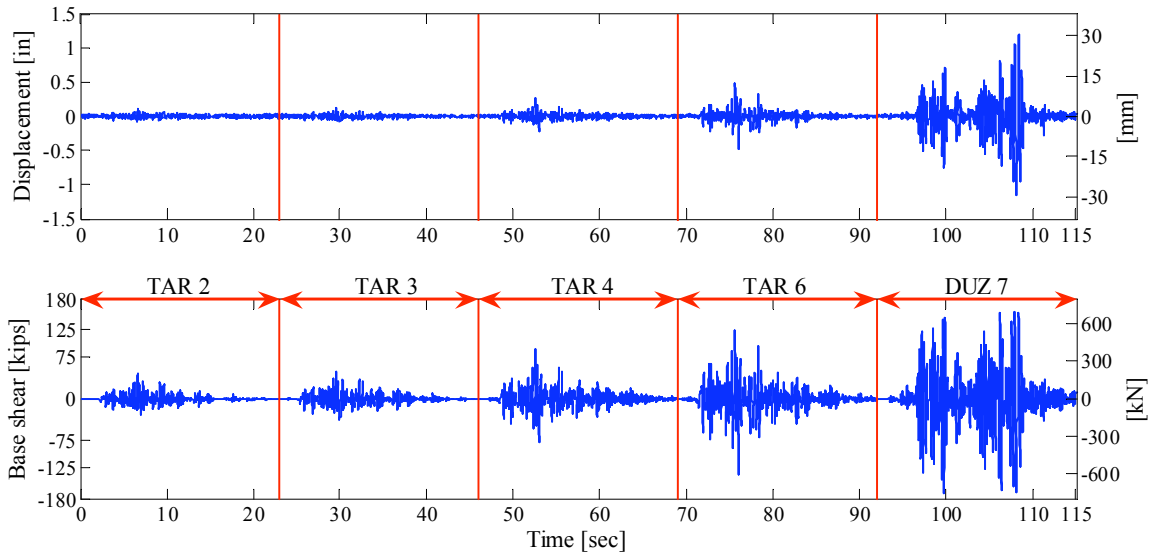


Fig. 7.4 Time-histories of shake-table experimental results.

7.2.3 Single-Strut FEMA Model

The FEMA 356 provisions prescribe a strut with an area equal to the thickness of the masonry infill panel times the strut width a given by Equation 7.3 in consistent units. Note that the term in parenthesis in Equation 7.3 is dimensionless. The modulus of elasticity of the strut material is assumed to be the same as the expected modulus of elasticity of the infill wall material. The expected in-plane shear strength V_{ine} of the URM infill wall is given by Equation 7.4.

$$a = 0.175 (\lambda_1 h_{col})^{-0.4} r_{inf} \quad (7.3)$$

$$V_{ine} = A_{ni} f_{vie} \quad (7.4)$$

where $\lambda_1 = \sqrt[4]{\frac{E_{me} t_{inf} \sin(2\theta)}{4 E_{fe} I_{col} h_{inf}}}$,

h_{col} column height between centerlines of beams,

h_{inf} height of infill wall,

E_{fe} expected modulus of elasticity of frame material,
 E_{me} expected modulus of elasticity of infill wall material,
 I_{col} moment of inertia of columns about the axis perpendicular to the loading direction,
 L_{inf} length of infill panel,
 r_{inf} diagonal length of infill panel,
 t_{inf} thickness of infill panel and equivalent strut,
 θ angle whose tangent is the infill height-to-length aspect ratio,
 A_{ni} area of net mortar/grouted section across infill panel, and
 f_{vie} expected shear strength of masonry infill not to exceed the expected masonry bed-joint shear strength v_{me} as defined in Equation 7.5.

$$v_{me} = 0.75 \left(v_{te} + \frac{P_{CE}}{A_n} \right) \quad (7.5)$$

where v_{te} is the average bed-joint shear strength, P_{CE} is the expected gravity compressive force applied on the URM infill wall, and A_n is the area of net mortared section of the URM infill wall.

For nonlinear analysis, FEMA 356 provisions also provide a maximum nonlinear drift ratio d corresponding to the sudden loss of the lateral strength of the URM infill wall. This drift is defined with respect to the height of the infill h_{inf} for different values of the wall aspect ratio and the frame-to-infill shear strength ratio. The value of the maximum nonlinear drift ratio is used to determine the ultimate strain for masonry material ϵ_{mu} as defined in Figure 7.2.

For the infilled RC frame of the test structure described in Chapter 3, $h_{col} = 108$ in. (2740 mm), $h_{inf} = 101.25$ in. (2570 mm), $E_{fe} = 4250$ ksi (29.3 GPa), $E_{me} = 898$ ksi (6.2 GPa), $I_{col} = 1728$ in⁴ (7.19×10^8 mm⁴), $L_{inf} = 150$ in. (3810 mm), $r_{inf} = 181$ in. (4600 mm), $t_{inf} = 3.75$ in. (95.3 mm), $\theta = 34^\circ$ and $A_{ni} = A_n = a L_{inf} = 562.5$ in.² (3.63×10^5 mm²). Also, $P_{CE} = 41.4$ kips (184 kN) is determined as one half the total gravity loads on the RC slab, including the weight of the RC beams and slab and v_{te} is assumed as 90 psi (620 kPa) resulting in $f_{vie} = v_{me} = 123$ psi (848 kPa) per Equation 7.5. Substituting these values in Equations 7.3 and 7.4, the width of the strut $a = 19.3$ in. (490 mm) and the shear strength $V_{ine} = 69.4$ kips (309 kN) are obtained. Based

on FEMA Table 7-9 for the wall aspect ratio of 1.48 and the frame-to-infill strength ratio of less than 0.7, the maximum nonlinear drift ratio $d = 0.35\%$ is obtained. Using these results, the material and geometric properties of the diagonal strut model, namely the area of the diagonal struts A_{strut} , yield strength of masonry f_{my} and its corresponding strain ϵ_{my} , and the masonry ultimate strain ϵ_{mu} can be determined as shown in Equations 7.6–7.9, respectively.

$$A_{strut} = a t_{inf} \quad (7.6)$$

$$f_{my} = \frac{V_{inf} r_{inf}}{A_{strut} L_{inf}} \quad (7.7)$$

$$\epsilon_{my} = \frac{f_{my}}{E_{me}} \quad (7.8)$$

$$\epsilon_{mu} = d \frac{h_{inf} L_{inf}}{r_{inf}^2} \quad (7.9)$$

By substituting the values obtained before in Equations 7.6–7.9, $A_{strut} = 72.5 \text{ in.}^2$ ($4.68 \times 10^4 \text{ mm}^2$), $f_{my} = 1.16 \text{ ksi}$ (8.00 MPa), $\epsilon_{my} = 0.00129$, and $\epsilon_{mu} = 0.00163$ are determined for the diagonal FEMA strut model.

Adopting the FEMA strut model in the OpenSees model of the test structure defined before, and performing nonlinear time-history analysis, the base shear and RC floor slab displacement time-histories are obtained and presented in Figure 7.5. The computational model shows 0.26 in. (6.6 mm) residual displacement at the end of level DUZ 7 in the test structure that is contradictory to the observed experimental results, as shown in Figure 7.4. The time history of the base shear predicted by the computational model may also be compared to the experimental results in Figure 7.4. The comparison suggests that the computationally predicted base shear agrees well with the experimental results up to level TAR 4, but is underestimated during levels TAR 6 and DUZ 7. The difference between the responses is quantified later in comparison with the results obtained from the calibrated strut model.

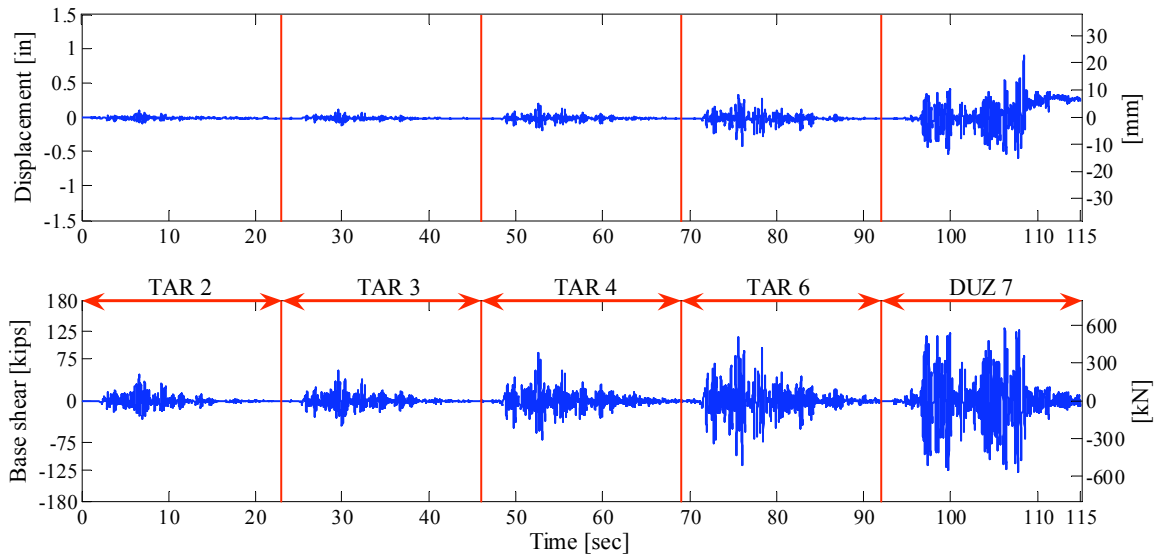


Fig. 7.5 OpenSees simulation results using FEMA strut model.

The results of the computational simulation and the experiments of the test structure in terms of the base shear versus displacement of the RC floor slab relationships are compared in Figures 7.6(a) and (b) for all levels up to DUZ 7. It can be observed that although the FEMA model captures the initial stiffness of the test structure, it underestimates the strength and ductility of the infilled test structure and misrepresents the shape of the global force-deformation plot.

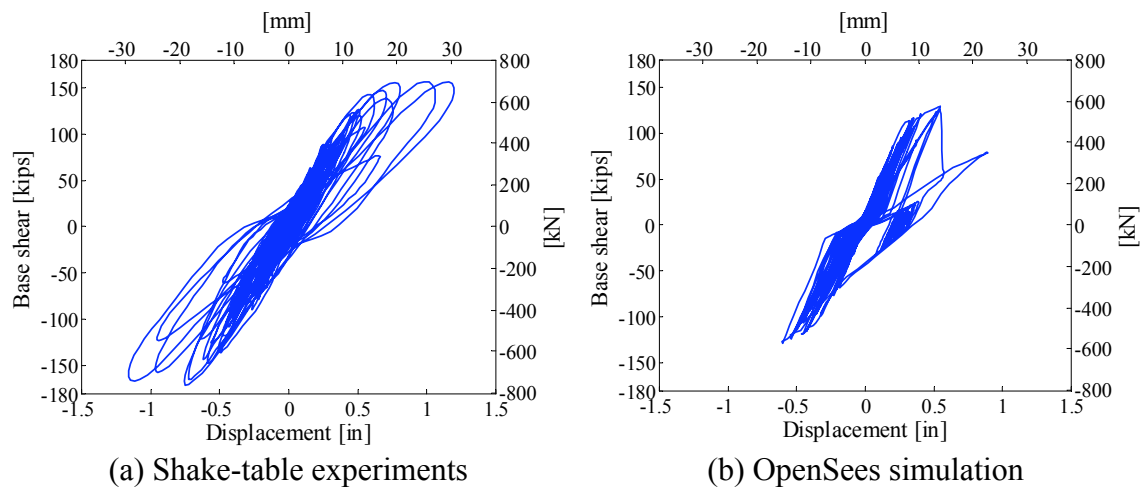


Fig. 7.6 Comparison between plots for base shear versus displacement of RC floor slab from experiments and simulations using FEMA strut model.

7.2.4 Calibrated Single-Strut Model

Due to the unsatisfactory predictions of the FEMA model especially in the nonlinear range of response, an alternative calibrated model is considered with compression material properties, i.e., maximum compressive strength f'_m , as measured in the URM uniaxial compression tests and a parabolic stress-strain curve with linear softening (see the corresponding insert in Fig. 7.2), i.e., $f_{mo} = f'_m = 2.46$ ksi (17.0 MPa). Other parameters of the strut model are calibrated to match the observed stiffness and strength of the shake-table experimental results, i.e., infill wall strength $V_{inf} = 85.0$ kips (378 kN) at corresponding lateral drift $\Delta_y = 0.65$ in. (17 mm). The residual strength of the wall V_{res} and its corresponding lateral displacement Δ_{res} are approximately estimated by observing the shake-table experimental results during levels DUZ 8 and DUZ 7-2 as 10 kips (44 kN) and 0.95 in. (24 mm), respectively. The parameters of the calibrated strut model as shown in Figure 7.2 are determined per Equations 7.10–7.13 as $A_{strut} = 34.6$ in.² (2.23×10^4 mm²), $\epsilon_{mo} = 0.00278$, $f_{mu} = 0.289$ ksi (1.99 MPa) and $\epsilon_{mu} = 0.0041$.

$$A_{strut} = \frac{V_{inf}}{f'_m} \quad (7.10)$$

$$\epsilon_{mo} = \frac{L_{inf}}{r_{inf}^2} \Delta_y \quad (7.11)$$

$$f_{mu} = \frac{V_{res}}{A_{strut}} \quad (7.12)$$

$$\epsilon_{mu} = \frac{L_{inf}}{r_{inf}^2} \Delta_{res} \quad (7.13)$$

where all parameters are as previously defined.

The analysis described above using the FEMA strut is repeated for the OpenSees model of the test structure with the calibrated strut model subjected to the same sequence of loading as depicted in Figure 7.3. The resulting RC floor slab displacement and base shear time-histories of these simulations are shown in Figure 7.7. These results show improved time-history characteristics compared to the results of the FEMA strut model (Fig. 7.5), i.e., no residual displacement at the end of level DUZ 7 consistent with the shake-table experimental results as shown in Figure 7.4 and better estimation of the base-shear time history.

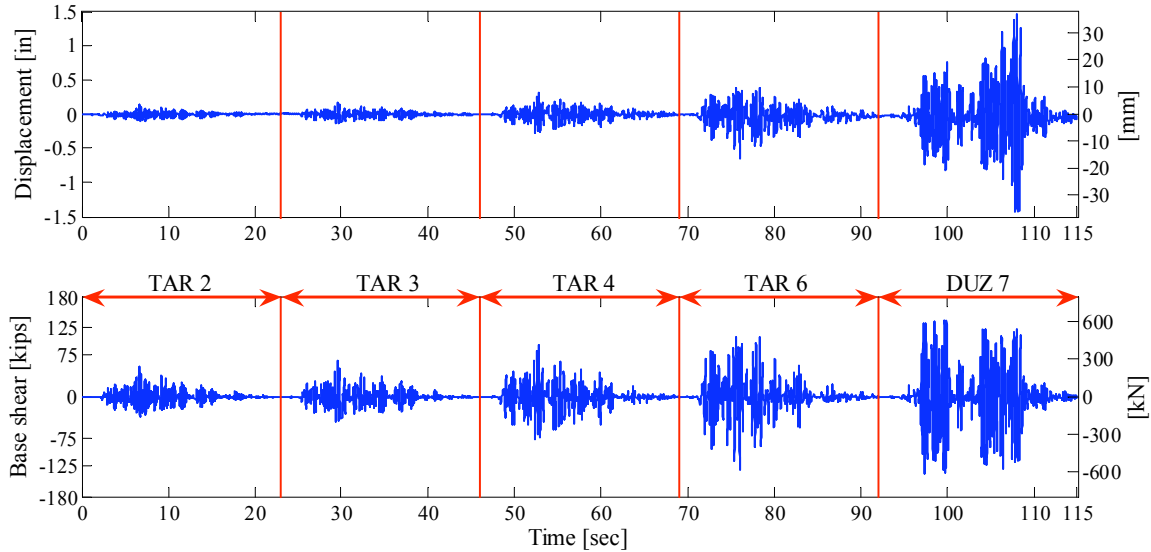


Fig. 7.7 OpenSees simulation results using calibrated strut model.

The outcome of the calibrated strut model is compared with the results of the shake-table experiments. Figures 7.8(a) and (b) present the base shear versus displacement relationship for both the simulations and the experiments. Although there is a clear mismatch between the simulations and experiments, the calibrated strut model represents the key features of the actual response such as the shapes of the loops, tangent stiffness, and peak response values much more convincingly than the FEMA strut model shown in Figure 7.6. Partial time-history plots of the base shear and the RC floor slab displacement during level DUZ 7 of the concatenated ground motion input are also compared with the experiments in Figure 7.8(c). It can be observed that the computational model results follow the results of the shake-table experiments rather closely, especially in terms of the base shear, even at large floor displacement amplitudes.

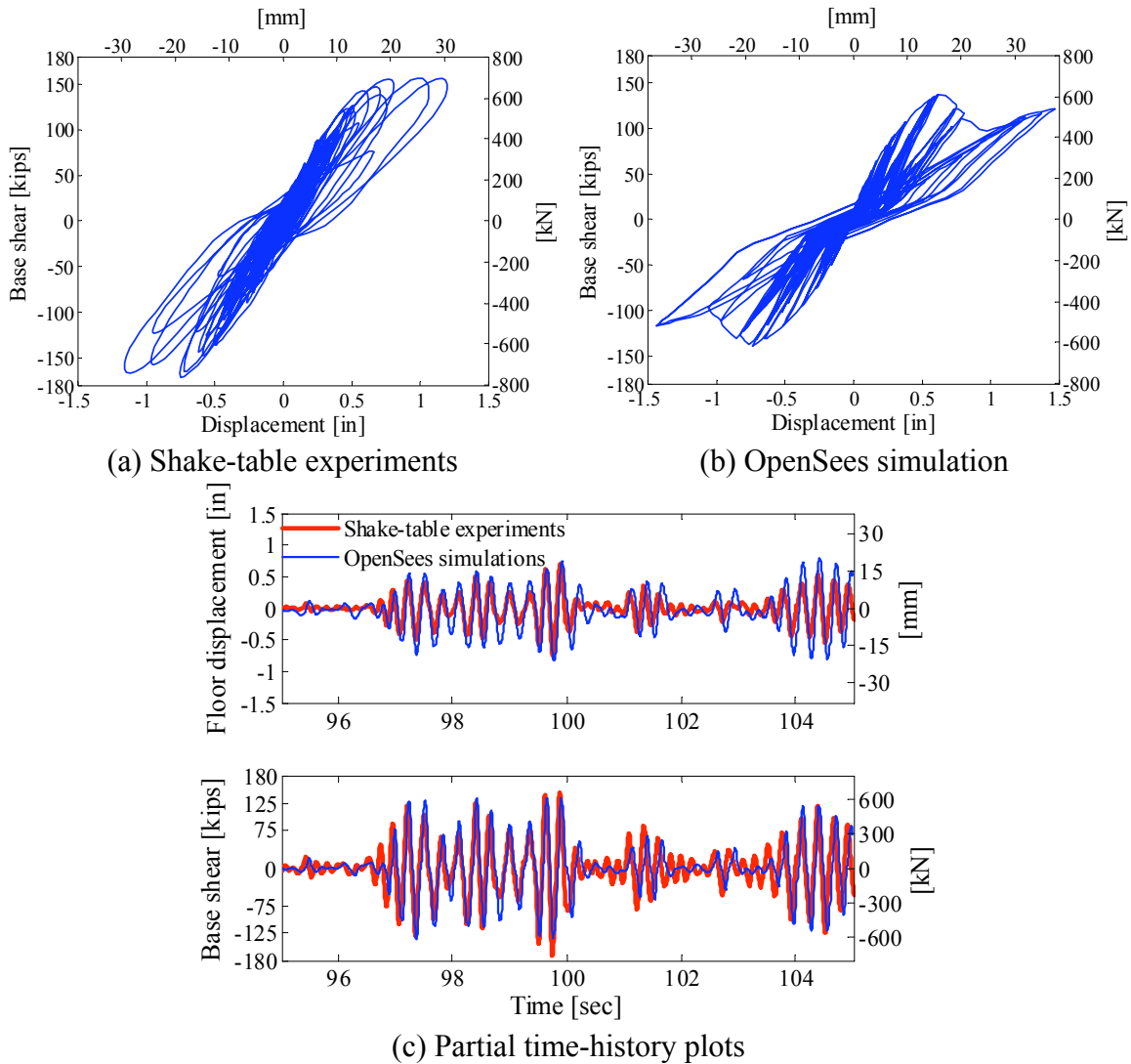


Fig. 7.8 Comparison of plots for base shear versus displacement of RC floor slab from experiments and simulations using calibrated strut model.

7.2.5 Comparison between FEMA and Calibrated Strut Models for URM Infill Wall

The plots of the maximum displacement of the RC floor slab and its corresponding base shear obtained using the computational models of the test structure with FEMA and the calibrated strut models are compared with the results obtained from the shake-table experiments in Figure 7.9. Considering the used simple models with a single strut in each diagonal of the URM infill wall, the OpenSees simulation results with the calibrated strut model are in good agreement with the experimental results. However, the computational model overestimates the peak RC floor slab displacement by 21% and underestimates the corresponding total base shear by 16% at level DUZ 7, leaving the door open for future refinement of the computational model to obtain closer

agreement with the experimental results. This should be contrasted with the prediction of the OpenSees simulations based on the FEMA strut. It is observed that for predicting the maximum demand points in terms of base shear and RC floor slab displacement of the test structure, the results of the FEMA model are acceptable up to level TAR 6. However, after the failure of the compression-only struts, the simulations reflect unconservative values for DUZ 7, underestimating the predicted maximum displacement by 26% and its corresponding base shear by 44%. It should be noted that the underestimation of the base shear in both models and the underestimation of the floor displacement in the FEMA strut model may lead to an unconservative design for the adjacent structural elements. However, the overestimation of the maximum floor displacement by the calibrated strut model would lead to a more conservative design when a deformation-limiting design criterion is considered.

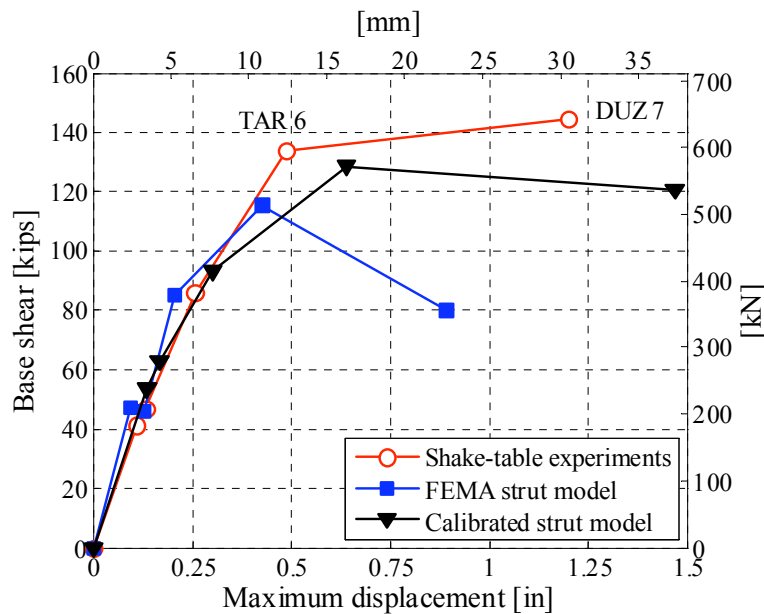


Fig. 7.9 Comparison of results of single-strut models and shake-table experiments.

It should be emphasized that the FEMA strut model constitutes a “blind” prediction of the behavior of the URM infill wall, while the calibrated strut model is defined in light of the experimental results. Both models are simple single-strut models that may serve as examples to show the benefits, e.g., practicality, and limitation, e.g., difficulties in estimating the parameters and the inaccuracies in the results, of this approach. It is suggested that these models should only be used in conjunction with more sophisticated experimental or computational studies to verify the URM infill wall behavior beyond its linear state. The shake-table experimental study in

support of such models is discussed in previous chapters. On the other hand, a detailed computational study using the FE method follows in the next section.

7.3 FINITE ELEMENT MODELS

The goals of this section are the development of a FE model of the test structure with URM infill wall and the verification of the accuracy of this FE model by comparing its results to those of the experiments. The models are generated and analyzed using the general-purpose FE software DIANA (2005). Benefiting from the results of the pseudo-dynamic experiments (Fig. 7.10) on the bare and the infilled frames as physical substructures of a structure identical to the shake-table test structure (Elkhoraibi and Mosalam 2007b), a two-dimensional (2D) FE model of the bare RC frame tested pseudo-dynamically is constructed and validated. Subsequently, the validated 2D FE model of the bare RC frame is extended to include the effect of the continuum URM infill wall, and the accuracy of the FE model of this infilled RC frame is again validated using the pseudo-dynamic experimental results. This process of developing and validating the computational FE model using the pseudo-dynamic experiments is justified based on the fact that the applied lateral displacement versus the resisting force history of the bare and infilled RC frames are directly available from the pseudo-dynamic test results. The 2D FE models are used to properly and effectively select the FE mesh size, material constitutive models, and boundary conditions to subsequently construct a representative three-dimensional (3D) model of the shake-table test structure without the need of several expensive runs to select these numerical parameters. In other words, the 2D models are used as the building blocks in developing the 3D FE model of the shake-table test structure. The 3D FE model is subjected to the same sequence of loading as the test structure in the shake-table experiments and the resulting base shear and RC floor slab displacement are compared with the experimental findings from the shake-table experiments. These validated FE models serve as means to perform further numerical simulations for investigating certain issues and parameters not included in the experimental study described in the previous chapters, such as the out-of-plane behavior of URM infill walls and the development of in-plane/out-of-plane failure surface for URM infill walls.

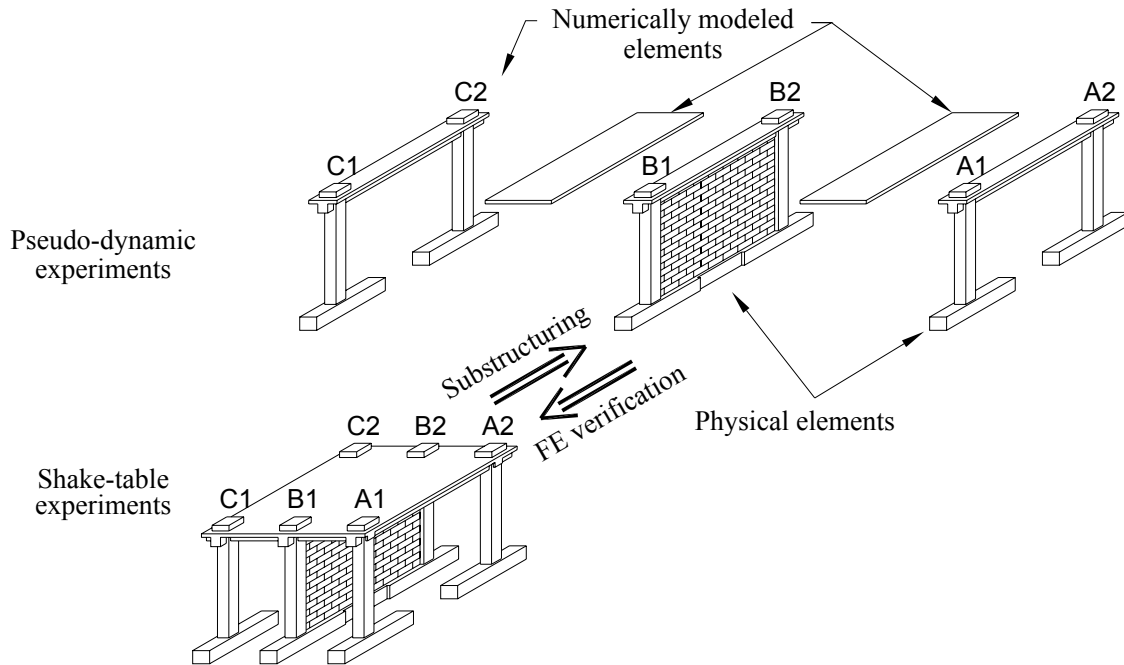


Fig. 7.10 Shake-table and pseudo-dynamic test structures used for verifying FE models.

7.3.1 FE Model of Bare RC Frame

First, discussed is the 2D FE model of the bare RC frame, frame A1-A2 in Figure 7.10. The beam and columns are modeled using 9 degrees of freedom 3-node 2D beam elements with 35 Gaussian integration points, i.e., 5 points at 7 cross sections along the length of each element. The beam and each column are divided into 5 and 8 elements, respectively. Longitudinal reinforcing steel bars are embedded in the beam and column elements at their exact locations, and perfect bond with the surrounding concrete is assumed. The prestressing bars are modeled using truss elements with geometrical nonlinearity and unbonded to the column elements to account for the re-centering effects of these bars, discussed in Section 6.4.3.3. Since beam elements are used to represent the RC beam and columns, the transverse reinforcements are neglected and no effort is made to adjust the concrete properties to match the confined concrete properties. This simplification is justified because the comparison with the experimental results are performed up to the levels at which no significant spalling is experimentally observed in the RC frames, i.e., up to level DUZ 7. Column bases are assumed to be fixed and no relative rotation at the beam-column joint is considered, i.e., beam-column joints are assumed rigid in the FE models. The element numbering and reinforcing bar arrangements for the model are shown in Figures 7.11 (a) and (b), respectively.

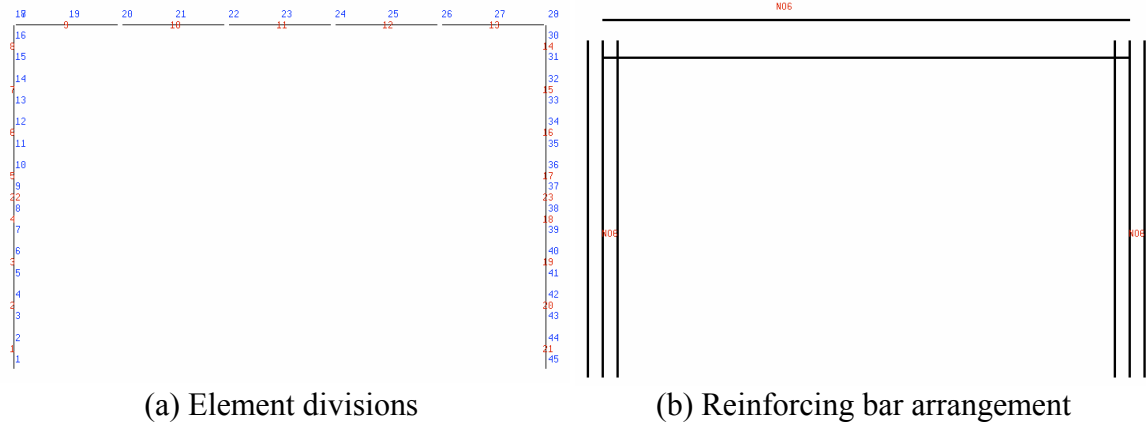


Fig. 7.11 FE model of bare RC frame.

Concrete material is modeled using a total strain rotating crack model (DIANA 2005) that describes the tensile and compressive behavior using one stress-strain relationship. The concrete in compression is defined using a parabolic stress-strain ($\sigma - \varepsilon$) relationship as shown in Figure 7.12(a) and defined by Equations 7.14–7.17. Numerical values of the parameters for the concrete compression material model are presented in Table 7.3. The tensile behavior of concrete is modeled using elastic with a linear softening relationship as shown in Figure 7.12(b) where f_{ct} is the tensile strength of concrete as determined in concrete split tension tests per Table 4.3, G_f^I is the fracture energy for mode I (opening mode) fracture, and h_t is the crack bandwidth over which the crack is smeared or distributed in the finite element and is taken as the length of the FE divided by the number of Gaussian integration points. The value of G_f^I is estimated per CEB-FIP (1990) in units of N/m as $G_f = \alpha_d f_{ck}^{0.7}$ where $\alpha_d = 6.75$ is a coefficient related to the maximum aggregate size and f_{ck} is the characteristic strength in units of MPa taken the same as f_{ct} in this study. Numerical values of the parameters for the concrete tension material model are presented in Table 7.4.

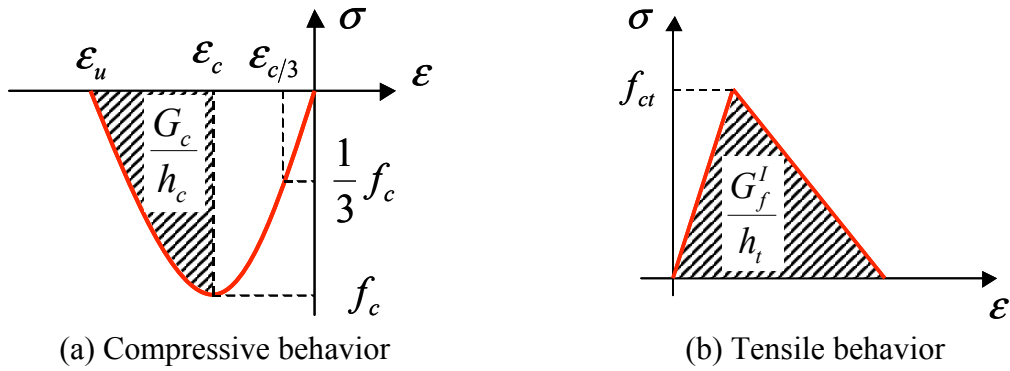


Fig. 7.12 Concrete material model for FE analysis.

$$\sigma = \begin{cases} \frac{f_c}{3} \frac{\epsilon}{\epsilon_{c/3}} & \text{if } 0 \geq \epsilon > \epsilon_{c/3} \\ \frac{f_c}{3} \left(1 + 4 \left(\frac{\epsilon - \epsilon_{c/3}}{\epsilon_c - \epsilon_{c/3}} \right) - 2 \left(\frac{\epsilon - \epsilon_{c/3}}{\epsilon_c - \epsilon_{c/3}} \right)^2 \right) & \text{if } \epsilon_{c/3} \geq \epsilon > \epsilon_c \\ f_c \left(1 - \left(\frac{\epsilon - \epsilon_c}{\epsilon_u - \epsilon_c} \right)^2 \right) & \text{if } \epsilon_c \geq \epsilon > \epsilon_u \\ 0 & \text{if } \epsilon_u \geq \epsilon \end{cases} \quad (7.14)$$

$$\epsilon_{c/3} = \frac{1}{3} \frac{f_c}{E_c} \quad (7.15)$$

$$\epsilon_c = \frac{4}{3} \frac{f_c}{E_c} = 4 \epsilon_{c/3} \quad (7.16)$$

$$\epsilon_u = \epsilon_c + \frac{3}{2} \frac{G_c}{h_c f_c} \quad (7.17)$$

where

f_c the maximum compressive (negative) strength based on uniaxial concrete compression test results for columns per Table 4.1;

E_c the initial modulus of elasticity of the concrete in compression estimated in units of psi as

$E_c = 57000 \sqrt{f'_c}$ with $f'_c = |f_c|$ as defined above;

$\epsilon_{c/3}$ the strain at which 1/3 of the maximum compressive strength is reached;

ϵ_c the strain at which the maximum compressive strength is reached;

ϵ_u the ultimate strain in compression at which the material has no strength;

G_c the fracture energy in compression determined to be consistent with the assumed value for ϵ_u per Table 7.3; and

h_c the characteristic element length related to the size of the test specimen which is used to determine the material properties.

Table 7.3 Parameters for concrete compression material model.

f_c [ksi (MPa)]	$\epsilon_{c/3}$	ϵ_c	ϵ_u	G_c [kips/in. (kN/mm)]	h_c [in. (mm)]
-5.39 (37.2)	-4.28×10^{-4}	-1.71×10^{-3}	-0.020	0.789 (0.138)	12.0 (305)

Table 7.4 Parameters for concrete tension material model.

f_{tc} [ksi (MPa)]	G_f^I [kips/in. (kN/mm)]	h_t [in. (mm)]
0.429 (2.96)	8.22×10^{-5} (1.43×10^{-5})	2.0 (51)

Reinforcing steel material is modeled using the Von Mises yield criterion with yield stress σ_y and isotropic hardening with hardening modulus estimated as 1% of the steel initial modulus of elasticity E_s . The high-strength steel for the post-tensioning rods is modeled using an elastic-perfectly-plastic model with yield stress σ_{ps} and initial modulus of elasticity E_{ps} . Numerical values of the parameters for the reinforcing steel and post-tensioning steel material models are defined from the data reported in the reinforcing bars mill certificate tests and the high-strength rod manufacturer certifications as presented in Table 7.5.

Table 7.5 Parameters for reinforcing steel material model.

σ_y [ksi (MPa)]	E_s [ksi (GPa)]	σ_{ps} [ksi (MPa)]	E_{ps} [ksi (GPa)]
66.5 (458)	29000 (200)	150 (1034)	27000 (186)

The FE model of the bare RC frame described above is subjected to the displacement history obtained from the pseudo-dynamic experiments, applied by a displacement-controlled hydraulic actuator, at the centerline of the beam. The resisting reaction from the FE model is compared to the resisting force recorded by the load cell attached to the hydraulic actuator during different levels of the pseudo-dynamic experiments. It is to be noted that the same shaking levels of the shake-table experiments are used for the pseudo-dynamic experiments. The resulting pseudo-time histories of the resisting force for levels TAR 2, TAR 4, TAR 6, and DUZ 7 are shown in Figures 7.13(a)–(d), respectively. The maximum displacement versus its corresponding base-shear plot for these levels is presented in Figure 7.14. The excellent agreement (only 3% error in predicting the maximum base shear in level DUZ 7) between the experimental and FE results confirms that the FE model of the bare RC frame very well represents the physical specimen. The 20times-exaggerated deformed shape of the FE model corresponding to the maximum deformation during level DUZ 7 is shown in Figure 7.15 reflecting the expected predominantly bending deformations of the bare RC frame.

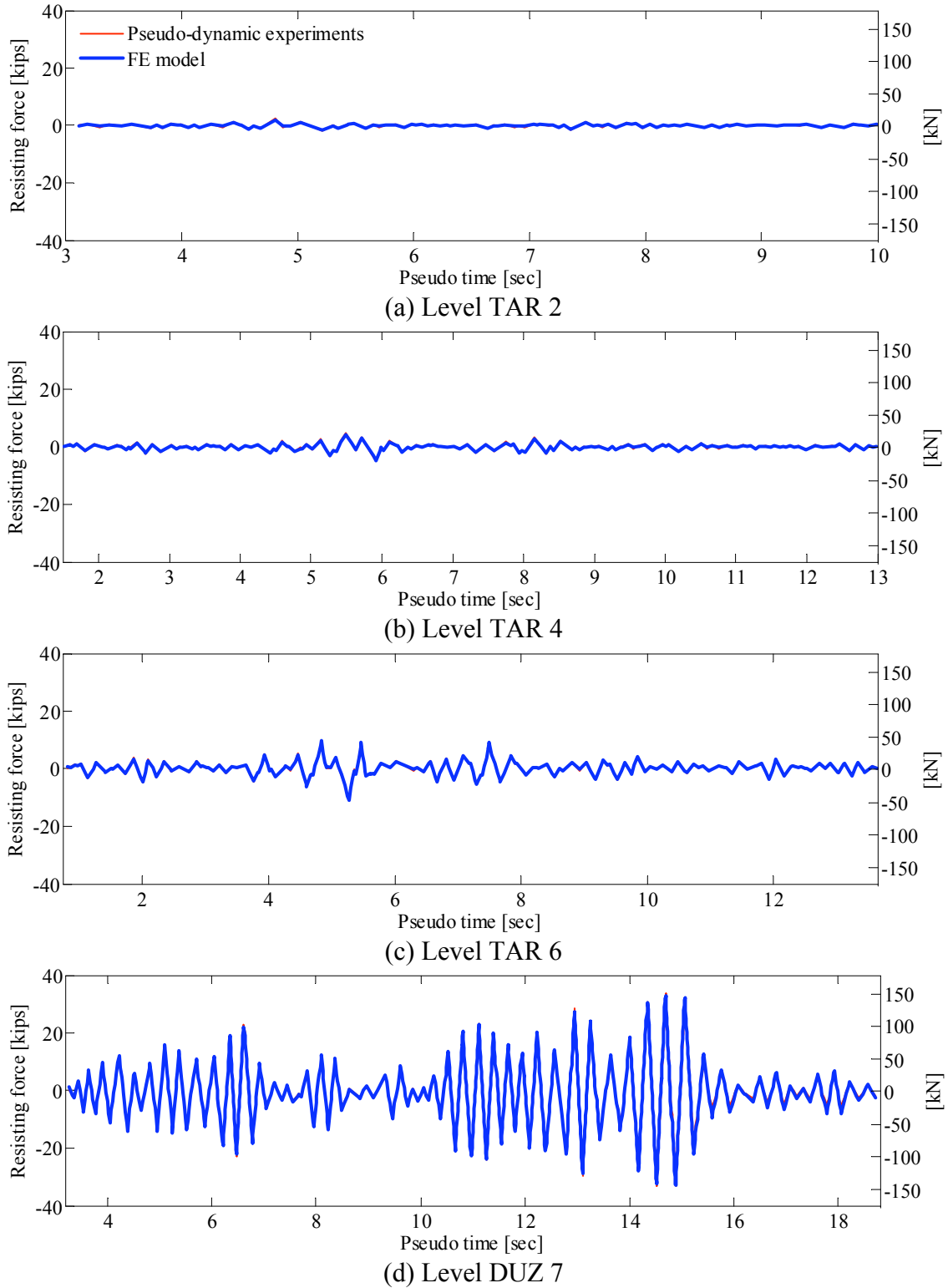


Fig. 7.13 Comparison of results of FE model and pseudo-dynamic experiments for bare RC frame.

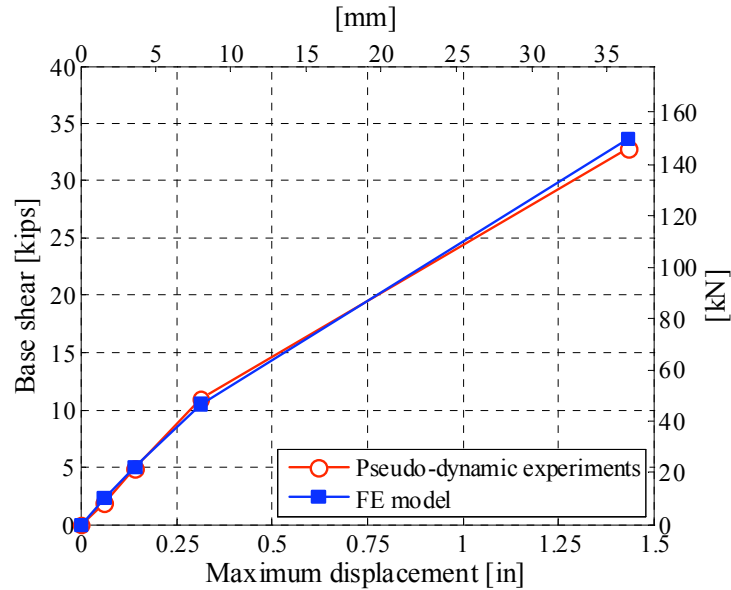


Fig. 7.14 Comparison of peak results of FE model and pseudo-dynamic experimental results for bare RC frame.

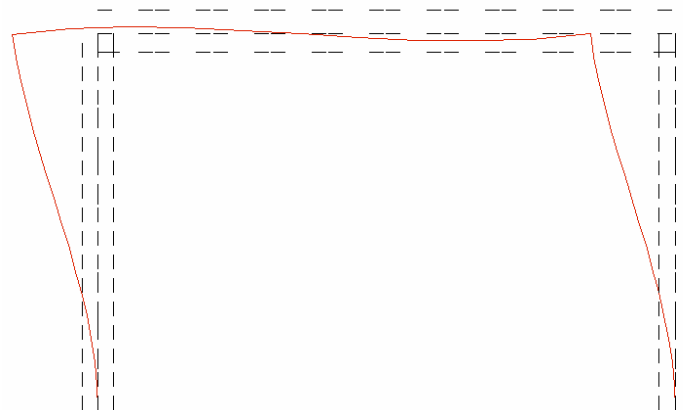
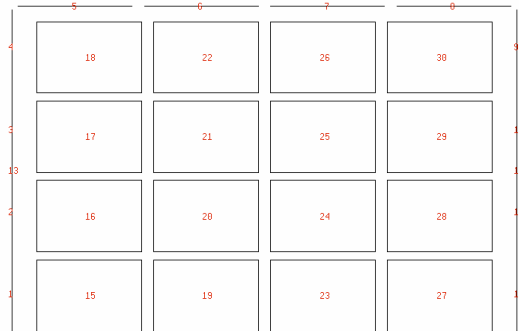


Fig. 7.15 Deformed shape of bare RC frame at maximum deformation during level DUZ 7.

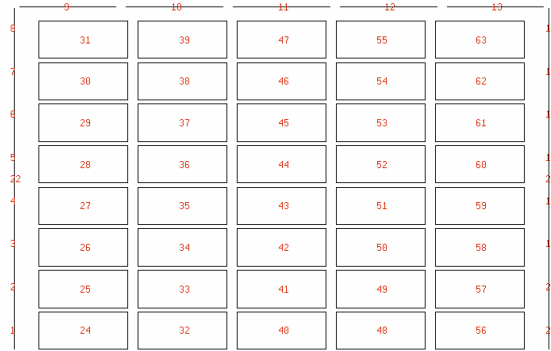
7.3.2 FE Model of Infilled RC Frame

The next step is to build upon the FE model of the bare RC frame and add the URM infill wall to obtain the FE model of the infilled RC frame. The URM infill wall is modeled using 8-node quadrilateral shell elements with 20 Gaussian integration points, i.e., 5 points through the thickness of each shell element in a 2×2 numerical integration method in the plane of the element. Two-dimensional, 6-node line-interface elements are used to model the interface between the URM infill wall and the beam and column elements with the 3-point Lobatto

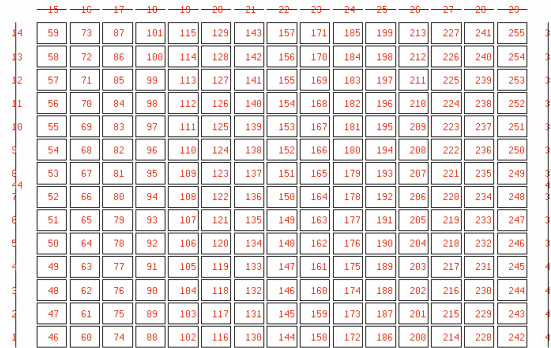
integration scheme (Diana 2005). In order to determine a manageable yet reliable mesh size for the FE model of the URM infill wall, three FE models with coarse, fine, and very fine mesh are considered as shown in Figures 7.16(a)–(c), respectively.



(a) Coarse wall mesh



(b) Fine wall mesh



(c) Very fine wall mesh

Fig. 7.16 FE models of URM infilled RC frame.

The material model for the URM is considered as linear-brittle in tension and elastic-plastic in compression as shown in Figure 7.17 with total strain rotating crack model (DIANA 2005). This model describes the tensile and compressive behavior of the material with one stress-strain relationship evaluated in the principal directions of the strain vector. In order to include the effects of lateral cracking, the peak compressive stress of masonry is reduced by the factor $\beta_{\sigma_{cr}}$

related to the resultant lateral crack strain $\epsilon_{lat} = \sqrt{\epsilon_{l,1}^2 + \epsilon_{l,2}^2}$ where $\epsilon_{l,1}$ and $\epsilon_{l,2}$ are the crack strains in the two lateral directions orthogonal to the direction of principal compression strain according to (Vecchio et al. 1993). Basic material properties for the URM material model are determined based on the uniaxial compression test results for masonry prisms and masonry bending tests discussed in Sections 4.1.3 and 4.1.5, respectively, and are presented in Table 7.6.

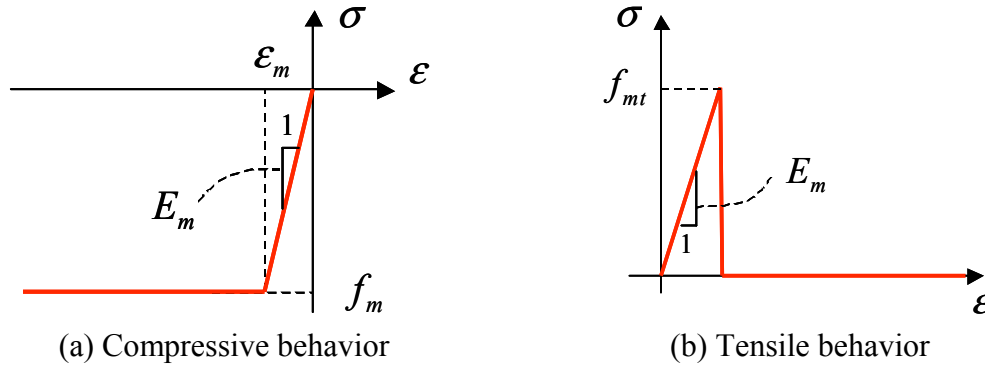


Fig. 7.17 Masonry material model for FE analysis.

Table 7.6 Parameters for URM material model.

f_m [ksi (MPa)]	$\epsilon_m = f_m/E_m$	Poisson ratio	f_{mt} [psi (kPa)]
-2.46 (17.0)	-0.00274	0.15	69 (476)

The interface elements are assumed as linear elastic with very high stiffness (10^4 kips/in. (1.75×10^3 kN/mm)) in compression and with a discrete cracking model (DIANA 2005) in tension with zero tensile strength and stiffness after cracking. The interface elements allow sliding with a small initial shear stiffness (10 lb/in. (1.75 N/mm)) for numerical stability, which is reduced to zero upon cracking.

For the three models with different mesh sizes (Fig. 7.16), in-plane pushover analyses are performed and the results are compared in Figure 7.18. It is observed that the coarse mesh fails to capture the sudden failure of the URM wall observed in the other two models with fine and very fine meshes. Considering the significant benefit of having fewer elements in performing detailed FE analyses and the close results obtained from the two fine and very fine mesh models, the FE model with fine mesh is deemed adequate. Therefore, all FE analyses described in the rest of this chapter are based upon the model shown in 7.16(b).

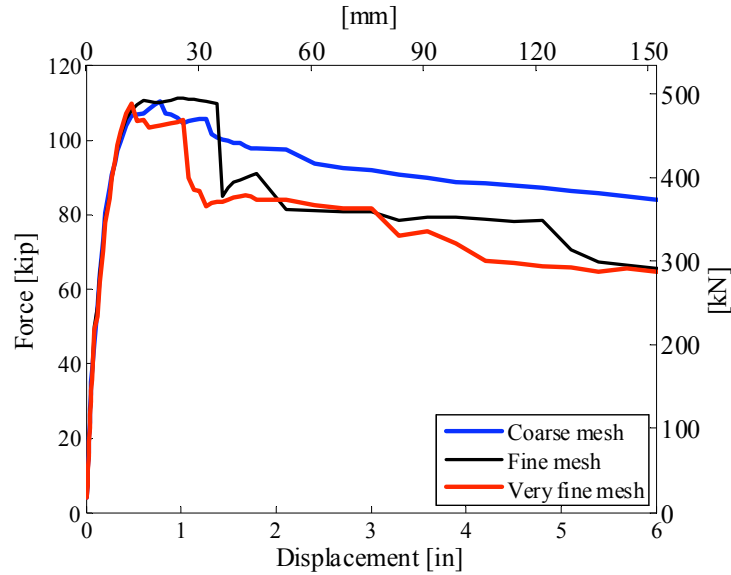


Fig. 7.18 Pushover curves for FE models of URM infilled RC frame.

Similar to the bare RC frame, the URM infilled RC frame model is also validated by comparing the results from the FE analyses with those from the pseudo-dynamic experiments. The input of the FE model is the displacement command applied statically by the hydraulic actuator at each pseudo-time step during different levels of the pseudo-dynamic experiments; the resisting forces from the FE model and the experiment are compared. The resulting pseudo-time histories of the resisting forces for levels TAR 2, TAR 4, TAR 6, and DUZ 7 are shown in Figures 7.19(a)–(d), respectively. The time-history plots of the base shear obtained from the FE model are in good agreement with the pseudo-dynamic test results through all runs. The maximum displacement versus maximum base-shear plot for these levels is presented in Figure 7.20. The FE model overestimates the base shear by a maximum error of 13% during levels TAR 2 to TAR 6 and slightly underestimates the base shear during level DUZ 7 by only 2% compared to the pseudo-dynamic test results.

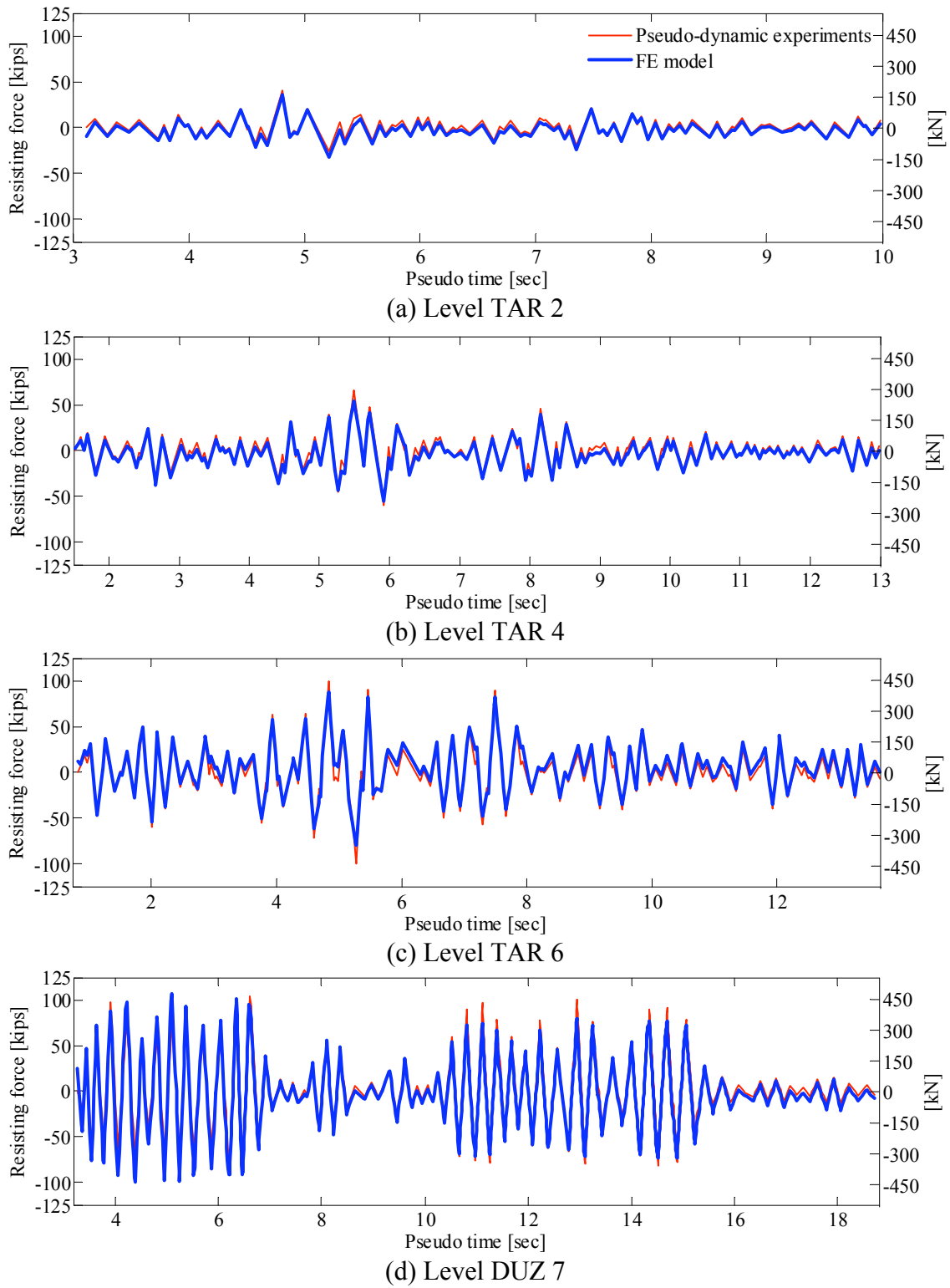


Fig. 7.19 Comparison of results of FE model and pseudo-dynamic experiments for URM infilled RC frame.

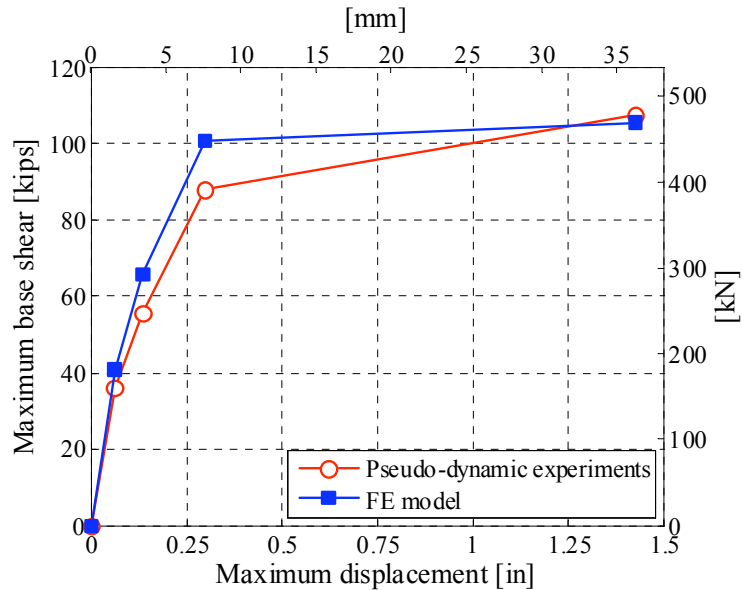


Fig. 7.20 Comparison of peak results of FE model and pseudo-dynamic experimental results for URM infilled RC frame.

Besides investigating the resisting force of the FE model of the URM infilled RC frame, an in-plane pushover analysis of the frame is performed and for different points on the pushover curve the failure mechanisms for the URM infill wall are discussed and compared with the final failure observed in the pseudo-dynamic experiments. The pushover curve is obtained by applying a monotonically increasing in-plane displacement at the centerline of the beam and recording the resulting resisting force in the URM infilled RC frame (Fig. 7.21). The maximum force calculated in the pushover analysis is 111 kips (494 kN) at 0.96 in. (24.4 mm) lateral displacement. The failure of the URM wall is predicted at 1.44 in. (35.3 mm) corresponding to about 77% of the maximum resisting force.

For the points marked with open squares on the pushover curve (Fig. 7.21), contours of principal compression stress, crack openings, and line contours of horizontal displacement on the URM infill wall are shown in Table 7.7. From the stress contours, the load path in the URM infill wall can be observed as the lateral displacement increases. At the RC floor lateral displacement of 0.12 in. (3.0 mm), the lateral load is mainly resisted diagonally with a compression stress concentration at opposite frame joints. At the RC floor lateral displacement of 1.14 in. (29.0 mm), where the maximum strength of the URM infill wall is reached, two distinct load paths (struts) are observed, one from the right beam-column joint to about one third height of the left column from the bottom and the other from about one third height of the right column

from the top to the left column-footing joint. At the RC floor lateral displacement of 1.44 in. (36.6 mm), the failure of the URM infill wall along the top load path (strut) is detected, while the lower load path continues to carry more lateral load. At this point the wall is considered as a short wall within the frame, and reinforcing steel yielding and concrete crack openings are predicted in the RC columns. With the failure of the lower path (strut) at RC floor lateral displacement of 1.80 in. (45.7 mm), the load-carrying capacity of the wall is exhausted and the RC frame deforms in bending as the lateral displacement increases up to the last analyzed point at 6.60 in. (167.6 mm). The crack opening plots for cracks with normal-to-crack strain of more than 0.002 are also shown for the five points mentioned above in the third column of Table 7.7. Each crack demonstrates the load path and the direction of the principal compression strain in the wall. As the lateral displacement increases and the wall fails, the cracks spread in the wall and their orientation changes due to the redistribution of forces in the wall. The horizontal line-contour plots help to observe the relative sliding occurring in the wall. Where the contour lines come together, they show concentration of relative lateral displacement, i.e., planes of long horizontal cracks in the wall. The locations and arrangement of these horizontal cracks are comparable with those observed at the completion of the pseudo-dynamic experiments as shown in Figure 7.22.

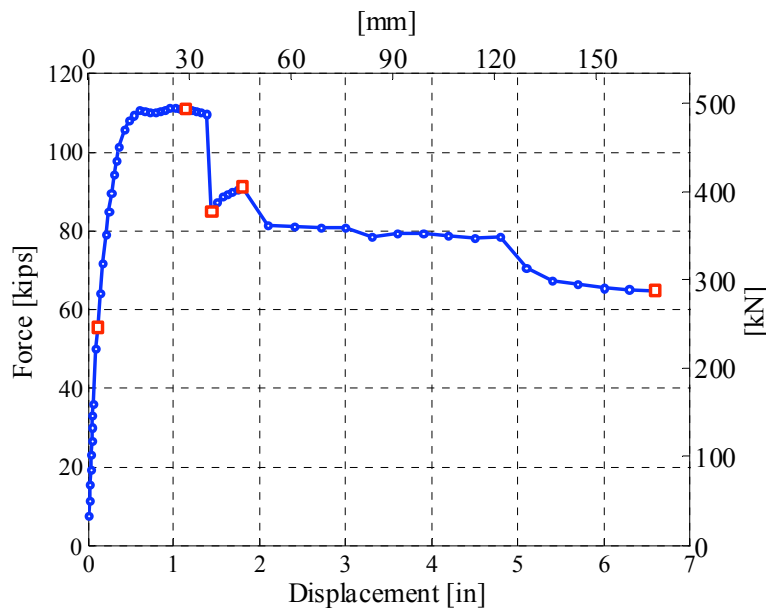
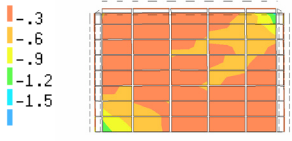
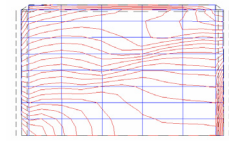
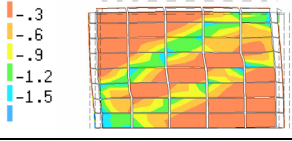
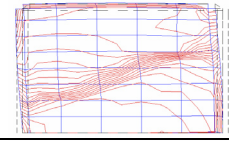
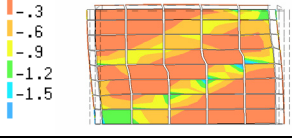
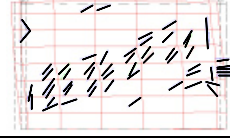
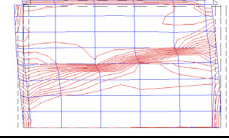
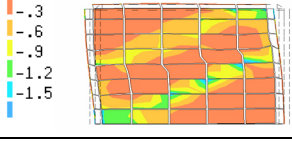
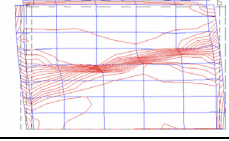
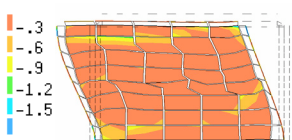
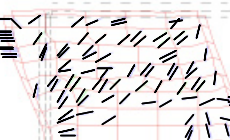
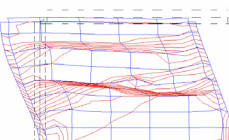


Fig. 7.21 Pushover analysis for FE model of RC frame with URM infill wall.

Table 7.7 Progression of damage in URM infilled RC frame during pushover analysis using FE model (1 ksi = 6.895 MPa).

RC floor lateral disp. [in. (mm)]	In-plane principal compression stress (ksi)	Crack openings (crack strain larger than 0.002)	Contours of horizontal displacement in infill wall	Remarks
0.12 (3.0)				Onset of cracking
1.14 (29.0)				Maximum strength, off-diagonal strut formation
1.44 (36.6)				Top strut fails, horizontal crack openings and sliding
1.80 (45.7)				Onset of second off-diagonal strut failure
6.60 (167.6)				Complete failure, a new sliding plane forms at the top.

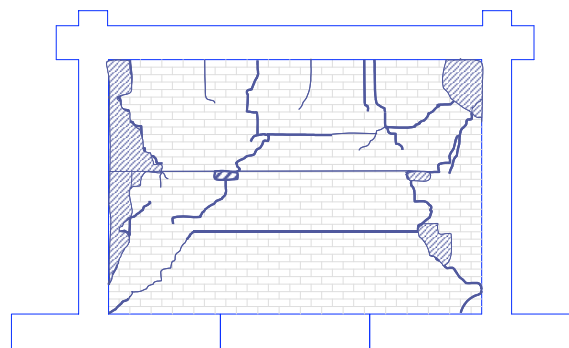


Fig. 7.22 Final crack pattern observed during pseudo-dynamic experiments.

7.3.3 Static and Modal FE Modeling of Shake-Table Test Structure

The agreements shown between the pseudo-dynamic experimental and FE results discussed above raise confidence in the methodology used to represent the RC frame with URM infill wall. The next step is to extend the 2D models of the bare and infilled RC frames to a 3D model and to add the RC slab and short direction beams to generate the FE model of the shake-table test structure as shown in Figure 7.23. The bases of the columns are assumed fixed in all directions and there are no relative rotations at the beam-column joints. The out-of-plane translational degrees of freedom at the base and top of the infill wall are constrained by slaving them to the adjacent beam and column elements. The material properties for the beam and column concrete, the URM infill wall, and the interface elements used in the 3D model are as described before for the 2D models. The beams in the short direction are modeled with the same element type and material properties as the frame beams. The RC slab is modeled using 8-node quadrilateral shell elements with the same integration scheme as that used in the elements of the shell elements representing the infill wall as discussed above. Since the RC slab is expected to remain elastic when subjected to the lateral loads, the concrete material is modeled as elastic in compression with modulus of elasticity of 4200 ksi (29.0 GPa) and linear brittle in tension with tensile strength of 430 psi (2.96 MPa). These assumptions are made for simplicity of the model and efficiency of the numerical solution. The reinforcing steel in the slab is also modeled as elastic with modulus of elasticity of 29000 ksi (200 GPa). For accurate modeling of the gravity and inertial forces, the unit mass of the RC slab is adjusted to account for the self-weight and the 72.0 kip (320 kN) additional weight on the test structure.

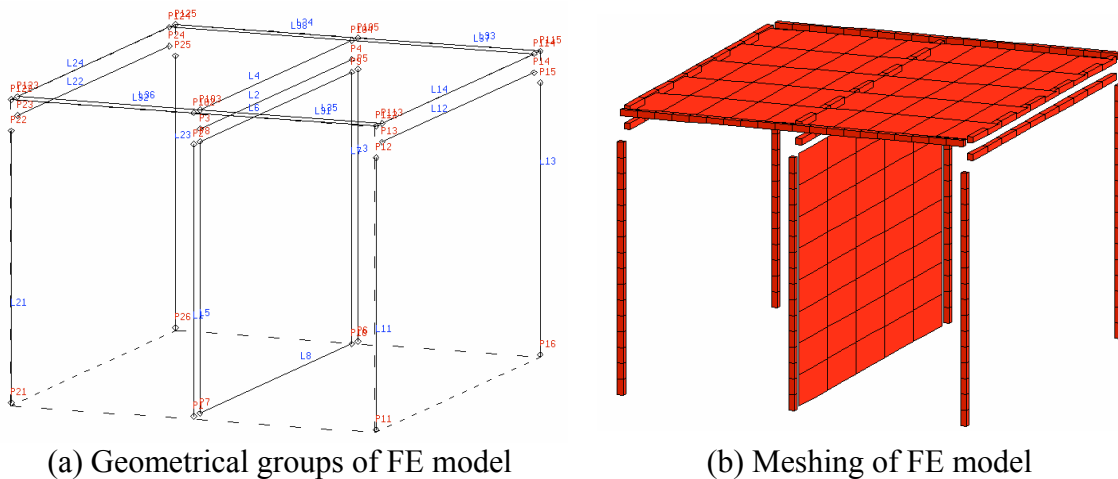
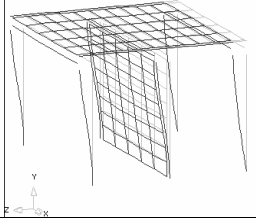
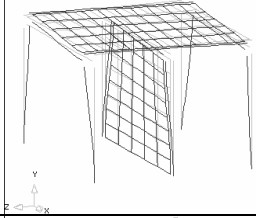
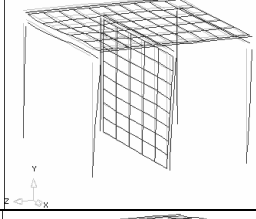
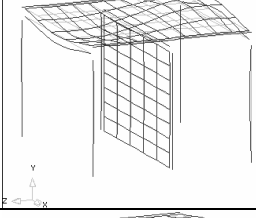
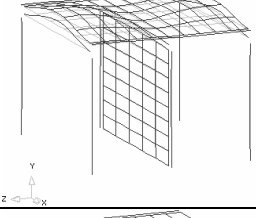
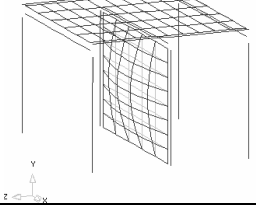


Fig. 7.23 Three-dimensional FE model of shake-table test structure.

Using the described FE model, the first six mode shapes of the test structure are determined and presented in Table 7.8. Comparisons between the first and third mode (out-of-plane and in-plane sway) natural periods of the FE model with the out-of-plane (0.232 sec) and in-plane (0.134 sec) natural periods of the test structure determined by the snap-back tests, and described in Chapter 4, reveal that the FE modal analysis overestimates the stiffness of the test structure, resulting in lower natural periods by 32% and 36% for the natural periods in the out-of-plane and in-plane directions, respectively. The reason is attributed to the existing shrinkage cracks in the concrete and masonry material in the test structure that are not considered in the numerical modal analysis of the FE model. This discrepancy, however, would not affect the lateral response of the FE model, since when subjected to small lateral loads, the cracks in the concrete and masonry materials are initiated according to the stress distribution in the FE model resulting in reduced stiffness and more realistic response, as discussed later.

The results of a pushover analysis of the 3D model are presented in Figure 7.24. The analysis is performed statically and monotonically by applying a gradually increasing lateral displacement through a support defined at the centerline of the beam in the infilled frame and monitoring the total base shear of the structure as the reaction force on this support. Although the lateral displacement is only applied to the middle frame, differential displacement is not observed between the three RC frames, since the RC slab is practically rigid in its own plane when compared to the RC frames (more than 50 times stiffer). The maximum base shear resisted by the FE model of the test structure is 197 kips (876 kN) at lateral displacement of 1.05 in. (26.7 mm). The maximum base shear for the 3D FE model is 77% higher than the results obtained for the 2D FE model of the infilled RC frame due to the contribution of the two bare RC frames in the 3D model. Compared to the results obtained from the shake-table experiments, the FE results of the maximum base shear and its corresponding lateral displacement are respectively 18% and 52% higher than the results obtained from the shake-table experiments. This discrepancy is attributed to the expected differences between monotonic versus cyclic loading and static versus dynamic excitations. Because of these reasons, it is expected that both the lateral force capacity and the corresponding lateral displacement of the test structure are overestimated in the pushover analysis. This overestimation is quantified later by comparing the results of the FE transient time-history analyses with the monotonic pushover results.

Table 7.8 Mode shapes and natural frequencies and periods of 3D FE model of test structure.

Mode	Description	Natural frequency (Hz)	Natural period (sec)	Mode shape
1	Out-of-plane sway	6.35	0.157	
2	In-plane rotation of RC slab with torsional deformation of structure	9.24	0.108	
3	In-plane sway	11.60	0.086	
4	Out-of-plane asymmetric bending of RC slab	15.50	0.065	
5	Out-of-plane symmetric bending of RC slab	17.30	0.058	
6	Out-of-plane bending of URM infill wall	18.60	0.054	

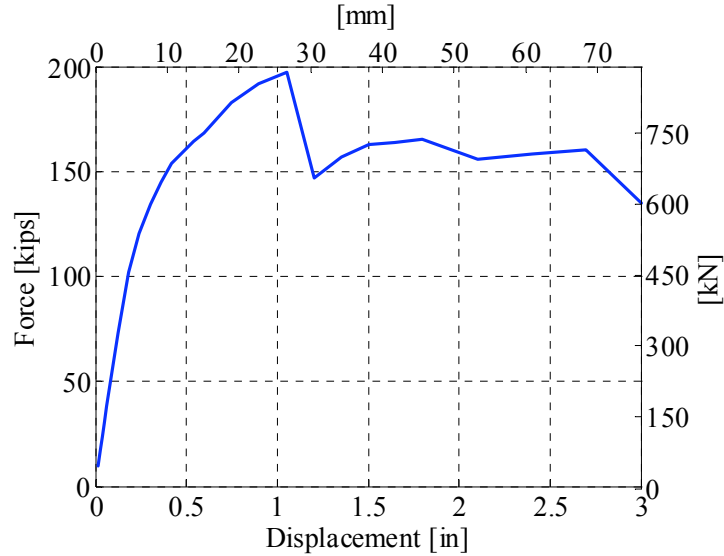


Fig. 7.24 Monotonic pushover curve for 3D FE model of test structure.

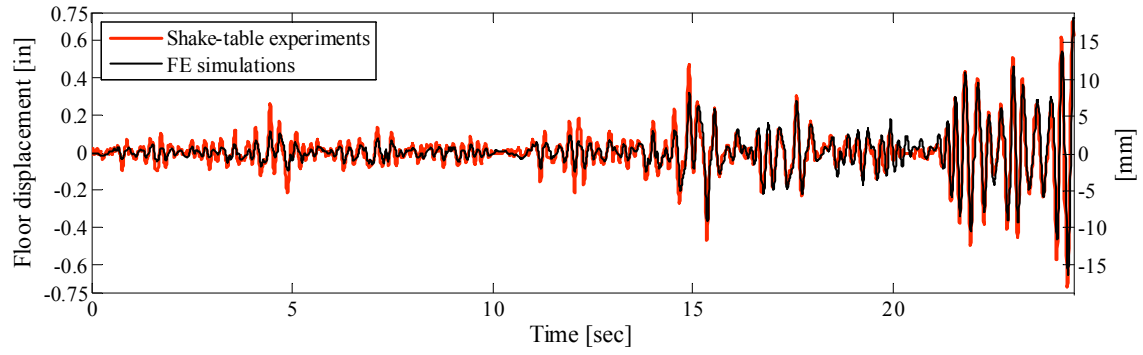
7.3.4 Dynamic FE Modeling of Shake-Table Test Structure

The 3D FE model of the test structure is subjected to the acceleration time history measured at the top of the shake table to evaluate the potency of the computational model by comparing the results of the FE analysis with the shake-table experiments. The transient FE analysis is performed using an explicitly defined time-step of 0.005 sec and Hilber-Hughes-Taylor numerical integration method, i.e., HHT or α method (Hilber et al. 1977), which uses the same finite difference formulas as the Newmark method with $\gamma = \frac{1}{2}(1 - 2\alpha)$ and $\beta = \frac{1}{4}(1 - \alpha)^2$ where

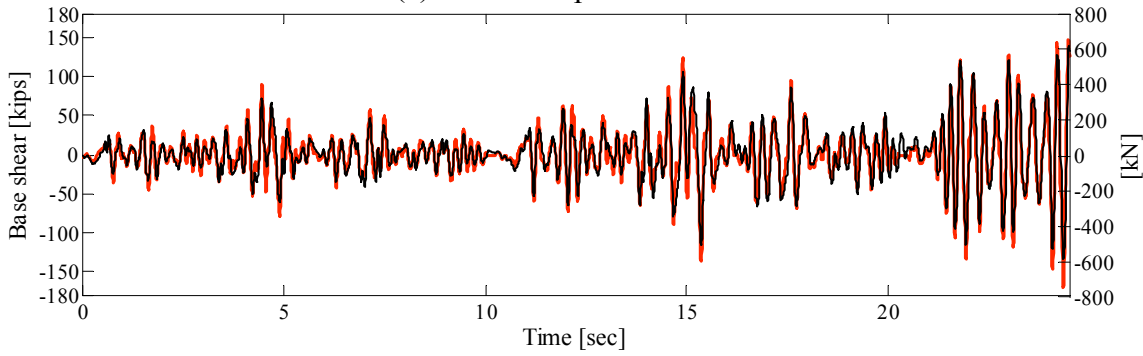
α is in the range of $-\frac{1}{3}$ and zero. The value chosen for α in this study is -0.1 that introduces numerical damping in the integration method and leads to a more stable solution. A classical damping matrix is assumed for the FE analysis using a 7% damping ratio ζ for the second and third modal frequencies per 7.8 (first two modes in the in-plane direction) to determine the stiffness and mass proportional coefficients of the damping matrix. The nonlinear solution is evaluated using the regular Newton-Raphson iterative process that assembles the stiffness matrix at every iteration. Since strong nonlinearity is expected in the model, a line-search algorithm (DIANA 2005) is used to increase the convergence rate by scaling the prediction of the displacement within each iteration increment. The optimum scale factor η is determined such that it minimizes the energy potential Π (the product of out-of-balance forces and their

corresponding displacements). The optimization is performed approximately by finding η such that $s(\eta) = \partial\Pi/\partial\eta < 0.8 s(0)$, where $s(0)$ is the value of the derivative of the energy potential with respect to η at the start of the iteration.

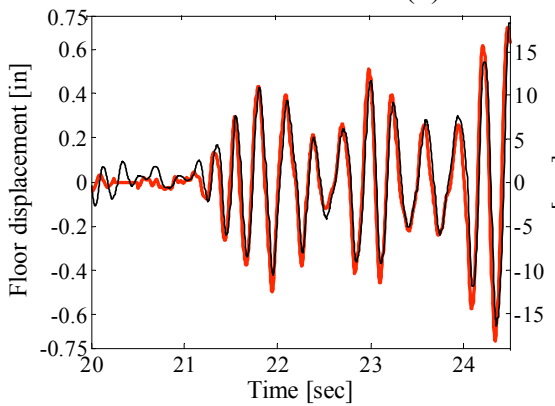
The base acceleration time history chosen for the FE analysis is the concatenated strong motion part of the acceleration measured at the base of the test structure during levels TAR 4, TAR 6, and DUZ 7 containing at least 92.7% of the total energy of the each ground motion level estimated according to Trifunac and Brady (1975). Base shear and RC floor slab lateral displacement time histories from the FE analysis as well as the shake-table experiments are shown in Figures 7.25(a) and (b), respectively. Figures 7.25(c) and (d) show the partial time history of base shear and RC floor slab lateral displacement, respectively, for the DUZ 7 portion of the input ground motions. Comparing the computational results with the experimental ones, the FE model represents the overall behavior of the test structure very well up to the last convergence point (4.6 sec into the DUZ 7). The convergence problem is attributed to the complicated nonlinear properties of the model, namely the nonlinear concrete model, cracking in the masonry, the nonlinear interface between the masonry and the infilled RC frame members, and yielding in the reinforcing bars. The problem may be resolved at the expense of some accuracy in the results by choosing simpler material models in the FE analysis. More generally, the capability of the used FE modeling approach based on the smeared crack methodology in predicting the brittle behavior of the URM infill wall and the post-cracking failure mechanism of the infill is limited due to its inherit continuum formulation of displacement and crack openings (Lotfi and Shing 1991). In order to alleviate this problem, more detailed FE approaches may be used where, smeared crack models are considered for the masonry units and the mortar joints are modeled using dilatant interface elements (Lotfi and Shing 1994; Mosalam 1996b), i.e., modeling cracks in the joints of the URM infill wall using discrete methodology. Such approaches, however, require considerably more computational effort and their application to large structures involving dynamic loading with FE time-history analyses is practically limited.



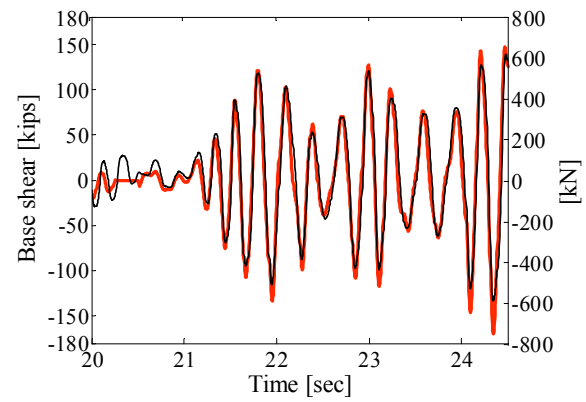
(a) Lateral displacement time histories



(b) Base-shear time histories

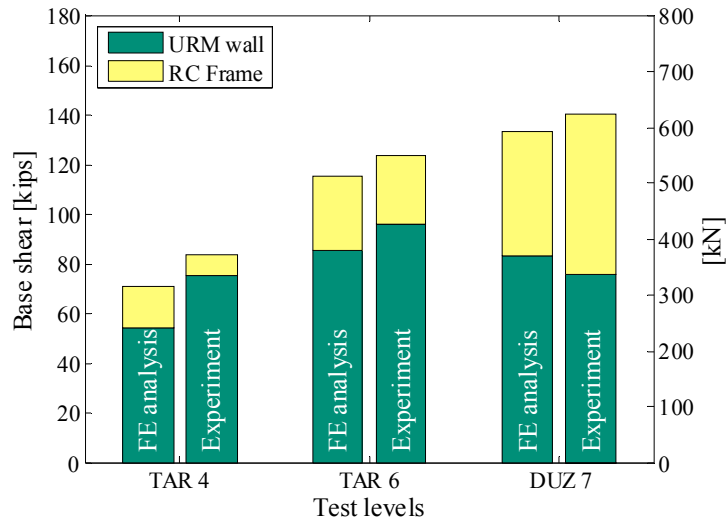


(c) Partial time history of RC floor slab displacement during DUZ 7

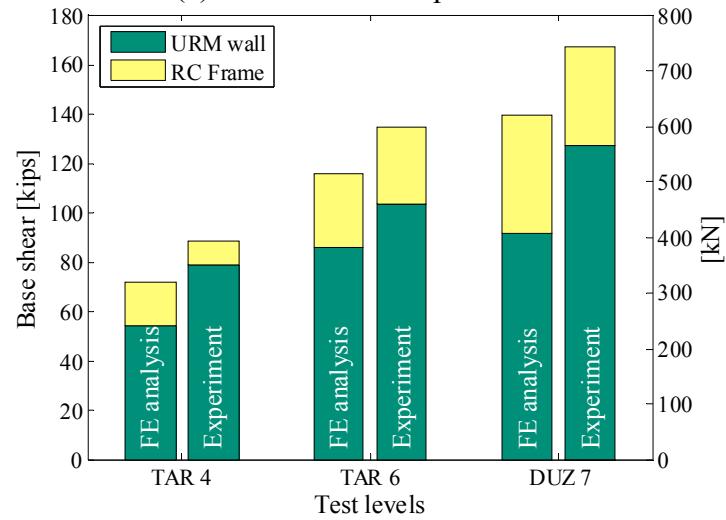


(d) Partial time history of base shear during DUZ 7

Fig. 7.25 Comparisons of 3D FE analysis and shake-table results.



(a) At maximum displacement



(b) At maximum base shear

Fig. 7.26 Comparison of distribution of forces in 3D FE model and test structure.

The distributions of lateral forces between the URM infill wall and the three RC frames in the structure obtained from the shake-table experiments and the FE analysis are presented in Figure 7.26 for the indicated levels. The two bar charts in this figure present the forces carried by the URM infill wall and the RC frames at the time corresponding to the maximum displacement and maximum base shear in each run. Both bar charts show that the URM infill wall carries a large portion of the total base shear during level TAR4 (e.g., 77% at maximum displacement) and that this ratio is reduced as the URM infill wall is damaged with further shaking at higher levels (e.g., 62% at maximum displacement during level DUZ 7). The comparison between the distribution of forces in the 3D FE model and that of the test structure shows that the same trend exists in the analysis as in the experiments and that the difference between the results of the 3D

FE model and those of the experiments for the ratio of the force resisted by the URM infill wall to the total base shear (at maximum displacement, Fig. 7.26(a)) is only 16 % at level DUZ 7, providing reasonable confidence in the accuracy of the 3D FE model described in this chapter.

The values of the force-displacement plot for the 3D FE model due to the transient analysis discussed above are presented in Figure 7.27, as well as the results of the monotonic pushover analysis from the same FE model (mirrored in both directions). It is observed that the maximum strength of the URM infill wall when subjected to the dynamic loading is 70% of the value obtained from the pushover analysis, and that the displacement corresponding to the maximum strength of the URM infill wall in the dynamic loading is only 61% of that obtained from the pushover analysis. The reduction in the compressive strength of masonry in the infill elements when subjected to dynamic loading is due to the effects of tensile cracking along the opposite compression diagonal when loading in one direction where the open cracks during the previous loading excursion do not fully close upon load reversal. The significance of this finding is in identifying the need to provide correction factors for the strength capacity of the infill walls obtained from monotonic pushover analyses, as discussed in Chapter 8.

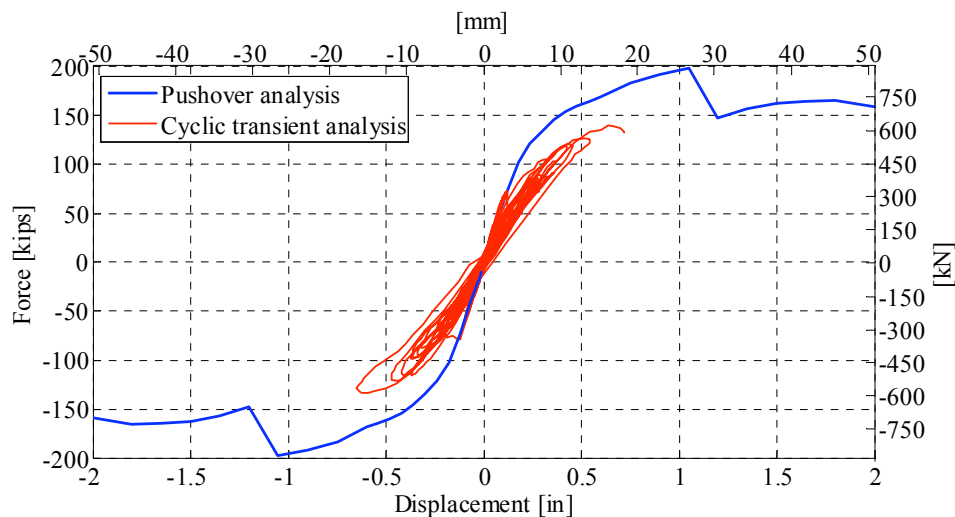


Fig. 7.27 Comparison of cyclic transient and pushover analyses obtained from 3D FE model of shake-table test structure.

7.4 OUT-OF-PLANE MODELING OF URM INFILL WALLS

In this section the background and available research literature on the out-of-plane capacity of infilled frames is briefly reviewed. The out-of-plane behavior of the URM infill wall of the test structure is computationally evaluated by utilizing the FE model of the infilled RC frame discussed in Section 7.3.2. Moreover, the outcome of the FE out-of-plane pushover analysis is compared to the estimated out-of-plane capacity of the URM infill wall based on empirical approaches suggested by other researchers.

7.4.1 Background

The out-of-plane behavior of URM infill walls has been studied both analytically and experimentally. The experimental studies can be summarized in three different categories. The first category includes subjecting the URM infill walls to a sudden air pressure such as detonating explosives or exposing to a shock tunnel, e.g., (Monk 1958 and Gabrielsen and Kaplan 1977). The second category includes loading the infill panel using hydraulic actuators or air bags and respectively applying a static concentrated or uniform load perpendicular to the surface of the wall at the central portion or on the entire surface area of the specimen to simulate the dynamic inertial forces, e.g., (Hill 1993; Drydale and Essawy 1988; Dawe and Seah 1990). The third category involves using the shake table to subject the infill panel to ground accelerations in the out-of-plane direction of the infill panel, e.g., (Bennett et al. 1996; Klingner et al. 1996).

Several analytical models are also introduced to represent the out-of-plane behavior of the infill panels. The simplest models assume that the infill panel acts as an elastic plate, and use the classical solution derived in (Timoshenko and Woinowsky 1959). Considering the two-way inelastic behavior, models based on the modified yield-line theory have been developed in Drysdale and Essawy (1988); Haseltine (1976); Haseltine et al. (1977); Hendry (1973); and Hendry and Kheir (1977). All these models depend on the tensile capacity of the masonry to carry the out-of plane forces, which is a valid assumption before crack development in the URM. However, after cracking of the masonry such models poorly predict the out-of-plane response.

Most experimental data suggest that after the initial cracking of the URM infill wall, the out-of-plane strength depends on the compressive strength of the masonry, not on its tensile

strength, due to the arching action of the URM infill wall. Analytical methods based on this arching action have been developed in McDowell et al., (1956); Angel and Abrams (1994); Klingner et al. (1996); and Dawe and Seah (1990); to name a few. Flanagan and Bennett (1999b) compared analytical methods in Angel and Abrams (1994); Klingner et al. (1996); and Dawe and Seah (1990) and determined that the approach developed in Dawe and Seah (1990) best represented the available experimental data.

FEMA 356 provisions also provide an approach for the out-of-plane capacity of URM infill walls, which is based on the method in Angel and Abrams (1994) but modified to represent a lower-bound strength. These provisions assume restrictions on the frame out-of-plane stiffness and the height-to-thickness ratio of the infill panel. A factor of 1.3 is considered by FEMA 356 provisions to translate the lower-bound masonry properties to the mean (expected) strength values. Since the lower-bound properties in FEMA 356 are defined as mean minus one standard deviation, the factor of 1.3 defined above corresponds to a coefficient of variation of 0.231 (Note: $f_c / (f_c - \sigma) = 1.3 \Rightarrow \delta = \sigma / f_c = 0.3 / 1.3 = 0.231$). For the infilled RC frame described in the previous sections, the mean out-of-plane capacity in terms of uniform pressure applied to the entire wall panel is calculated as 1.08 psi (7.45 kPa) based on FEMA 356 and as 1.39 psi (9.55 kPa) based on the approach given in (Dawe and Seah 1990). The detailed calculations to obtain these out-of-plane capacity estimates are given in Appendix D.

7.4.2 FE Model

The FE model of the infilled RC frame described in the previous sections is used to evaluate the out-of-plane capacity of the infill wall. Two models are considered, one assuming a two-way action for the out-of-plane direction of the URM infill wall by constraining the infill to the columns as well as the top beam and bottom support. The other model, assumes a one-way out-of-plane action for the URM infill wall that spans from the top beam to the bottom support with free sides, i.e., no connections with the columns. Researchers have shown that fixed connection between the URM infill wall and the RC frame members would overestimate the stiffness of the infill wall in the out-of-plane direction (Flanagan and Bennett 1999a). Therefore, the infill wall in this study is assumed to be pinned to the RC frame members such that the out-of-plane movement “walking” of the URM infill wall from the RC frame is prevented, but relative rotations around the common edges between the frame members and the URM infill wall are

allowed. It should be noted that the in-plane interface elements between the URM infill wall and the RC frame members are defined with the same properties as for the 2D frame defined in Section 7.3.2 which allow in-plane sliding and opening between the URM infill wall and the RC frame members. For both models, force-controlled pushover analyses are performed by gradually increasing the out-of-plane pressure on the infill wall and recording the out-of-plane displacement of a point at the center of the infill wall. The exaggerated deformed shapes for both models, without and with side releases, are shown in Figures 7.28(a) and (b), respectively. The pushover results as well as the capacity values obtained from FEMA 356 and the approach by (Dawe and Seah 1990) are also presented in Figure 7.29.

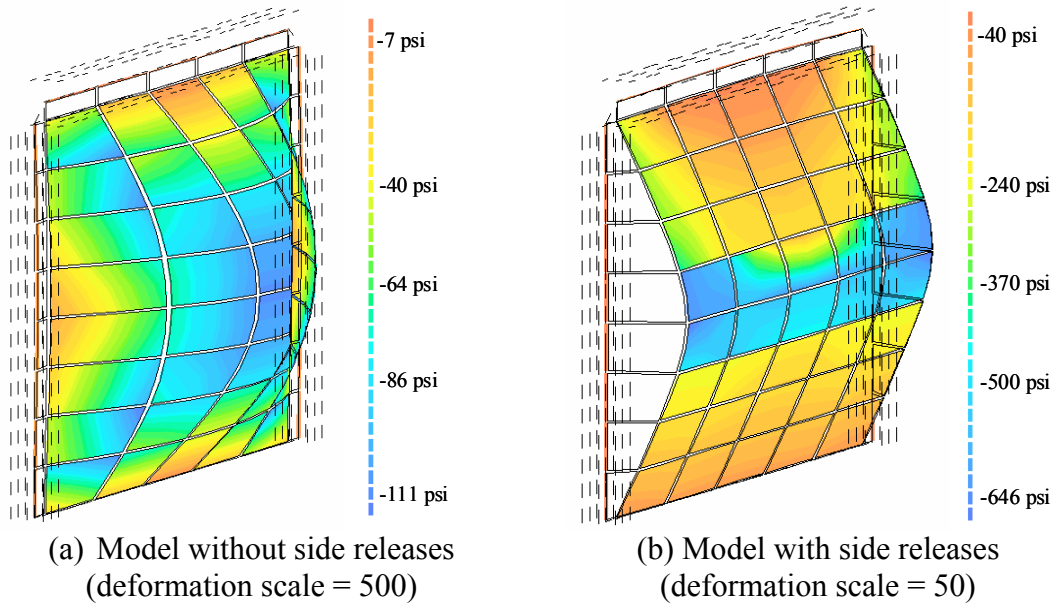


Fig. 7.28 Exaggerated deformed shapes of FE models subject to uniform out-of-plane pressure (1 psi = 6.895 kPa).

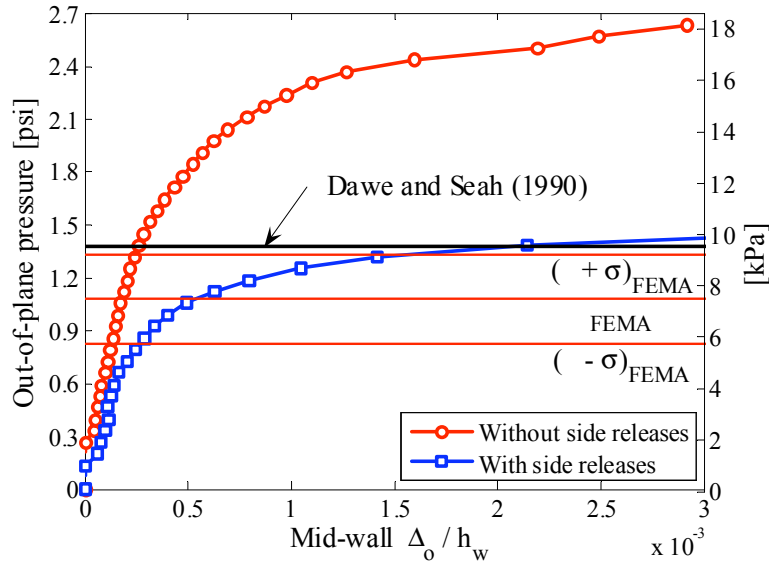


Fig. 7.29 Out-of-plane FE pushover analysis results compared with empirical approaches.

The comparisons between the pushover results and the capacity estimated by the empirical approaches (Fig. 7.29) suggest that the FE model with side releases offers better estimate of the out-of-plane behavior of the URM infill wall which is consistent with the findings by Flanagan and Bennet (1999a) when comparing their FE model and experimental results. The capacity obtained by the present FE model with side releases falls well (for the range of about 0.02%–0.15% of the mid-wall out-of-plane deformation with respect to the wall height h_w) between the mean \pm one standard deviation, $\pm\sigma$, of the results provided by FEMA 356 provisions and very close to the results obtained by (Dawe and Seah,1990), providing confidence in the accuracy of the developed FE model.

7.5 COMBINED IN-PLANE AND OUT-OF-PLANE MODELING OF URM INFILL WALLS

In this section the background and limited experimental research available on the interaction between the in-plane and the out-of-plane behaviors of the URM infill walls are summarized. The FE model of the infilled RC frame discussed in the previous section is used to apply simultaneous in-plane and out-of-plane loads to the URM infill wall, and the effects of the bidirectional loadings are investigated. The outcome of this section is a framework for determining the bidirectional failure surface for the URM infill wall and its application to the type of the RC buildings with URM infill walls discussed throughout this report.

7.5.1 Background

As previously discussed, the capacity of the URM infill walls is strongly related to the compressive strength of masonry material in both in-plane and out-of-plane (through arching action) directions. The effects of orthogonal loadings on URM infill walls, however, have been briefly studied experimentally and analytically. Few experiments include out-of-plane loading of already cracked or damaged infill walls or simultaneous bidirectional loading of infilled RC frames. Angel and Abrams (1994) report that the out-of-plane capacity of the URM brick infill walls decreases by as much as a factor of 2.0 depending on the amount of in-plane damage. They also suggest that the effects of the in-plane cracking on the out-of-plane capacity increases by the increase in the slenderness ratio (height to thickness ratio) of the infill wall. Flanagan and Bennett (1999a) describe a series of in-plane, out-of-plane, and combined in-plane and out-of-plane experiments for a one-story single-bay clay tile infilled RC frame. Three combined loading experiments are described: (1) Loading in the in-plane direction to a certain value, removing the load and applying the out-of-plane pressure until failure (frame 19); (2) loading in the out-of-plane direction to a certain value, removing the load and applying the in-plane force until failure (frame 20); and (3) loading simultaneously in the in-plane and out-of-plane directions by holding the in-plane deformation and applying the out-of-plane pressure until failure (frame 23). Figure 7.30 presents the peak in-plane and out-of-plane loads reported for each experiment in addition to two control experiments with pure in-plane and pure out-of-plane loadings, frames 2 and 18, respectively. Although these results do not show strong interaction when the orthogonal loads are applied sequentially, frames 19 and 20, they reveal strong interaction when the infilled frame is subjected to simultaneous application of in-plane and out-of-plane forces, frame 23, which shows a 42% drop in the in-plane capacity of the infill wall when it is subjected to out-of-plane pressure equal to 57% of its capacity. Motivated by this experimental observation, the FE model discussed previously is utilized to computationally determine the interaction relationship between the in-plane and the out-of-plane capacities of the RC frame with URM infill wall used in the test structure.

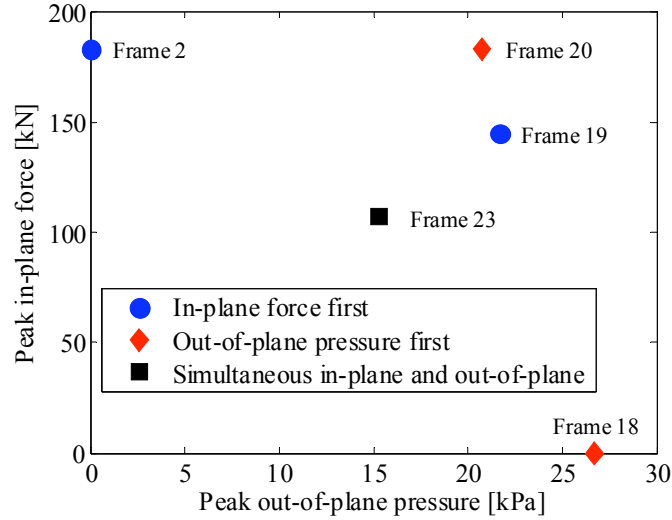


Fig. 7.30 Experimental results reported by Flanagan and Bennett (1999a) on bidirectional testing of clay tile infilled RC frames.

7.5.2 FE Model

In order to computationally study the effects of the bidirectional loading of the URM infill wall described in the previous sections, the FE model of the infilled RC frame tested pseudo-dynamically and discussed in Section 7.3 is considered. Several in-plane pushover analyses are performed on the infilled RC frame with different values of constant out-of-plane pressure on the URM infill wall. The results are presented as a family of in-plane pushover curves as shown in Figure 7.31. In these plots, the out-of-plane pressure is reported as normal force P_N , which is calculated as the product of the applied out-of-plane pressure and one half the surface area of the infill wall (one-way arching action where the other half of the load goes directly and equally to the bounding frame elements above and below the URM infill wall). The point indicated on each plot by a circle corresponds to the maximum in-plane capacity which is used to construct the interaction curve for the in-plane and out-of-plane forces on the URM infill wall. The exaggerated deformed shape (with an amplification factor of 100) of the FE model under bidirectional loading and fully open cracks (with crack strain exceeding f_{mt}/E_m as defined in Figure 7.17(b)) in the URM infill wall are also shown in Figures 7.32(a) and (b), respectively. The deformed shape presented suggests a diagonal out-of-plane arch forming between the two opposite top and bottom corners of the infilled RC frame, which is the conceptual basis for the 3D SAT model presented in the next section. It is observed that increasing the out-of-plane force

significantly reduces the in-plane force capacity of the infilled RC frame, and the FE analyses suggest a strong interaction between the in-plane and the out-of-plane loadings, which significantly affects the infill wall capacity when subjected to simultaneous bidirectional loading.

The final goal of these FE analyses using the computational platform DIANA (2005) is represented by the interaction curve in Figure 7.33 with the shown mathematical expression to best fit the computational results. The points on the interaction curve are extracted directly from the pushover curves presented in Figure 7.31 as defined above. The analysis is also performed for constant out-of-plane force of 11 kips (48.9 kN) but the solution fails at convergence for the first step of the in-plane displacement increment. Therefore, the in-plane capacity corresponding to 11.0 kips (48.9 kN) of an out-of-plane force is assumed as zero in the interaction curve.

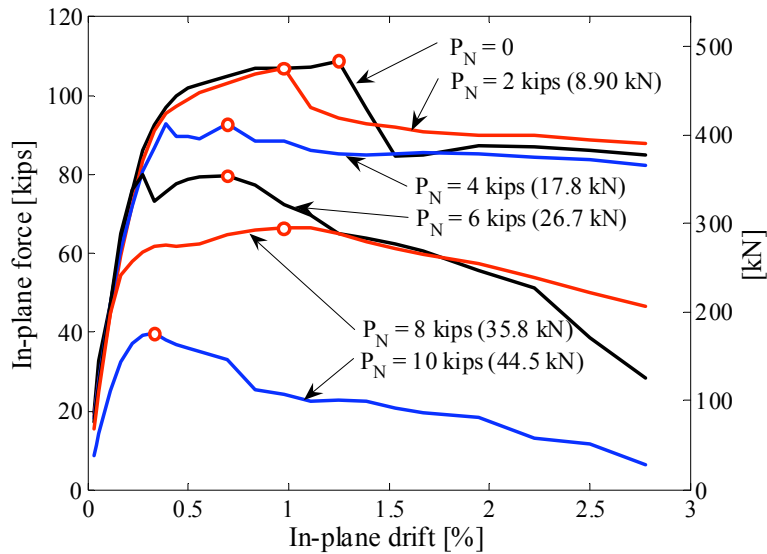
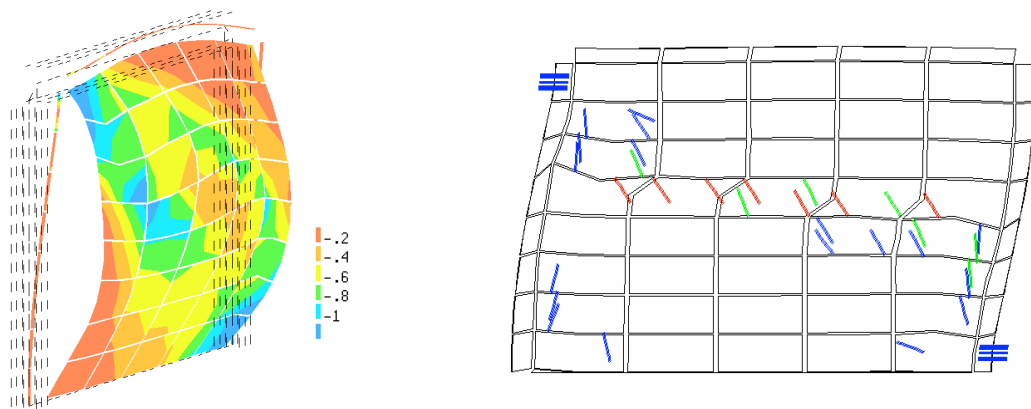


Fig. 7.31 In-plane pushover curves with varying out-of-plane force P_N .



(a) Deformed shape and stress contour (ksi) (b) Deformed shape and fully open cracks

Fig. 7.32 FE model of infilled RC frame subject to bidirectional loading (1 ksi = 6.895 MPa).

It should be noted that the results presented in Figure 7.33 are specific to the configuration, geometry, and material properties of the studied test structure and are not intended to serve as a generalized interaction relationship. Also, the sequence of applying the in-plane and out-of-plane forces causing different initial crack patterns in the URM infill wall may affect the pushover results and the corresponding capacities derived from them. Nevertheless, it is believed that the presented computational study in this section demonstrates a general framework for including the in-plane and out-of-plane interaction in analyses involving URM infill walls such as the simplified reliability analysis performed on the prototype building to determine its fragility functions as discussed in Chapter 8. The study of the effects of different loading sequences (Fig. 7.30) on the interaction curve is an involved problem for future investigations and may lead to interesting implications especially in conjunction with the cross correlations between the in-plane and the out-of-plane demands on the URM infill walls.

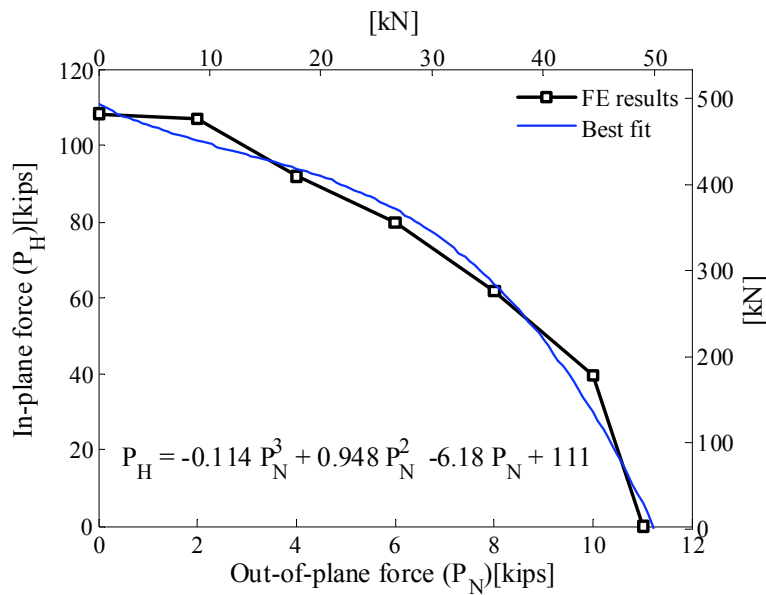


Fig. 7.33 Interaction diagram for URM infill wall.

7.6 THREE-DIMENSIONAL SAT MODEL FOR URM INFILL WALLS

Different SAT models to represent the in-plane behavior of infilled RC frames are discussed earlier in this chapter. The benefits and limitations of such models are also highlighted by comparing the experimental results with the results obtained from a simple strut model, and it is suggested that when carefully calibrated, such simple models lead to acceptable results in the in-plane direction. The common practice in the evaluation of infilled RC frames in the out-of-plane

direction has generally been limited to determining the normal forces on the infill wall using some indirect method such as using average response of the floors above and below the infill wall and comparing those forces with the out-of-plane capacity of the infill wall. Consequently, the interaction between the in-plane and out-of-plane loadings in determining the infill wall capacity is typically neglected in evaluating the seismic responses of infilled frames.

The use of detailed FE modeling of infill walls in the computational modeling of infilled structures to include the bidirectional interaction is computationally very expensive and impractical. Instead, a 3D SAT model is suggested in this section to directly couple the in-plane and the out-of-plane forces in the URM infill wall by introducing a normal-to-the-wall degree-of-freedom at the center of the infill wall, which can be assigned mass and out-of-plane force. Figure 7.34 shows a schematic illustration of this novel 3D SAT model. The dashed lines in the figure represent the nonlinear compression-only members (see the insert of the material model of these struts), and the solid line in the center of the infill wall represents a tension-only elastic link element.

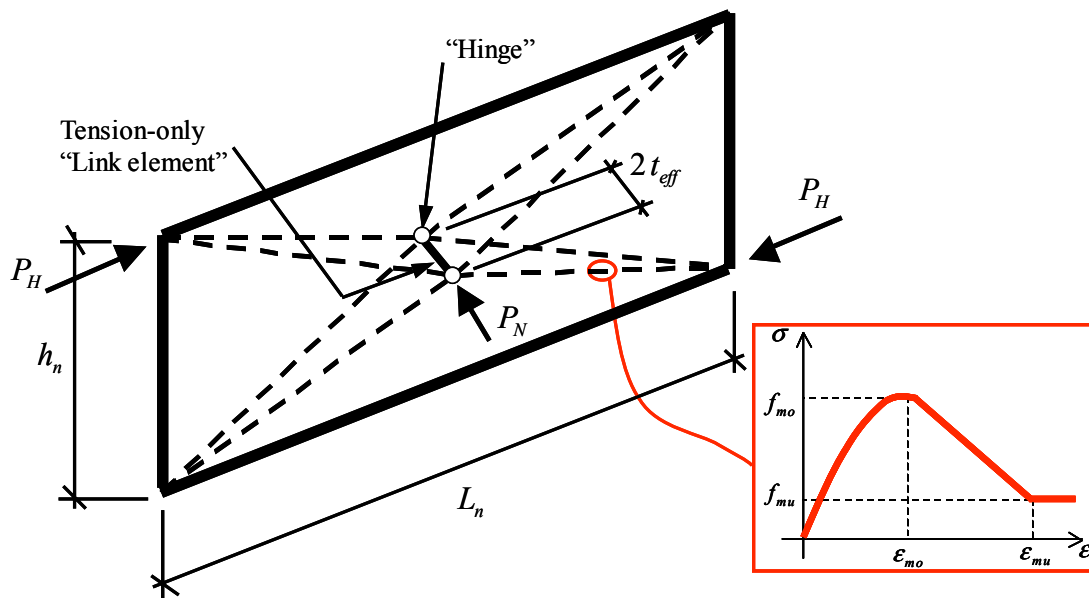


Fig. 7.34 Three-dimensional SAT model of URM infill wall.

By systematically determining the geometrical parameter t_{eff} , (Fig. 7.34) and the material and geometrical properties of the elements of this 3D SAT model, not only the in-plane and out-of-plane capacities but also their interaction diagram (failure surface as defined by Fig. 7.33) can be introduced as part of the computational model. Such a failure surface may be determined by experimental data or detailed FE analyses as before. The model can also be combined with

additional diagonal or off-diagonal struts to achieve different degrees of coupling and failure mechanisms. In order to demonstrate the effect of each parameter and the variety of possibilities in calibration of this 3D SAT model, several sets of parameters are chosen to generate different failure surfaces as summarized in Table 7.9 where A_{total} is the total cross-sectional area of the diagonal and any off-diagonal strut assembly in each direction, and A_{OD} is the cross-sectional area assigned to off-diagonal struts, not shown in Figure 7.34. Other parameters in this table are defined in Figure 7.34. The tension-only link element in these models is assumed to be rigid in tension by defining a very large elastic modulus for this element. For each set, a series of in-plane pushover analyses with different constant out-of-plane forces and out-of-plane pushover analyses with different constant in-plane forces are performed and the peak forces are recorded and plotted together to generate the failure surfaces shown in Figure 7.35. It should be noted that unlike the FE model, the sequence of loading for the 3D SAT model does not change the failure surface, since the failure is dependent only on the current state of stresses and deformations in the SAT elements. Therefore, both the in-plane and the out-of-plane pushover analyses described above result in consistent results for the failure surfaces. Comparing the interaction curves obtained from sets 2–8 with set 1 (reference set) as defined in Table 7.9, it is observed that the interaction curve may be scaled up and down by increasing and decreasing the compressive strength of the struts f_{mo} , respectively (sets 2 and 3). The change in the peak strain ϵ_{mo} significantly affects both the in-plane and the out-of-plane capacities of the 3D SAT assembly and the curvature of the interaction curve (sets 4 and 5). The parameter t_{eff} may also be varied in order to increase the out-of-plane capacity with constant in-plane capacity (sets 6 and 7). By defining a portion of the total cross-sectional area of the strut in one direction to an off-diagonal strut (not part of the 3D SAT), the interaction between the in-plane and out-of-plane capacities may also be reduced resulting in a more rectangular interaction relationship (set 8). Although not shown here, the material model for the link element may be adjusted to sustain permanent deformation due to excessive in-plane or out-of-plane forces, thus reducing the capacity of the infill due to cyclic loading or previous damage. This can be implemented by using a rigid-plastic tension-only material for the link element with unloading and reloading to the farthest point reached previously on the plastic plateau. The hinges shown in Figure 7.34 may also be replaced by rotational springs with assigned threshold moment capacities corresponding to the onset of cracking in order to differentiate between the pre- and post-cracking behavior of the infill wall.

Table 7.9 Parameter sets used for 3D SAT model to generate different failure surfaces.

Set	A_{total} [in. ² (cm ²)]	A_{OD} [in. ² (cm ²)]	f_{mo} [ksi (MPa)]	f_{mu} [ksi (MPa)]	ϵ_{mo}	ϵ_{mu}	t_{eff} [in. (mm)]
1	34.6 (223)	0	2.46 (17.0)	0.29 (2.0)	0.0028	0.0041	9.1 (231)
2	34.6 (223)	0	4.0 (27.6)	0.47 (3.2)	0.0028	0.0041	9.1 (231)
3	34.6 (223)	0	1.15 (7.93)	0.14 (0.97)	0.0028	0.0041	9.1 (231)
4	34.6 (223)	0	2.46 (17.0)	0.29 (2.0)	0.01	0.0150	9.1 (231)
5	34.6 (223)	0	2.46 (17.0)	0.29 (2.0)	0.0005	0.0041	9.1 (231)
6	34.6 (223)	0	2.46 (17.0)	0.29 (2.0)	0.0028	0.0041	5.0 (127)
7	34.6 (223)	0	2.46 (17.0)	0.29 (2.0)	0.0028	0.0041	11.3 (286)
8	34.6 (223)	17.3 (112)	2.46 (17.0)	0.29 (2.0)	0.0028	0.0041	9.1 (231)

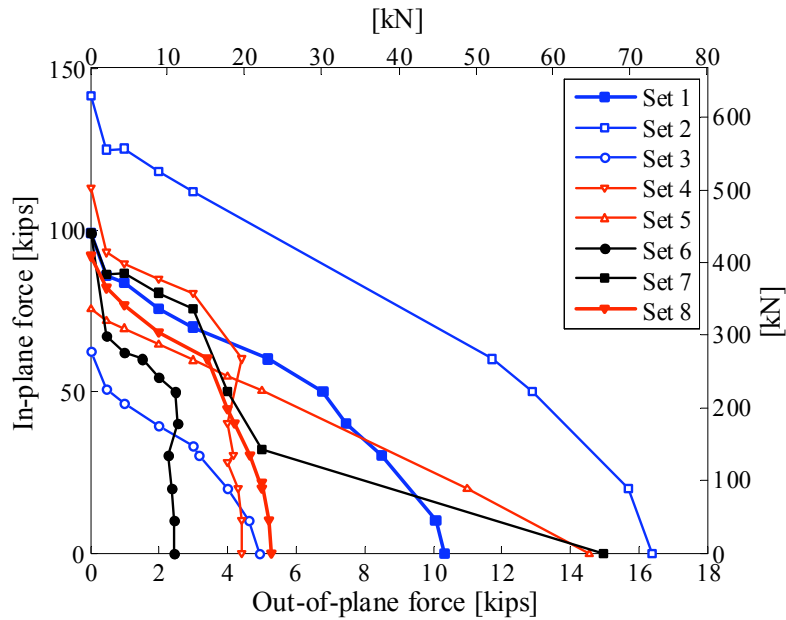


Fig. 7.35 Failure surfaces for 3D SAT models.

As an example, the 3D SAT model is calibrated to match the failure surface obtained from the FE analysis shown in Figure 7.33. The calibrated model parameters are listed in Table 7.10 with the detailed calculations to determine the strut cross-sectional area and t_{eff} shown in Appendix E. Other parameters such as masonry material properties or link element material model can also be adjusted to obtain better matches with the experimental or the FE results. The resulting bidirectional failure surface and the target failure surface obtained from FE analysis are shown in Figure 7.36, where reasonable agreement can be observed.

Table 7.10 Parameter set used for 3D SAT model to generate FE failure surface.

Model Parameters	A_{total} [in. ² (cm ²)]	A_{OD} [in. ² (cm ²)]	f_{mo} [ksi (MPa)]	f_{mu} [ksi (MPa)]	ϵ_{mo}	ϵ_{mu}	t_{eff} [in. (mm)]
Calibrated values	42.4 (274)	0	2.46	0.29	0.0056	0.0082	10.0 (254)

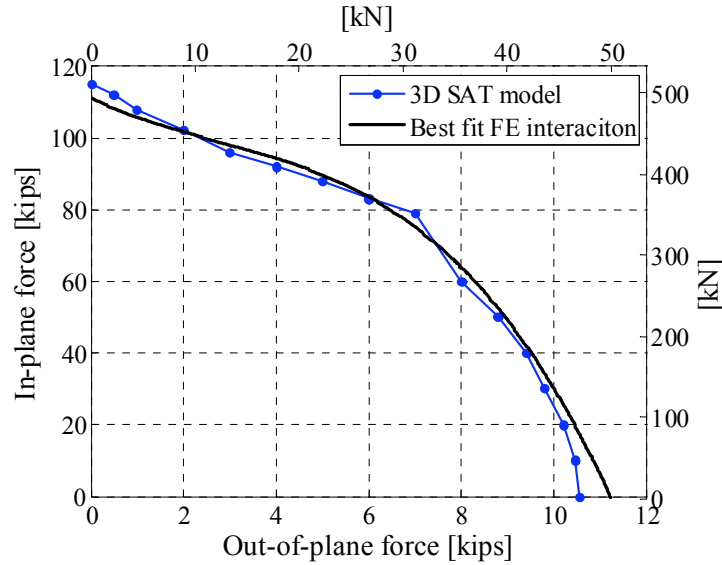


Fig. 7.36 Failure surface for calibrated 3D SAT model compared to best-fit FE analysis results.

7.7 SUMMARY

Different modeling techniques to represent URM infill walls within a larger structural system are discussed. The simplest models consist of diagonal compression struts with predefined cross-sectional area and material properties that generally perform well in the linear range and are very easy to implement. More detailed models intend to capture different failure modes and post-cracking behavior of infill walls include SAT assemblies with complex geometry and nonlinear material properties, which require careful calibration before they are implemented in the structural model. The calibration may be performed using experimental data—if available—or using results from FE analyses of the infilled frames.

Finite element models of the bare and infilled RC frames used in the pseudo-dynamic experiments described in Chapter 1, are constructed and their accuracy is validated by comparing the experimental responses with the FE results. These models are used as the basis for a series of

in-plane and out-of-plane study of the infilled RC frame aiming at understanding the in-plane, out-of-plane, and bidirectional capacities of URM infill walls.

The FE models of the bare and infilled RC frames are also used as building blocks to construct the 3D FE model of the shake-table test structure described in Chapter 3. The resulting FE model is subjected to the same dynamic loading sequence as the test structure during the shake-table experiments, and the response of the actual specimen and the FE model are compared. This validated model may be used as a tool for further analysis and parametric study of the test structure such as the progressive collapse computational simulation performed in Talaat and Mosalam (2006, forthcoming 2007a).

Realizing the computational limitations of using detailed FE models to represent the bidirectional (in-plane and out-of-plane) behavior of infill walls in large structures, and the strong interaction between forces in these directions suggested by the FE analyses and by published experimental data, a 3D SAT model is introduced. This novel model represents a practical approach to simulate the effects of the out-of-plane forces on the URM infill wall, as well as the bidirectional interaction between the in-plane and the out-of-plane forces. This 3D SAT model is easy to implement and may be calibrated to match any target failure surface determined by experiments or by FE analyses.

8 Generalized Fragility Functions for URM Infill Walls

RC frames with URM infill walls are common building systems worldwide. Such systems often experience significant damage during earthquakes due to in-plane and out-of-plane failures. In this chapter, the five-story RC prototype structure with URM infill walls defined in Chapter 2 is considered as a case study to set a framework for reliability analysis of such buildings. The computational model of the structure using diagonal strut model to represent the URM infill walls is subjected to a series of ground motions scaled to different hazard levels ranging from spectral accelerations of 0.5g–2.75g. Utilizing this computational model, the statistical properties of the URM infill wall in-plane and out-of-plane demand forces at different seismic hazard levels are determined. The in-plane and out-of-plane capacities of the URM infill wall and their interaction curve are estimated using FEMA356 provisions and FE analyses. Defining failure as the loss of the infill walls, limit-state functions corresponding to reaching the in-plane, out-of-plane, and combined bidirectional capacities of the URM infill wall are determined. At each seismic hazard level, using the first-order reliability method (FORM) (Haldar and Mahadevan 2000), the probabilities of failure corresponding to each limit-state function for the URM infill walls at the first, third, and roof levels of the prototype building are calculated. The results are summarized in probability tables and presented as fragility functions for in-plane, out-of-plane, and combined failures for different floor levels.

8.1 INTRODUCTION

Fragility functions are increasingly used in modern performance-based design and evaluation of structures to relate the seismic hazard of the site conditions to the failure probability for the assumed limit states of the structure. These limit states correspond to different local and global

engineering demand parameters, e.g., in-plane or out-of-plane demand forces of infills or story drifts.

URM is one of the most common materials used as infill walls in RC or steel frame structures. As discussed in previous chapters, the URM infill walls have been historically treated as nonstructural elements and their effects on the lateral behavior of buildings are considered as an added benefit to stiffen and strengthen the bare structure. In modern earthquake engineering practice, however, it is recognized that the URM infill walls in a structure significantly change its seismic performance and dynamic properties, as discussed in Chapter 6, and may have beneficial or adverse effects on the safety and stability of the building. However, fewer probability-based analyses have been reported on such structural systems (Mosalam et al. 1997a), partly due to the difficulties in modeling infill walls and partly due to the extensive computational effort required for such analyses especially when out-of-plane response is taken into account.

Accurate modeling of URM infill walls, using detailed FE analysis, is computationally expensive and impractical when applied to large structures, especially for probabilistic evaluations. The common practice to model the URM infill walls in the in-plane direction is to substitute the URM infill wall with diagonal or off-diagonal struts (compression-only elements) with appropriate properties, e.g., FEMA 356 (2000). In the out-of-plane direction, the URM infill walls are generally ignored and at best checked independently to ensure that they can sustain the out-of-plane floor accelerations. Refer to Chapter 7 for further discussion on the modeling approaches of URM infill walls for in-plane and out-of-plane responses.

This chapter builds upon the common methodology to assess the structural reliability applied herein for URM infill walls in the case study RC structure at different stories. It defines the failure criterion as the loss of the URM infill wall and introduces for the first time a method to properly include the interaction between the bidirectional forces on these walls and compares the results for different stories. Noting the significance of the out-of-plane forces and the bidirectional interaction for the reliability assessment of the structural system, the new 3D SAT model described in Chapter 7 is proposed to be used in the future within the same framework to perform reliability analyses of structures similar to the case study building when the failure state is defined in terms of other structural engineering demand parameters than the failure of the URM infill walls.

8.2 CASE STUDY BUILDING

The considered structure for the case study is the five-story RC structure with URM infill walls in its middle frames. As discussed in the previous chapters, this structure is considered as the prototype building for the shake-table experiments and described in detail in Chapter 2. A nonlinear model of the structure is constructed in the computational platform OpenSees (Mazzoni et al. 2006). Beams and columns are modeled using beam elements based on force formulation that considers the spread of plasticity along the length of the element. Cross sections are defined using fiber discretization with distinct fibers for longitudinal reinforcement. Concrete material is modeled using a uniaxial concrete material object with degraded linear unloading/reloading stiffness in compression and no tensile strength. Confining effect due to the prescribed transverse reinforcement is accounted for using confined concrete properties (Mander et al. 1988ab) for the column core concrete material. Steel reinforcing bars are modeled using a uniaxial bilinear material object with kinematic hardening. The URM infill wall is modeled using equivalent diagonal compression-only elastic struts with cross-sectional area of 34.6 in.^2 (223 cm^2) and elastic modulus of 1770 ksi (12.2 GPa) obtained from the initial stiffness of the calibrated single-strut model discussed in Chapter 7. The elastic modeling of the diagonal struts is consistent with the commonly adopted assumption of elastic-brittle behavior for the URM infill walls in compression, since the goal of the presented reliability analyses is to determine the maximum demand on the URM infill walls. The RC slab at each floor level is modeled using horizontal elastic truss members representing rigid diaphragms. Based on the above modeling assumptions, the first-mode natural periods of the structure in both the longitudinal (in-plane of the URM infill wall) and transverse (out-of-plane of the URM infill wall) directions are numerically determined as $T_{1x} = 0.24 \text{ sec}$ and $T_{1y} = 0.35 \text{ sec}$, respectively. Figure 2.1 shows a schematic 3D view of the prototype structure and its typical floor plan. Further details of the design, properties, and modeling of this case study structure can be found in Chapter 2.

8.3 GROUND MOTIONS

Twenty near-fault ground motions are selected for the presented reliability analyses as presented in Table 8.1. In this table, the name of each earthquake and its designation used in this chapter, the earthquake moment magnitude M_w , the station at which the acceleration time history of the

ground motion is recorded, and its site class condition and distance from the fault are listed. These ground motions were extensively studied and carefully selected for the seismic evaluation of the UC-Berkeley laboratory building under the testbed program of PEER (Lee and Mosalam 2006). The fault-parallel and fault-normal components of the ground motions were rotated clockwise by 17.5 degrees (due to the specifics of the testbed study) to produce longitudinal (parallel to the URM infill walls) and transverse (normal to the URM infill walls) components, respectively. The ground motions are scaled to five different intensity levels, namely $SA = 0.50$ g, 1.00g, 1.61g (10/50), 2.05g (5/50), and 2.75g (2/50) in terms of the spectral accelerations (SA) at the first-mode natural period of the structure in both the longitudinal and transverse directions where A/B notation means A% probability of being exceeded in B years. The intensity levels are determined based on the seismic hazard maps available at the USGS website (2007) for an assumed site on the UC Berkeley campus (zip code CA 94710) and modified for site class D conditions. As a reference, based on NEHRP seismic provisions (2000) for this site $S_s = 1.90$ g, $S_1 = 0.816$ g and the design 5% damped spectral acceleration is 1.27g where S_s and S_1 are the maximum considered earthquake (MCE), 5% damped, spectral accelerations at short periods and at one second period, respectively. As an example, the scaled spectra for all 20 ground motions used in this study at level $SA = 1.61$ g (10/50) in the longitudinal and the transverse directions are shown in Figures 8.1(a) and (b), respectively. The first-mode natural periods of the case study structure in each direction used as reference periods in scaling these ground motions are also indicated in these figures.

The majority of the resulting scale factors are within the reasonable range of 0.3–3.0 as shown in Figure 8.2 where open and filled markers refer to the scale factors for the longitudinal and the transverse components, respectively. The minimum and the maximum scale factors used are 0.18 and 11, respectively. For the purpose of this study, the wide range of scale factors is deemed acceptable, as the focus is not on the ground motion uncertainties.

Table 8.1 Ground motion characteristics for testbed study (Lee and Mosalam 2006).

Earthquake	M_w	Station	Designation	Distance	Site
Coyote Lake, 6/8/1979	5.7	Coyote Lake Dam abutment	CL-clyd	4.0 km	C
		Gilroy #6	CL-gil6	1.2 km	C
Erzincan, Turkey, 3/13/1992	6.7	Erzincan	EZ-erzi	1.8 km	C
Kobe, Japan, 1/17/1995	6.9	Kobe JMA	KB-kobj	0.5 km	C
Loma Prieta, 10/17/1989	7.0	Corralitos	LP-cor	3.4 km	C
		Gavilan College	LP-gav	9.5 km	C
		Gilroy historic	LP-gilb		C
		Lexington Dam abutment	LP-lex1	6.3 km	C
		Los Gatos Presentation Center	LP-lgpc	3.5 km	C
		Saratoga Aloha Ave	LP-srtg	8.3 km	C
Livermore, 1/27/1980	5.5	Fagundes Ranch	LV-fgnr	4.1 km	D
		Morgan Territory Park	LV-mgnp	8.1 km	C
Morgan Hill, 4/24/1984	6.2	Anderson Dam Downstream	MH-andd	4.5 km	C
		Coyote Lake Dam abutment	MH-clyd	0.1 km	C
		Halls Valley	MH-hall	2.5 km	C
Parkfield, 6/27/1966	6.0	Array #5	PF-cs05	3.7 km	D
		Array #8	PF-cs08	8.0 km	D
		Temblor	PF-temb	4.4 km	C
Tottori, Japan, 10/6/2000	6.6	Kofu	TO-ttr007	10.0 km	C
		Hino	TO-ttrh02	1.0 km	C

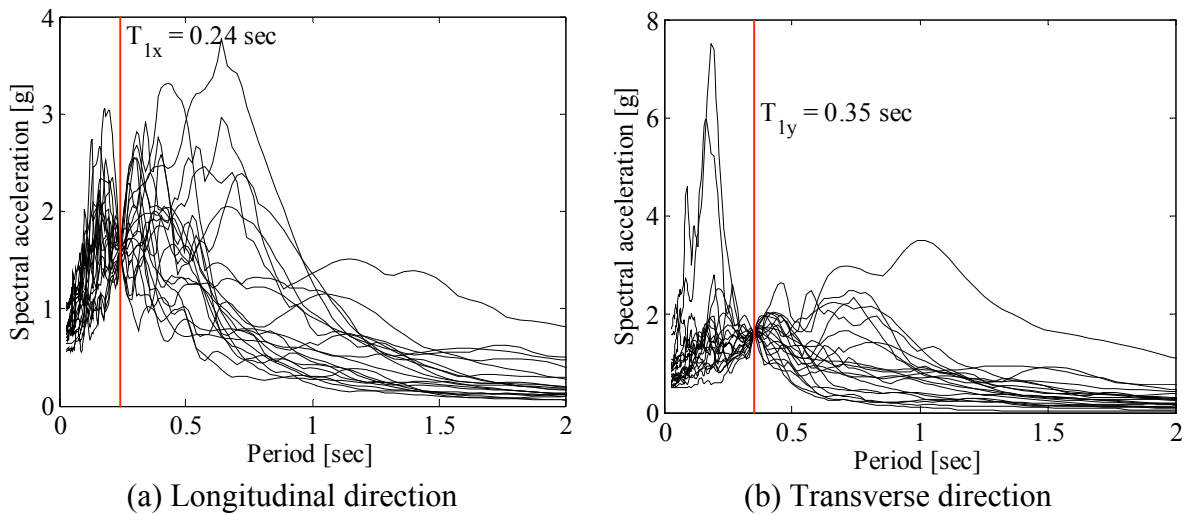


Fig. 8.1 Scaled earthquake spectra for level $SA = 1.61 \text{ g}$ (10/50).

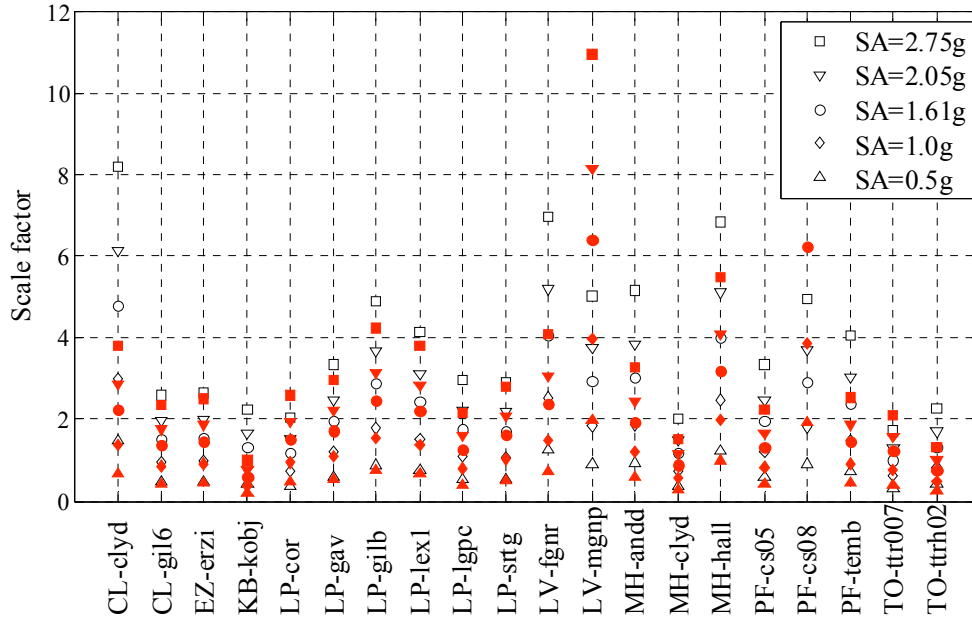


Fig. 8.2 Scale factors for selected ground motions (earthquake designations specified in Table 8.1).

8.4 DEMAND ANALYSIS

Using the computational model of the case study structure in the program OpenSees, a series of bidirectional nonlinear time-history analyses are performed and the resulting demand forces for the in-plane and the out-of-plane directions of the URM infill walls are determined. The roof displacement time history of the structure subjected to CL-clyd ground motion (Table 8.1) at level $SA = 2.75g$ (2/50) is shown in Figure 8.3(a) as an example. The deformed shapes of the structure at the identified points on the time-history plots of the longitudinal and transverse directions are presented in Figures 8.3(b) and (c), respectively.

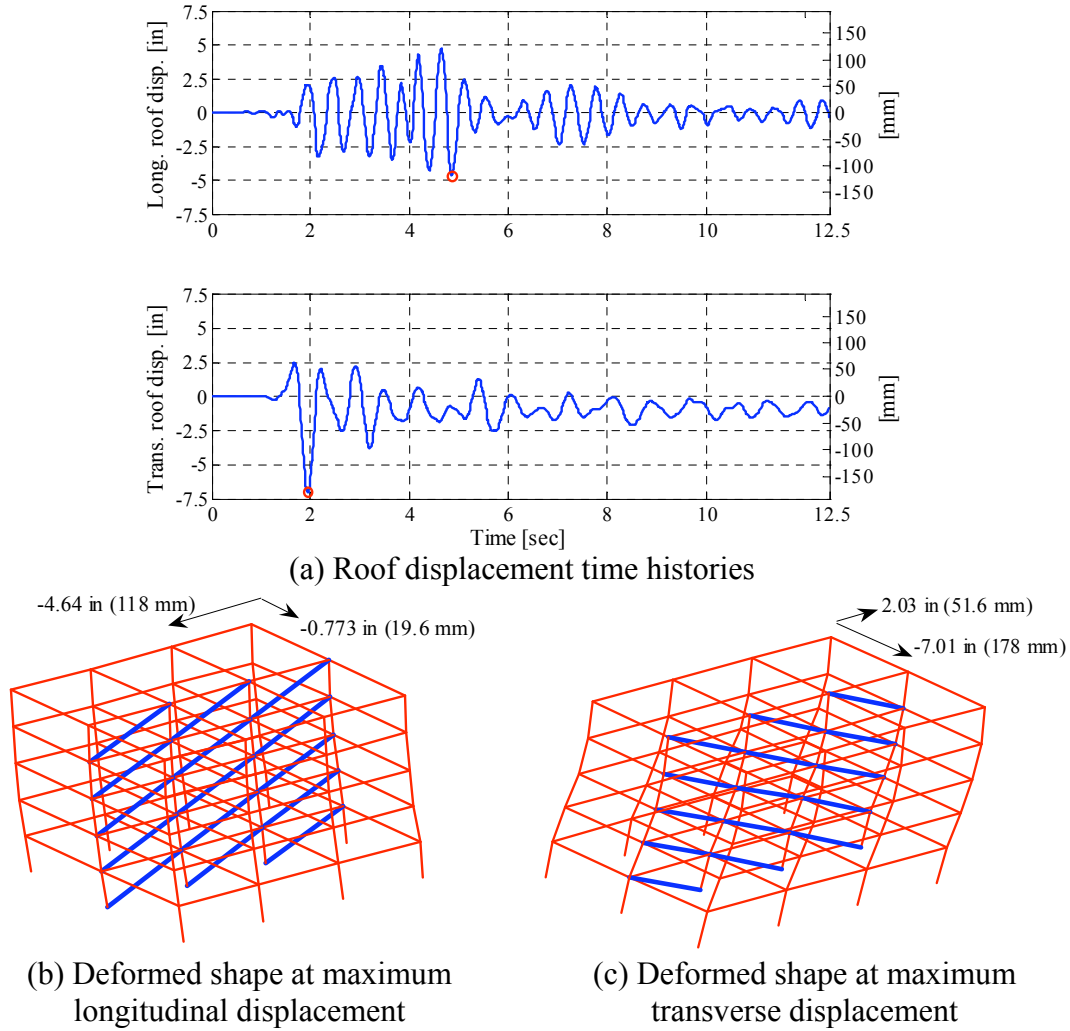


Fig. 8.3 Sample results of nonlinear time-history analysis for CL-clyd ground motion at level $SA = 2.75\text{ g}$ (2/50).

The sum of the horizontal components of the forces in the struts of all the URM infill panels is considered as the in-plane demand force. On the other hand, the force corresponding to the average mid-floor accelerations above and below each story times half the mass of the URM infill wall, i.e., assuming one-way arching action, is considered as the out-of-plane demand force. This force is calculated using moment equilibrium at the mid-height of the URM infill wall as shown in Figure 8.4 where m is the mass of each URM infill wall between two floors, a_i is to the out-of-plane acceleration of the i^{th} floor, and $p_{out-of-plane,i}$ and $F_{out-of-plane,i}$ are respectively the pressure of the out-of-plane inertial force and the applied force to the URM infill wall located above the i^{th} floor.

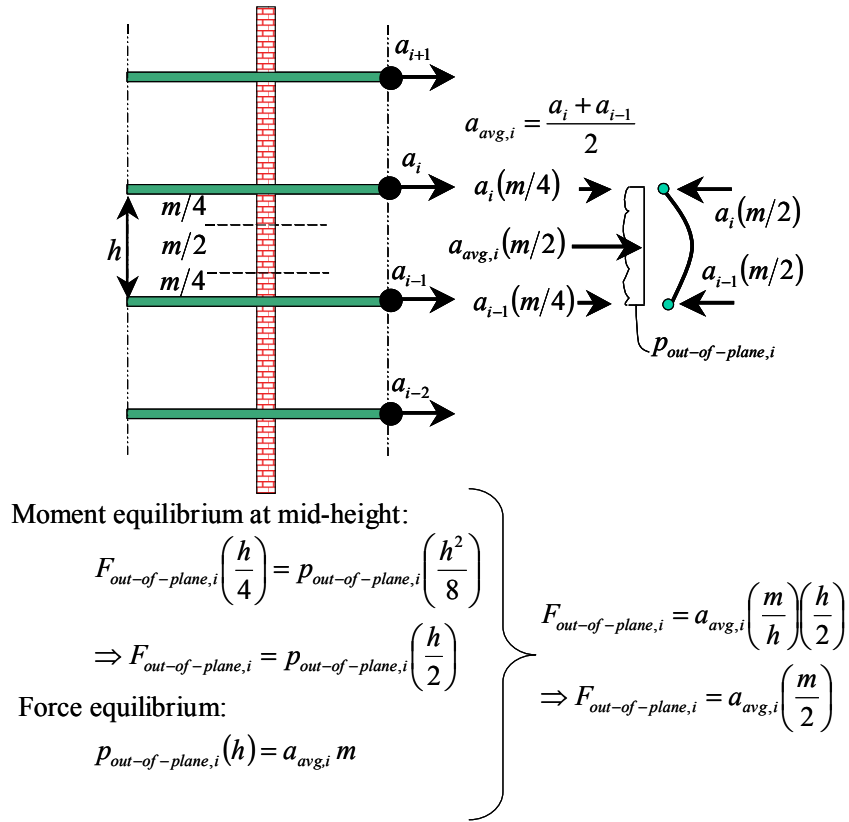


Fig. 8.4 Out-of-plane force calculation for URM infill wall located below i^{th} floor.

As an example the time-histories of the in-plane and the out-of-plane force demands of the URM infill wall below the third floor of the case study building during CL-clyd ground motion, refer to Table 8.1; at level $SA = 2.75\text{ g}$ (2/50) are shown in Figures 8.5(a) and (b), respectively. The maximum values are indicated with the circle marks in these time histories.

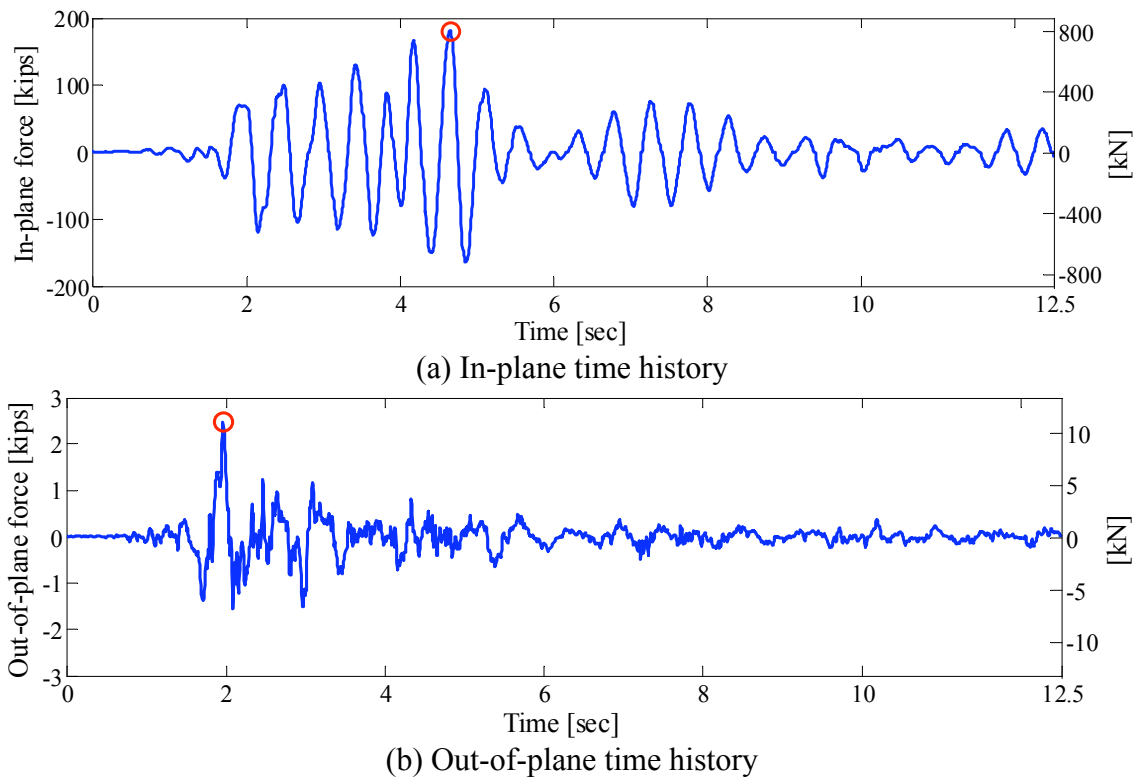


Fig. 8.5 Time-histories of URM infill wall forces below third floor of case study building during CL-clyd ground motion at level $SA = 2.75\text{ g}$ (2/50).

The maximum values of the in-plane and the out-of-plane forces are determined for the URM infill walls below the first and third floors and for the roof level for the 20 ground motions scaled at the five ground motion intensity levels discussed above. These maximum values are used to establish the statistical properties of the demand forces on the URM infill walls in the case study structure, Figures 8.6–8.8. In Figure 8.6, these maximum forces are plotted together with the deterministic interaction curves defining the failure surface of the URM infill wall (the dash-dot line) as discussed in Chapter 7 and the limit-state functions (the solid and dashed lines) defined later in this chapter. The large number of data points outside the limit-state functions suggests that there is high probability of failure expected for the URM infill walls, as discussed later in this chapter.

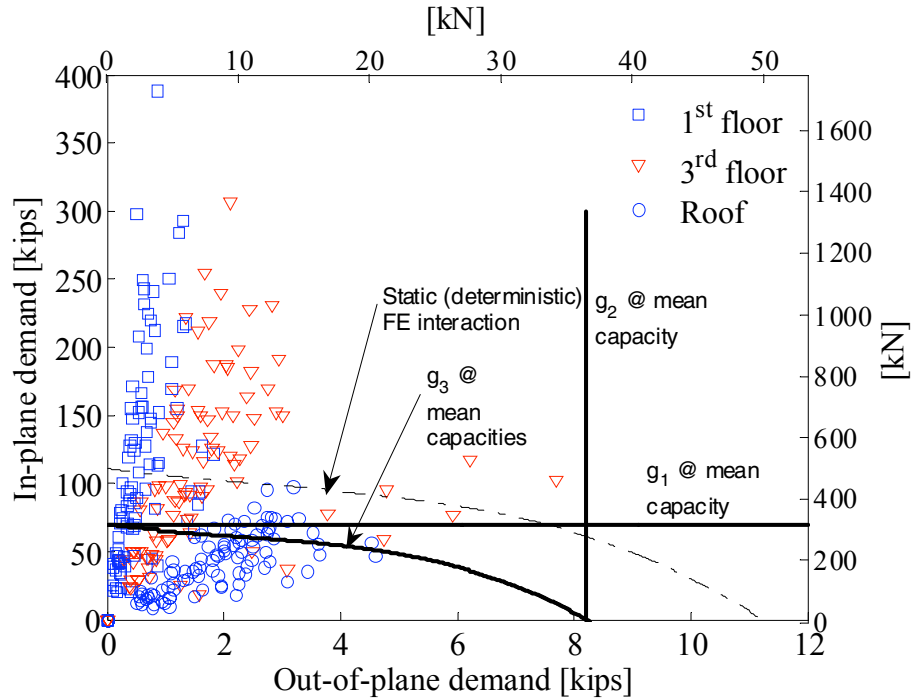


Fig. 8.6 Dispersion of URM infill wall bidirectional forces compared with capacity interaction curves.

Assuming jointly lognormal distribution for all demand forces, the obtained distributions of maximum demand forces are shown at different intensity levels in Figure 8.7, where distributions of the third floor are to the right and those of the first floor and roof are to the left. Note that the in-plane demand forces are always higher in means and variances for the first floor than the roof, while the out-of-plane demand forces have the opposite trends for the first floor and roof. This is also illustrated by Figure 8.8, which shows the distributions of the mean and standard deviations along the height of the building for the in-plane and the out-of-plane forces for the indicated ground motion intensity levels. Figure 8.8 clearly indicates larger variances of the out-of-plane forces at the third-floor level, which is attributed to possible higher mode effects in the case study structure.

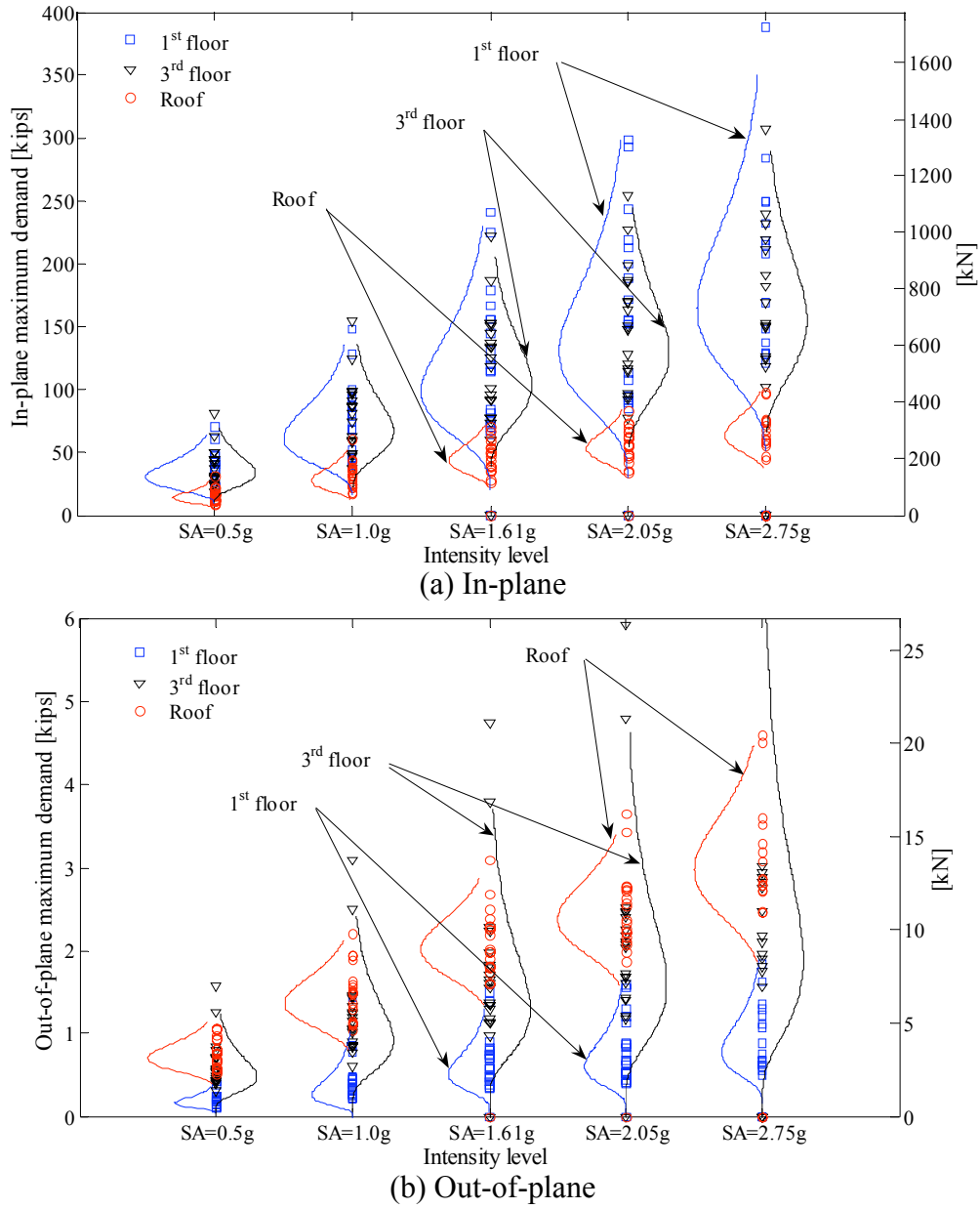
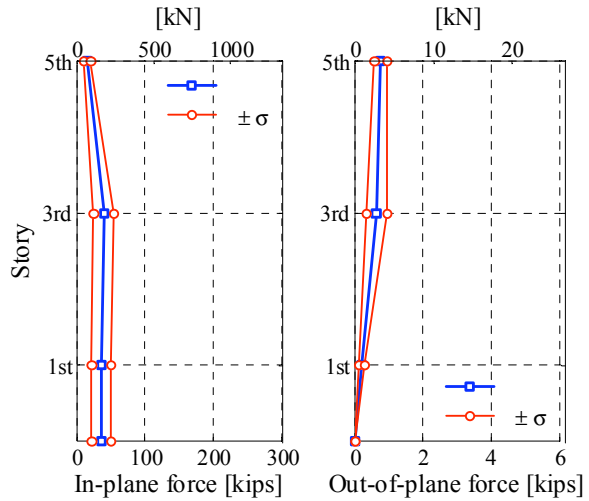
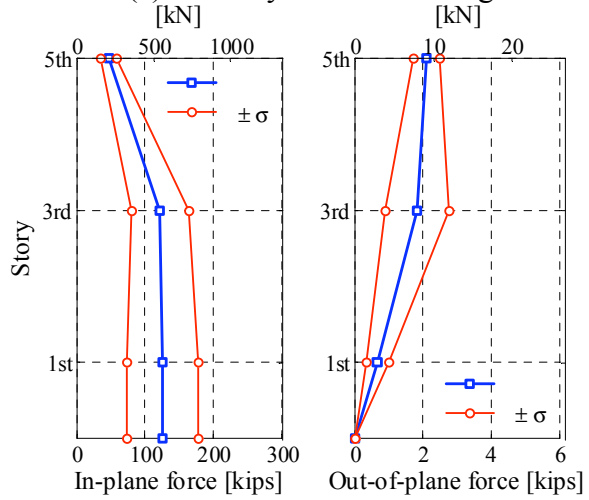


Fig. 8.7 Distributions of demand forces.

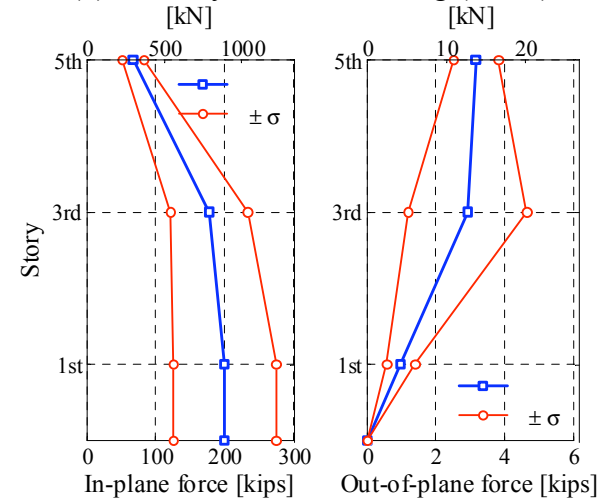
The numerical values of the mean μ , standard deviation σ , and coefficient of variation δ , at different stories for the in-plane (IP) and the out-of-plane (OP) forces are listed in Table 8.2. The correlation coefficients between the in-plane and the out-of-plane forces of the URM infill walls are listed in Table 8.3.



(a) Intensity level $SA = 0.5\text{ g}$



(b) Intensity level $SA = 1.61\text{ g}$ (10/50)



(c) Intensity level $SA = 2.75\text{ g}$ (2/50)

Fig. 8.8 Demand distributions along building height.

Table 8.2 Demand statistics for URM infill walls in case study structure.

<i>SA</i> (g)	Statistical property	1 st floor		3 rd floor		Roof	
		IP	OP	IP	OP	IP	OP
0.5	[kips (kN)]	36.4 (162)	0.20 (0.90)	40.2 (179)	0.65 (2.88)	15.8 (70)	0.77 (3.40)
	σ [kips (kN)]	13.8 (61)	0.08 (0.36)	15.0 (67)	0.30 (1.35)	5.24 (23)	0.19 (0.82)
	δ	0.38	0.40	0.37	0.47	0.33	0.24
1.0	[kips (kN)]	75.6 (336)	0.44 (1.98)	79.6 (354)	1.24 (5.52)	31.4 (140)	1.47 (6.53)
	σ [kips (kN)]	30.0 (133)	0.29 (1.29)	28.6 (127)	0.59 (2.63)	10.2 (46)	0.33 (1.47)
	δ	0.40	0.65	0.36	0.48	0.33	0.22
1.61	[kips (kN)]	125 (558)	0.68 (3.03)	122 (543)	1.84 (8.16)	47.3 (210)	2.12 (9.41)
	σ [kips (kN)]	52.6 (234)	0.32 (1.40)	41.6 (185)	0.94 (4.19)	12.3 (55)	0.38 (1.71)
	δ	0.42	0.46	0.34	0.51	0.26	0.18
2.05	[kips (kN)]	164 (729)	0.81 (3.60)	149 (663)	2.27 (10.1)	56.9 (253)	2.49 (11.1)
	σ [kips (kN)]	67.2 (299)	0.38 (1.67)	47.8 (212)	1.18 (5.26)	13.2 (59)	0.46 (2.05)
	δ	0.41	0.46	0.32	0.52	0.23	0.18
2.75	[kips (kN)]	200 (890)	0.98 (4.38)	178 (791)	2.93 (13.1)	67.9 (302)	3.16 (14.1)
	σ [kips (kN)]	74.9 (333)	0.41 (1.84)	55.9 (248)	1.72 (7.66)	15.4 (68)	0.66 (2.92)
	δ	0.37	0.42	0.31	0.59	0.23	0.21

Table 8.3 Correlation coefficient between in-plane and out-of-plane demands.

<i>SA</i> (g)	0.50	1.00	1.61	2.05	2.75
1st floor	-0.19	0.01	-0.11	-0.07	-0.11
3rd floor	-0.31	-0.36	-0.30	-0.32	-0.27
Roof	-0.10	-0.22	-0.37	-0.28	-0.32

8.5 CAPACITY ESTIMATION

The values and statistical properties of the in-plane and the out-of-plane capacities of the URM infill walls should ideally be determined by either an extensive experimental study with a sufficient number of tests for statistical analysis, or by performing a probabilistic FE analysis (Lee and Mosalam 2004), e.g., using the Monte Carlo method, with frame and infill material and geometrical parameters represented as random variables. As such, both the experimental data and the deterministic FE results provided in Chapters 6 and 7, respectively, are insufficient in determining the necessary statistical properties of the URM infill wall capacities. Nevertheless, the main goal here is to present a framework for a practical reliability study, and the presented illustrative results should be viewed with these limitations in mind. For these reasons, the statistical properties of the in-plane and the out-of-plane capacities of the URM infill walls are

adopted from the FEMA 356 provisions and shown in Table 8.4 where a coefficient of variation of 0.231 is assumed in agreement with the 1.3 factor defined in Table 7-2 of FEMA 356 provisions (2000) as the ratio between the mean and the mean minus one standard deviation, i.e., $\mu/(\mu - \sigma) = 1.3 \Rightarrow \delta = \sigma/\mu = 0.3/1.3 = 0.231$. The detailed calculations leading to the values in Table 8.4 are discussed in Chapter 7. In this study, a jointly lognormal distribution with a correlation coefficient of 0.3 is assumed for the in-plane and the out-of-plane capacities. A parametric study of the effects of the correlation coefficient of the capacities on the failure probability of the URM infill wall, Section 8.4, suggests that the results are not sensitive to the value chosen for this correlation coefficient.

Table 8.4 Capacity statistics for URM infill wall per FEMA 356 provisions.

	[kips (kN)]	σ [kips (kN)]
In-plane (R_H)	69.4 (309)	16.0 (71.2)
Out-of-plane (R_N)	8.19 (36.4)	1.89 (8.40)

The FEMA 356 provisions does not discuss the interaction between the in-plane and the out-of-plane forces on the URM infill walls. In order to account for this interaction, the best-fit bidirectional interaction curve obtained from the detailed FE model of the URM infill wall described in Chapter 7 is considered.

8.6 LIMIT-STATE FUNCTIONS

The third-degree polynomial defined as the best fit to the in-plane and out-of-plane interaction results of the FE analysis in Figure 7.33 is considered as the basis for the combined in-plane and out-of-plane limit-state function used in the subsequent reliability analysis. It should be pointed out that on the one hand, the FE analyses are performed *statically* and thus overestimate the in-plane capacities when compared to transient dynamic analysis results as shown in Chapter 7, (Fig. 7.27). On the other hand, since the performed FE analyses are *deterministic*, no information on the statistical properties of the parameters of this interaction relationship is available. However, by scaling the third-degree polynomial using the statistical properties in Table 8.4, a reasonable limit-state function can be obtained incorporating the uncertainties in both demand and capacity, as shown by the solid line in Figure 8.6. The factors used in this scaling are R_H/θ_4

and R_N/θ_5 for the in-plane and the out-of-plane axes, respectively, where R_H and R_N refer to the in-plane and the out-of-plane capacities and θ_4 and θ_5 are the intersections of the best-fit third-degree polynomial (the dash-dot line in Fig. 8.6) with the vertical (in-plane) and horizontal (out-of-plane) axes, respectively. Accordingly, limit-state functions g_1 , g_2 , and g_3 are respectively proposed for the pure in-plane, pure out-of-plane, and combined in-plane and out-of-plane failures of the URM infill wall as defined below.

$$g_1 = R_H - P_H \quad (8.1)$$

$$g_2 = R_N - P_N \quad (8.2)$$

$$g_3 = \left(\theta_1 \left(\theta_5 \frac{P_N}{R_N} \right)^3 + \theta_2 \left(\theta_5 \frac{P_N}{R_N} \right)^2 + \theta_3 \left(\theta_5 \frac{P_N}{R_N} \right) + \theta_4 \right) \frac{R_H}{\theta_4} - P_H \quad (8.3)$$

where the coefficients $\theta_1 = -0.114$, $\theta_2 = 0.948$, $\theta_3 = -6.18$, $\theta_4 = 111$, and $\theta_5 = 11.2$. The random variables P_H and P_N refer to the in-plane and the out-of-plane demands, respectively. The above three limit-state functions are shown in Figure 8.6 with capacity random variables at their mean values.

8.7 RELIABILITY ANALYSIS AND DISCUSSION

The first-order reliability method (FORM) (Haldar and Mahadevan 2000), which uses linear approximation of the limit-state function close to the design point in the normal space of random variables, is utilized using the program FERUM (Haukaas and Der Kiureghian 2003) to obtain the probability of failure and the reliability indices for the three limit-state functions, i.e., in-plane (IP), out-of-plane (OP), and combined failures, for the URM infill walls in the case study structure using the demand and capacity statistical properties as defined in previous sections. It is to be noted that the demand and capacity random variables are assumed to be statistically independent. The results are summarized in Tables 8.5 and 8.6 for the failure probability and reliability indices, respectively, for different ground motion intensity levels.

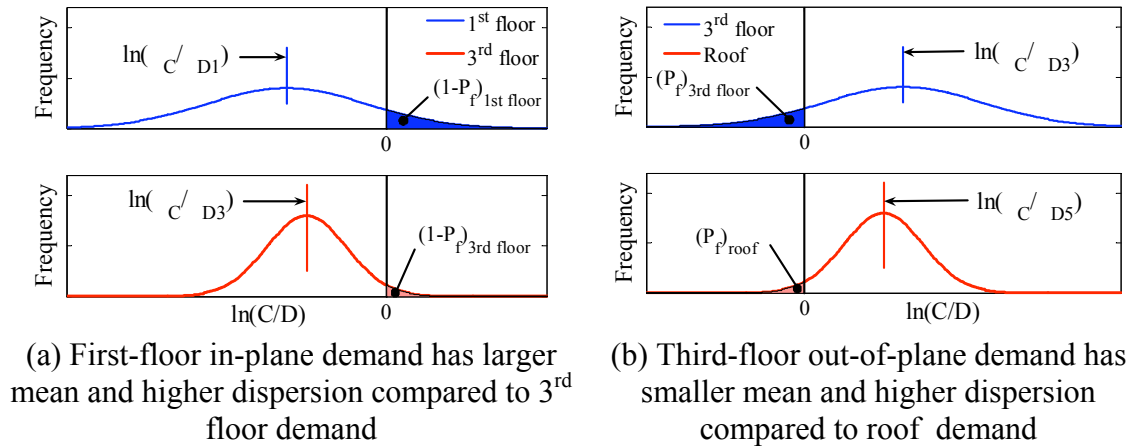


Fig. 8.9 Schematic demand and capacity distributions.

For the in-plane limit-state function g_1 , the reliability index β is lower, i.e., higher probability of failure, at the first and the third floors compared to the roof. The lowest reliability index is observed at the third-floor level. At low intensity levels, e.g., $SA = 0.5\text{ g}$, this is attributed to higher in-plane demand force at the third floor compared to the first floor (Fig. 8.8(a)). At high-intensity levels, e.g., $SA = 1.61\text{ g}$, although the mean in-plane demand is higher at the first floor at the third floor, the probability of failure is lower at the first floor due to higher dispersion (standard deviation) of the first-floor results. To illustrate this point, schematic distributions of the natural log of the ratio of the in-plane capacity over the in-plane demand for the first and third floors similar to the above case are shown in Figure 8.9(a), where the first-floor demand has higher mean ($\ln(c'/D_1) < \ln(c'/D_3)$) and higher standard deviation than the third floor but lower probability of failure. This becomes clearer by comparing the complementary to the probability of failure in this figure; thus the quantity $1 - P_f$ is highlighted where P_f is the probability of failure in the URM infill wall below the indicated floors. The lightly shaded area in Figure 8.9(a) corresponds to $1 - P_f$ for the third-floor URM infill walls, which is smaller than the dark shading corresponding to $1 - P_f$ for the first-floor URM infill walls.

For the out-of-plane limit-state function g_2 , the highest reliability index is obtained at the first floor due to small out-of-plane demand forces. Although the mean out-of-plane demand forces are generally higher at the roof compared to the third floor, the resulting failure probability is higher at the third floor due to higher dispersion (standard deviation) of the out-of-

plane demand forces at this floor (Fig. 8.8). To illustrate this point, schematic distributions of the natural logarithm of the ratio of out-of-plane capacity over out-of-plane demand for the third floor and roof similar to the above case are shown in Figure 8.9(b), where the third-floor demand has smaller mean ($\ln(c/D_3) > \ln(c/D_5)$) and higher standard deviation than the roof but higher probability of failure. The lightly shaded area in Figure 8.9(b) corresponds to the probability of failure for the roof URM infill walls, which is smaller than the dark shading corresponding to the probability of failure for the third-floor URM infill walls.

Table 8.5 Failure probability (%) of URM infill walls in case study structure for in-plane (IP), out-of-plane (OP), and combined limit-state functions.

	<i>SA</i> (g)	0.50	1.00	1.61	2.05	2.75
1st floor	IP	5.56	53.40	87.70	96.20	99.10
	OP	0.00	7.76×10^{-5}	1.28×10^{-5}	8.03×10^{-5}	1.40×10^{-4}
	Combined	6.00	55.80	89.30	96.90	99.40
3rd floor	IP	8.5	59.60	90.80	97.30	99.20
	OP	9.61×10^{-6}	5.27×10^{-3}	0.15	0.54	2.58
	Combined	10.5	65.70	93.60	98.40	99.60
Roof	IP	6.94×10^{-3}	1.82	12.70	27.00	47.40
	OP	3.23×10^{-11}	3.36×10^{-6}	1.88×10^{-4}	2.75×10^{-3}	0.10
	Combined	1.30×10^{-2}	3.35	22.40	43.10	67.60

Table 8.6 Reliability indices (β) for URM infill walls in case study structure for in-plane (IP), out-of-plane (OP), and combined limit-state functions.

	<i>SA</i> (g)	0.50	1.00	1.61	2.05	2.75
1st floor	IP	1.59	-0.09	-1.16	-1.77	-2.39
	OP	8.34	4.80	5.15	4.80	4.68
	Combined	1.55	-0.15	-1.24	-1.87	-2.50
3rd floor	IP	1.37	-0.24	-1.33	-1.92	-2.41
	OP	5.21	3.88	2.97	2.55	1.95
	Combined	1.26	-0.41	-1.52	-2.13	-2.65
Roof	IP	3.81	2.09	1.14	0.61	0.07
	OP	7.19	5.40	4.62	4.03	3.08
	Combined	3.65	1.83	0.76	0.17	-0.46

For the combined in-plane and out-of-plane limit-state function g_3 , the smallest reliability index, i.e., highest failure probability, is obtained for the third-floor URM infill walls.

This is an expected result based on the above discussion for the two extreme limit states of g_1 and g_2 which should bound the solution for the combined limit state g_3 (Fig. 8.6).

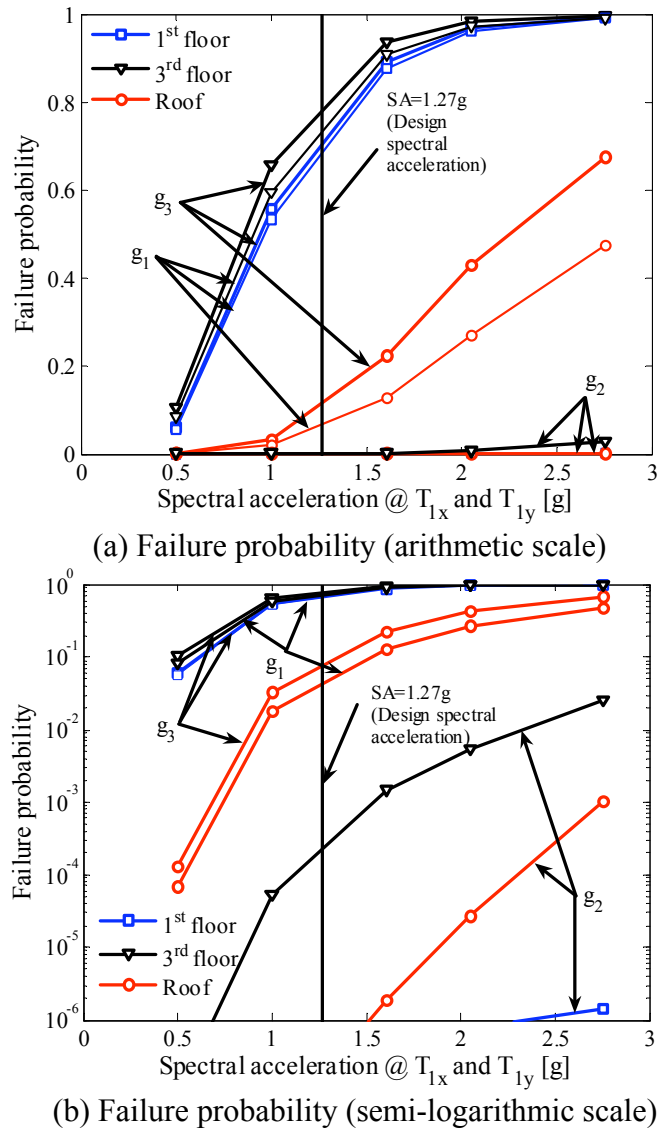


Fig. 8.10 Fragility curves for in-plane (g_1), out-of-plane (g_2), and combined in-plane and out-of-plane (g_3) limit-state functions with actual in-plane capacity.

Combining the results for different bidirectional ground motion intensity levels measured by the spectral acceleration at the natural period of the case study structure ($T_{1x} = 0.24$ sec and $T_{1y} = 0.35$ sec), discussed in Section 8.3, the fragility curves for the in-plane, the out-of-plane, and the combined limit-state functions are obtained as illustrated in Figure 8.10. While the failure probability of the URM infill walls due to the out-of-plane forces alone are negligible for the first floor and small for the third floor and roof, these forces have significant effects on the

combined failure probability, and the higher these URM infill walls in the structure, the more important is the consideration of the out-of-plane forces. For example, at the design spectral acceleration $SA = 1.27$ g, discussed in Section 8.3, for the URM infill walls in the story below the roof level of the case study structure, the failure probability based only on the in-plane limit-state function is 6.7% and based only on the out-of-plane limit-state function is as negligible as 8.5×10^{-5} %. However, by considering the combined effects of the in-plane and the out-of-plane forces, a significantly higher failure probability of 11.8% is obtained.

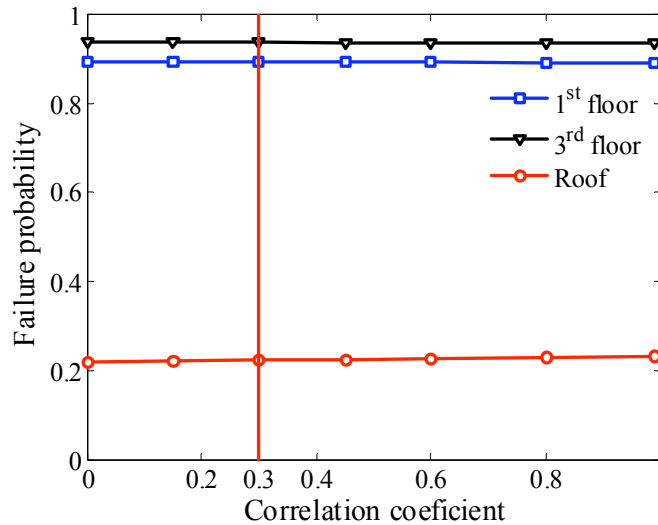


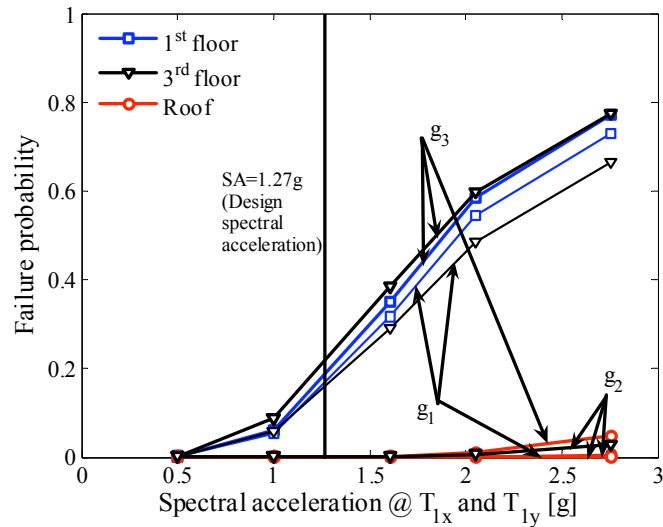
Fig. 8.11 Variation of failure probability with respect to correlation coefficient between in-plane and out-of-plane capacities of URM infill wall for intensity level $SA = 1.61$ g (10/50).

In order to investigate the sensitivity of the results with respect to the assumed correlation coefficient between the in-plane and the out-of-plane capacities, the analysis procedure described above is repeated, and the failure probability of the URM infill wall due to the combined effects of the in-plane and the out-of-plane demand forces is evaluated at intensity level $SA = 1.61$ g for different values of the correlation coefficients ranging from zero to one. The results are presented for the first floor, third floor, and roof in Figure 8.11, with the vertical line representing the correlation coefficient assumed in Section 8.5. From this figure, it is observed that the failure probabilities vary slightly by less than 1% for the first and third floors and by about 5% for the roof over the whole range of variation of the correlation coefficient. These small variations suggest that the results are not sensitive to the choice of the capacity correlation coefficient and the assumed value of 0.3 in Section 8.5 is therefore acceptable.

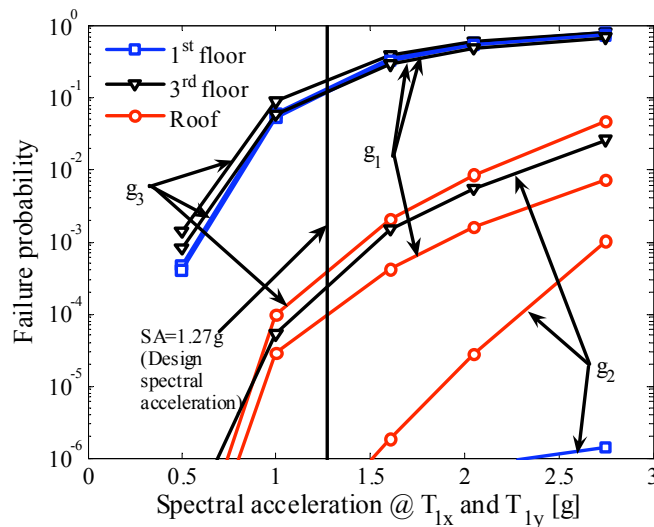
In the calculation of the in-plane capacity of the URM infill wall based on FEMA 356 provisions (2000), discussed in Chapter 7, the value of the expected shear strength of the masonry material of the infill wall f_{vie} is limited to the expected masonry shear strength, $v_{me} = 123$ psi (848 kPa) defined in Equation 7.5. Relieving this requirement, the shear strength of masonry would have been obtained from the masonry shear experiments (see Chapter 4) as 263 psi (1.81 MPa) resulting in the in-plane capacity R_H with the mean of 148 kips (658 kN) and standard deviation of 34.2 kips (152 kN) instead of the reported values of 69.4 kips (309 kN) and 16.0 kips (71.2 kN), respectively, in Table 8.4 for FEMA 356 provisions. Although these values overestimate the in-plane capacity obtained from the experimental data (Fig. 6.17) and the FE results (Fig. 7.21) by 18% and 30%, respectively, it is informative to investigate the effect of the increase of the in-plane capacity on the resulting fragility curves. Following similar reliability analyses as described above, the failure probabilities for the URM infill walls at the first floor, third floor, and roof of the case study structure are determined and presented at different hazard levels in arithmetic and semi-logarithmic scales in Figures 7.12(a) and (b), respectively.

For the URM infill walls with increased in-plane capacity (unchanged out-of-plane capacity), the maximum in-plane-only (g_1) probability of failure is associated with the first-floor URM infill walls. On the other hand, for the combined in-plane and out-of-plane limit-state function (g_3), the highest failure probability is obtained for the third-floor URM infill walls due to the added effects of the out-of-plane forces to the in-plane failure of the URM infill walls, making them the most vulnerable URM infill walls in the structure. Similar to the case of actual in-plane capacity (Fig. 8.10), it is observed that while the failure probability of the URM infill walls due to the out-of-plane forces alone is negligible for the first floor and small for the third floor and roof, the out-of-plane forces have significant effects on the combined failure probability, and the higher the URM infill walls in the structure, the more important to consider the out-of-plane forces. For example, at the design spectral acceleration $SA = 1.27$ g (refer to Section 8.3), for the URM infill walls in the story below the third floor of the case study structure, the failure probability based only on the in-plane limit-state function is 16.0% and based only on the out-of-plane limit-state function is as small as 0.07%. However, by considering the combined effects of the in-plane and the out-of-plane forces, the significantly higher failure probability of 22.0% is obtained. Therefore, neglecting the out-of-plane force

contribution leads to not only unconservative risk assessment for the URM infill walls but also misidentification of the most vulnerable URM infill walls in the structure.



(a) Failure probability (arithmetic scale)



(b) Failure probability (semi-logarithmic scale)

Fig. 8.12 Fragility curves for in-plane (g_1), out-of-plane (g_2), and combined in-plane and out-of-plane (g_3) limit-state functions with increased in-plane capacity.

The phenomenon of more URM infill wall damage accruing in the middle stories of an URM infilled RC building has been observed in real earthquakes (Fig. 8.13). However, this phenomenon should not be considered as the only possibility based on the limited study presented in this chapter and the few available observations as the one in Figure 8.13. Instead,

this phenomenon is one of the possible failures and should be properly modeled and evaluated for the considered structure when subjected to different earthquake scenarios.



Fig. 8.13 Five-story RC building with URM infill walls damaged during magnitude 6.19 Nicaragua earthquake, 12/23/1972. (Courtesy Godden Collection, EERC, University of California, Berkeley.)

8.8 LIMITATIONS AND FUTURE EXTENSION

As mentioned before, the significant effects of URM infill walls on the dynamic behavior of structures is a well-established fact. Noting the results obtained in the previous sections, the importance of considering in-plane and out-of-plane interaction when evaluating the reliability of URM infill walls in a structure is clear. In this chapter, each URM infill wall is simply modeled by a single diagonal compression-only elastic strut in each direction. While such an approach is reasonable when discussing the infill demand forces, it is not adequate if the goal is to study the

reliability of the whole structural system beyond the failure of the URM infill walls. More accurate yet complex in-plane strut models have been introduced to capture different in-plane failure mechanisms, e.g., (Mosalam et al. 1997b and 1998), and the corresponding change in the structural response. However, none of these models addresses the important effects of the out-of-plane forces.

To alleviate the deficiency in out-of-plane computational modeling of URM infill walls, the new 3-D SAT model introduced in Chapter 7 is recommended to be utilized. As demonstrated in Chapter 7, by systematically determining the new geometrical parameter, t_{eff} , and the material and geometrical properties of the elements of this 3-D SAT model, not only the in-plane and the out-of-plane capacities, but also their interaction capacity diagram (failure surface) can be introduced as part of the computational model. The resulting model would be capable of predicting the loss of URM infill walls in the structure and the corresponding effects on the force distribution and the local and the global structural behaviors. Therefore, it is possible to subject the structure to an ensemble of ground motions and gather statistical information on selected local (e.g., rotations of RC beam-column joints) and global (e.g., floor accelerations of inter-story drifts) engineering demand parameters (Lee and Mosalam 2005) a defining new criterion for failure (and its associated probability and seismic fragility) of the structure.

It should also be noted that the maximum in-plane and the out-of-plane demand forces on the URM infill wall determined in this chapter do not necessarily occur at the same time. Therefore, the current results represent conservative estimates of the failure probability. A proper consideration of the cross-correlation between these forces, e.g., response spectrum-based procedure to determine the envelope that bounds the demand forces (Menun and Der Kiureghian 2000), in conjunction with the study of the effects of the sequence of in-plane and out-of-plane loading on the failure surface and limit-state functions for the URM infill wall is needed to alleviate this conservatism in estimating the failure probabilities (fragility).

8.9 SUMMARY

Generalized, i.e., addressing the individual and combined in-plane and out-of-plane limit-state functions for a typical case study building, fragility curves are constructed for URM infill walls in a hypothetical five-story RC concrete structure including the interaction between the in-plane

and out-of-plane demand forces and capacities. The significant effects of the out-of-plane forces on the failure probability of URM infill walls are demonstrated, and it is concluded that neglecting the bidirectional interaction between these in-plane and out-of-plane seismic forces may lead to unconservative results both in identifying the most vulnerable elements and in determining the reliability of URM infill walls especially at higher elevations in the building.

In order to include bidirectional interaction for the URM infill walls, the 3D SAT model is proposed in Chapter 7. This model can be calibrated to match the experimentally or computationally determined properties of URM infill walls and used within the common structural analysis program, e.g., OpenSees, to study the structural response and reliability in the case of bidirectional ground motions including and beyond the failure of the URM infill walls.

9 Summary, Conclusions, and Future Extensions

9.1 SUMMARY

The study presented in this report was conducted in three phases. The first phase was experimental as discussed in Chapters 2–6. The second phase was analytical as discussed in Chapter 7. Finally, the third phase was probabilistic as discussed in Chapter 8.

To represent typical RC structures with URM infill walls, a five-story three bay by two bay prototype building with RC framing and URM infill wall inside the interior frames is considered. A substructure of the prototype structure containing the middle frames of the first story of the prototype structure is investigated in this report. A $\frac{3}{4}$ -scale test structure is constructed to represent the selected substructure in a simplified manner to be within the limits of the available shake table. The relationship between the demand parameters of the test structure and those of the prototype substructure is computationally established. Additional masses are added to the test structure to match the demand parameters of the prototype substructure in terms of the base shear and the floor displacement during several seismic events. The effects of the column axial force due to the weight of the upper stories on the prototype substructure are included by post-tensioning the columns of the test structure. The effects of the overturning moment due to the lateral forces on the higher stories and the effects of higher mode contributions on the prototype substructure are also evaluated and found to be negligible.

Before the start of the shake-table experiments, the material properties of concrete and masonry used in the construction of the test structure are determined using standard material tests. Moreover, several snap-back tests are performed on the test structure in both the in-plane and out-of-plane directions to determine the stiffness, natural period, and damping ratio of the test structure.

Three ground motions are selected for the shake-table experiments to evaluate the performance of the test structure during different stages of its behavior. These ground motions are scaled with reference to the NEHRP design spectrum to generate different intensity levels for the shake-table experiments. Three distinct stages of the shake-table experiments are defined and the sequence of loading for each stage presented. These three stages are (1) stage one for infilled structure with columns post-tensioned, (2) stage two, same as stage one, after removal of the collapsed URM infill wall, and (3) stage three, same as stage two, after removal of the columns post-tensioning to bring the test structure to the verge of collapse.

The results of the shake-table experiments are presented and discussed in detail. The global responses, in terms of the variation of the natural period, damping ratio, and stiffness due to damage accumulation, of the test structure during stage one of the experiments are quantified. On the other hand, the local responses, in terms of the load path and crack patterns in the URM infill wall, the distribution of forces between different structural elements, the deformed shape of the URM infill wall, and the contact length between the URM infill wall and the bounding frame, of the test structure during stage one of the experiments are discussed. The presented results from stage two of the experiments include the description of damage, the effective RC slab width in resisting the lateral forces, and the effects of the post-tensioning rods in the columns on the lateral behavior of the test structure and their self-centering effects. The state of the test structure during and after the completion of stage three of the experiments is also discussed. Important engineering demand parameters such as maximum base shear, maximum drift and residual displacements, and important structural properties of the test structure such as natural frequency, stiffness, and damping ratio are compared for all three stages of the experiments.

The analytical phase of the study consists of different computational modeling methods to represent URM infill walls in RC structures. Compression-only strut and SAT models are reviewed and the benefits and limitations of the use of such models in representing the in-plane behavior of URM infill walls in larger structural systems are discussed by comparison with the shake-table experimental results. Two-dimensional FE models of bare and infilled RC frames are constructed and verified by comparison with results obtained from pseudo-dynamic experiments. Building upon these 2D models, a 3D FE model of the test structure is developed and the results of the 3D nonlinear time-history analysis on the FE model are compared to the results obtained from the shake-table experiments. Expanding the 2D FE model of the infilled RC frame to a 3D FE model, the out-of-plane capacity and bidirectional interaction between the in-plane and the

out-of-plane forces for the URM infill wall are computationally determined and the results are compared with the experimental results obtained from the literature. A new 3D SAT model is introduced as a practical solution for including the bidirectional interaction between the in-plane and the out-of-plane forces in modeling URM infill walls in large structures. This model can be calibrated to match different experimentally or computationally determined interaction curves.

Considering the prototype structure as a case study building, a framework for determining the probability of failure of the URM infill walls at different floors of the building due to in-plane, out-of-plane and bidirectional loads is presented. As a step toward a performance-based earthquake engineering approach for RC buildings with URM infill walls, these failure probabilities are evaluated and summarized in the form of fragility functions for different ground motion intensity levels.

9.2 CONCLUSIONS

Major concluding remarks of the study presented in this report are listed in the following general points:

URM infill walls have a significant role in the strength and ductility of RC frame structures and should be considered in both analysis and design. Globally, these walls make the structure significantly stiffer, reduce the natural period of the structure, and increase the damping coefficient. Such changes significantly affect the level of demand forces and displacements on the structure. Locally, URM infill walls change the load path, the distribution of forces between different elements of the structure, and the demand forces on their adjacent elements of the bounding frame.

Due to the high relative stiffness of the URM infilled frames, they act as the main lateral load-resisting system and attract larger portions of the earthquake-induced inertial forces. In addition, it is the floor diaphragm (e.g., RC slab) that delivers the inertial forces in the structure to the URM infilled frames. This load path, in general, causes a significant increase in the demand forces on the diaphragm and collector elements. Both the frame and the floor system should be adequately designed for such increase in the demand forces due to the presence of URM infill walls.

The experimental results suggest that the presence of stiff elements in the structure such as URM infill walls reduces the effective RC slab width that may be considered in determining the lateral resistance of the URM infilled RC frames.

The cracks in the RC slab due to the gravity loads reduce its lateral stiffness. However, under sustained gravity loads, the RC slab shear force – shear deformation relationship can be practically described as linear.

The post-tensioning of the columns to simulate the weight of upper stories has a self-centering effect on the modeled lower stories of the structure and plays an important role in preventing excessive permanent floor lateral displacement and collapse of the system.

Beyond the linear range, the structural properties of RC structures with URM infill walls change during increasing levels of ground shaking. During the strong motion shaking, lower stiffness values, higher natural period and higher damping ratios are expected.

Using low-amplitude white-noise signals is not a reliable source in determining the dynamic properties of structures as these signals can not detect the extent of damage in the structures. More reliable results can be obtained using the data obtained during the actual ground shaking.

Simple compression-only strut models or more complex SAT models can be used to adequately capture the in-plane behavior of structure with URM infill walls within the linear range of the response of the masonry composite material. However, beyond the mortar cracking or failure of the URM infill walls, these models need to be carefully calibrated based on experimental results or FE studies of URM infill walls.

The developed and validated (using pseudo-dynamic and shake-table experimental results) FE models for RC frames with and without URM infill wall can be used as a powerful tool for further analyses and parametric studies of structures with different geometrical configurations and loading conditions.

Results from experimental (from published literature) and FE (from current study) investigations suggest a strong interaction between in-plane and out-of-plane capacities of the URM infill walls. Neglecting this interaction may lead to not only unconservative seismic risk evaluation but also misidentification of the most vulnerable elements in RC frame structures containing URM infill walls.

An accurate and versatile 3D SAT model is developed for practical implementation in common structural analysis programs and can be calibrated to account for the mechanical

behavior and modes of failure for URM infill walls subjected to bidirectional (in-plane and out-of-plane) loading.

A simplified framework is established for seismic reliability study of buildings containing URM infill walls including the effects of bidirectional (in-plane and out-of-plane) ground motions. This framework is utilized to determine generalized, i.e., accounting for individual and combined in-plane and out-of-plane limit-state functions, fragility functions for RC building with URM infill walls.

9.3 FUTURE EXTENSIONS

The present study fulfills its objectives in evaluating the seismic response of RC structures including the effects of URM infill walls. The experimental phase of the current study should be further pursued to include the effects of bidirectional ground motions and investigate the effect of non-seismic details for the RC frames. Future experimental studies are needed to provide a more extensive database for structural properties of buildings with URM infill walls at different infill damage states to allow quantification of the variation of damping and stiffness in such common structural systems.

The developed FE models can be used as the basis for an extensive parametric study of structures with different geometrical configurations, different loading and boundary conditions, and alternative materials. These FE models may also be used to evaluate different retrofit schemes for URM infill walls and RC frames. Furthermore, different compression-only strut models or more complex SAT models may be calibrated using the results of the FE models for any of the above-mentioned variations and used to perform a complete parametric study of the response of the URM infilled RC buildings under different loading conditions. It is worth mentioning that a computational study of a 3D URM infilled RC frame structure has been conducted by the author in Hashemi and Mosalam (2004) for blast loading.

The effects of different in-plane and out-of-plane loading sequences on the bidirectional failure surface of the URM infill walls should be investigated in conjunction with the expected cross-correlation between the in-plane and the out-of-plane demand forces. The expected outcome of this refinement is more accurate estimates of the failure probability of the URM infill walls in buildings for individual and combined in-plane and out-of-plane limit-state functions.

The introduced 3D SAT model can be modified to include the effect of different previous loading sequences and damage history through alternative material models for the tie (link) element of the model and be implemented in bidirectional reliability analysis of RC buildings with URM infill walls. Using this model, the limit-state functions may be defined in terms of other important engineering demand parameters such as column shear, story drift, or maximum floor acceleration. The 3D SAT model will enable the accurate prediction of the failure of the URM infill wall and its subsequent effects on the overall fragility of the building.

REFERENCES

- ACI Committee 318 (2002). "Building Code Requirements for Structural Concrete and Commentary." ACI 318-02 and ACI 318R-02. American Concrete Institute, Farmington Hills, MI: 443.
- American Society for Testing and Materials (2007). "Standard Specification for Deformed and Plain Carbon-Steel Bars for Concrete Reinforcement." ASTM A 615/A 615M, West Conshohocken, PA.
- American Society for Testing and Materials (2007). "Standard Specification for Mortar for Unit Masonry." ASTM C 270, West Conshohocken, PA.
- American Society for Testing and Materials (1999). "Standard Test Method for Compressive Strength of Concrete Cylinders Cast-in-Place in Cylindrical Molds." ASTM C 837, West Conshohocken, PA.
- American Society for Testing and Materials (2003). "Standard Test Method for Compressive Strength of Masonry Prisms." ASTM C 1314, West Conshohocken, PA.
- Federal Emergency Management Agency (2000). "Prestandard and Commentary for the Seismic Rehabilitation of Buildings." FEMA356, Washington, D.C.
- Angel R. and Abrams D. (1994). "Behavior of Reinforced Concrete Frames with Masonry Infills." *Structural Engineering and Structural Mechanics Research Series*, University of Illinois at Urbana.
- Benjamin, J.R. and Williams, H.A. (1958). "The Behavior of One-Story Brick Shear Walls." *Journal of Structural Division, ASCE*, Proceedings Paper 1723, 84, ST4.
- Bennett, R.M., Fowler, J.J., and Flanagan, R.D. (1996). "Shake Table Testing of Structural Clay Tile Infilled Frames." *Proceedings of the 7th North American Masonry Conference*, Notre Dame, 497-507.
- Building Seismic Safety Council (2001). "NEHRP Recommended Provisions for Seismic Regulations for New Buildings and Other Structures." Building Seismic Safety Council, Washington, D.C.
- Buonopane S.G. (1997). "Seismic Evaluation of a Masonry Infilled Reinforced Concrete Frame by Pseudo-dynamic Testing." *M.Sc. Thesis*, Cornell University, Ithaca, N.Y.
- Chopra, A.K. (2001). "Dynamics of Structures: Theory and Applications to Earthquake Engineering." Prentice Hall, Upper Saddle River, NJ.

- Chrysostomou, C.Z. (1991). "Effect of Degrading Infill Walls on the Nonlinear Seismic Response of Two-Dimensional Steel Frames." *PhD dissertation*, Cornell University, Ithaca, N.Y.
- Comité Euro-international du Béton – Fédération Internationale de la Précontrainte. (1993). "CEB-FIP Model Code 1990: Design Code." First draft, CEB, Paris, Bulletin d'Information 195.
- Crisfield M.A. (1991). "Non-Linear Finite Element Analysis of Solids and Structures." Wiley, Chichester; New York.
- Dawe J.L., Schriver A.B. and Sofocleous C. (1989). "Masonry Infilled Steel Frames Subjected to Dynamic Load." *Canadian Journal of Civil Engineering*, Volume 16: 877-885.
- Dawe J.L. and Seah C.K. (1990). "Out-of-Plane Resistance of Concrete Masonry Infilled Panels." *Journal of the Canadian Society of Civil Engineering*: 854-864.
- Dermitzakis S.N. and Mahin S.A. (1985). "Development of Substructuring Techniques for on-Line Computer Controlled Seismic Performance Testing." *University of California Earthquake Engineering Research Center*, UBC/EERC-85/04, Berkeley, CA.
- DIANA (2005). "DIANA Finite Element Analysis." Release 9, TNO DIANA BV, Delft, The Netherlands, <http://www.tnodiana.com>.
- Dolce M., Cardone D., Ponzo F. C. and Valente C. (2005). "Shaking Table Tests on Reinforced Concrete Frames without and with Passive Control Systems." *Earthquake Engineering and Structural Dynamics*, Volume 34, No. 14: 1687-1717.
- Drydale R.G. and Essawy A.S. (1988). "Out-of-Plane Bending of Concrete Block Walls." *Journal of the structural Division, ASCE*, Volume 114, No. ST1: 121-133.
- Durrani A. J. and Haider S. (1996). "Seismic Response of RC Frames with Unreinforced Masonry Infills." *Proceedings of the Eleventh World Conference on Earthquake Engineering*. Elsevier, Oxford.
- El-Dakhkhni W.W., Elgaaly M. and Hamid A. (2003). "Three-Strut Model for Concrete Masonry-Infilled Steel Frames." *Journal of Structural Engineering, ASCE*, Volume 129, No. 2: 177-185.
- Elkhoraibi T. and Mosalam K.M. (2007). "Towards Error-Free Hybrid Simulation Using Mixed Variables." *Earthquake Engineering and Structural Dynamics*. In press.

- Elkhoraibi T. (2007). "A Generalized Hybrid Simulation Framework for Structural Systems Subjected to Seismic Loading." *Ph.D. Dissertation*, Civil and Environmental Engineering, University of California, Berkeley.
- Fardis M. N., Bousias S. N., Franchioni G. and Panagiotakos T. B. (1999a). "Seismic Response and Design of RC Structures with Plan-Eccentric Masonry Infills." *Earthquake Engineering and Structural Dynamics*, Volume 28, No. 2: 173-191.
- Fardis M. N., Negro P., Bousias S. N. and Colombo A. (1999b). "Seismic Design of Open-Story Infilled RC Buildings." *Journal of Earthquake Engineering*, Volume 3, No. 2: 173-197.
- Flanagan R.D. and Bennett R.M. (1999a). "Bidirectional Behavior of Structural Clay Tile Infilled Frames." *Journal of Structural Engineering, ASCE*, Volume 125, No. 3: 236-244.
- Flanagan R.D. and Bennett R.M. (1999b). "Arching of Masonry Infilled Frames: Comparison of Analytical Methods." *Practice Periodical on Structural Design and Construction*, Volume 4, No.3: 105-110.
- Gabrielsen B.L. and Kaplan K. (1977). "Arching in Masonry Walls Subjected to out-of-Plane Forces." *Earthquake Resistant Design of Masonry Construction*, NBS Building Science Service, Volume 106: 283-313.
- Gergely P., White R.N. and Mosalam K.M. (1994). "Evaluation and Modeling of Infilled Frames." *NCEER Workshop: Seismic Response of Masonry Infills*, San Francisco, USA.
- Haldar A. and Mahadevan S. (2000). "Reliability Assessment Using Stochastic Finite Element Analysis." John Wiley & Sons, New York.
- Hamburger R.O. (1993). "Methodology for Seismic Capacity Evaluation of Steel-Frame Buildings with Infill Unreinforced Masonry." *Proceedings of 1993 National Earthquake Conference*, Central U.S. Earthquake Consortium, Memphis, Tennessee, Volume 2.
- Haseltine B.A. (1976). "Design of Laterally Loaded Wall Panels." *Proceedings of the British Ceramic Society*, U.K., Volume 5.
- Haseltine B.A., West H.W.H. and Tutt J.N. (1977). "Design of Walls to Resist Lateral Loads." *The Structural Engineers*, Volume 55, No. 10: 422-430.
- Hashemi A. and Mosalam K.M. (2004). "Transient Analysis of Reinforced Concrete Frame with and without Masonry Infill Wall under Blast." *Emirates Journal for Engineering Research*, Volume 9, No. 2: 97-103.
- Haukaas T. and Der Kiureghian A. (2003). "FERUM; Finite Element Reliability Using Matlab." <http://www.ce.berkeley.edu/FERUM/>.

- Hendry A.W. (1973). "The Lateral Strength of Unreinforced Brickwork." *The Structural Engineers*, Volume 51, No. 2: 43-50.
- Hendry A.W. and Kheir A.M.A. (1976). "The Lateral Strength of Certain Brickwork Panels." *Proceedings of the Fourth International Brick Masonry Conference*, Brugge, Belgium.
- Hilber H.M., Hughes T.J.R. and Taylor R.L. (1977). "Improved Numerical Dissipation for Time Integration Algorithms in Structural Dynamics." *Earthquake Engineering and Structural Dynamics*, Volume 5, No. 3: 283-292.
- Hill J.A. (1993). "Full-Scale Testing of Unreinforced Masonry Infill Frame Panels." *Structural Engineering in Natural Hazards Mitigation, Proceeding of the Structural Congress*, Irvine, CA.
- Holmes M. (1963). "Combined Loading on Infilled Frames." *Proceeding Of The Institution Of Civil Engineers*, Volume 25: 31-38.
- Klingner R.E., Rubiano N.R., Bashandy T.R. and Sweeney S.C. (1996). "Evaluation and Analytical Verification of Shaking Table Data from Infilled Frames. Part 2: Out-of-Plane Behavior." *Proceedings of the 7th North American Masonry Conference*, Notre Dame.
- Lee T.H. and Mosalam K.M. (2004). "Probabilistic Fiber Element Modeling of Reinforced Concrete Structures." *Computers and Structures*, Volume 82, No. 27: 2285-2299.
- Lee T.H. and Mosalam K.M. (2006). "Probabilistic Seismic Evaluation of Reinforced Concrete Structural Components and Systems." *PEER Technical Report 2006/04*.
- Liau T.C. and Kwan K.H. (1985a). "Static and Cyclic Behaviors of Multistory Infilled Frames with Different Interface Conditions." *Journal of Sounds and Vibrations*, Volume 99, No. 2: 275-283.
- Liau T.C. and Kwan K.H. (1985b). "Unified Plastic Analysis for Infilled Frames." *Journal of Structural Engineering, ASCE*, Volume 111, No. 7: 1427-1448.
- Lotfi H.R. and Shing P.B. (1991). "An Appraisal of Smeared Crack Models for Masonry Shear Wall Analysis." *Computers and Structures*, Volume 41, No. 3: 413-425.
- Lotfi H.R. and Shing P.B. (1994). "Interface Model Applied to Fracture of Masonry Structures." *Journal of Structural Engineering, ASCE*, Volume 120, No. 1: 63-80.
- Lourenço P.B. (1996). "Computational Strategies for Masonry Structures." *PhD Dissertation*, Delft University of Technology, Netherlands.

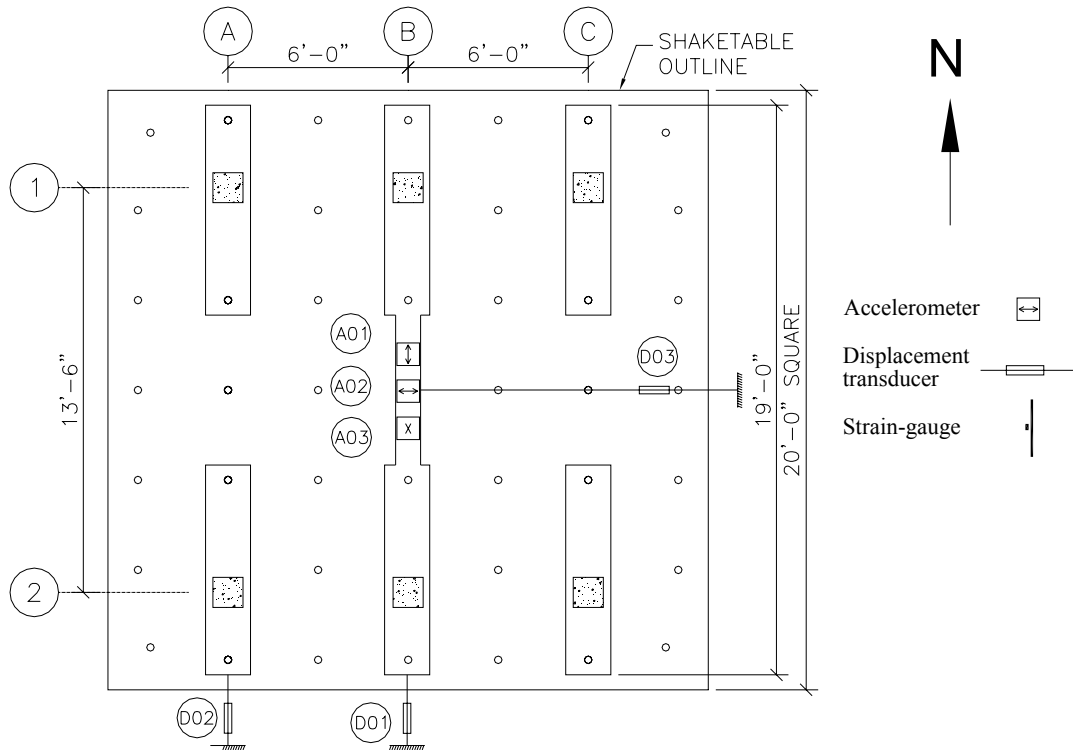
- Mander J.B., Nair B., Wojtkowski K. and Ma J. (1993). "An Experimental Study of the Seismic Performance of Brick Infilled Frames with and without Retrofit." *Technical Report NCEER-93-0001*, State University of New York at Buffalo.
- Mander J.B., Priestley M.J.N. and Park R. (1988a). "Observed Stress – Strain Behavior of Confined Concrete." *Journal of Structural Engineering, ASCE*, Volume 114, No. 8: 1827-1849.
- Mander J.B., Priestley M.J.N. and Park R. (1988b). "Theoretical Stress – Strain Behavior of Confined Concrete." *Journal of Structural Engineering, ASCE*, Volume 114, No. 8: 1804-1826.
- Manzouri T. and Shing P.B. (1995). "Repair and Retrofit of Reinforced Masonry Walls: Experimental Evaluation and Finite Element Analysis." *Structural Engineering and Structural Mechanics Research Series, CU/SR-95/2*, University of Colorado, Boulder, CO.
- Mazzoni S., McKenna F., Scott M.H., and Fenves G.L. (2006). "Open System for Earthquake Engineering Simulation (OpenSees), User Command-Language Manual." Pacific Earthquake Engineering Research Center, University of California, Berkeley, <http://opensees.berkeley.edu/OpenSees/manuals/>.
- McDowell E.L., McKee K.E. and Sevin E. (1956). "Discussion of Arching Action Theory of Masonry Walls." *Journal of Structural Division, ASCE*, Volume 92, No.2: 915:1-915:18.
- Mehrabi, A.B., Shing P.B., Schuller M.P., and Noland J.L. (1994). "Performance of Masonry-Infilled R/C Frames under in-Plane Lateral Loads." *Structural Engineering and Structural Mechanics Research Series, CU/SR-94/6*, University of Colorado, Boulder, CO.
- Menun C. and Der Kiureghian A. (2000). "Envelopes for Seismic Response Vectors. I: Theory." *Journal of Structural Engineering, ASCE*, Volume 126, No. 4: 467-473.
- Moghaddam H.A. and Dowling P.J. (1987). "The State of the Art in Infilled Frames." *ESEE Research Report*, Civil Engineering Department, Imperial College of Science and Technology, London, No. 87-2.
- Monk C.B. (1958). "Resistance of Structural Clay Masonry to Dynamic Forces." *Structural Clay Products Research Foundation*, Research Report No. 7, Geneva, Illinois.
- Mosalam K.M. (1996a). "Experimental and Computational Strategies for the Behavior Evaluation of Frames with Infill Walls." *PhD Dissertation*, Cornell University, Ithaca, N.Y.
- Mosalam K.M. (1996b). "Modeling of the Nonlinear Seismic Behavior of Gravity Load Designed Frames." *Earthquake Spectra*, Volume 12, No. 3: 479-492.

- Mosalam K.M., Ayala G., White R.N. and Roth C. (1997a). "Seismic Fragility of LRC Frames with and without Masonry Infill Walls." *Journal of Earthquake Engineering*, Volume 1, No. 4: 693-720.
- Mosalam K.M., White R.N. and Gergely P. (1997b). "Static Response of Infilled Frames Using Quasi-Static Experimentation." *Journal of Structural Engineering, ASCE*, Volume 123, No. 11: 1462-1469.
- Mosalam K.M., White R.N. and Ayala G. (1998). "Response of Infilled Frames Using Pseudo-Dynamic Experimentation." *Earthquake Engineering and Structural Dynamics*, Volume 27, No. 6: 589-608.
- Mosalam K.M. (1998). "Seismic Behavior of Infilled Frames." *MCEER Bulletin*, Volume 12, No. 2.
- Negro P. and Verzeletti G. (1996). "Effect of Infills on the Global Behavior of RC Frames: Energy Considerations from Pseudo-Dynamic Tests." *Earthquake Engineering and Structural Dynamics*, Volume 25, No. 8: 753-773.
- Pires F., Rodrigues J. and Campos-Costa A. (1998). "Experimental Study of the Behavior under Horizontal Actions of Repaired Masonry Infilled RC Frames." *Proceedings of the Eleventh European Conference on Earthquake Engineering*, Balkema, Rotterdam.
- Sabnis G.M., Harris H.G., White R.N. and Mirza M.S. (1983). "Structural Modeling and Experimental Techniques." Prentice-Hall, Inc., Englewood Cliffs, NJ.
- Stafford-Smith B.S. (1962). "Lateral Stiffness of Infilled Frames." *Journal of Structural Division, ASCE*, Volume 88, No. ST1: 183-199.
- Stafford-Smith B.S. (1966). "Behavior of Square Infilled Frames." *Journal of Structural Division, ASCE*, Volume 92, No. ST1: 381-403.
- Stafford-Smith B.S. (1968). "Model Test Results of Vertical and Horizontal Loading of Infilled Frames." *ACI Journal*, Volume 65, No. 8: 618-625.
- Talaat M. and Mosalam K.M. (2006). "Progressive Collapse Modeling of Reinforced Concrete Framed Structures Containing Masonry Infill Walls." *Proceedings of the 2nd NEES/E-Defense Workshop on Collapse Simulation of Reinforced Concrete Building Structures*, Kobe, Japan.
- Talaat M. and Mosalam K.M. (2007). "Towards Modeling Progressive Collapse in Reinforced Concrete Buildings." *Proceedings of the 2007 Structures Congress, SEI/ASCE*, Long Beach, CA.

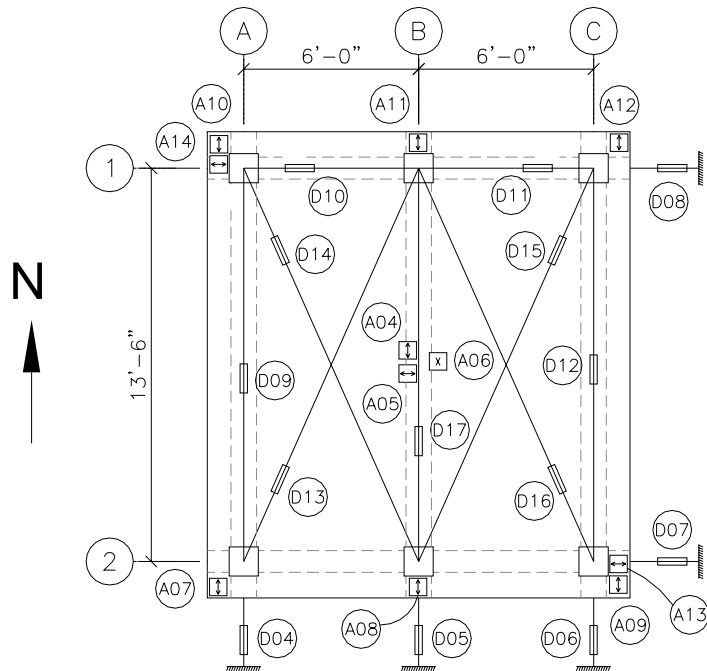
- Talaat M. (2007). "Computational Modeling of Progressive Collapse in Reinforced Concrete Framed Structures" *Ph.D. Dissertation*, Civil and Environmental Engineering, University of California, Berkeley.
- Thiruvengadam V. (1985). "On the Natural Frequencies of Infilled Frames." *Earthquake Engineering and Structural Dynamics*, Volume 13, No. 3: 401-419.
- Timishenko S. and Woinowsky S. (1959). "Theory of Plates and Shells." McGraw-Hill, New York, N.Y.
- Trifunac M.D. and Brady A.G. (1975). "A Study on the Duration of Strong Earthquake Ground Motion." *Bulletin of the Seismological Society of America*, Volume 65, No. 3: 581-626.
- US Geological Survey (2007). <http://earthquake.usgs.gov>.
- Vecchio F.J. and Collins M.P. (1993). "Compression Response of Cracked Reinforced Concrete." *Journal of Structural Engineering, ASCE*, Volume 119, No. 12: 3590-3610.
- Zarnic R., Gosti S., Crewe A.J. and Taylor C.A. (2001). "Shaking Table Tests of 1:4 Reduced-Scale Models of Masonry Infilled Reinforced Concrete Frame Buildings." *Earthquake Engineering and Structural Dynamics*, Volume 30, No. 6: 819-834.

Appendix A: Instrumentation Details

In this appendix, detailed drawings of all instrumentation are presented. Figure A.1 shows displacement transducers and accelerometers on the levels of the shake table and the RC floor slab. Displacement transducers on the vertical planes are shown in Figure A.2. Strain gages on the reinforcing steel bars for different locations in the RC frames and the RC slab are illustrated in Figures A.3 and A.4, respectively. It should be noted that in Figures A.3 and A.4, only the strain gages that are used during the shake-table experiments are numbered. In these figures, the tag number for displacement transducers are preceded by the letter D, and the tag number for accelerometers are preceded by the letter A. The gaged reinforcing bars are also identified by filled circles on the cross sections of the structural elements.

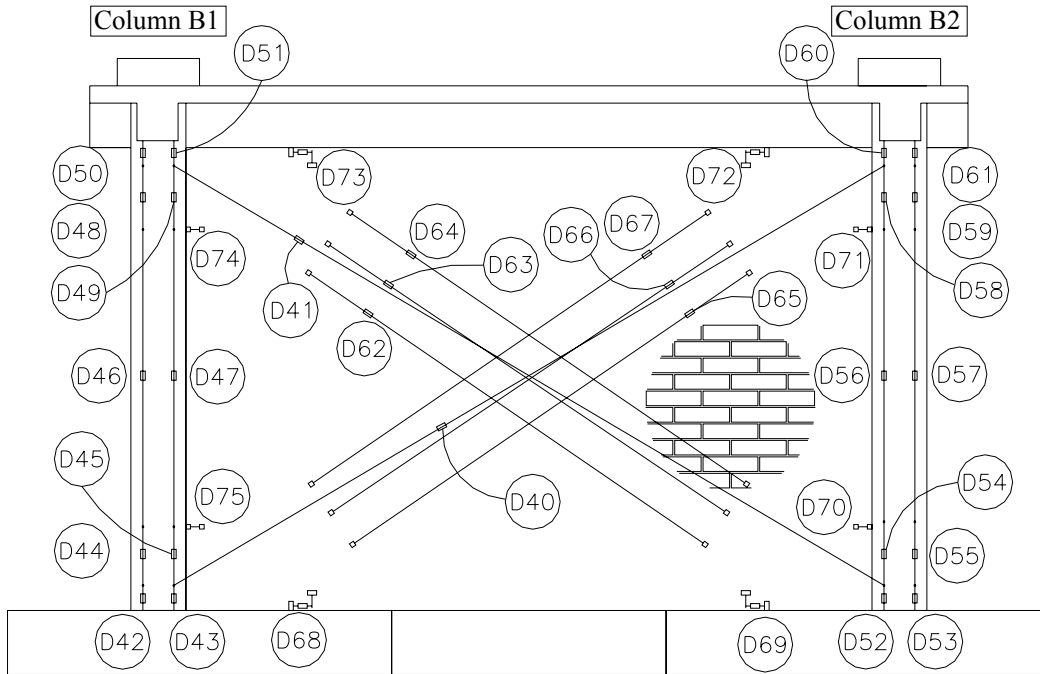


(a) Instrumentation plan on level of shake table

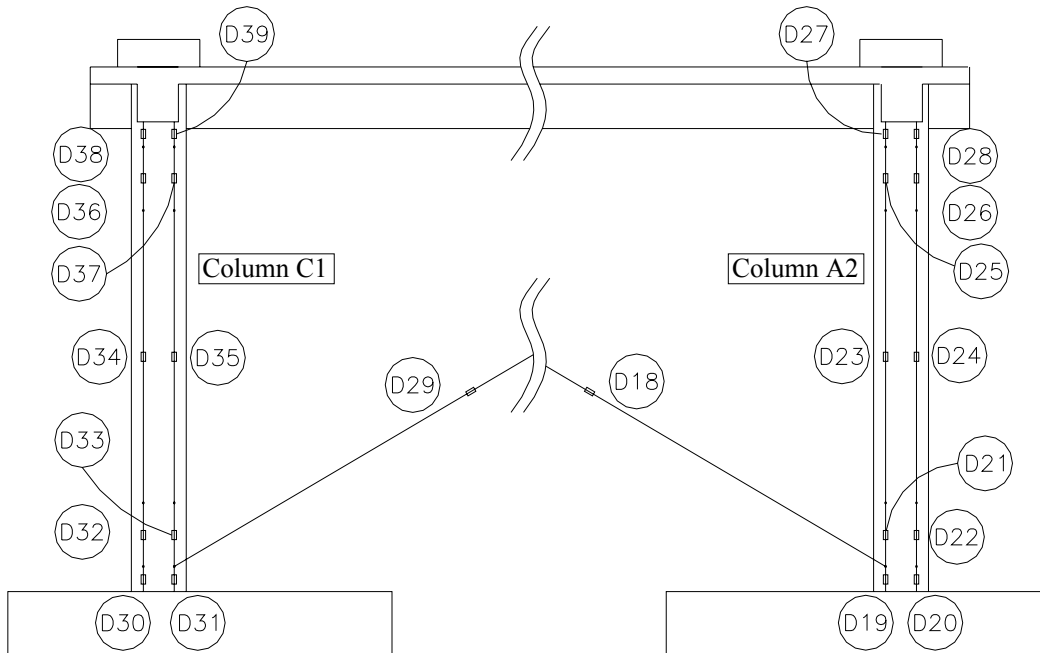


(b) Instrumentation plan on level of RC floor slab

Fig. A.1 Displacement transducers and accelerometers in horizontal planes (1" = 25.4 mm, 1' = 30.48 cm).

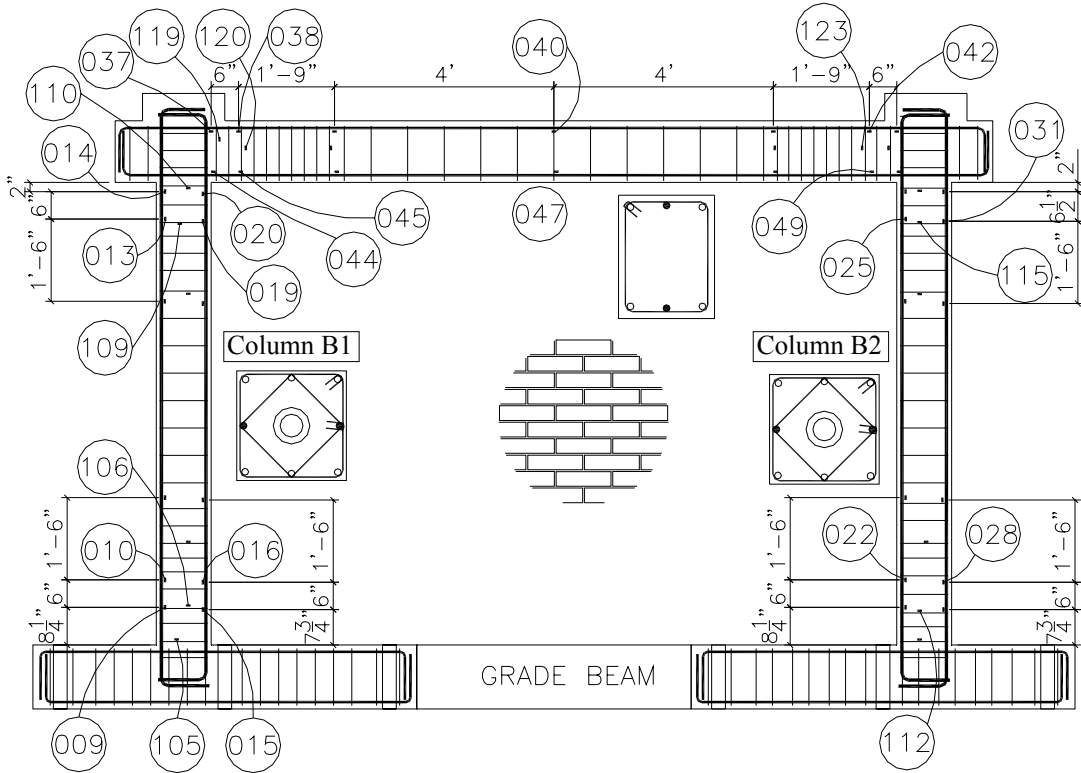


(a) Instrumentation elevation in plane of URM infill wall

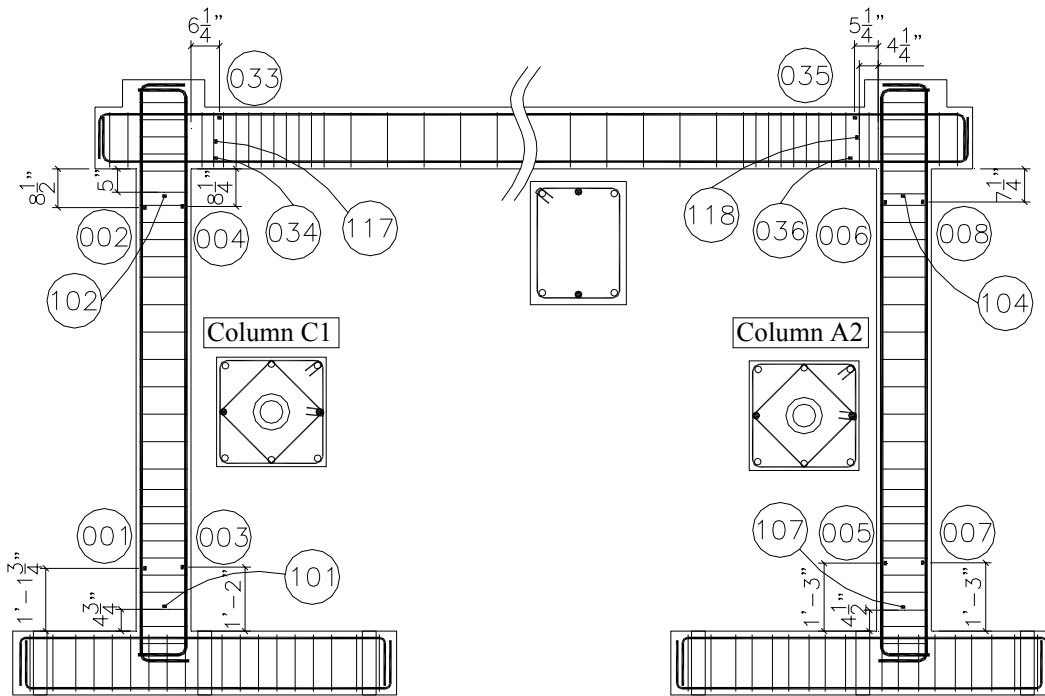


(b) Instrumentation elevation in plane of bare frames A and C

Fig. A.2 Displacement transducers in vertical planes.



(a) Infilled frame



(b) Bare frame

Fig. A.3 Strain gages for steel reinforcing bars of RC frames (1" = 25.4 mm, 1' = 30.48 cm).

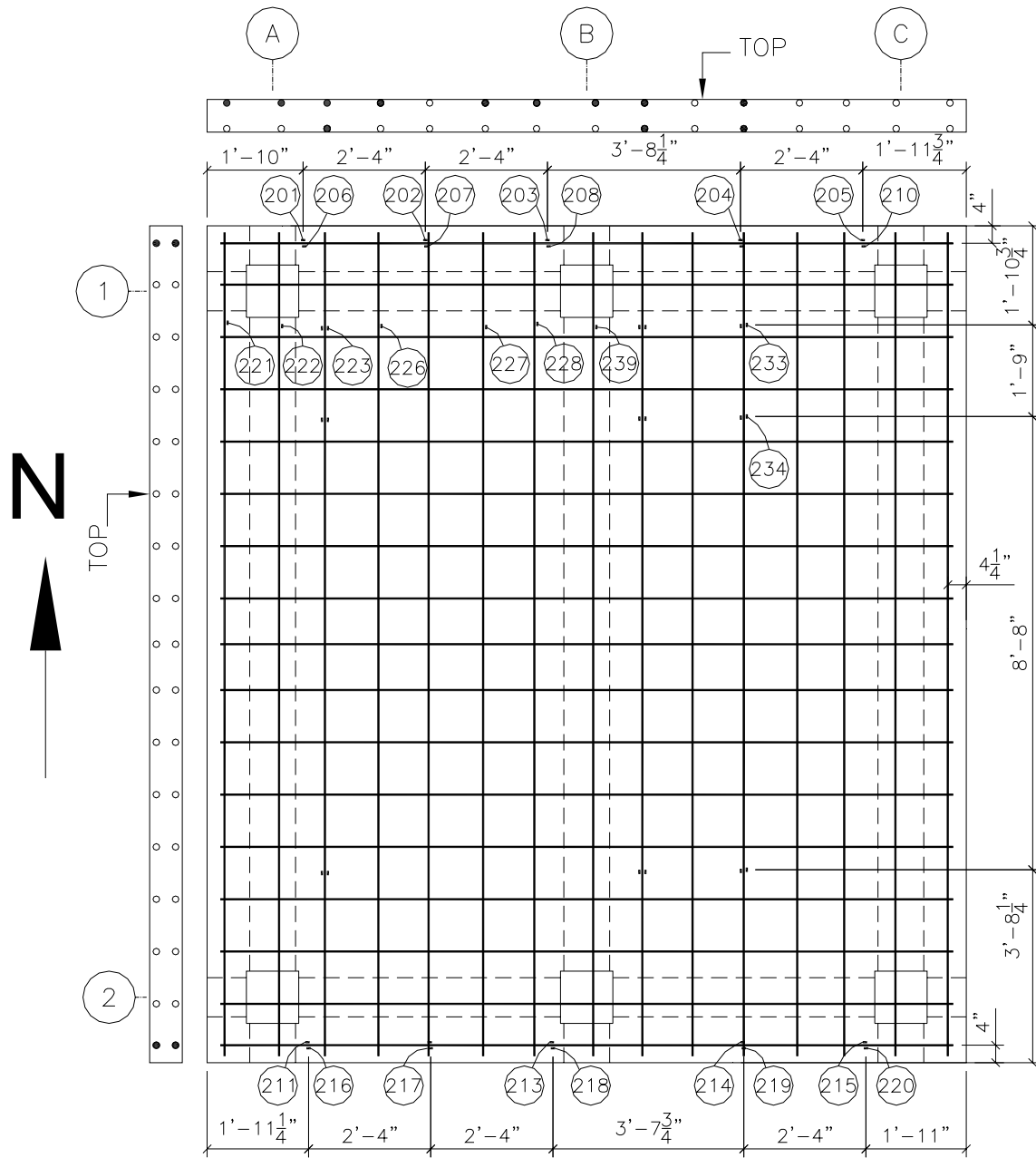


Fig. A.4 Strain gages for steel reinforcing bars of RC slab (1" = 25.4 mm, 1' = 30.48 cm).

Appendix B: Snap-Back Test Results

This appendix includes all test results for the pull (snap-back) tests performed on the test structure for different construction phases. These tasks were conducted before any of the shake-table experiments. These construction phases include the following:

1. Before building the URM infill wall and before post-tensioning of the columns without any additional mass, Table B.1 and Figure B.1.
2. After building the URM infill wall including post-tensioning the columns but without any additional mass, Table B.2 and Figure B.2.
3. After building the URM infill wall including post-tensioning the columns and after adding the mass, Table B.3 and Figure B.3. This phase was carried out just before conducting the shake-table experiments.

The force-displacement records during the pulling phase for each test were used to determine the stiffness of the test structure. The free vibration (FV) RC slab acceleration response of the test structure is analyzed in the frequency domain using the fast Fourier transform (FFT) to determine the natural frequency of the test structure. Moreover, the time domain response of the FV RC slab acceleration response of the test structure is used to determine the damping ratio.

Table B.1 Snap-back tests before building URM infill wall and before post-tensioning columns (no additional mass).

Direction	Test No.	Evaluation method	Natural frequency (Hz)	Natural period (sec)	Stiffness* [kips/in.]	Damping ratio (%)
North-South (longitudinal or in-plane)	1	Force-displacement	-	-	107	-
		FV: frequency domain	7.56	0.132	-	-
		FV: time domain	7.23	0.138	-	5.1
	2	Force-displacement	-	-	108	-
		FV: frequency domain	7.67	0.130	-	-
		FV: time domain	7.50	0.133	-	5.4
	3	Force-displacement	-	-	117	-
		FV: frequency domain	7.55	0.132	-	-
		FV: time domain	7.20	0.139	-	4.9
	Mean		7.41	0.135	111	4.3
COV (%)		2.6	2.6	5.0	4.9	
East-west (transverse or out-of-plane)	1	Force-displacement	-	-	-	-
		FV: frequency domain	7.68	0.130	-	-
		FV: time domain	7.41	0.135	-	4.5
	2	Force-displacement	-	-	123	-
		FV: frequency domain	7.58	0.132	-	-
		FV: time domain	7.25	0.138	-	4.2
	3	Force-displacement	-	-	120	-
		FV: frequency domain	7.64	0.131	-	-
		FV: time domain	7.52	0.133	-	5.1
	Mean		7.46	0.134	122	4.4
COV (%)		2.2	2.2	1.7	10	

*(1 kip/in. = 0.175 kN/mm)

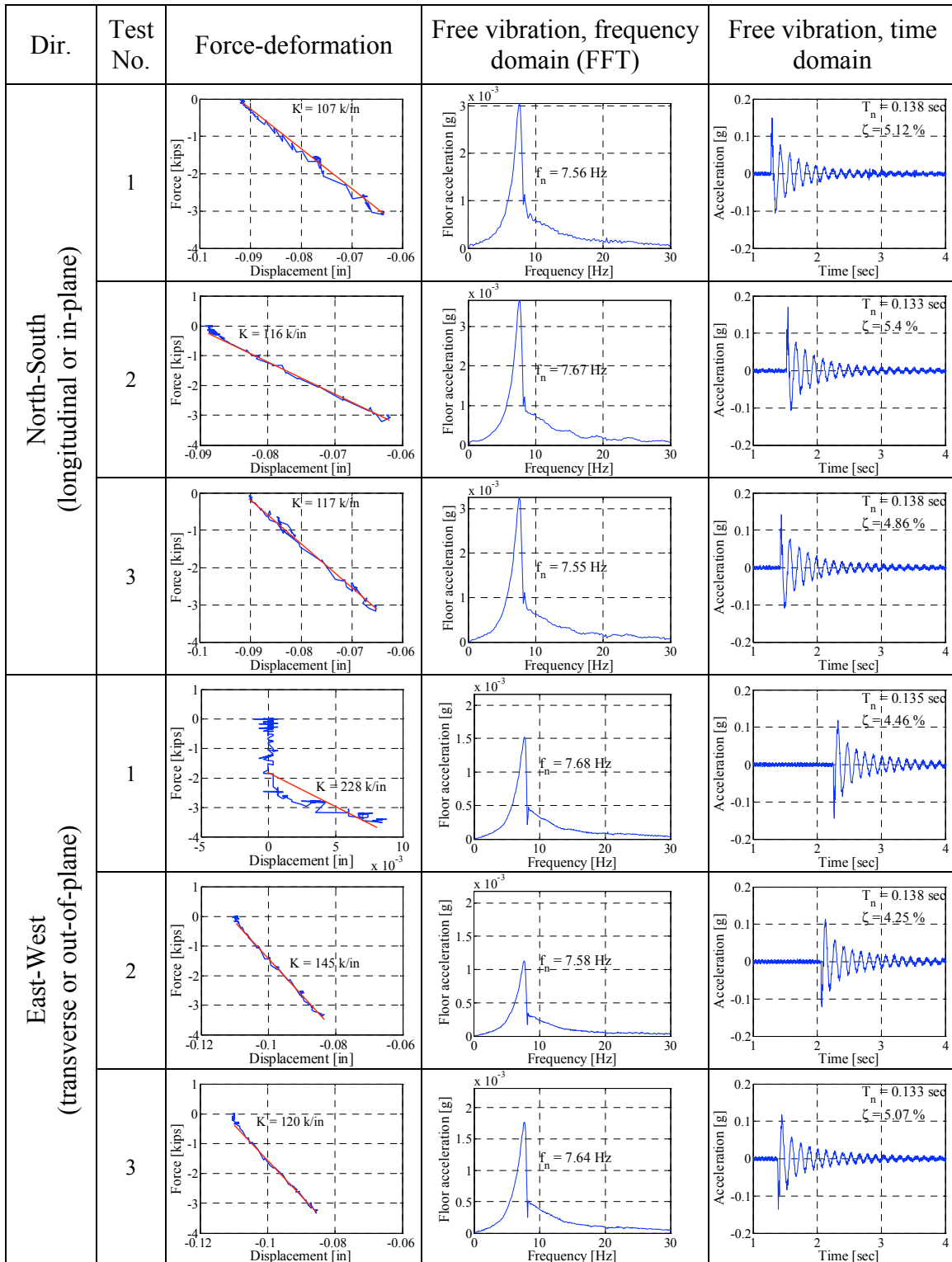


Fig. B.1 Snap-back tests before building URM infill wall and before post-tensioning columns (no additional mass) (1 kip = 4.45 kN, 1 in. = 25.4 mm).

Table B.2 Snap-back tests after building URM infill wall and after post-tensioning columns (no additional mass).

Direction	Test No.	Evaluation method	Natural frequency (Hz)	Natural period (sec)	Stiffness* [kips/in.]	Damping ratio (%)
North-South (longitudinal or in-plane)	1	Force-displacement	-	-	416	-
		FV: frequency domain	17.9	0.0557	-	-
		FV: time domain	18.2	0.0550	-	7.3
	2	Force-displacement	-	-	434	-
		FV: frequency domain	18.2	0.0548	-	-
		FV: time domain	17.4	0.0575	-	5.0
	3	Force-displacement	-	-	427	-
		FV: frequency domain	18.2	0.0550	-	-
		FV: time domain	18.2	0.0550	-	4.9
	Mean		18.0	0.0550	426	5.7
COV (%)		1.8	1.8	2.1	2.4	
East-West (transverse or out-of-plane)	1	Force-displacement	-	-	179	-
		FV: frequency domain	8.48	0.117	-	-
		FV: time domain	8.16	0.123	-	4.8
	2	Force-displacement	-	-	166	-
		FV: frequency domain	8.43	0.119	-	-
		FV: time domain	7.84	0.128	-	4.0
	3	Force-displacement	-	-	156	-
		FV: frequency domain	8.43	0.119	-	-
		FV: time domain	7.69	0.130	-	4.1
	Mean		8.17	0.122	167	4.3
COV (%)		3.6	3.6	6.9	10	

*(1 kip/in. = 0.175 kN/mm)

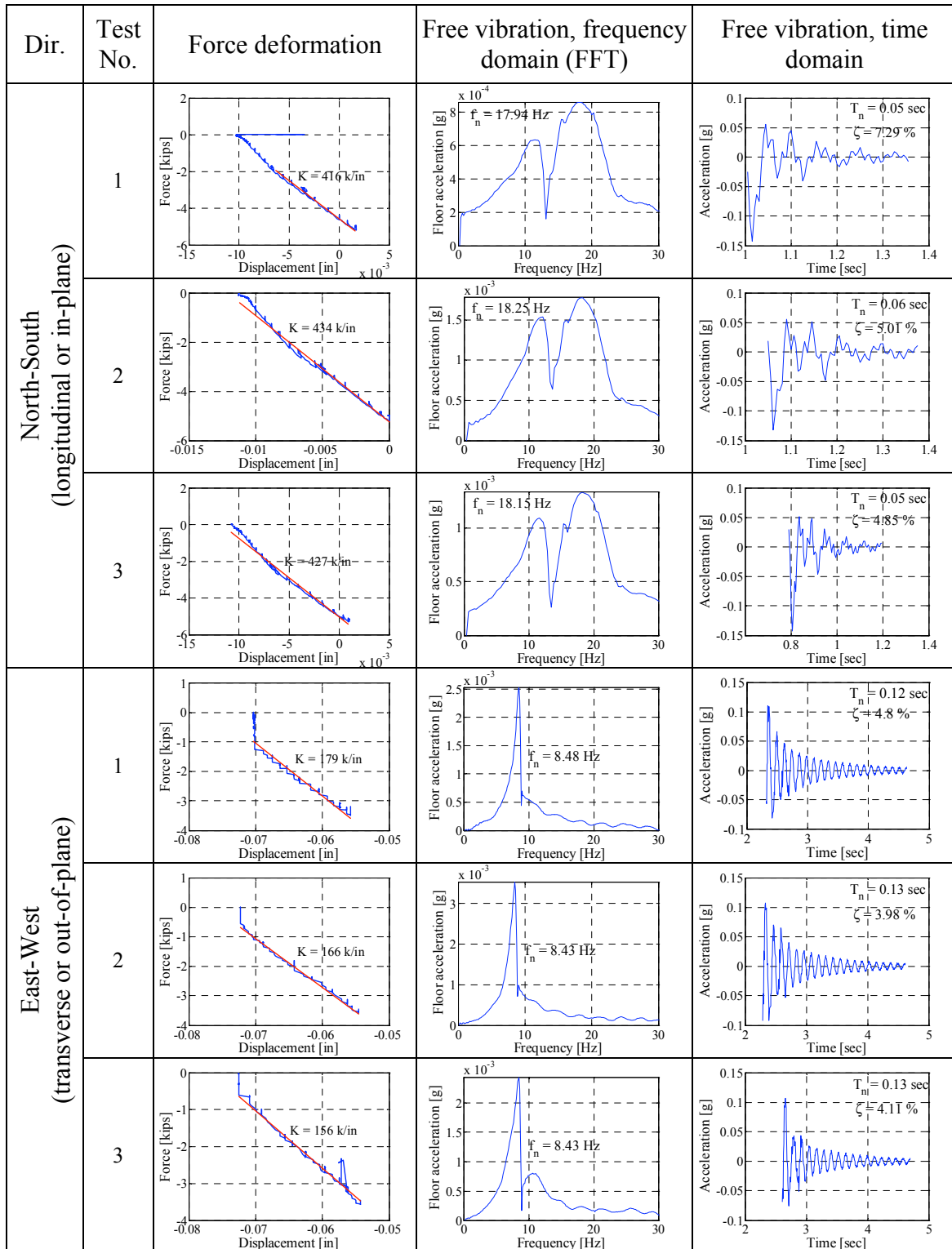


Fig. B.2 Snap-back tests after building URM infill wall and post-tensioning columns (no additional mass) (1 kip = 4.45 kN, 1 in. = 25.4 mm).

Table B.3 Snap-back tests after building URM infill wall, post-tensioning columns and adding mass.

Direction	Test No.	Evaluation method	Natural frequency (Hz)	Natural period (sec)	Stiffness* [kips/in.]	Damping ratio (%)	
North-South (longitudinal or in-plane)	1	Force-displacement	-	-	406	-	
		FV: frequency domain	7.80	0.128	-	-	
		FV: time domain	7.41	0.135	-	6.1	
	2	Force-displacement	-	-	464	-	
		FV: frequency domain	7.86	0.127	-	-	
		FV: time domain	7.14	0.140	-	6.0	
	3	Force-displacement	-	-	437	-	
		FV: frequency domain	7.57	0.132	-	-	
		FV: time domain	7.14	0.140	-	6.7	
	4	Force-displacement	-	-	418	-	
		FV: frequency domain	7.13	0.140	-	-	
		FV: time domain	7.69	0.130	-	8.7	
Mean			7.46	0.134	431	6.9	
COV (%)			4.1	4.1	5.9	19	
East-West (transverse or out-of-plane)	1	FV: frequency domain	4.51	0.222	-	-	
		FV: time domain	4.17	0.240	-	5.0	
	2	FV: frequency domain	4.45	0.225	-	-	
		FV: time domain	4.12	0.243	-	3.5	
	Mean			4.31	0.232	-	4.3
	COV (%)			4.5	4.5	-	24

*(1 kip/in. = 0.175 kN/mm)

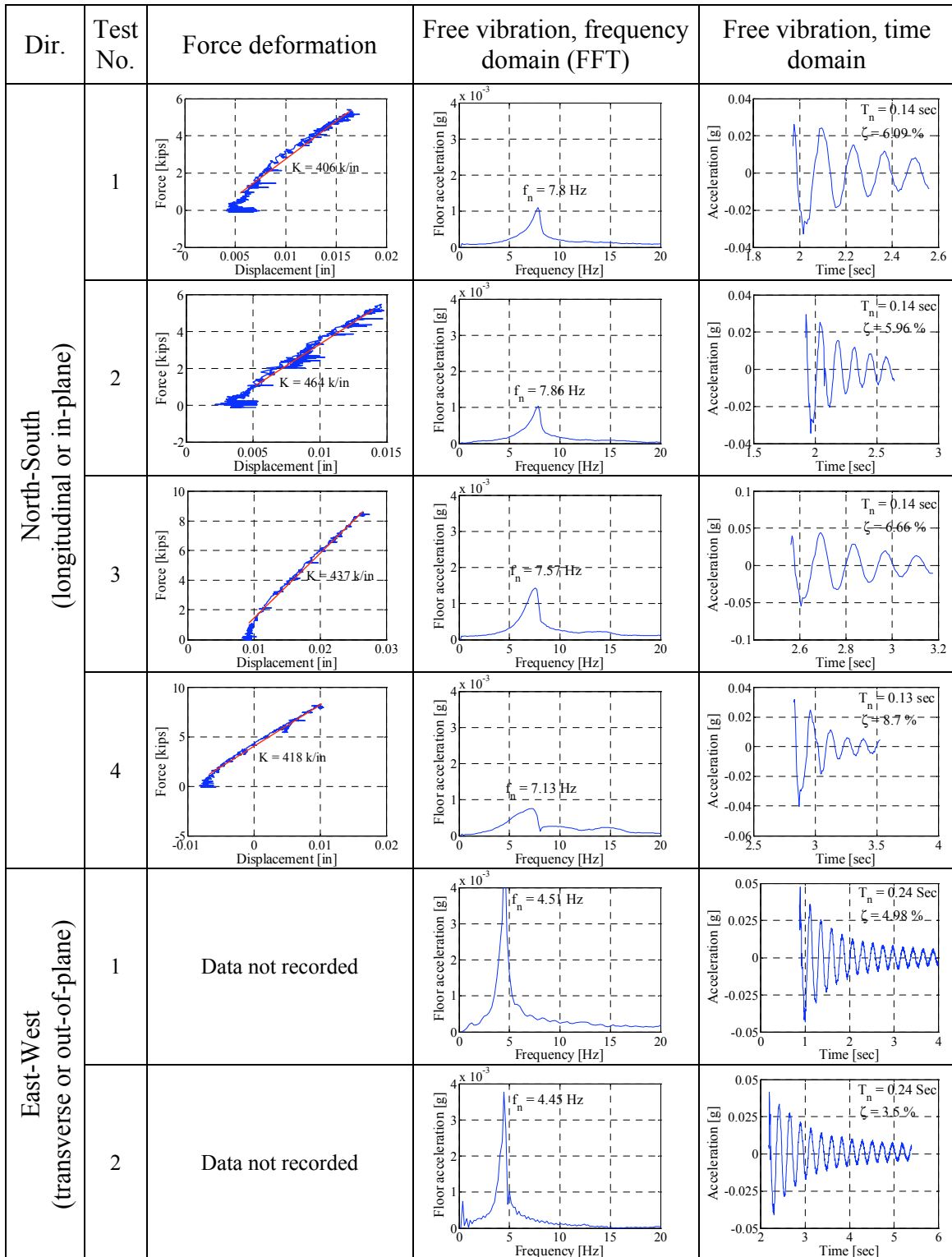
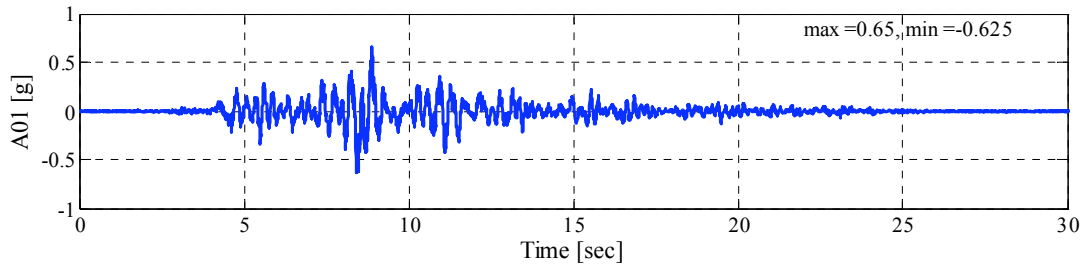


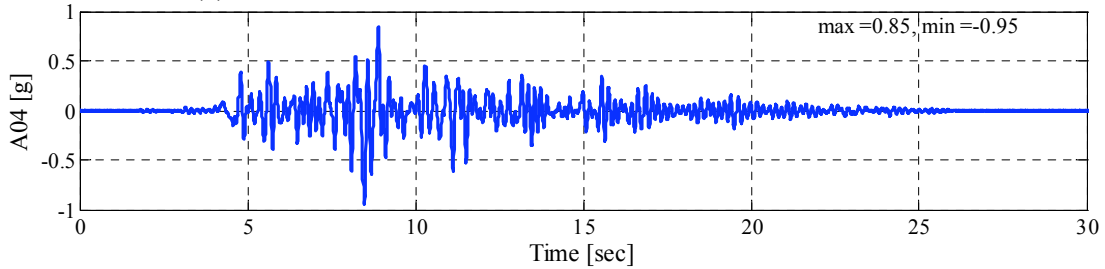
Fig. B.3 Snap-back tests after building URM infill wall, post-tensioning columns, and adding mass (1 kip = 4.45 kN, 1 in. = 25.4 mm).

Appendix C: Samples of Raw Experimental Data

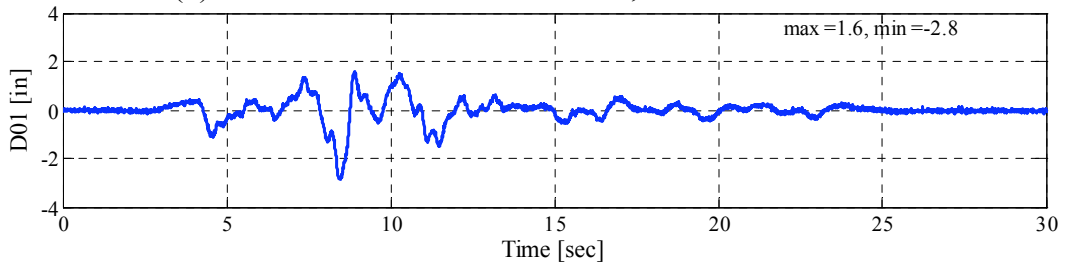
In this appendix, a small subset of the raw data gathered during the shake-table experiments is presented for levels TAR 4, TAR 6, DUZ 7, DUZ 8, AWR-TAR 6, AWR-DUZ 7, LomaPr 9, and LomaPr 9-2-1 in Figures C-1–C-8, respectively. Each figure contains plots of shake table and test structure roof acceleration and displacement in the longitudinal (X) direction as well as sample strain gage data in the columns and a few sample displacement transducers throughout the test structure. The designation and exact locations of the featured instruments are presented in Appendix A. The sequence of loading and the detailed explanation of each ground motion level are discussed in Chapter 5. The results of the shake-table experimental data are analyzed and discussed in detail in Chapter 6. A complete documentation of the raw data can be found on the Network for Earthquake Engineering Simulation (NEES) central data repository at <https://central.nees.org/>.



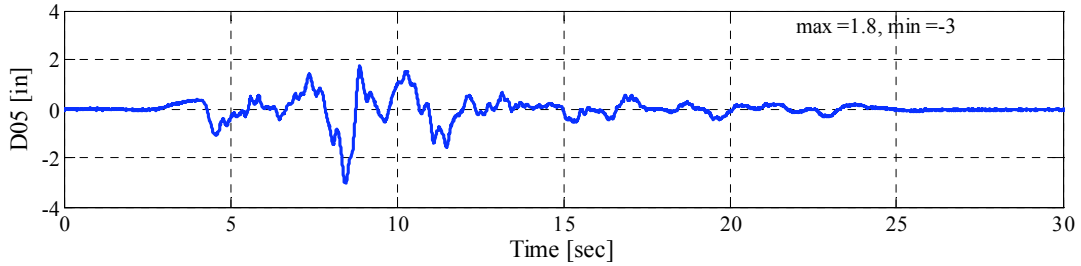
(a) Table acceleration in X direction, accelerometer A01



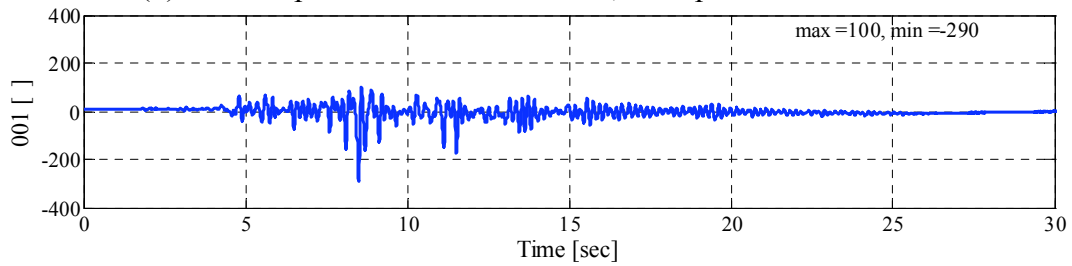
(b) Roof acceleration in X direction, accelerometer A04



(c) Table displacement in X direction, wire-potentiometer D01

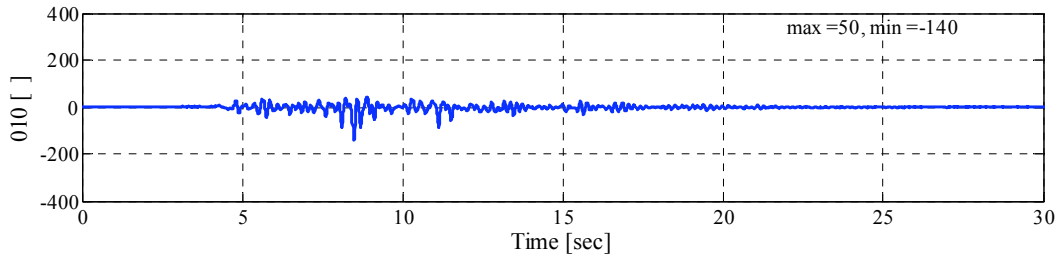


(d) Roof displacement in X direction, wire-potentiometer D05

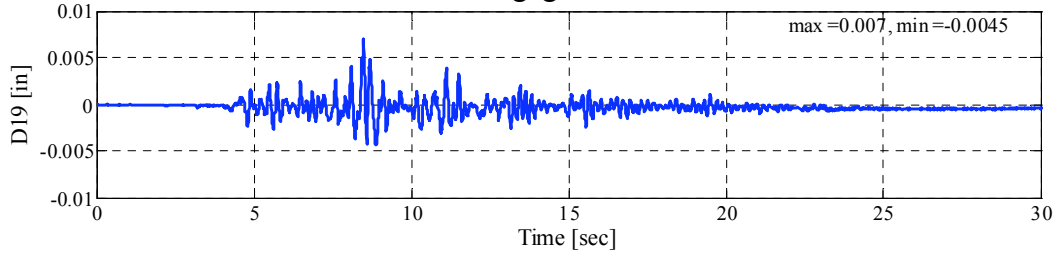


(e) Longitudinal reinforcing bar strain (in micro-strain ($\mu\epsilon$)) at base of column C1, strain gage 001

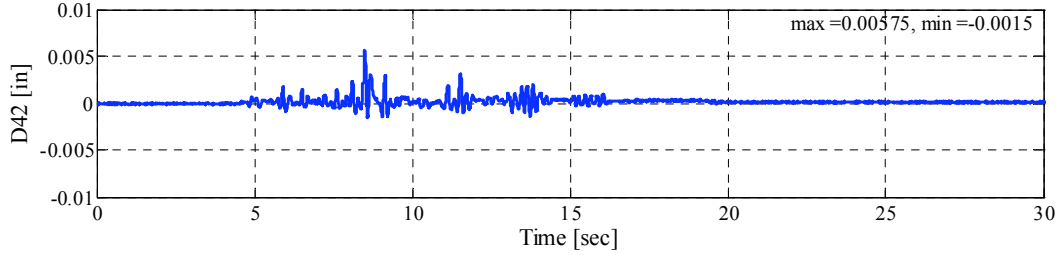
Fig. C.1 Selected raw data recorded during level TAR 4 (1 in. = 25.4 mm).



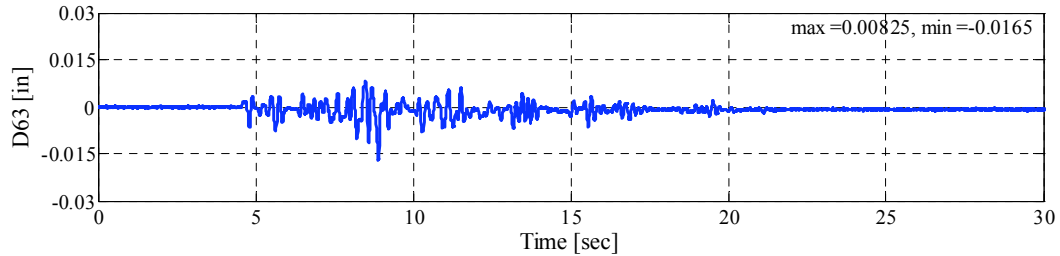
(f) Longitudinal reinforcing bar strain (in micro-strain ($\mu\epsilon$)) at base of column B1, strain gage 010



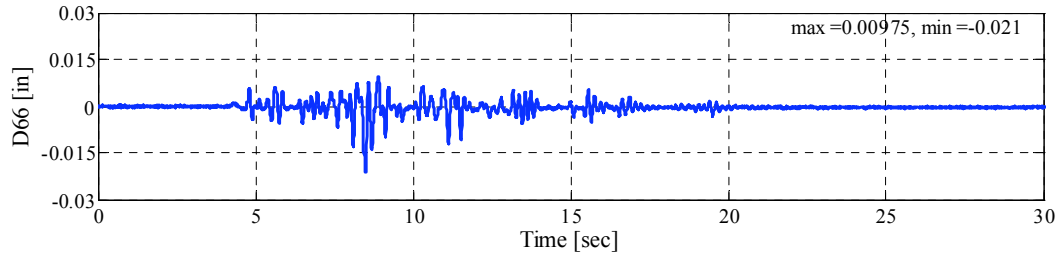
(g) Displacement measurement at base of column A2, displacement transducer D19



(h) Displacement measurement at base of column B1, displacement transducer D42

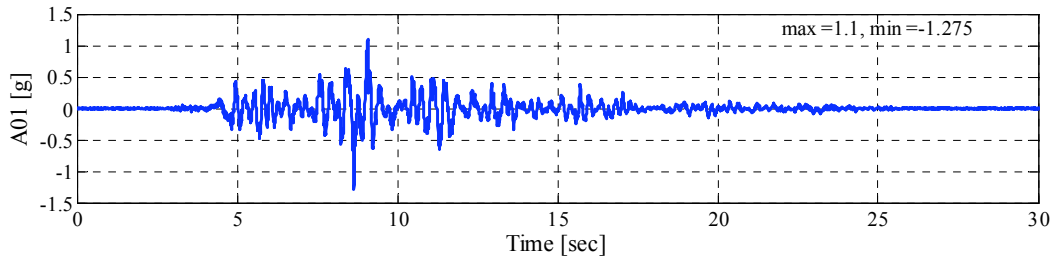


(i) Wall in-plane displacement measurement, displacement transducer D63

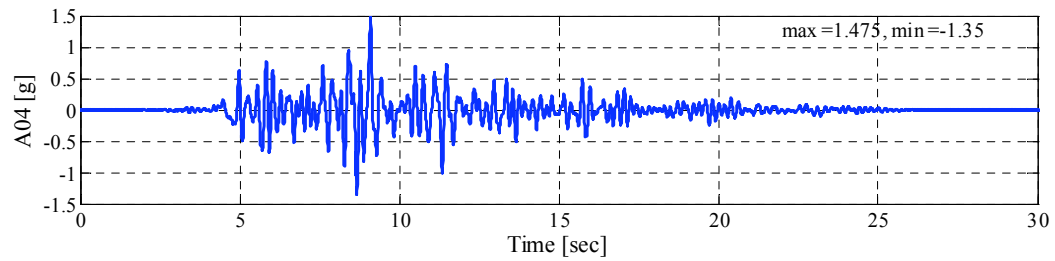


(j) Wall in-plane displacement measurement, displacement transducer D66

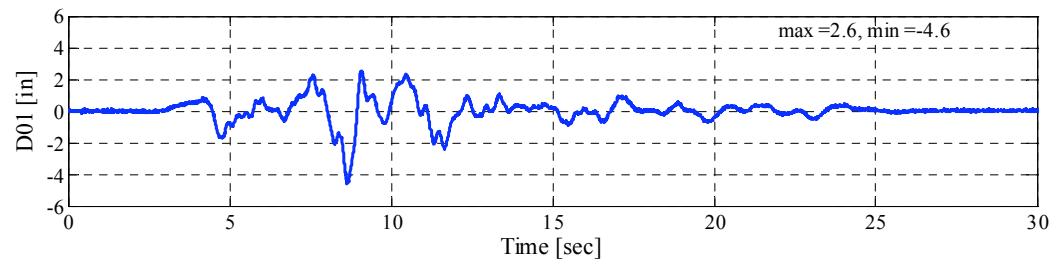
Fig. C.1—Continued



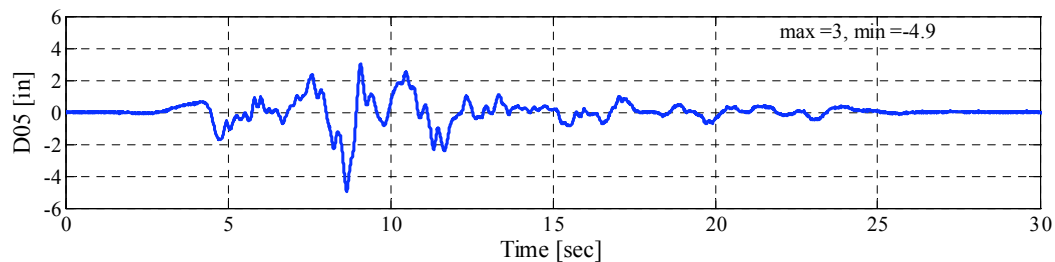
(a) Table acceleration in X direction, accelerometer A01



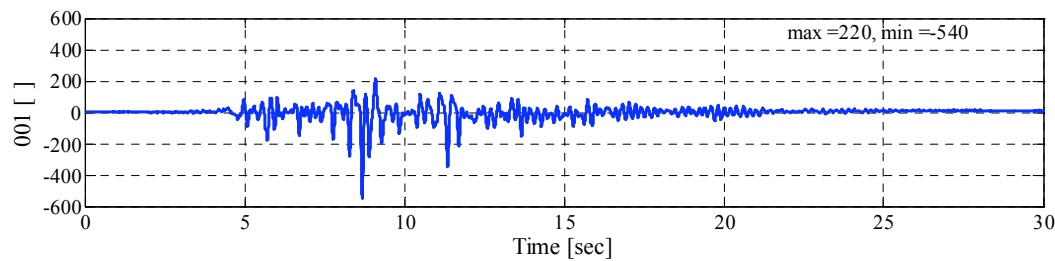
(b) Roof acceleration in X direction, accelerometer A04



(c) Table displacement in X direction, wire-potentiometer D01

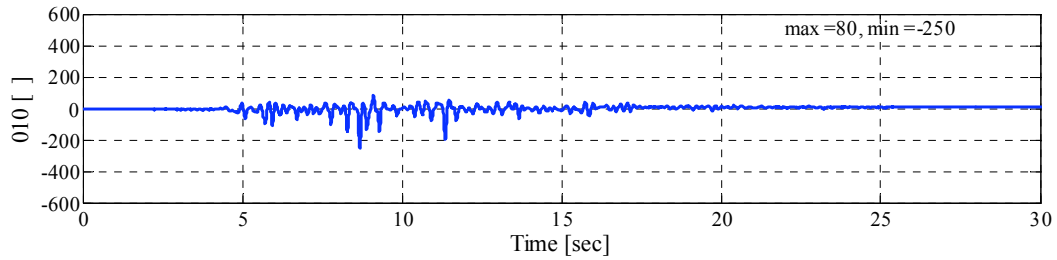


(d) Roof displacement in X direction, wire-potentiometer D05

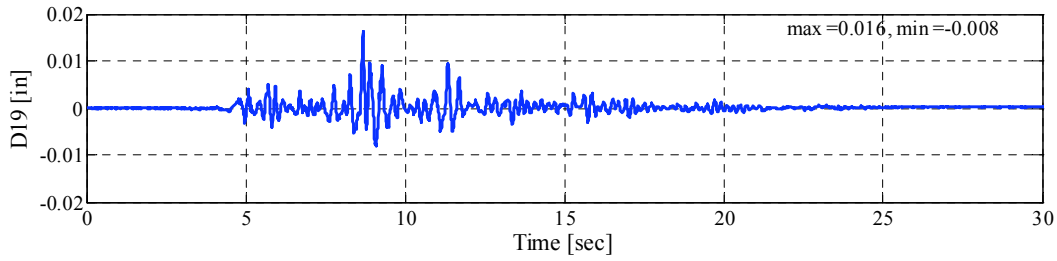


(e) Longitudinal reinforcing bar strain (in micro-strain ($\mu\epsilon$)) at base of column C1, strain gage 001

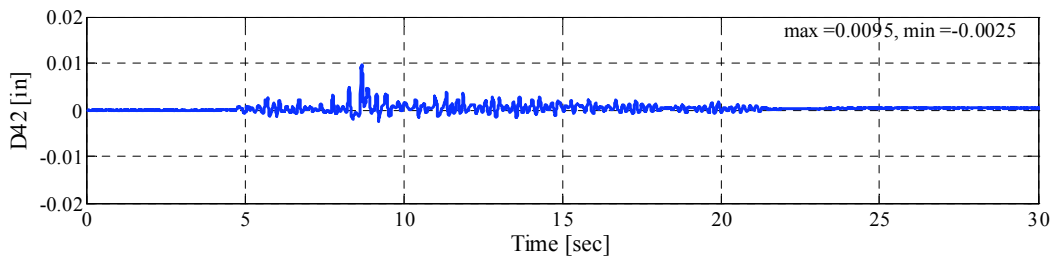
Fig. C.2 Selected raw data recorded during level TAR 6 (1 in. = 25.4 mm).



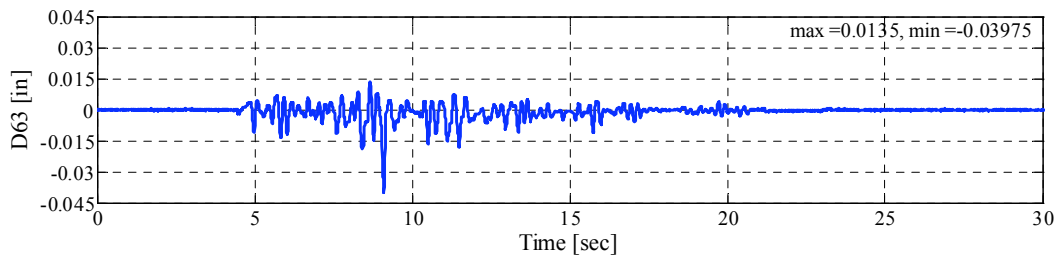
(f) Longitudinal reinforcing bar strain (in micro-strain ($\mu\epsilon$)) at base of column B1, strain gage 010



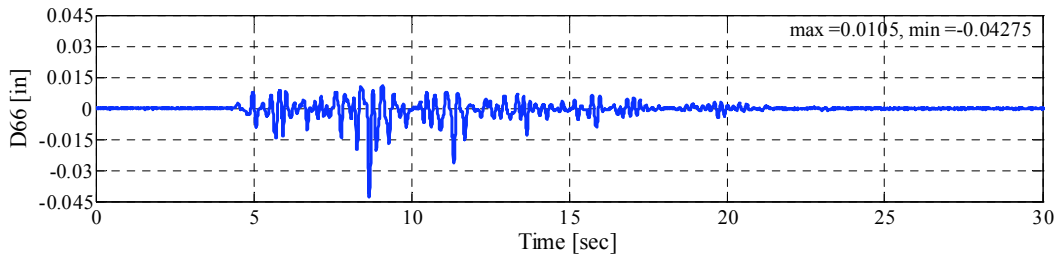
(g) Displacement measurement at base of column A2, displacement transducer D19



(h) Displacement measurement at base of column B1, displacement transducer D42

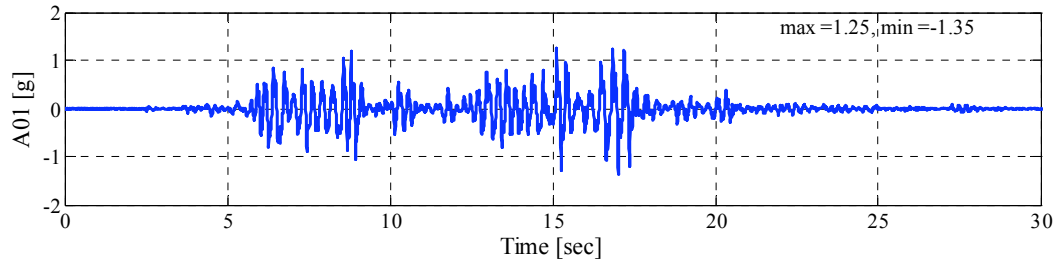


(i) Wall in-plane displacement measurement, displacement transducer D63

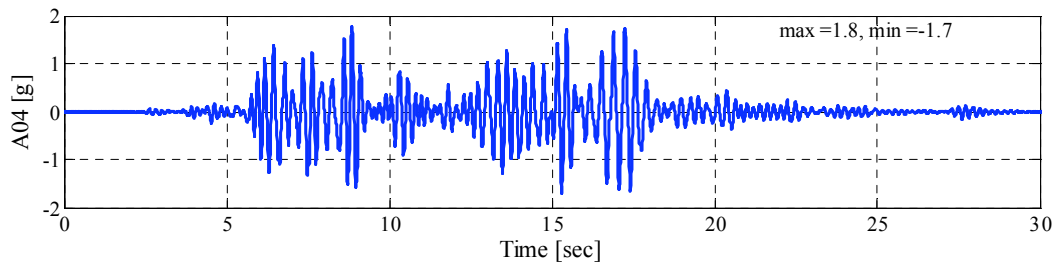


(j) Wall in-plane displacement measurement, displacement transducer D66

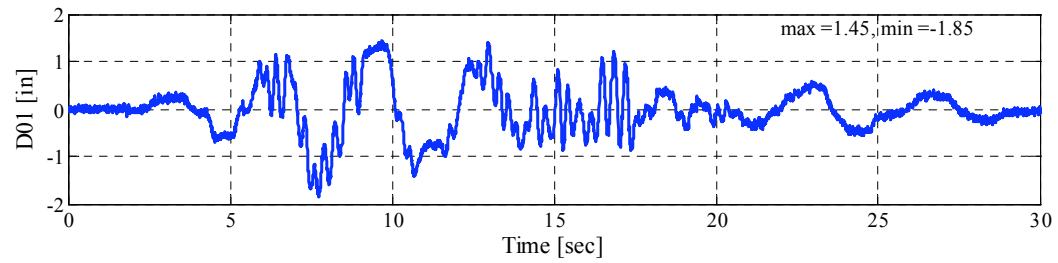
Fig. C.2—Continued



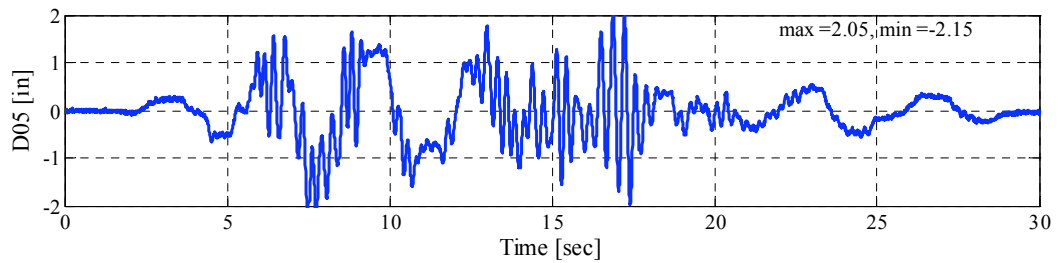
(a) Table acceleration in X direction, accelerometer A01



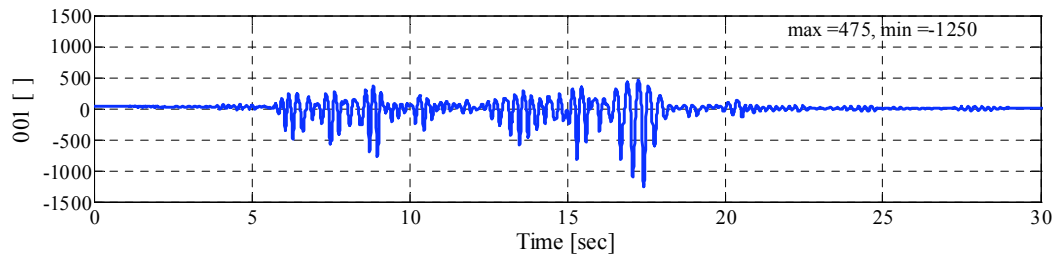
(b) Roof acceleration in X direction, accelerometer A04



(c) Table displacement in X direction, wire-potentiometer D01

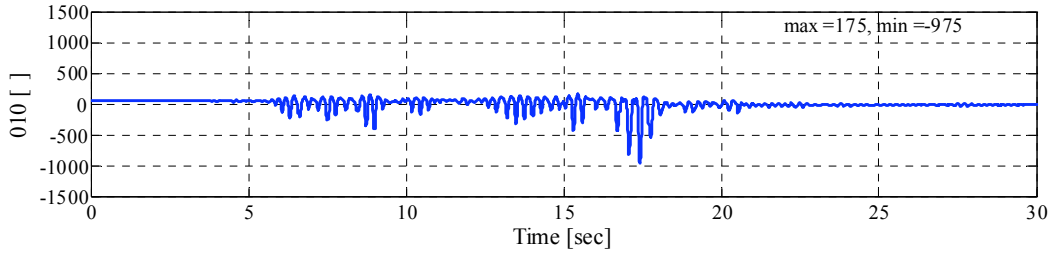


(d) Roof displacement in X direction, wire-potentiometer D05

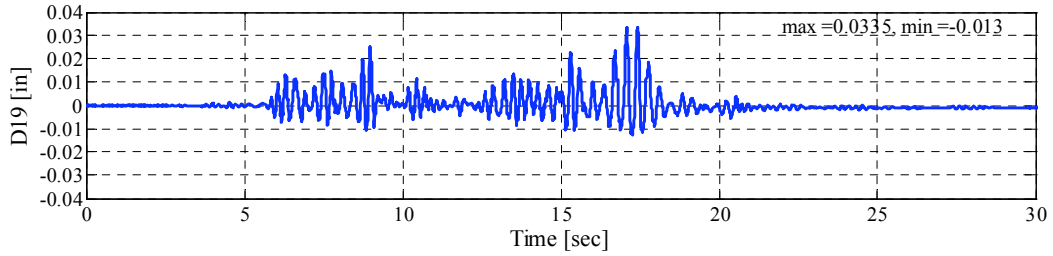


(e) Longitudinal reinforcing bar strain (in micro-strain ($\mu\epsilon$)) at base of column C1, strain gage 001

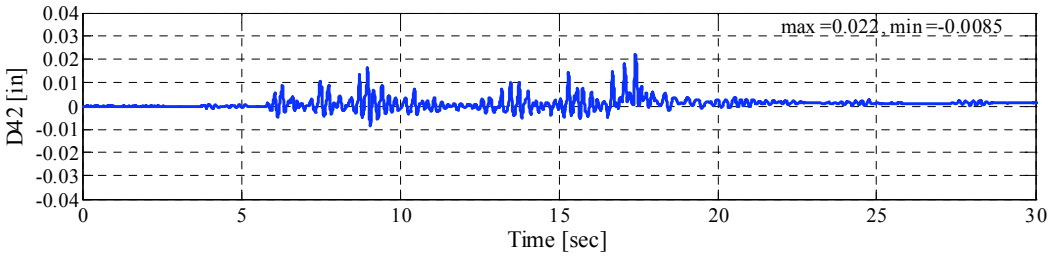
Fig. C.3 Selected raw data recorded during level DUZ 7 (1 in. = 25.4 mm).



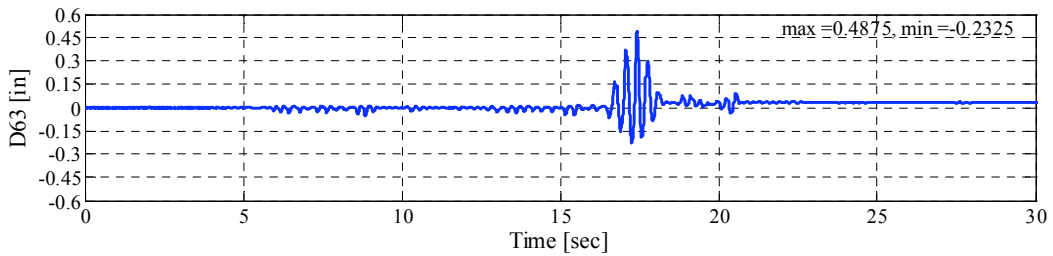
(f) Longitudinal reinforcing bar strain (in micro-strain ($\mu\epsilon$)) at base of column B1, strain gage 010



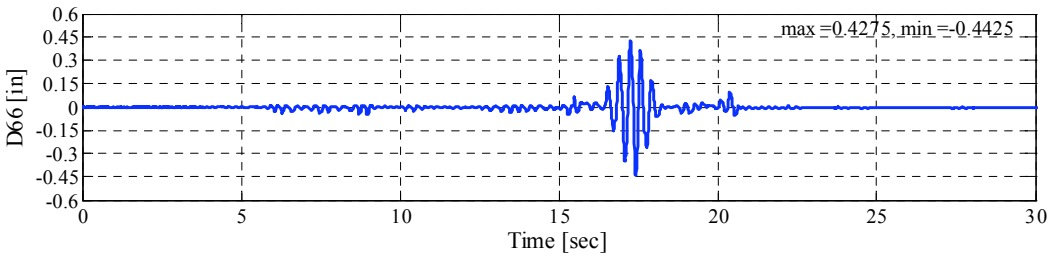
(g) Displacement measurement at base of column A2, displacement transducer D19



(h) Displacement measurement at base of column B1, displacement transducer D42

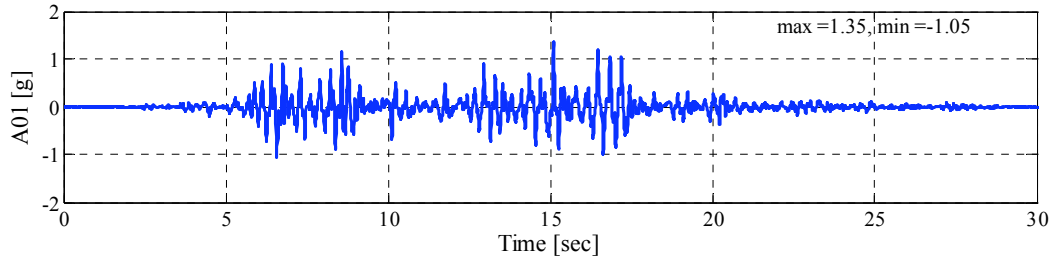


(i) Wall in-plane displacement measurement, displacement transducer D63

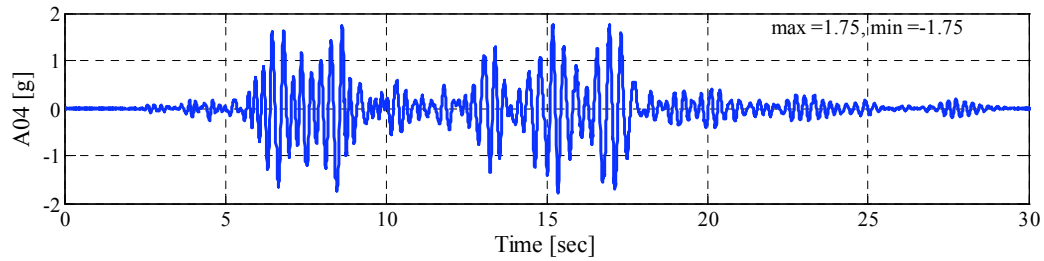


(j) Wall in-plane displacement measurement, displacement transducer D66

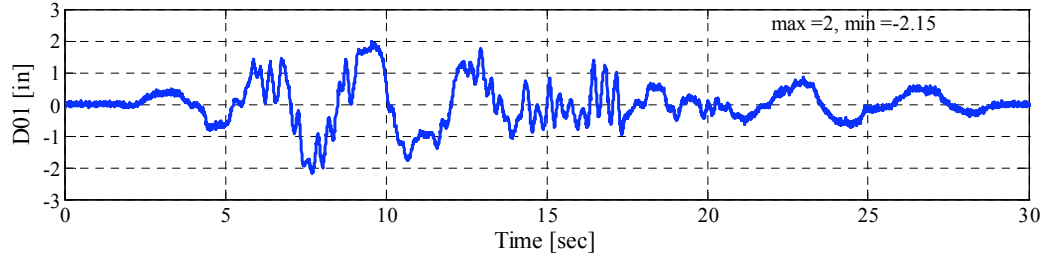
Fig. C.3—Continued



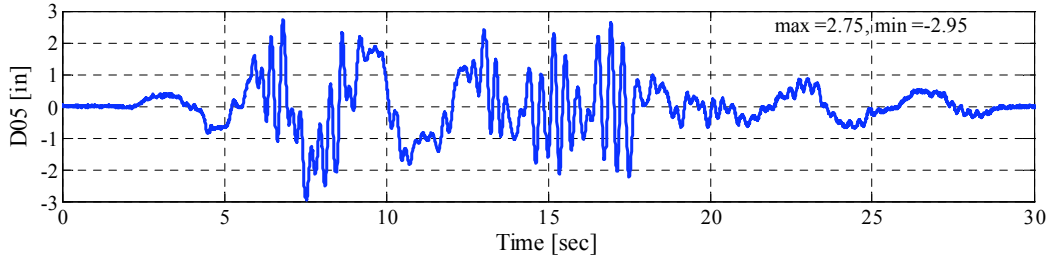
(a) Table acceleration in X direction, accelerometer A01



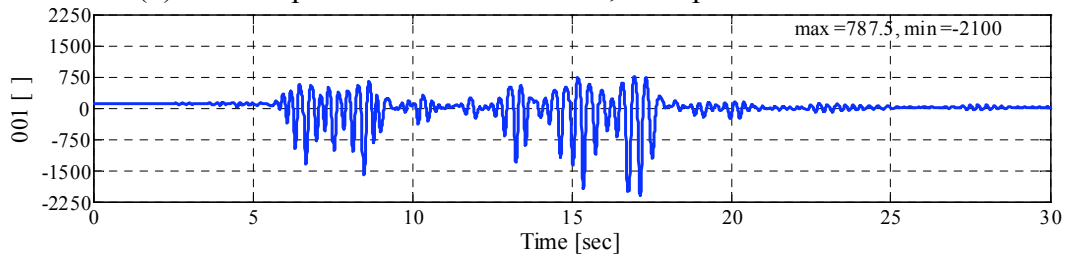
(b) Roof acceleration in X direction, accelerometer A04



(c) Table displacement in X direction, wire-potentiometer D01

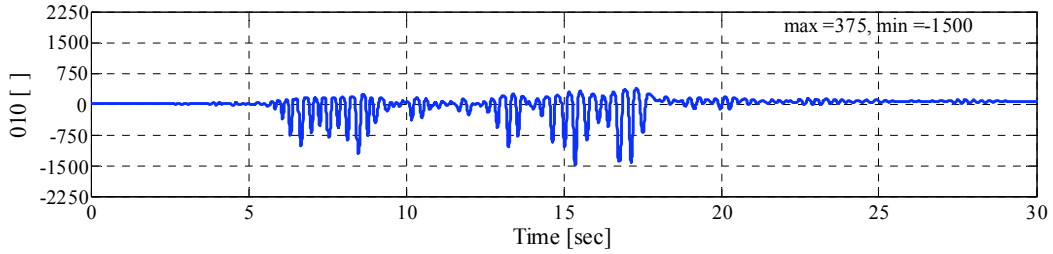


(d) Roof displacement in X direction, wire-potentiometer D05

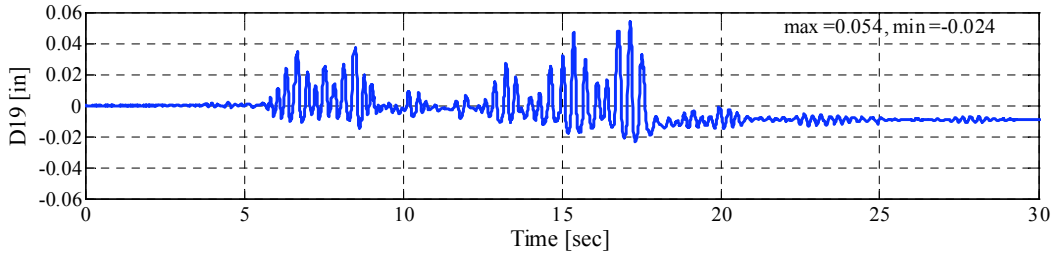


(e) Longitudinal reinforcing bar strain (in micro-strain ()) at base of column C1, strain gage 001

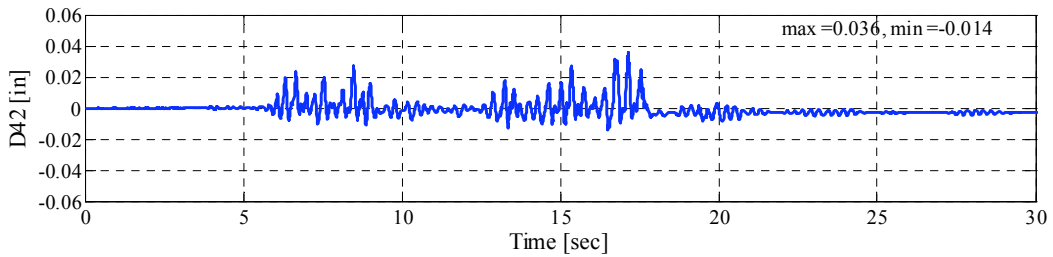
Fig. C.4 Selected raw data recorded during level DUZ 8 (1 in. = 25.4 mm).



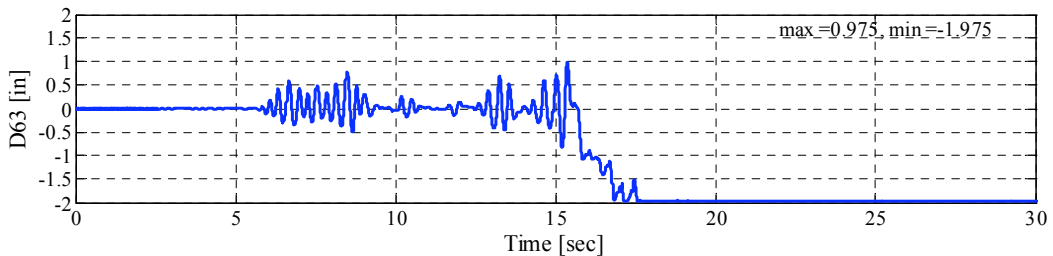
(f) Longitudinal reinforcing bar strain (in micro-strain ($\mu\epsilon$)) at base of column B1, strain gage 010



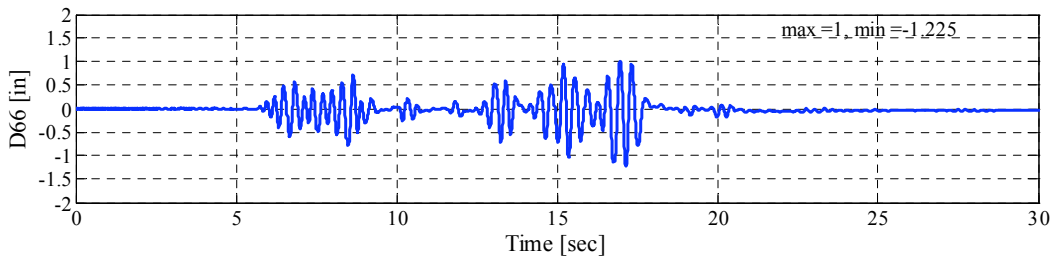
(g) Displacement measurement at base of column A2, displacement transducer D19



(h) Displacement measurement at base of column B1, displacement transducer D42

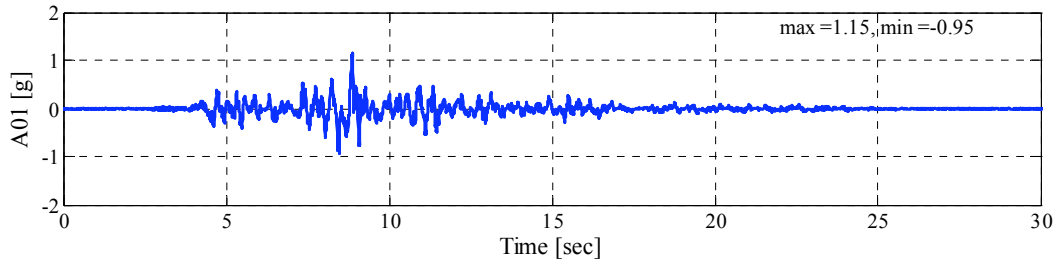


(i) Wall in-plane displacement measurement, displacement transducer D63

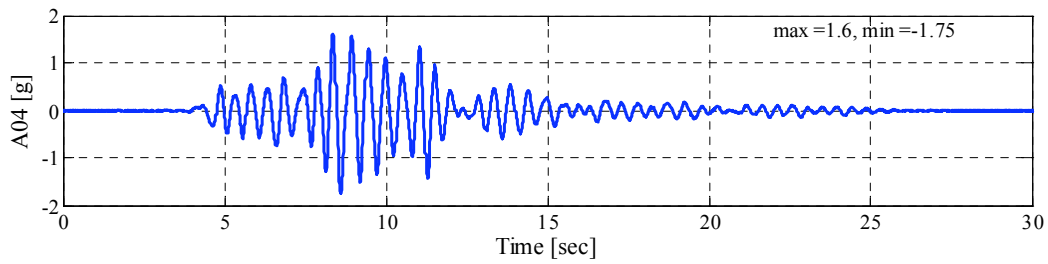


(j) Wall in-plane displacement measurement, displacement transducer D66

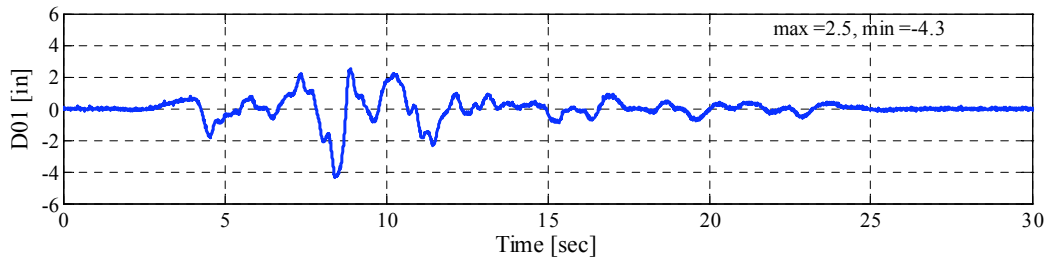
Fig. C.4—Continued



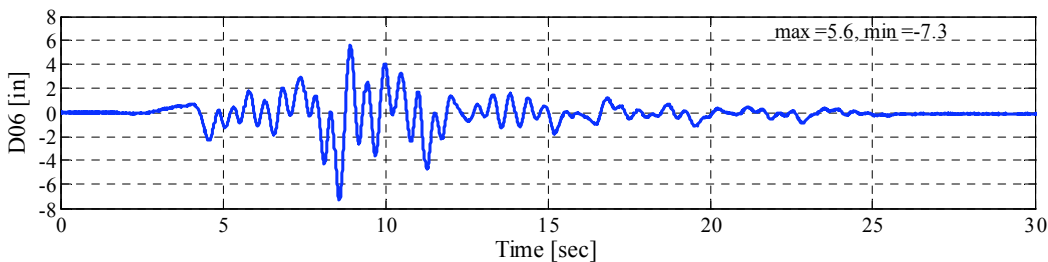
(a) Table acceleration in X direction, accelerometer A01



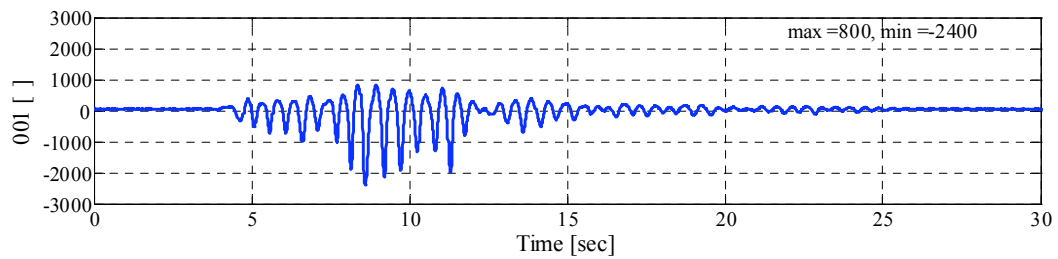
(b) Roof acceleration in X direction, accelerometer A04



(c) Table displacement in X direction, wire-potentiometer D01

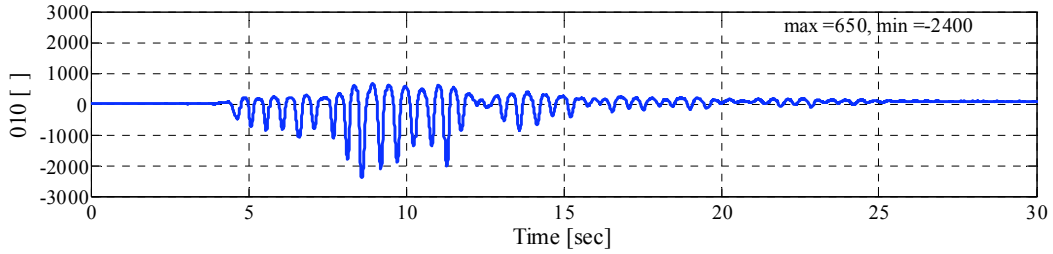


(d) Roof displacement in X direction, wire-potentiometer D06

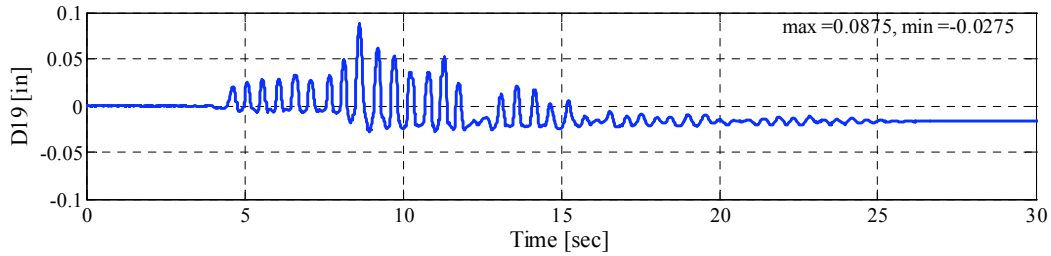


(e) Longitudinal reinforcing bar strain (in micro-strain ()) at base of column C1, strain gage 001

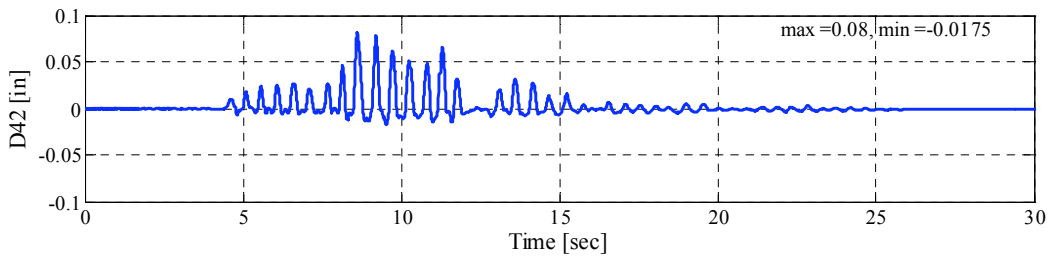
Fig. C.5 Selected raw data recorded during level AWR-TAR 6 (1 in. = 25.4 mm).



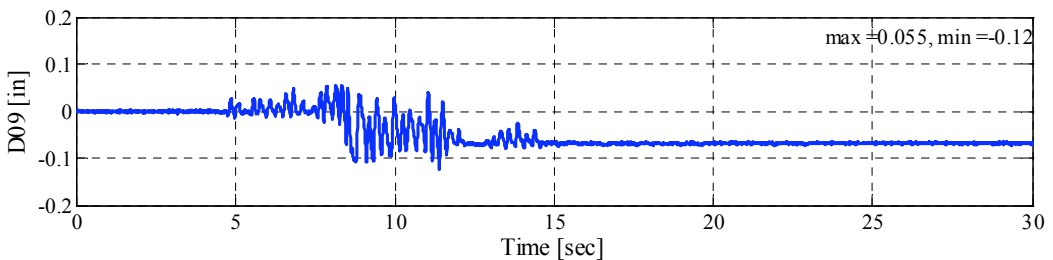
(f) Longitudinal reinforcing bar strain (in micro-strain ($\mu\epsilon$)) at base of column B1, strain gage 010



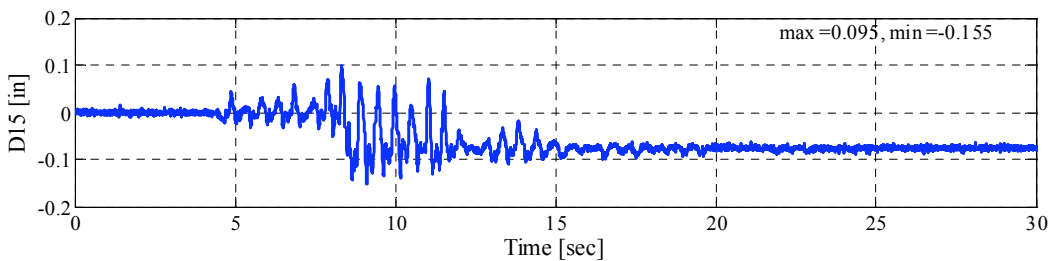
(g) Displacement measurement at base of column A2, displacement transducer D19



(h) Displacement measurement at base of column B1, displacement transducer D42

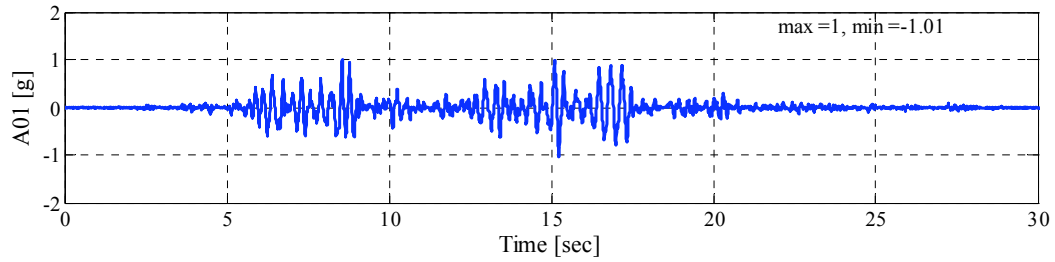


(i) Slab in-plane displacement measurement, displacement transducer D09

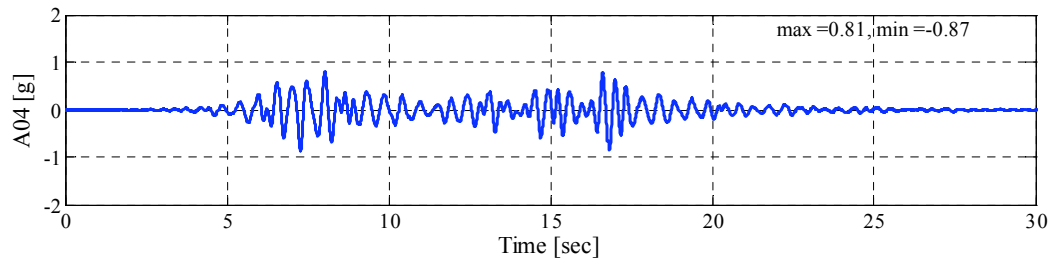


(j) Slab in-plane displacement measurement, displacement transducer D15

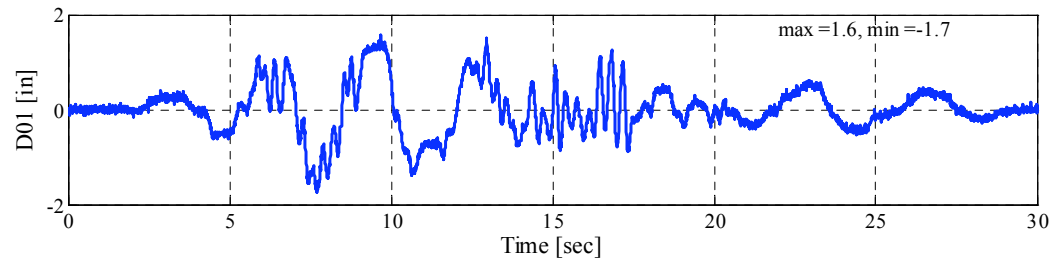
Fig. C.5—Continued



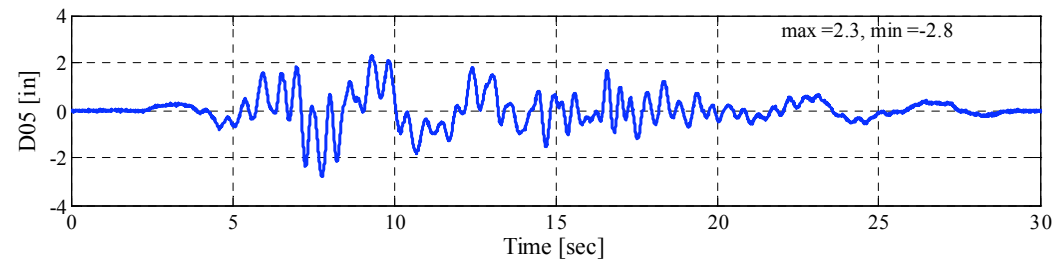
(a) Table acceleration in X direction, accelerometer A01



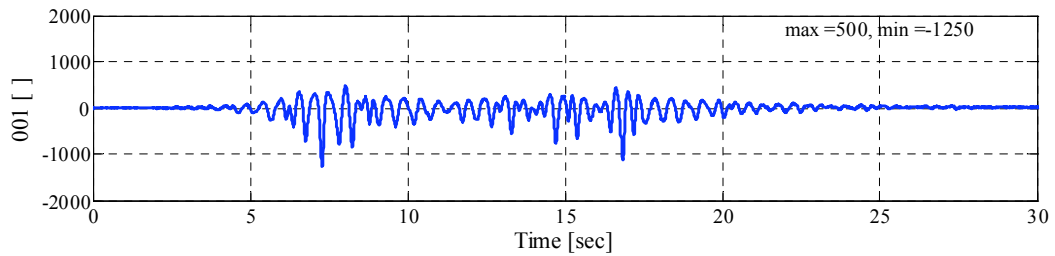
(b) Roof acceleration in X direction, accelerometer A04



(c) Table displacement in X direction, wire-potentiometer D01

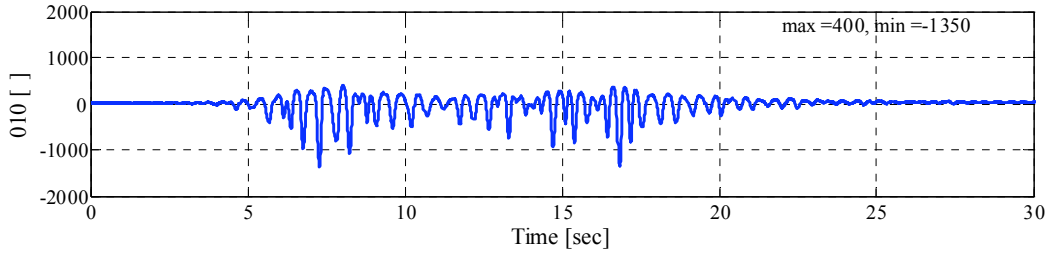


(d) Roof displacement in X direction, wire-potentiometer D05

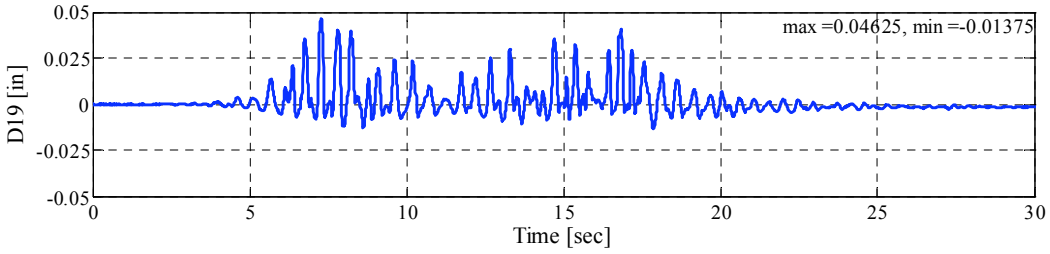


(e) Longitudinal reinforcing bar strain (in micro-strain ($\mu\epsilon$)) at base of column C1, strain gage 001

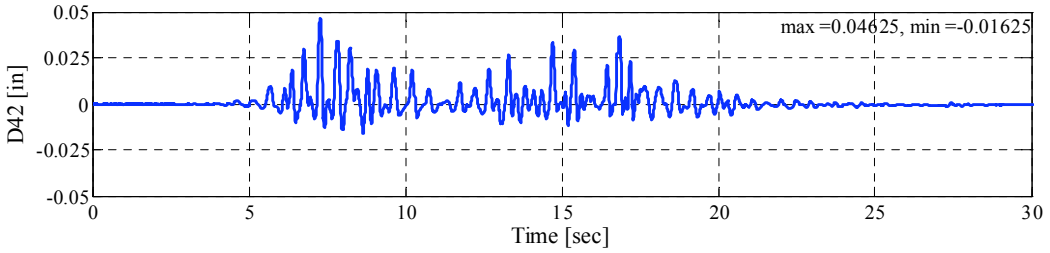
Fig. C.6 Selected raw data recorded during level AWR-DUZ 7 (1 in. = 25.4 mm).



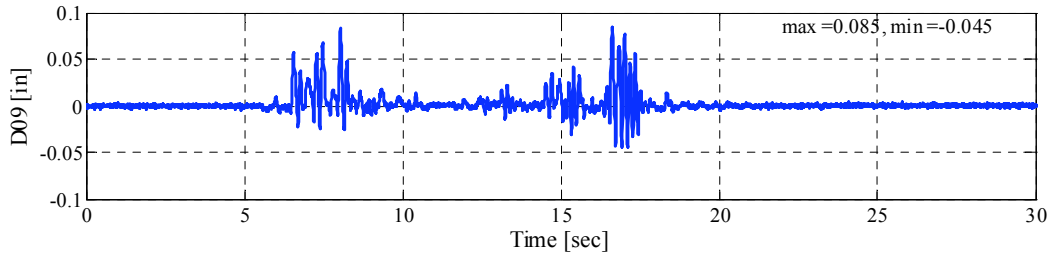
(f) Longitudinal reinforcing bar strain (in micro-strain ($\mu\epsilon$)) at base of column B1, strain gage 010



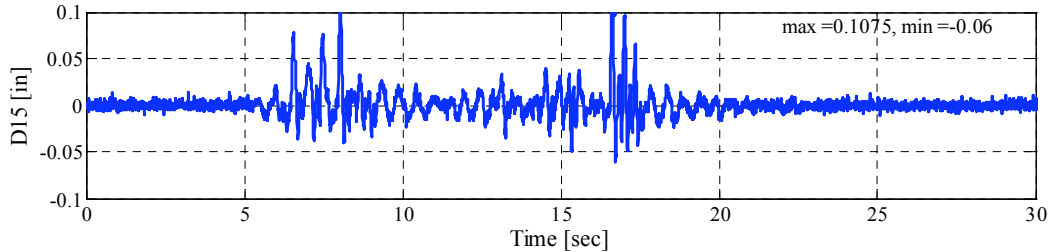
(g) Displacement measurement at base of column A2, displacement transducer D19



(h) Displacement measurement at base of column B1, displacement transducer D42

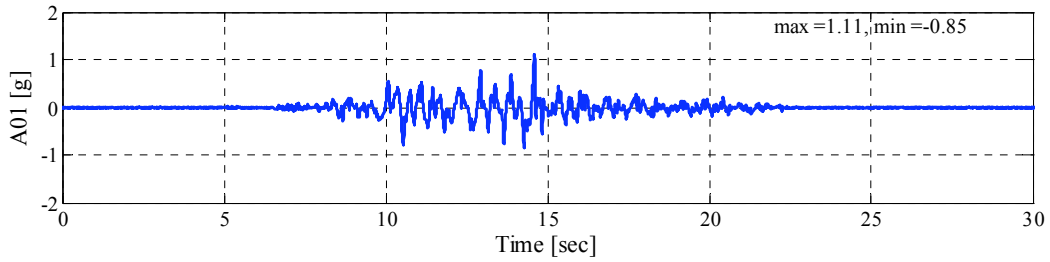


(i) Slab in-plane displacement measurement, displacement transducer D09

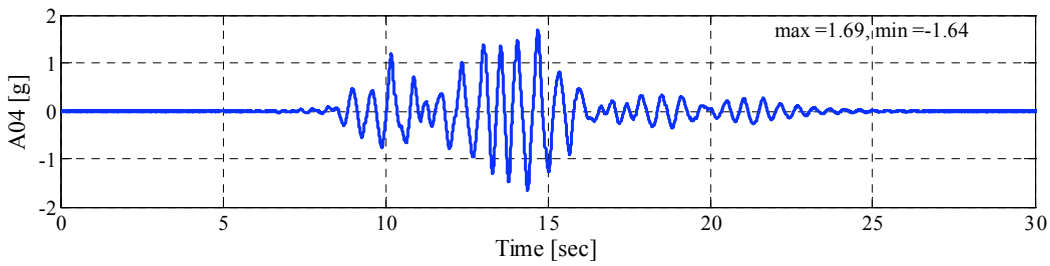


(j) Slab in-plane displacement measurement, displacement transducer D15

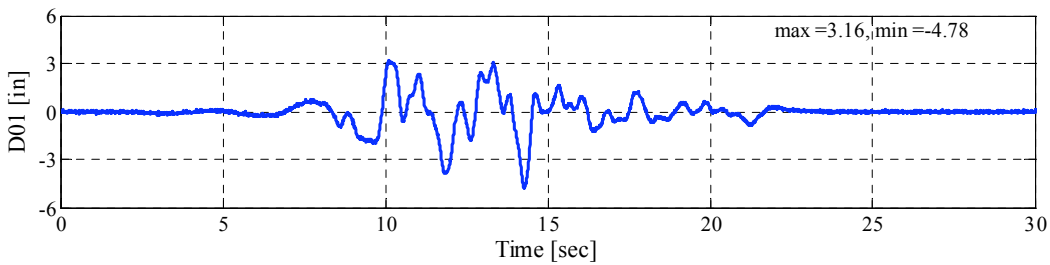
Fig. C.6—Continued



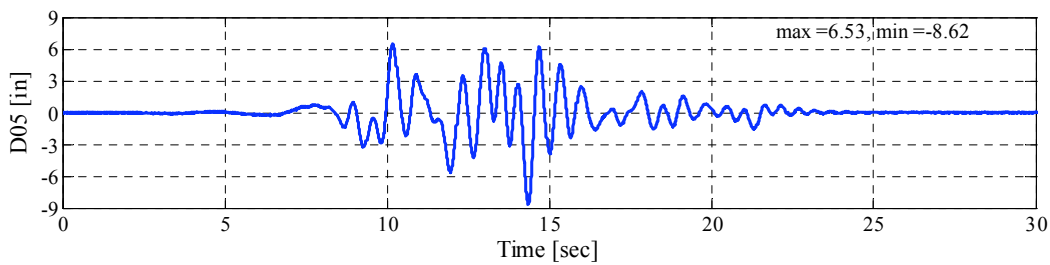
(a) Table acceleration in X direction, accelerometer A01



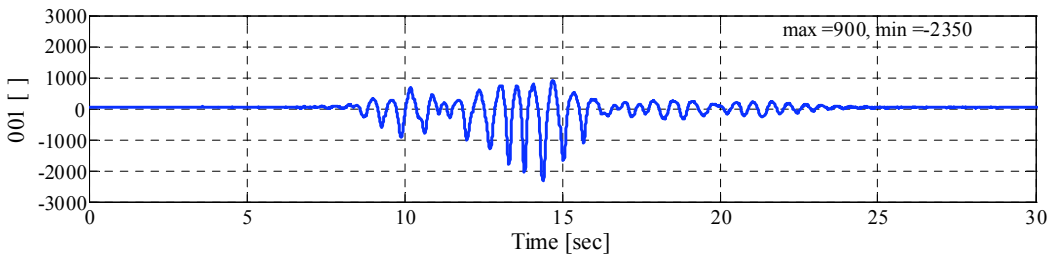
(b) Roof acceleration in X direction, accelerometer A04



(c) Table displacement in X direction, wire-potentiometer D01

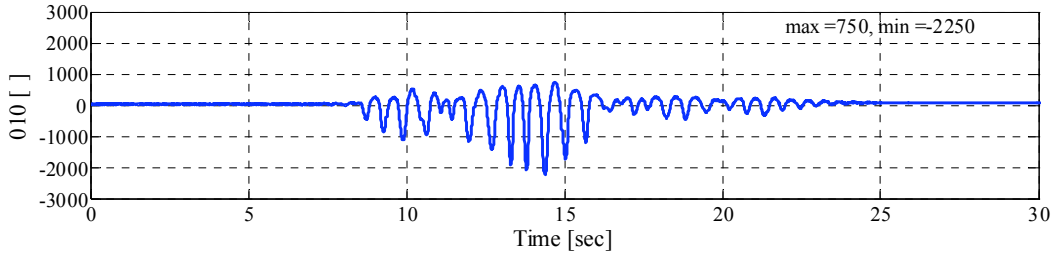


(d) Roof displacement in X direction, wire-potentiometer D05

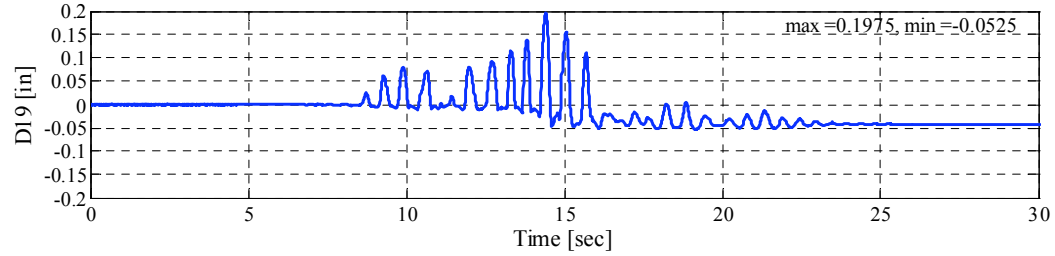


(e) Longitudinal reinforcing bar strain (in micro-strain ($\mu\epsilon$)) at base of column C1, strain gage 001

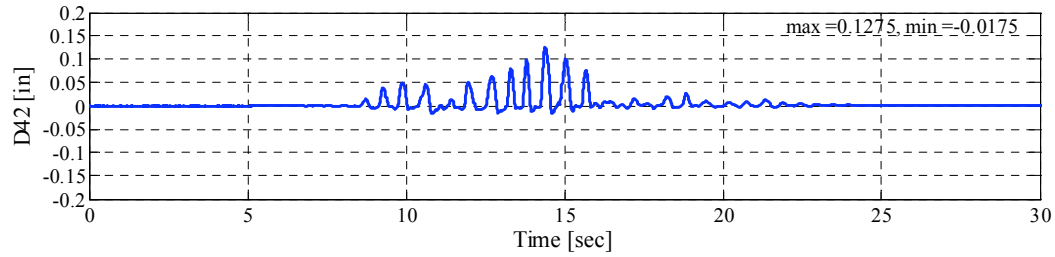
Fig. C.7 Selected raw data recorded during level LomaPr 9 (1 in. = 25.4 mm)



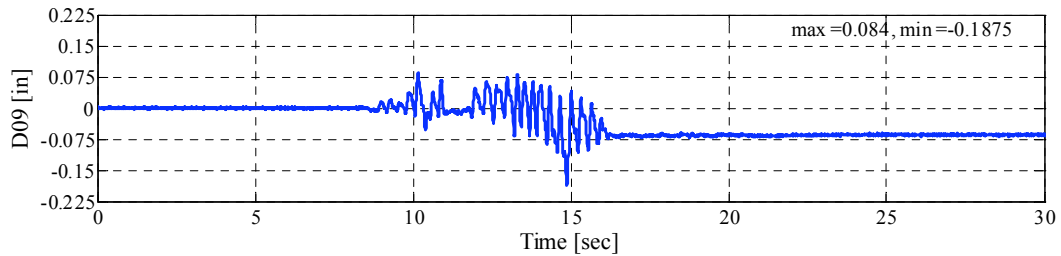
(f) Longitudinal reinforcing bar strain (in micro-strain ($\mu\epsilon$)) at base of column B1, strain gage 010



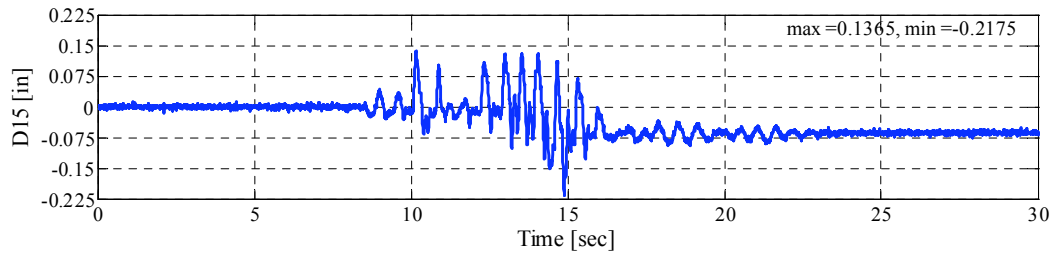
(g) Displacement measurement at base of column A2, displacement transducer D19



(h) Displacement measurement at base of column B1, displacement transducer D42

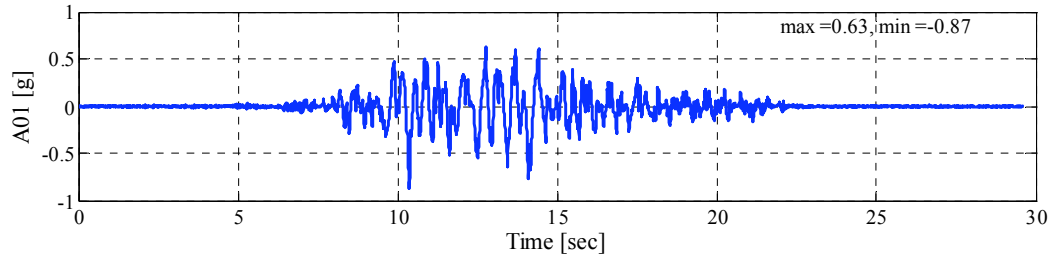


(i) Slab in-plane displacement measurement, displacement transducer D09

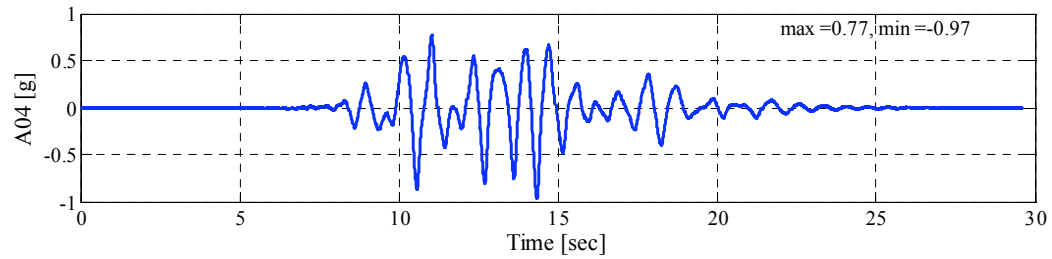


(j) Slab in-plane displacement measurement, displacement transducer D15

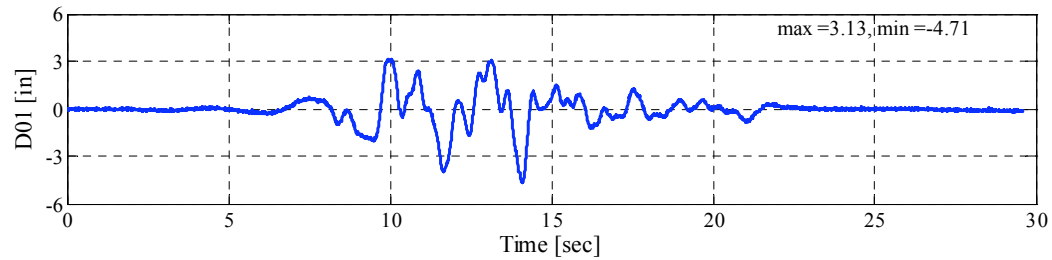
Fig. C-7—Continued



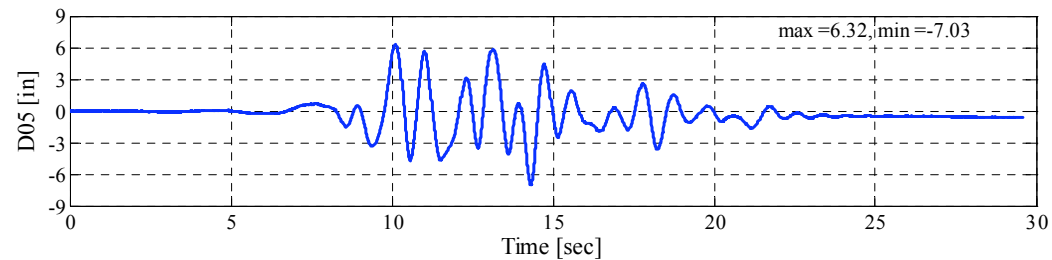
(a) Table acceleration in X direction, accelerometer A01



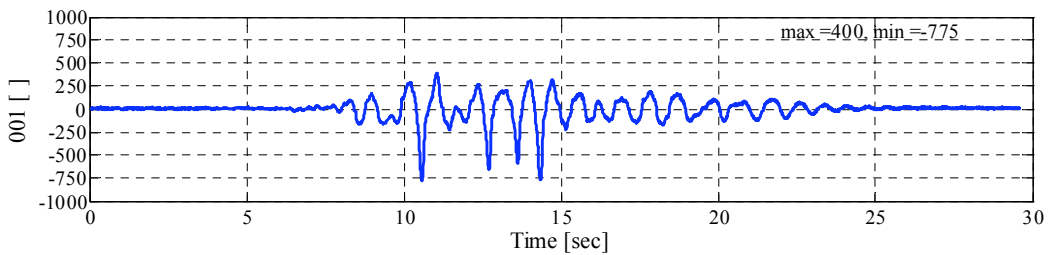
(b) Roof acceleration in X direction, accelerometer A04



(c) Table displacement in X direction, wire-potentiometer D01

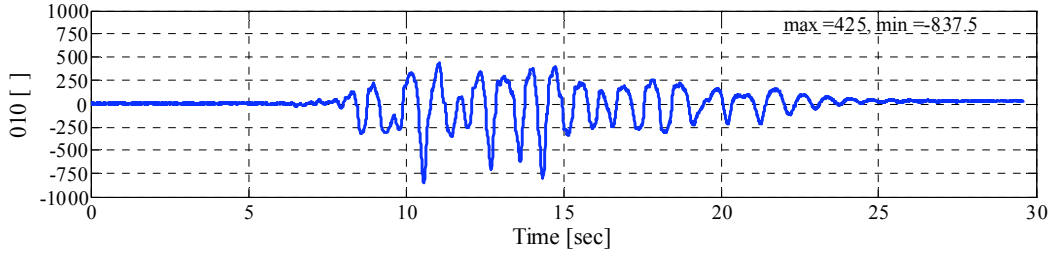


(d) Roof displacement in X direction, wire-potentiometer D05

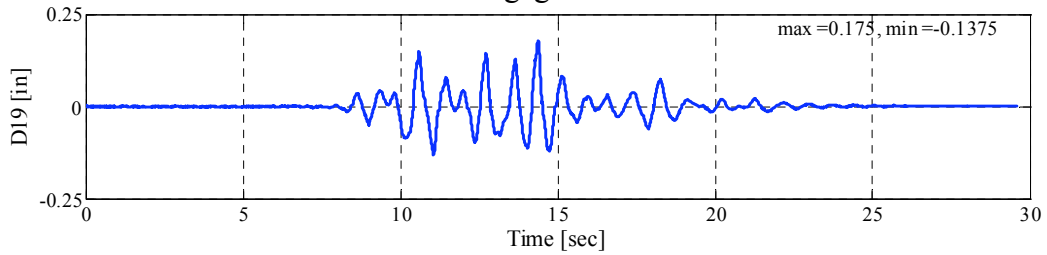


(e) Longitudinal reinforcing bar strain (in micro-strain ($\mu\epsilon$)) at base of column C1, strain gage 001

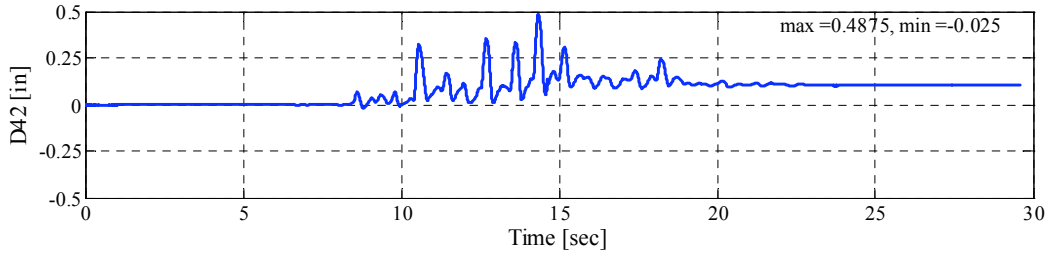
Fig. C.8 Selected raw data recorded during level LomaPr 9-2-1 (1 in. = 25.4 mm).



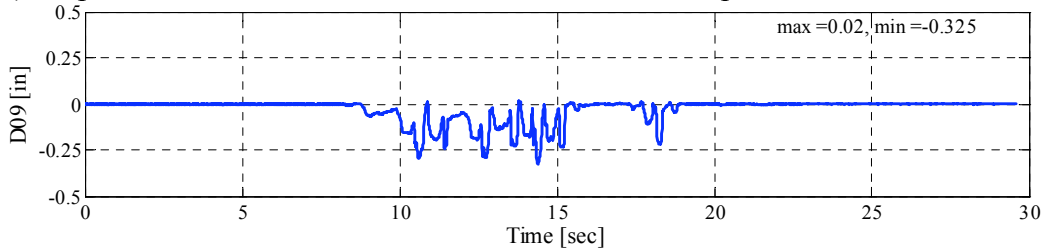
(f) Longitudinal reinforcing bar strain (in micro-strain ($\mu\epsilon$)) at base of column B1, strain gage 010



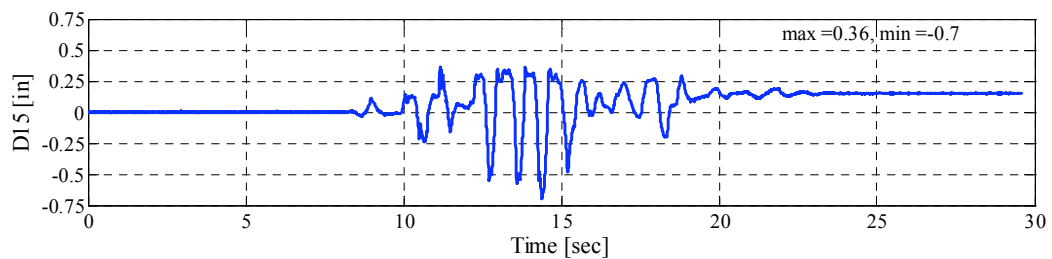
(g) Displacement measurement at base of column A2, displacement transducer D19



(h) Displacement measurement at base of column B1, displacement transducer D42



(i) Slab in-plane displacement measurement, displacement transducer D09



(j) Slab in-plane displacement measurement, displacement transducer D15

Fig. C-8—Continued

Appendix D: Out-Of-Plane Capacity of URM Infill Walls

In this appendix, detailed calculations to obtain the out-of-plane capacity of the URM infill wall described in Chapter 7 per FEMA 356 (2000) guidelines and the formulation developed by Dawe and Seah (1990) are shown. The calculations presented are parts of a MathCad spreadsheet and include the formulation as well as the definition and value of each parameter used in estimating the out-of-plane capacity of the URM infill wall of the test structure.

FEMA 356 (2000) Formulation

$h_{inf} := 101.25\text{in}$ Height of infill panel, in

$t_{inf} := 3.75\text{in}$ Thickness of infill panel and equivalent strut, in

$\frac{h_{inf}}{t_{inf}} = 27$ This exceeds the limit value of 25 defined by FEMA 356 but it is less than 30 (the limit value in the original formulation by Angel and Abrams (1994))

For $\frac{h_{inf}}{t_{inf}} = 25$, $\lambda_2 := 0.013$ (FEMA 356, Table 7-11)

$f_m := 2.46\text{ksi}$ Masonry compressive strength

$q_{in} := \frac{0.7 \cdot f_m \cdot \lambda_2}{\frac{h_{inf}}{t_{inf}}}$ FEMA 356 Equation (7-21) $q_{in} = 0.829\text{psi}$ Lower bound value for out-of-plane capacity

lower bound = mean - standard deviation = $-\sigma$

Factor from FEMA 356, Table 7-2 = 1.3

$q := 1.3 \cdot q_{in}$	$q = 1.078\text{psi}$	$q = 7.431\text{kPa}$	Mean out-of-plane capacity
$\sigma_q := q - q_{in}$	$\sigma_q = 0.249\text{psi}$	$\sigma_q = 1.715\text{kPa}$	Standard deviation
$\delta_q := \frac{\sigma_q}{q}$	$\delta_q = 0.231$		Coefficient of variation

Dawe and Seah (1990) Formulation

$f_c := 5.39 \cdot \text{ksi}$	Compression strength of concrete	
$E_c := 57000 \sqrt{\text{psi}} \cdot \sqrt{f_c}$	$E_c = 4.185 \times 10^3 \text{ ksi}$	$E_c = 28.853 \text{ GPa}$ Elastic modulus of concrete
$\nu := 0.15$	poisson ratio for concrete	
$G_c := \frac{E_c}{2(1 + \nu)}$	$G_c = 1.819 \times 10^3 \text{ ksi}$	$G_c = 12.545 \text{ GPa}$ Shear modulus of concrete
$h := 101.25 \text{ in}$	$h = 2.572 \times 10^3 \text{ mm}$	Height of the URM infill wall
$L := 150 \text{ in}$	$L = 3.81 \times 10^3 \text{ mm}$	Width of the URM infill wall
$t := 3.75 \text{ in}$	$t = 95.25 \text{ mm}$	Thickness of the URM infill wall
$I_c := \frac{(12 \text{ in})^4}{12}$	$I_c = 7.192 \times 10^8 \text{ mm}^4$	Moment of inertia of the column
$J_c := 2 \cdot I_c$	$J_c = 1.438 \times 10^9 \text{ mm}^4$	Torsional moment of inertia of the column
$I_b := \frac{[10.5 \text{ in} \cdot (13.5 \text{ in})^3]}{12}$	$I_b = 8.961 \times 10^8 \text{ mm}^4$	Moment of inertia of the beam
$J_b := 2 \cdot I_b$	$J_b = 1.792 \times 10^9 \text{ mm}^4$	Torsional moment of inertia of the beam
$f_m := 2.46 \text{ ksi}$	$f_m = 1.696 \times 10^7 \text{ Pa}$	Masonry compressive strength
$\alpha := \frac{1}{\left(\frac{h}{\text{mm}}\right)} \cdot \left[\frac{E_c}{\text{MPa}} \cdot \frac{I_c}{\text{mm}^4} \cdot \left(\frac{h}{\text{mm}}\right)^2 + \frac{G_c}{\text{MPa}} \cdot \frac{J_c}{\text{mm}^4} \cdot \frac{t}{\text{mm}} \cdot \frac{h}{\text{mm}} \right]^{0.25}$		Use consistent units!! α and β in $F^{0.25}$
$\beta := \frac{1}{\left(\frac{L}{\text{mm}}\right)} \cdot \left[\frac{E_c}{\text{MPa}} \cdot \frac{I_b}{\text{mm}^4} \cdot \left(\frac{L}{\text{mm}}\right)^2 + \frac{G_c}{\text{MPa}} \cdot \frac{J_b}{\text{mm}^4} \cdot \frac{t}{\text{mm}} \cdot \frac{L}{\text{mm}} \right]^{0.25}$		$\beta = 36.729$
$q_{OP} := 4.5 \cdot \left(\frac{f_m}{1 \text{ kPa}}\right)^{0.75} \cdot \left(\frac{t}{1 \text{ mm}}\right)^2 \cdot \left[\frac{\alpha}{\left(\frac{L}{1 \text{ mm}}\right)^{2.5}} + \frac{\beta}{\left(\frac{h}{1 \text{ mm}}\right)^{2.5}} \right] \cdot \text{kPa}$		
$q_{OP} = 9.517 \text{ kPa}$	$q_{OP} = 1.38 \text{ psi}$	Out-of-plane capacity of the URM infill wall

Appendix E: Formulation of 3D SAT Model for URM Infill Walls

In this appendix, the calibration calculations to determine the area and effective thickness of the three-dimensional strut and tie (3D SAT) model for URM masonry infill walls are shown. The calculations presented are parts of a MathCad spreadsheet and include the formulation as well as the definition and value of each parameter used in the application of the 3D SAT model for the URM infill walls used in this study.

Calibration of the 3D SAT model to match the results of the FE analysis:

$R_{H_target} := 111 \text{ kip}$ In-plane target capacity from FE analysis

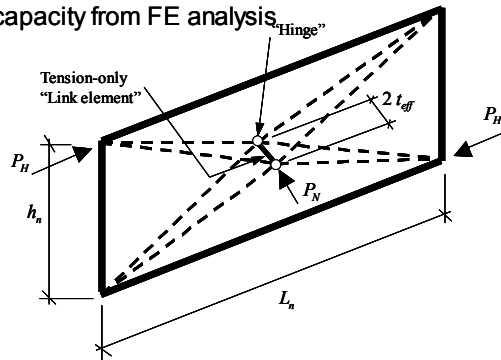
$R_{N_target} := 11 \text{ kip}$ Out-of-plane target capacity from FE analysis

$L_n := 150 \text{ in}$

$h_n := 101 \text{ in}$

$t := 3.75 \text{ in}$

$f_{mo} := 2.46 \text{ ksi}$



In-plane capacity

First we subtract the contribution of the RC frame from the lateral capacity of the infill at estimated failure displacement of the wall, namely 0.61 inches. Assuming that the frame is still elastic at this point, with lateral stiffness of 40 kip/in, the modified lateral capacity for the infill is obtained as follows:

$$R_{H_modified} := R_{H_target} - (0.61 \cdot \text{in}) \cdot \left(40 \cdot \frac{\text{kip}}{\text{in}} \right) \quad R_{H_modified} = 86.6 \text{ kip}$$

From statics:

$$\text{Force in each diagonal strut} = \frac{A_{total}}{2} \cdot f_m := \frac{\sqrt{\left(\frac{L_n}{2}\right)^2 + \left(\frac{h_n}{2}\right)^2 + t_{eff}^2}}{L_n} \cdot R_{H_modified}$$

Assuming that t_{eff} is small with respect to L_n and h_n :

$$A_{total} := 2 \cdot \frac{\sqrt{\left(\frac{L_n}{2}\right)^2 + \left(\frac{h_n}{2}\right)^2}}{L_n} \cdot \frac{R_{H_modified}}{f_{mo}} \quad A_{total} = 42.44 \text{ in}^2$$

Out-of-plane capacity

To determine the out-of-plane capacity of the 3D SAT model, it is more convenient to use an iterative approach. First a value for t_{eff} is assumed and the capacity of the SAT assembly is determined as follows. The estimated value is modified until the desired capacity is reached.

Try: $t_{eff} := 10 \text{ in}$

$$A_d := \frac{A_{total}}{2} \quad \text{Area of each strut}$$

$$d := \sqrt{\left(\frac{L_n}{2}\right)^2 + \left(\frac{h_n}{2}\right)^2} \quad d_s := \sqrt{t_{eff}^2 + d^2} \quad d_s = 90.968 \text{ in} \quad \text{Length of each strut}$$

Assumed material properties for masonry material:

$$\varepsilon_{mo} := 0.0028 \quad \varepsilon_y := 2 \cdot \varepsilon_{mo} \quad \text{adjusted to achieve required shape of failure surface}$$

$$\sigma(\varepsilon) := \frac{-f_{mo}}{\varepsilon_y} \varepsilon^2 + 2 \frac{f_{mo}}{\varepsilon_y} \varepsilon \quad \text{Parabolic material } \sigma\text{-}\varepsilon \text{ relationship for masonry is assumed with peak stress } f_{mo} \text{ and corresponding strain } \varepsilon_{mo}$$

$$\varepsilon(\sigma) := \varepsilon_y \left(1 - \sqrt{1 - \frac{\sigma}{f_{mo}}} \right)$$

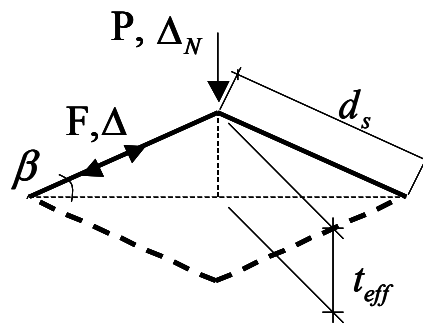
From kinematics of the 3D SAT model, considering the nonlinear geometry as shown in figure below we have:

$$\beta = \sin^{-1} \left(\frac{t_{eff} - \Delta_N}{d_s} \right)$$

$$\Delta_N = \frac{\Delta}{\sin \beta}$$

$$\Delta = \frac{t_{eff} - \Delta_N}{d_s} \Delta_N$$

$$P = 4F \sin \beta$$

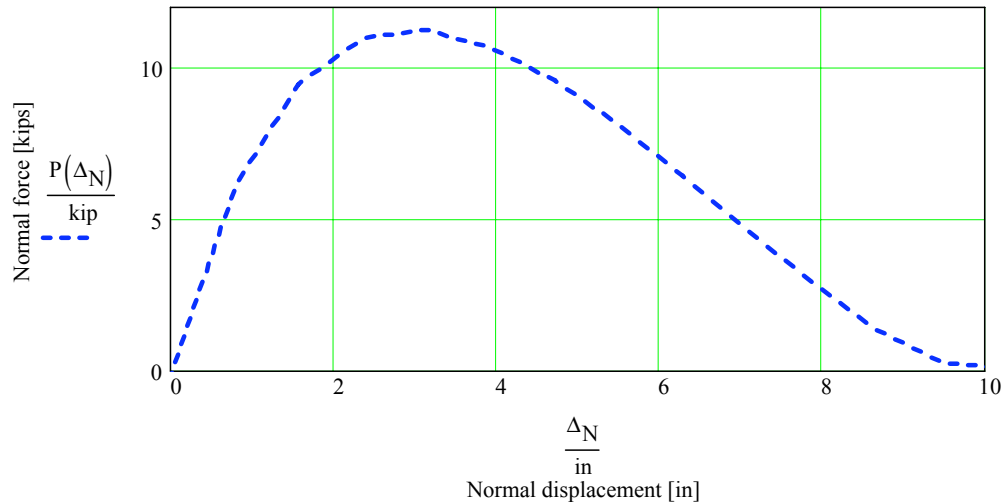


where, Δ is the axial deformation of the strut and Δ_N is the out-of-plane deformation of the 3D SAT model.

$$\Delta(\Delta_N) := \frac{t_{\text{eff}} - \Delta_N}{d_s} \cdot \Delta_N$$

$$\varepsilon(\Delta_N) := \frac{\Delta(\Delta_N)}{d_s} \quad \text{strain in each strut due to the out-of-plane force}$$

$$P(\Delta_N) := \sigma(\varepsilon(\Delta_N)) \cdot A_d \cdot \left(4 \frac{t_{\text{eff}} - \Delta_N}{d_s} \right) \quad \text{Out-of-plane resistance of the 3D SAT assembly}$$



$$x := 5$$

$$x_2 := 5 \text{ in}$$

Given

$$x \geq 0 \quad x \leq \frac{t_{\text{eff}}}{\text{in}}$$

$$X := \text{Maximize}(P, x_2) \quad X = 2.937 \text{ in} \quad P(X) = 11.266 \text{ kip}$$

Check:

$$\Delta_N := X \quad \Delta := \frac{t_{\text{eff}} - \Delta_N}{d_s} \cdot \Delta_N \quad \Delta = 0.228 \text{ in}$$

$$\varepsilon_m := \frac{\Delta}{d_s} \quad \varepsilon_m = 2.507 \times 10^{-3} \quad F := \sigma(\varepsilon_m) \cdot A_d \quad F = 36.273 \text{ kip}$$

$$\beta := \text{atan}\left(\frac{t_{\text{eff}} - \Delta_N}{d}\right) \quad P := 4 \cdot F \cdot \sin(\beta) \quad P = 11.3 \text{ kip} \quad \text{Close enough!}$$

PEER REPORTS

PEER reports are available from the National Information Service for Earthquake Engineering (NISEE). To order PEER reports, please contact the Pacific Earthquake Engineering Research Center, 1301 South 46th Street, Richmond, California 94804-4698. Tel.: (510) 665-3405; Fax: (510) 665-3420.

- PEER 2007/02** *Campbell-Bozorgnia NGA Ground Motion Relations for the Geometric Mean Horizontal Component of Peak and Spectral Ground Motion Parameters.* Kenneth W. Campbell and Yousef Bozorgnia. May 2007.
- PEER 2007/01** *Boore-Atkinson NGA Ground Motion Relations for the Geometric Mean Horizontal Component of Peak and Spectral Ground Motion Parameters.* David M. Boore and Gail M. Atkinson. May. May 2007.
- PEER 2006/12** *Societal Implications of Performance-Based Earthquake Engineering.* Peter J. May. May 2007.
- PEER 2006/11** *Probabilistic Seismic Demand Analysis Using Advanced Ground Motion Intensity Measures, Attenuation Relationships, and Near-Fault Effects.* Polsak Tothong and C. Allin Cornell. March 2007.
- PEER 2006/10** *Application of the PEER PBEE Methodology to the I-880 Viaduct.* Sashi Kunnath. February 2007.
- PEER 2006/09** *Quantifying Economic Losses from Travel Forgone Following a Large Metropolitan Earthquake.* James Moore, Sungbin Cho, Yue Yue Fan, and Stuart Werner. November 2006.
- PEER 2006/08** *Vector-Valued Ground Motion Intensity Measures for Probabilistic Seismic Demand Analysis.* Jack W. Baker and C. Allin Cornell. October 2006.
- PEER 2006/07** *Analytical Modeling of Reinforced Concrete Walls for Predicting Flexural and Coupled-Shear-Flexural Responses.* Kutay Orakcal, Loenardo M. Massone, and John W. Wallace. October 2006.
- PEER 2006/06** *Nonlinear Analysis of a Soil-Drilled Pier System under Static and Dynamic Axial Loading.* Gang Wang and Nicholas Sitar. November 2006.
- PEER 2006/05** *Advanced Seismic Assessment Guidelines.* Paolo Bazzurro, C. Allin Cornell, Charles Menun, Maziar Motahari, and Nicolas Luco. September 2006.
- PEER 2006/04** *Probabilistic Seismic Evaluation of Reinforced Concrete Structural Components and Systems.* Tae Hyung Lee and Khalid M. Mosalam. August 2006.
- PEER 2006/03** *Performance of Lifelines Subjected to Lateral Spreading.* Scott A. Ashford and Teerawut Juirnarongrit. July 2006.
- PEER 2006/02** *Pacific Earthquake Engineering Research Center Highway Demonstration Project.* Anne Kiremidjian, James Moore, Yue Yue Fan, Nesrin Basoz, Ozgur Yazali, and Meredith Williams. April 2006.
- PEER 2006/01** *Bracing Berkeley. A Guide to Seismic Safety on the UC Berkeley Campus.* Mary C. Comerio, Stephen Tobriner, and Ariane Fehrenkamp. January 2006.
- PEER 2005/16** *Seismic Response and Reliability of Electrical Substation Equipment and Systems.* Junho Song, Armen Der Kiureghian, and Jerome L. Sackman. April 2006.
- PEER 2005/15** *CPT-Based Probabilistic Assessment of Seismic Soil Liquefaction Initiation.* R. E. S. Moss, R. B. Seed, R. E. Kayen, J. P. Stewart, and A. Der Kiureghian. April 2006.
- PEER 2005/14** *Workshop on Modeling of Nonlinear Cyclic Load-Deformation Behavior of Shallow Foundations.* Bruce L. Kutter, Geoffrey Martin, Tara Hutchinson, Chad Harden, Sivapalan Gajan, and Justin Phalen. March 2006.
- PEER 2005/13** *Stochastic Characterization and Decision Bases under Time-Dependent Aftershock Risk in Performance-Based Earthquake Engineering.* Gee Liek Yeo and C. Allin Cornell. July 2005.
- PEER 2005/12** *PEER Testbed Study on a Laboratory Building: Exercising Seismic Performance Assessment.* Mary C. Comerio, editor. November 2005.
- PEER 2005/11** *Van Nuys Hotel Building Testbed Report: Exercising Seismic Performance Assessment.* Helmut Krawinkler, editor. October 2005.
- PEER 2005/10** *First NEES/E-Defense Workshop on Collapse Simulation of Reinforced Concrete Building Structures.* September 2005.
- PEER 2005/09** *Test Applications of Advanced Seismic Assessment Guidelines.* Joe Maffei, Karl Telleen, Danya Mohr, William Holmes, and Yuki Nakayama. August 2006.
- PEER 2005/08** *Damage Accumulation in Lightly Confined Reinforced Concrete Bridge Columns.* R. Tyler Ranf, Jared M. Nelson, Zach Price, Marc O. Eberhard, and John F. Stanton. April 2006.

- PEER 2005/07** *Experimental and Analytical Studies on the Seismic Response of Freestanding and Anchored Laboratory Equipment.* Dimitrios Konstantinidis and Nicos Makris. January 2005.
- PEER 2005/06** *Global Collapse of Frame Structures under Seismic Excitations.* Luis F. Ibarra and Helmut Krawinkler. September 2005.
- PEER 2005/05** *Performance Characterization of Bench- and Shelf-Mounted Equipment.* Samit Ray Chaudhuri and Tara C. Hutchinson. May 2006.
- PEER 2005/04** *Numerical Modeling of the Nonlinear Cyclic Response of Shallow Foundations.* Chad Harden, Tara Hutchinson, Geoffrey R. Martin, and Bruce L. Kutter. August 2005.
- PEER 2005/03** *A Taxonomy of Building Components for Performance-Based Earthquake Engineering.* Keith A. Porter. September 2005.
- PEER 2005/02** *Fragility Basis for California Highway Overpass Bridge Seismic Decision Making.* Kevin R. Mackie and Bozidar Stojadinovic. June 2005.
- PEER 2005/01** *Empirical Characterization of Site Conditions on Strong Ground Motion.* Jonathan P. Stewart, Yoojoong Choi, and Robert W. Graves. June 2005.
- PEER 2004/09** *Electrical Substation Equipment Interaction: Experimental Rigid Conductor Studies.* Christopher Stearns and André Filiatrault. February 2005.
- PEER 2004/08** *Seismic Qualification and Fragility Testing of Line Break 550-kV Disconnect Switches.* Shakhzod M. Takhirov, Gregory L. Fenves, and Eric Fujisaki. January 2005.
- PEER 2004/07** *Ground Motions for Earthquake Simulator Qualification of Electrical Substation Equipment.* Shakhzod M. Takhirov, Gregory L. Fenves, Eric Fujisaki, and Don Clyde. January 2005.
- PEER 2004/06** *Performance-Based Regulation and Regulatory Regimes.* Peter J. May and Chris Koski. September 2004.
- PEER 2004/05** *Performance-Based Seismic Design Concepts and Implementation: Proceedings of an International Workshop.* Peter Fajfar and Helmut Krawinkler, editors. September 2004.
- PEER 2004/04** *Seismic Performance of an Instrumented Tilt-up Wall Building.* James C. Anderson and Vitelmo V. Bertero. July 2004.
- PEER 2004/03** *Evaluation and Application of Concrete Tilt-up Assessment Methodologies.* Timothy Graf and James O. Malley. October 2004.
- PEER 2004/02** *Analytical Investigations of New Methods for Reducing Residual Displacements of Reinforced Concrete Bridge Columns.* Junichi Sakai and Stephen A. Mahin. August 2004.
- PEER 2004/01** *Seismic Performance of Masonry Buildings and Design Implications.* Kerri Anne Taeko Tokoro, James C. Anderson, and Vitelmo V. Bertero. February 2004.
- PEER 2003/18** *Performance Models for Flexural Damage in Reinforced Concrete Columns.* Michael Berry and Marc Eberhard. August 2003.
- PEER 2003/17** *Predicting Earthquake Damage in Older Reinforced Concrete Beam-Column Joints.* Catherine Pagni and Laura Lowes. October 2004.
- PEER 2003/16** *Seismic Demands for Performance-Based Design of Bridges.* Kevin Mackie and Božidar Stojadinovic. August 2003.
- PEER 2003/15** *Seismic Demands for Nondeteriorating Frame Structures and Their Dependence on Ground Motions.* Ricardo Antonio Medina and Helmut Krawinkler. May 2004.
- PEER 2003/14** *Finite Element Reliability and Sensitivity Methods for Performance-Based Earthquake Engineering.* Terje Haukaas and Armen Der Kiureghian. April 2004.
- PEER 2003/13** *Effects of Connection Hysteretic Degradation on the Seismic Behavior of Steel Moment-Resisting Frames.* Janise E. Rodgers and Stephen A. Mahin. March 2004.
- PEER 2003/12** *Implementation Manual for the Seismic Protection of Laboratory Contents: Format and Case Studies.* William T. Holmes and Mary C. Comerio. October 2003.
- PEER 2003/11** *Fifth U.S.-Japan Workshop on Performance-Based Earthquake Engineering Methodology for Reinforced Concrete Building Structures.* February 2004.
- PEER 2003/10** *A Beam-Column Joint Model for Simulating the Earthquake Response of Reinforced Concrete Frames.* Laura N. Lowes, Nilanjan Mitra, and Arash Altoontash. February 2004.
- PEER 2003/09** *Sequencing Repairs after an Earthquake: An Economic Approach.* Marco Casari and Simon J. Wilkie. April 2004.

- PEER 2003/08** *A Technical Framework for Probability-Based Demand and Capacity Factor Design (DCFD) Seismic Formats.* Fatemeh Jalayer and C. Allin Cornell. November 2003.
- PEER 2003/07** *Uncertainty Specification and Propagation for Loss Estimation Using FOSM Methods.* Jack W. Baker and C. Allin Cornell. September 2003.
- PEER 2003/06** *Performance of Circular Reinforced Concrete Bridge Columns under Bidirectional Earthquake Loading.* Mahmoud M. Hachem, Stephen A. Mahin, and Jack P. Moehle. February 2003.
- PEER 2003/05** *Response Assessment for Building-Specific Loss Estimation.* Eduardo Miranda and Shahram Taghavi. September 2003.
- PEER 2003/04** *Experimental Assessment of Columns with Short Lap Splices Subjected to Cyclic Loads.* Murat Melek, John W. Wallace, and Joel Conte. April 2003.
- PEER 2003/03** *Probabilistic Response Assessment for Building-Specific Loss Estimation.* Eduardo Miranda and Hesameddin Aslani. September 2003.
- PEER 2003/02** *Software Framework for Collaborative Development of Nonlinear Dynamic Analysis Program.* Jun Peng and Kincho H. Law. September 2003.
- PEER 2003/01** *Shake Table Tests and Analytical Studies on the Gravity Load Collapse of Reinforced Concrete Frames.* Kenneth John Elwood and Jack P. Moehle. November 2003.
- PEER 2002/24** *Performance of Beam to Column Bridge Joints Subjected to a Large Velocity Pulse.* Natalie Gibson, André Filiatrault, and Scott A. Ashford. April 2002.
- PEER 2002/23** *Effects of Large Velocity Pulses on Reinforced Concrete Bridge Columns.* Greg L. Orozco and Scott A. Ashford. April 2002.
- PEER 2002/22** *Characterization of Large Velocity Pulses for Laboratory Testing.* Kenneth E. Cox and Scott A. Ashford. April 2002.
- PEER 2002/21** *Fourth U.S.-Japan Workshop on Performance-Based Earthquake Engineering Methodology for Reinforced Concrete Building Structures.* December 2002.
- PEER 2002/20** *Barriers to Adoption and Implementation of PBEE Innovations.* Peter J. May. August 2002.
- PEER 2002/19** *Economic-Engineered Integrated Models for Earthquakes: Socioeconomic Impacts.* Peter Gordon, James E. Moore II, and Harry W. Richardson. July 2002.
- PEER 2002/18** *Assessment of Reinforced Concrete Building Exterior Joints with Substandard Details.* Chris P. Pantelides, Jon Hansen, Justin Nadauld, and Lawrence D. Reaveley. May 2002.
- PEER 2002/17** *Structural Characterization and Seismic Response Analysis of a Highway Overcrossing Equipped with Elastomeric Bearings and Fluid Dampers: A Case Study.* Nicos Makris and Jian Zhang. November 2002.
- PEER 2002/16** *Estimation of Uncertainty in Geotechnical Properties for Performance-Based Earthquake Engineering.* Allen L. Jones, Steven L. Kramer, and Pedro Arduino. December 2002.
- PEER 2002/15** *Seismic Behavior of Bridge Columns Subjected to Various Loading Patterns.* Asadollah Esmaeily-Gh. and Yan Xiao. December 2002.
- PEER 2002/14** *Inelastic Seismic Response of Extended Pile Shaft Supported Bridge Structures.* T.C. Hutchinson, R.W. Boulanger, Y.H. Chai, and I.M. Idriss. December 2002.
- PEER 2002/13** *Probabilistic Models and Fragility Estimates for Bridge Components and Systems.* Paolo Gardoni, Armen Der Kiureghian, and Khalid M. Mosalam. June 2002.
- PEER 2002/12** *Effects of Fault Dip and Slip Rake on Near-Source Ground Motions: Why Chi-Chi Was a Relatively Mild M7.6 Earthquake.* Brad T. Aagaard, John F. Hall, and Thomas H. Heaton. December 2002.
- PEER 2002/11** *Analytical and Experimental Study of Fiber-Reinforced Strip Isolators.* James M. Kelly and Shakhzod M. Takhirov. September 2002.
- PEER 2002/10** *Centrifuge Modeling of Settlement and Lateral Spreading with Comparisons to Numerical Analyses.* Sivapalan Gajan and Bruce L. Kutter. January 2003.
- PEER 2002/09** *Documentation and Analysis of Field Case Histories of Seismic Compression during the 1994 Northridge, California, Earthquake.* Jonathan P. Stewart, Patrick M. Smith, Daniel H. Whang, and Jonathan D. Bray. October 2002.
- PEER 2002/08** *Component Testing, Stability Analysis and Characterization of Buckling-Restrained Unbonded Braces™.* Cameron Black, Nicos Makris, and Ian Aiken. September 2002.

- PEER 2002/07** *Seismic Performance of Pile-Wharf Connections*. Charles W. Roeder, Robert Graff, Jennifer Soderstrom, and Jun Han Yoo. December 2001.
- PEER 2002/06** *The Use of Benefit-Cost Analysis for Evaluation of Performance-Based Earthquake Engineering Decisions*. Richard O. Zerbe and Anthony Falit-Baiamonte. September 2001.
- PEER 2002/05** *Guidelines, Specifications, and Seismic Performance Characterization of Nonstructural Building Components and Equipment*. André Filiatrault, Constantin Christopoulos, and Christopher Stearns. September 2001.
- PEER 2002/04** *Consortium of Organizations for Strong-Motion Observation Systems and the Pacific Earthquake Engineering Research Center Lifelines Program: Invited Workshop on Archiving and Web Dissemination of Geotechnical Data, 4–5 October 2001*. September 2002.
- PEER 2002/03** *Investigation of Sensitivity of Building Loss Estimates to Major Uncertain Variables for the Van Nuys Testbed*. Keith A. Porter, James L. Beck, and Rustem V. Shaikhutdinov. August 2002.
- PEER 2002/02** *The Third U.S.-Japan Workshop on Performance-Based Earthquake Engineering Methodology for Reinforced Concrete Building Structures*. July 2002.
- PEER 2002/01** *Nonstructural Loss Estimation: The UC Berkeley Case Study*. Mary C. Comerio and John C. Stallmeyer. December 2001.
- PEER 2001/16** *Statistics of SDF-System Estimate of Roof Displacement for Pushover Analysis of Buildings*. Anil K. Chopra, Rakesh K. Goel, and Chatpan Chintanapakdee. December 2001.
- PEER 2001/15** *Damage to Bridges during the 2001 Nisqually Earthquake*. R. Tyler Ranf, Marc O. Eberhard, and Michael P. Berry. November 2001.
- PEER 2001/14** *Rocking Response of Equipment Anchored to a Base Foundation*. Nicos Makris and Cameron J. Black. September 2001.
- PEER 2001/13** *Modeling Soil Liquefaction Hazards for Performance-Based Earthquake Engineering*. Steven L. Kramer and Ahmed-W. Elgamal. February 2001.
- PEER 2001/12** *Development of Geotechnical Capabilities in OpenSees*. Boris Jeremi . September 2001.
- PEER 2001/11** *Analytical and Experimental Study of Fiber-Reinforced Elastomeric Isolators*. James M. Kelly and Shakhzod M. Takhirov. September 2001.
- PEER 2001/10** *Amplification Factors for Spectral Acceleration in Active Regions*. Jonathan P. Stewart, Andrew H. Liu, Yoojoong Choi, and Mehmet B. Baturay. December 2001.
- PEER 2001/09** *Ground Motion Evaluation Procedures for Performance-Based Design*. Jonathan P. Stewart, Shyh-Jeng Chiou, Jonathan D. Bray, Robert W. Graves, Paul G. Somerville, and Norman A. Abrahamson. September 2001.
- PEER 2001/08** *Experimental and Computational Evaluation of Reinforced Concrete Bridge Beam-Column Connections for Seismic Performance*. Clay J. Naito, Jack P. Moehle, and Khalid M. Mosalam. November 2001.
- PEER 2001/07** *The Rocking Spectrum and the Shortcomings of Design Guidelines*. Nicos Makris and Dimitrios Konstantinidis. August 2001.
- PEER 2001/06** *Development of an Electrical Substation Equipment Performance Database for Evaluation of Equipment Fragilities*. Thalia Agnanos. April 1999.
- PEER 2001/05** *Stiffness Analysis of Fiber-Reinforced Elastomeric Isolators*. Hsiang-Chuan Tsai and James M. Kelly. May 2001.
- PEER 2001/04** *Organizational and Societal Considerations for Performance-Based Earthquake Engineering*. Peter J. May. April 2001.
- PEER 2001/03** *A Modal Pushover Analysis Procedure to Estimate Seismic Demands for Buildings: Theory and Preliminary Evaluation*. Anil K. Chopra and Rakesh K. Goel. January 2001.
- PEER 2001/02** *Seismic Response Analysis of Highway Overcrossings Including Soil-Structure Interaction*. Jian Zhang and Nicos Makris. March 2001.
- PEER 2001/01** *Experimental Study of Large Seismic Steel Beam-to-Column Connections*. Egor P. Popov and Shakhzod M. Takhirov. November 2000.
- PEER 2000/10** *The Second U.S.-Japan Workshop on Performance-Based Earthquake Engineering Methodology for Reinforced Concrete Building Structures*. March 2000.
- PEER 2000/09** *Structural Engineering Reconnaissance of the August 17, 1999 Earthquake: Kocaeli (Izmit), Turkey*. Halil Sezen, Kenneth J. Elwood, Andrew S. Whittaker, Khalid Mosalam, John J. Wallace, and John F. Stanton. December 2000.

- PEER 2000/08** *Behavior of Reinforced Concrete Bridge Columns Having Varying Aspect Ratios and Varying Lengths of Confinement.* Anthony J. Calderone, Dawn E. Lehman, and Jack P. Moehle. January 2001.
- PEER 2000/07** *Cover-Plate and Flange-Plate Reinforced Steel Moment-Resisting Connections.* Taejin Kim, Andrew S. Whittaker, Amir S. Gilani, Vitelmo V. Bertero, and Shakhzod M. Takhirov. September 2000.
- PEER 2000/06** *Seismic Evaluation and Analysis of 230-kV Disconnect Switches.* Amir S. J. Gilani, Andrew S. Whittaker, Gregory L. Fenves, Chun-Hao Chen, Henry Ho, and Eric Fujisaki. July 2000.
- PEER 2000/05** *Performance-Based Evaluation of Exterior Reinforced Concrete Building Joints for Seismic Excitation.* Chandra Clyde, Chris P. Pantelides, and Lawrence D. Reaveley. July 2000.
- PEER 2000/04** *An Evaluation of Seismic Energy Demand: An Attenuation Approach.* Chung-Che Chou and Chia-Ming Uang. July 1999.
- PEER 2000/03** *Framing Earthquake Retrofitting Decisions: The Case of Hillside Homes in Los Angeles.* Detlof von Winterfeldt, Nels Roselund, and Alicia Kitsuse. March 2000.
- PEER 2000/02** *U.S.-Japan Workshop on the Effects of Near-Field Earthquake Shaking.* Andrew Whittaker, ed. July 2000.
- PEER 2000/01** *Further Studies on Seismic Interaction in Interconnected Electrical Substation Equipment.* Armen Der Kiureghian, Kee-Jeung Hong, and Jerome L. Sackman. November 1999.
- PEER 1999/14** *Seismic Evaluation and Retrofit of 230-kV Porcelain Transformer Bushings.* Amir S. Gilani, Andrew S. Whittaker, Gregory L. Fenves, and Eric Fujisaki. December 1999.
- PEER 1999/13** *Building Vulnerability Studies: Modeling and Evaluation of Tilt-up and Steel Reinforced Concrete Buildings.* John W. Wallace, Jonathan P. Stewart, and Andrew S. Whittaker, editors. December 1999.
- PEER 1999/12** *Rehabilitation of Nonductile RC Frame Building Using Encasement Plates and Energy-Dissipating Devices.* Mehrdad Sasani, Vitelmo V. Bertero, James C. Anderson. December 1999.
- PEER 1999/11** *Performance Evaluation Database for Concrete Bridge Components and Systems under Simulated Seismic Loads.* Yael D. Hose and Frieder Seible. November 1999.
- PEER 1999/10** *U.S.-Japan Workshop on Performance-Based Earthquake Engineering Methodology for Reinforced Concrete Building Structures.* December 1999.
- PEER 1999/09** *Performance Improvement of Long Period Building Structures Subjected to Severe Pulse-Type Ground Motions.* James C. Anderson, Vitelmo V. Bertero, and Raul Bertero. October 1999.
- PEER 1999/08** *Envelopes for Seismic Response Vectors.* Charles Menun and Armen Der Kiureghian. July 1999.
- PEER 1999/07** *Documentation of Strengths and Weaknesses of Current Computer Analysis Methods for Seismic Performance of Reinforced Concrete Members.* William F. Cofer. November 1999.
- PEER 1999/06** *Rocking Response and Overturning of Anchored Equipment under Seismic Excitations.* Nicos Makris and Jian Zhang. November 1999.
- PEER 1999/05** *Seismic Evaluation of 550 kV Porcelain Transformer Bushings.* Amir S. Gilani, Andrew S. Whittaker, Gregory L. Fenves, and Eric Fujisaki. October 1999.
- PEER 1999/04** *Adoption and Enforcement of Earthquake Risk-Reduction Measures.* Peter J. May, Raymond J. Burby, T. Jens Feeley, and Robert Wood.
- PEER 1999/03** *Task 3 Characterization of Site Response General Site Categories.* Adrian Rodriguez-Marek, Jonathan D. Bray, and Norman Abrahamson. February 1999.
- PEER 1999/02** *Capacity-Demand-Diagram Methods for Estimating Seismic Deformation of Inelastic Structures: SDF Systems.* Anil K. Chopra and Rakesh Goel. April 1999.
- PEER 1999/01** *Interaction in Interconnected Electrical Substation Equipment Subjected to Earthquake Ground Motions.* Armen Der Kiureghian, Jerome L. Sackman, and Kee-Jeung Hong. February 1999.
- PEER 1998/08** *Behavior and Failure Analysis of a Multiple-Frame Highway Bridge in the 1994 Northridge Earthquake.* Gregory L. Fenves and Michael Ellery. December 1998.
- PEER 1998/07** *Empirical Evaluation of Inertial Soil-Structure Interaction Effects.* Jonathan P. Stewart, Raymond B. Seed, and Gregory L. Fenves. November 1998.
- PEER 1998/06** *Effect of Damping Mechanisms on the Response of Seismic Isolated Structures.* Nicos Makris and Shih-Po Chang. November 1998.
- PEER 1998/05** *Rocking Response and Overturning of Equipment under Horizontal Pulse-Type Motions.* Nicos Makris and Yiannis Roussos. October 1998.

- PEER 1998/04** *Pacific Earthquake Engineering Research Invitational Workshop Proceedings, May 14–15, 1998: Defining the Links between Planning, Policy Analysis, Economics and Earthquake Engineering.* Mary Comerio and Peter Gordon. September 1998.
- PEER 1998/03** *Repair/Upgrade Procedures for Welded Beam to Column Connections.* James C. Anderson and Xiaojing Duan. May 1998.
- PEER 1998/02** *Seismic Evaluation of 196 kV Porcelain Transformer Bushings.* Amir S. Gilani, Juan W. Chavez, Gregory L. Fennes, and Andrew S. Whittaker. May 1998.
- PEER 1998/01** *Seismic Performance of Well-Confined Concrete Bridge Columns.* Dawn E. Lehman and Jack P. Moehle. December 2000.

ONLINE REPORTS

The following PEER reports are available by Internet only at http://peer.berkeley.edu/publications/peer_reports.html

PEER 2007/101 *Generalized Hybrid Simulation Framework for Structural Systems Subjected to Seismic Loading.* Tarek Elkhoraibi and Khalid M. Mosalam. July 2007.

PEER 2007/100 *Seismic Evaluation of Reinforced Concrete Buildings Including Effects of Masonry Infill Walls.* Alidad Hashemi and Khalid M. Mosalam. July 2007.